



HAL
open science

Effect of the fuel composition of syngas on the combustion process in Dual-Fuel engine

Ricardo Rabello de Castro

► **To cite this version:**

Ricardo Rabello de Castro. Effect of the fuel composition of syngas on the combustion process in Dual-Fuel engine. Mechanics [physics.med-ph]. Université d'Orléans, 2024. English. NNT : 2024ORLE1032 . tel-04839641

HAL Id: tel-04839641

<https://theses.hal.science/tel-04839641v1>

Submitted on 16 Dec 2024

HAL is a multi-disciplinary open access archive for the deposit and dissemination of scientific research documents, whether they are published or not. The documents may come from teaching and research institutions in France or abroad, or from public or private research centers.

L'archive ouverte pluridisciplinaire **HAL**, est destinée au dépôt et à la diffusion de documents scientifiques de niveau recherche, publiés ou non, émanant des établissements d'enseignement et de recherche français ou étrangers, des laboratoires publics ou privés.

UNIVERSIT  D'ORL ANS

* COLE DOCTORALE : ENERGIE, MATERIAUX, SCIENCES DE
LA TERRE ET DE L'UNIVERS*

Laboratoire PRISME

TH SE pr sent e par :

Ricardo RABELLO DE CASTRO

soutenue le : **04 d cembre 2024**

pour obtenir le grade de: **Docteur de l'Universit  d'Orl ans**

Discipline/ Sp cialit : Energ tique, M canique

Effect of the fuel composition of syngas on the combustion process in Dual-Fuel engine

TH SE dirig e par :

Mme. MOUNA M-ROUSSELLE Christine Professeur, Universit  d'Orl ans – PRISME

ENCADRANT :

M. BR QUIGNY Pierre Ma tre de conf rences, Universit  d'Orl ans- PRISME

RAPPORTEURS :

M. JEANMART Herv  Professeur, Universit  Catholique de Louvain, Belgique

M. BELLENOUE Marc Professeur des Universit s, PPRIME-ENSMA, Poitiers

JURY :

M. RENOU Bruno Professeur, INSA Rouen, Pr sident du jury

M. FIGUEIRA Luis Fernando Charg  de recherche CNRS, PPRIME, Poitiers

M. DURAISAMY Ganesh Professeur, Anna University, India

Table of Contents

<i>Acknowledgements</i>	5
Nomenclature.....	6
List of tables	8
List of figures	9
French summary of this thesis	13
1. Introduction.....	29
1.1. Synthesis gas (Syngas)	34
1.1.1. Feedstock types.....	34
1.1.2. Types of gasifiers	35
1.1.3. Syngas cleaning methods	38
1.1.4. Choice of different syngas compositions during this study.....	39
1.2. Syngas as a fuel for power generation	40
1.2.1. Gas turbines: Integrated Gasification Combined Cycle (IGCC).....	40
1.2.2. Internal Combustion Engines (ICE).....	41
1.3. Plan of this manuscript.....	42
2. State of the art in syngas/diesel dual-fuel engine: performance and emissions research .	43
3. Experimental characteristics of laminar syngas/air premixed flame	49
3.1. Introduction.....	49
3.1.1. Laminar flame propagation	50
3.2. Experimental Set-up	53
3.2.1. Uncertainty Analysis on the experimental value of S_u^0	58
3.2.2. Laminar flame speed simulation	58
3.3. Background Literature: the case of syngas.....	61
3.4. Results and discussion.....	63
3.4.1. Laminar flame speed	63
3.4.2. Laminar Flame Speed Dependence on Initial Pressure and Temperature	71
3.4.3. Markstein length	73
3.4.4. Laminar speed of syngas/decane mixtures	77
3.5. Conclusion	81

4.	A multiparameter analysis of syngas/diesel dual-fuel engine performance and emissions with the three syngas compositions	83
4.1.	Introduction.....	83
4.2.	Experimental set-up and post-processing	84
4.2.1.	Experimental Set-up	84
4.2.2.	Post-processing method.....	86
4.2.3.	Determination of the injected decane mass	87
4.3.	Results and discussion.....	88
4.3.1.	Effect of premixed equivalence ratio.....	88
4.3.2.	Effect of pilot fuel injection quantity.....	94
4.3.3.	Effect of CH ₄ and CO ₂ concentration	99
4.3.4.	Relationship between fundamental composition properties and engine operation 103	
4.4.	Conclusion	106
5.	Visualization of the syngas/diesel dual-fuel combustion in an optically-accessible engine 107	
5.1.	State of art of Chemiluminescence studies for syngas combustion in ICE.....	107
5.2.	Experimental set-up	110
5.2.1.	Optical imaging set-up.....	112
5.2.2.	Imaging post-processing.....	115
5.3.	Results and discussion.....	115
5.3.1.	The case of the decane pilot injection by itself.....	115
5.3.2.	Comparison of the different syngas compositions	117
5.3.3.	Effect of the CO ₂ and CH ₄ content on the syngas composition.	122
5.4.	Conclusions	132
6.	Final conclusions and suggestions for future work.....	133
	Bibliography.....	137

Remerciements

Je tiens tout d'abord à remercier mes parents, Newton et Tania. Pour avoir pris des décisions difficiles concernant mon traitement, alors que beaucoup ne le recommandaient pas. De plus, le coût personnel de déménager dans un autre pays pour m'accompagner, deux fois, ne peut être mesuré. Ensemble, mes frères et sœurs, Catarina, Gustavo et Vitória, ont joué un rôle fondamental en soutenant mes parents, afin de faciliter ces transitions en cette période troublée.

Ce soutien de mes parents s'est accompagné des bons choix de professionnels et, sans eux, je n'en serais pas là. Je tiens à mentionner tous ceux qui ont fait partie de cette courbe de progrès, mais je crains que les « Remerciements » puissent devenir plus long que la thèse elle-même. Je tiens à remercier José Vicente qui, avec son équipe de physiothérapeutes, m'a remis sur pied. Je tiens à remercier Talita, dont l'adaptation à la dactylographie m'a aidée à taper toutes ces pages. En plus de la récupération motrice, il a récupéré la parole. Je tiens à féliciter le travail des orthophonistes Camille, Clarice, Camila et Jessica, et j'espère ne pas bégayer en soutenant cette thèse !

Cela dit, tout ce travail sur ma guérison m'a « seulement » donné les outils nécessaires à la réalisation de cette thèse. Le rôle de la directrice de thèse, Christine, et l'encadrant, Pierre, ne fut pas seulement celui qu'on attend d'une équipe de direction. Les révisions ne sont pas seulement venues de cette équipe de direction, je tiens à remercier Sandro et Seif pour leurs révisions et améliorations de ce manuscrit.

Acknowledgements

I would like to thank, first of all, my parents, Newton and Tania. For making difficult decisions in terms of my treatment, when many did not recommend it. In addition, the personal cost of moving to another country to be with me, twice, cannot be measured. My siblings, Catarina, Gustavo and Vitória, played a fundamental role in supporting my parents, in order to facilitate these transitions in these uncertain times.

This support from my parents was accompanied by the right choices of professionals and, without them, I would not have reached this point. I want to mention everyone who was part of this progress curve, but I fear that the 'Acknowledgements' may be longer than the thesis itself. I would like to thank José Vicente who, together with his team of physiotherapists, got me back on my feet. I would like to thank Talita, whose adaptation to typing helped me type all these pages. In addition to motor recovery, I also recovered my speech. I would like to praise the work of phonoaudiologists Camille, Clarice, Camila and Jessica, and I hope I don't stutter when defending this thesis!

With that said, all this work on my recovery 'only' gave me the tools I needed to write this thesis. The role of my advisors, Christine and Pierre, was not only what one would expect from advisors. The guidance's did not come just only from the advisors. I would like to thank Sandro and Seif for the reviews and improvements of this manuscript.

Nomenclature

(unit used, if applicable)

Abbreviations

- ATDC After Top Dead Center
- BMEP Brake Mean Effective Pressure (bar)
- BP Bandpass Filter
- BTDC Before Top Dead Center
- CAD Crank Angle Degree (°)
- CAXX Crank Angle Degree when XX% of the fuel is burned (CAD)
- CD Combustion Duration (CAD)
- CHP Combined Heat and Power
- CI Compression Ignition
- CR Compression Ratio
- EAS Electrochemical Ammonia Synthesis
- EGR Exhaust Gas Recirculation
- ER Equivalence Ratio
- ESS Energy Share of Syngas (%)
- GHG Green-House Gas(es)
- GT Gas Turbine
- GWP Global Warming Potential
- HHV Higher Heating Value (MJ/m³)
- HRR Heat Release Rate (J/CAD)
- HRSG Heat Recovery Steam Generator
- ID Ignition Delay
- IDT Ignition Delay Time (ms)
- IGCC Integrated Gasification Combined Cycle
- IMEP Indicated Mean Effective Pressure (bar)
- IMEP_{cov} Coefficient of IMEP variation (%)
- IP Injection Pressure (bar)
- IQ Injection Quantity (mg)
- IT Injection Timing (CAD)
- LFS Laminar Flame Speed (cm/s)
- LP Low Pass filter
- LHV Lower Heating Value (MJ/m³)
- MPRR Maximum Pressure Rise Rate (bar/CAD)
- MSW Municipal Solid Waste
- NG Natural Gas
- NL Natural Luminosity
- PG Producer Gas
- PLIF Planar Laser-Induced Fluorescence
- PM Particulate Matter
- RCCI Reactivity-Control Compression Ignition
- RCEM Rapid Compression–Expansion Machine

- RPM Rotation Per Minute - Engine Speed (rpm)
- SCR Selective Catalytic Reduction
- SI Spark-Ignition
- SOI Start of Injection (CAD)
- TDC Top Dead Center
- THC Total Hydrocarbons

Roman

- %_{w/w} Weight-to-Weight ratio
- S_u^0 Unburned Unstretched Laminar flame speed (m/s)
- \dot{V} Volumetric flowrate (m³/s)
- \dot{m} Mass Flowrate (g/s)
- b Cylinder Bore (mm)
- V_{cyl} Displaced volume (cm³)
- P Pressure (bar)
- T Temperature (K)
- V Volume (m³)

Greek

- ϕ Equivalence Ratio
- η Efficiency (%)
- v Piston Linear Speed (m/s)

List of tables

Table 1: Biofuels: composition, production and fundamental combustion properties.	33
Table 2: Advantages and drawbacks of gasifier design (adapted from Sikarwar et al. [61])	38
Table 3: Typical syngas cleaning requirements per application [57].	39
Table 4: Selected syngas compositions and resulting properties.	39
Table 5: Physicochemical properties of a typical syngas mixtures compared to other fuels (adapted from the work of Paykani et al. [28])	44
Table 6 : Literature review on syngas/diesel dual-fuel engine.	48
Table 7: Experimental test conditions.	55
Table 8: Flame radiuses used to extrapolate the S_u^0	57
Table 9: Mechanisms description	59
Table 10: Typical syngas properties of syngas compositions from selected gasifiers.	63
Table 11: Difference between mechanism predictions and experimental results for Downdraft.	68
Table 12: Difference between mechanism predictions and experimental results for Updraft. ...	68
Table 13: Difference between mechanism predictions and experimental results for Fluidbed. ...	69
Table 14: Difference between simulation ($S_u^0 sim$) and experimental result ($S_u^0 exp$) (Kawka et al.[122])	70
Table 15: Summary of different empirical correlation for S_u^0	71
Table 16: Errors for correlation predictions and experimental measurement.	72
Table 17: Temperature and pressure dependence coefficients for different equivalence ratios fitted on experimental and mechanism data.	73
Table 18: Different tested mixtures of the three syngas compositions with two different amounts of decane.	78
Table 19: Syngas Compositions.	83
Table 20: Engine Characteristics	84
Table 21: Flowmeter Controllers.	84
Table 22: Characteristics of the Bosch CRI 2.2 used in the experiments.	87
Table 23: Injected decane mass (mg) for the selected injector on different injection durations and system pressures.	88
Table 24: Start Of Injection (SOI) configuration.	92
Table 25: Experimental conditions to study the effect of pilot fuel injection quantity.	94
Table 26: Variations on the original Syngas compositions.	100
Table 27: Engine characteristics.	112
Table 28: Mass Flow Controllers	112
Table 29: Syngas compositions	117
Table 30: Variations on the original Syngas compositions.	123
Table 31: Properties of the OD homogenous reactor used.	124

List of figures

Figure 1: Global warming contributions by gas and source, World, 1950 to 2021(adapted from [15] with data from Jones et al. [16]).	30
Figure 2: World energy consumption by source (from [17] with data of Vaclav Smil [18])	31
Figure 3: Global bioenergy supply by type and scenario, 2022-2050 (adapted from the IEA World Energy Outlook [24]).	32
Figure 4: Common types of fixed and fluidized bed autothermal gasifiers (adapted from V. Belgiorno et al. [59]).	36
Figure 5: Product characteristics of allothermal and autothermal biomass gasification (adapted from R. Thomson et al. [50]).	37
Figure 6: Diagram of IGCC (adapted from Ganjikunta [67])	40
Figure 7: Schematic of a Combined Heat and Power (CHP) plant that uses an Internal Combustion Engine (ICE) (adapted from Brandin et al. [64])	41
Figure 8: Illustration of the dual-fuel engine operation (image adapted from [186])	43
Figure 9: Example of a two Heat-Release Rate (HRR), reproduced from the work of Roy et al. [2].	45
Figure 10: Results of Sharma and Kaushal [3] in dual-fuel producer gas/Diesel.	45
Figure 11: Fuel conversion efficiency (η_f) of the dual-fuel, comparing the 3 ESS (35/50/65%:low/medium/high) and pilot fuel injection only (dashed line-'_bio'), with two injection pressures, 500 and 1000 bar (adapted from the work of Carlucci et al.[90])	46
Figure 12: Schematic of a premixed flame (reproduced from [96]).	50
Figure 13: Schematic of the contours of local propagation and displacement speed of a premixed laminar flame (adapted from [96]).	51
Figure 14: Relation of the Lewis number (Le) and the Markstein length (Lu , related to the burned Lb by the expansion ratio) with the flame stability (adapted from [96]).	53
Figure 15: Schlieren Optical Set-up.	54
Figure 16: Post-processing steps illustrated by the unprocessed image (left), the binarized image (center) and the resulting flame contour traced over the unprocessed image (right).	55
Figure 17: Example of flame speed evolution as a function of stretch - downdraft composition at 1 bar, 373 K and $\phi = 1.2$.	56
Figure 18: Example of the instabilities, thermal-diffusive (left) and buoyancy (right), we can obtain in this study.	57
Figure 19: Example of experimental and simulated S_u^0 results for 3 syngas compositions at 1 bar and 323 K.	60
Figure 20: Unstretched laminar flame speed (S_u^0) versus equivalence ratio (ϕ) plot of the 3 reference compositions at 293 K and 1 bar ((reproduced from the work of Monteiro et al. [5])	62
Figure 21: Comparison of S_u^0 results at 1 bar 298 K with results from Monteiro et al. [5] (1 bar 293 K) and Oliveira et al. [7] (0.954 bar 298 K); methane S_u^0 results provided by [133]	64
Figure 22: Experimental and simulated S_u^0 results at 1 bar for four initial temperatures (298, 323, 373 and 423 K).	65

Figure 23: Kinetics mechanisms performances with varying the initial temperatures at stoichiometric condition.	66
Figure 24: Experimental and simulated S_u^0 results at 323 K initial temperature for 3 and 5 bar.	67
Figure 25: Comparison of the effect of pressure on the S_u^0 for the three compositions at 3 equivalence ratios at $T_{in}=323$ K ($\phi= 0.8, 1.0$ and 1.2).....	68
Figure 26: Comparison of current work correlation (solid line) and Monteiro and Rouboa [6] (dashed line) agreements with experimental data.	72
Figure 27: Present work experimental Markstein length results at 1 bar 298 K (filled symbols) compared to Monteiro et al. [5] results at 1 bar 293 K (empty symbols). Diamonds - Hydrogen at 1 bar and 298 K from [133].	74
Figure 28: Markstein length results of the Fluidbed and the Downdraft compositions, for different temperatures and 3 equivalence ratios.	75
Figure 29: Zoom of the previous figure; experimental Markstein length results at 1 bar 298 K (filled symbols) compared to Monteiro et al. [5] results at 1 bar 293 K (empty symbols).....	76
Figure 30: Effect of the addition of CO_2 and CH_4 on the effective Lewis number (Le_{eff}) and the critical radius of the appearance of flame instabilities (adapted from Lapalme et al [128]).....	77
Figure 31: S_u^0 of pure decane of the present work compared with simulation results [119] and literature data [139,140].	79
Figure 32: Evolution of laminar flame speed as a function of syngas/air equivalence ratio for three decane contents at 1 bar and 423 K. a- Downdraft composition, b- Updraft, c- fluidbed syngas composition, simulation results, using the Madison mechanism [119], in the dashed line.....	80
Figure 33: Effect of pressure and the decane addition for a fixed equivalence ratio ($\phi_{syngas/air} = 0.7$) on the laminar flame speed (S_u0) (MF \rightarrow Mass Fraction).	81
Figure 34: Experimental Set-up scheme.....	86
Figure 35: Schematic of the IAV injection analyzer used along with an example of the fuel of interest pressure trace (reproduced from the IAV Gmbh. brochure).	87
Figure 36: Evolution of Heat Release Rate for all premixed equivalence ratios and the three compositions (N=1200 RPM, $P_{intake} = 1$ bar, $T_{intake}= 300$ K).	89
Figure 37. Evolution of In-Cylinder Pressure for all premixed equivalence ratio. (N=1200 RPM, $P_{intake} = 1$ bar, $T_{intake}= 300$ K).	90
Figure 38. a) IMEP (empty symbols) and Epilot (filled symbols) and b) IMEPCov (empty symbols) and MPRR (filled symbols) as function of $\phi_{premixed}$	91
Figure 39: Effect of premixed equivalence ratio on ignition phasing (continuous lines) and first half of combustion (dotted lines) (N= 1200 RPM $P_{intake} = 1$ bar $T_{intake}= 300$ K).....	92
Figure 40: The effect of $\phi_{premixed}$ on the combustion phasing (1200 RPM, $P_{intake} = 1$ bar, $T_{intake}= 300$ K).	92
Figure 41: Efficiencies and exhaust gases emissions as a function of premixed equivalence ratio for the three Syngas compositions (1200 RPM, $P_{intake} = 1$ bar, $T_{intake}= 300$ K, Optimum SOI).	93
Figure 42: a- Heat release rate from the fuel pilot injection in air and air with diluents compared to Downdraft dual-fuel. ($\phi_{premixed} = 0.7$) and b- zoom between -5 and 0 CAD.	95
Figure 43: Effect of pilot fuel energy share on ignition delay (empty symbols, dashed lines) and combustion phasing CA50 (filled symbols, continuous lines) for three Syngas compositions (1200 RPM, $P_{intake} = 1$ bar, $T_{intake}= 300$ K, $\phi_{premixed}= 0.7$).	96

Figure 44: Efficiencies and emissions as a function of decane energy share for the three Syngas compositions. Filled symbols/continuous lines: a) Combustion efficiency, b) CO, c) NOx emissions. Empty symbols/Dashed lines: Thermal Efficiency, THC and Soot emissions for a, b and c respectively (1200 RPM, $P_{intake} = 1 \text{ bar}$, $T_{intake} = 300\text{K}$, $\phi_{premixed} = 0.7$).....	98
Figure 45: Specific emissions of NOx (continuous line) and CO (dashed line) as a function of combustion phasing (left) and global equivalence ratio (right) (1200 RPM $P_{intake} = 1 \text{ bar}$, $T_{intake} = 300\text{K}$, $\phi_{premixed} = 0.7$).....	99
Figure 46: Heat Release Rate profiles for varying CO ₂ (top) and CH ₄ (bottom) contents (1200 RPM $P_{intake} = 1 \text{ bar}$, $T_{intake} = 300\text{K}$, $\phi_{premixed} = 0.7$ $SOI = -18 \text{ CAD BTDC}$).....	101
Figure 47. Effect of Syngas components a) CO ₂ and b) CH ₄ on engine efficiencies and exhaust emissions (1200 RPM, $P_{intake} = 1 \text{ bar}$, $T_{intake} = 300\text{K}$, $\phi_{premixed} = 0.7$, $SOI = -17 \text{ BTDC}$).....	102
Figure 48: Relationship between a- combustion duration and b- stability (IMEP _{cov}) as a function of syngas Laminar Flame Speed. (1200 RPM, $P_{intake} = 1 \text{ bar}$, $T_{intake} = 300\text{K}$, $\phi_{premixed} = 0.7$ $SOI = -18 \text{ CAD BTDC}$).....	104
Figure 49: Relationship between THC emissions and intake CH ₄ (a), Exhaust and Intake CO (b), NOx and T_{ad} (c) (1200 RPM, $P_{intake} = 1 \text{ bar}$, $T_{intake} = 300\text{K}$, $\phi_{premixed} = 0.7$ $SOI = -18 \text{ CAD BTDC}$).....	105
Figure 50: Example of chemiluminescence spectrum in syngas flame as a function of H ₂ , CO and CO ₂ concentration (reproduced from Huang et al. [162]).....	108
Figure 51: Example of natural luminosity of syngas stoichiometric flame for same flame area (5-10-20-30-50-60%) – M : methane, S50 : 50%H ₂ -50%CO, S50D : 25%H ₂ -25%CO-15%CO ₂ -35%N ₂ (reprinted from Martinez-Boggio et al. [172]).	109
Figure 52: scheme of the optical engine set-up.	111
Figure 53: Optical piston (bowl-type).....	113
Figure 54: Filter combination used for OH* chemiluminescence imaging.	113
Figure 55: Optical imaging set-up for OH* chemiluminescence.	114
Figure 56: Filters used for the CH* and CH ₂ O* chemiluminescence.....	114
Figure 57: Schematic view of chemiluminescence image post-processing.....	115
Figure 58: OH* chemiluminescence images averaged on 40 cycles and the bar plot of the corresponding average signal for the pilot decane injection on air (without syngas, N= 750 RPM).	116
Figure 59: OH* chemiluminescence images averaged on 40 cycles and the bar plot of the corresponding average signal for the pilot decane injection on air (without syngas, N= 750 RPM).	116
Figure 60: OH* chemiluminescence images for the original compositions in a dual-fuel engine (a- Downdraft and Updraft and b- Fluidbed ; $\phi_{premixed} = 0.7$, N= 750 RPM).....	118
Figure 61: Average OH* chemiluminescence signal of the compositions.....	118
Figure 62: Instantaneous OH* Image along same combustion cycle for the 3 original compositions ($\phi_{premixed} = 0.7$, N= 750 RPM).	119
Figure 63: Comparison of the apparent Heat Release Ratio (HRR) and the OH* chemiluminescence signals for the 3 original compositions ($\phi_{premixed} = 0.7$, N= 750 RPM).....	120
Figure 64: Comparison of the average apparent HRR with the normalized chemiluminescence of OH* (left) and CH*/CH ₂ O* (right) ($\phi_{premixed} = 0.7$, N= 750 RPM).	121

Figure 65: Temperature profiles of two ϕ_{decane}/air , 0.6 and 1.8, mixed with a premixed charge of Fluidbed/air at $\phi_{premixed}=0.7$	125
Figure 66: The effect of CO ₂ amount (from 0 to 20%) on the Ignition Delays of Syngas/Decane mixture for the 3 syngas compositions (Tin= 800K, Pin= 30 bar, $\phi_{syngas}/air = 0.7$ using the Madison Mechanism).....	125
Figure 67: Effect of CH ₄ variation in the reactive species in syngas on the IDT.	126
Figure 68: Effect of the CO ₂ share on OH* chemiluminescence averaged images for Updraft-based compositions, ignited by the pilot injection ($\phi_{syngas}/air = 0.7$, N= 750 RPM).	127
Figure 69: a- Effect of CO ₂ on the average OH* chemiluminescence signal b- Comparison of the OH* average signal with the apparent Heat-Release Rate (HRR), grouped by the original composition ($\phi_{syngas}/air = 0.7$, N= 750 RPM).	128
Figure 70: Effect of CO ₂ addition in total amount of dilution (N ₂ +CO ₂) on Heat Release Rate (HRR) for the 3 original compositions ($\phi_{syngas}/air = 0.7$, N= 750 RPM).	129
Figure 71: Effect of the CH ₄ share on the OH* chemiluminescence averaged images for Updraft-based compositions ($\phi_{syngas}/air = 0.7$, N= 750 RPM).	130
Figure 72: a- Effect of CH ₄ on the average OH* chemiluminescence signal b- Comparison of the OH* average signal with the apparent Heat-Release Rate (HRR), grouped by the original composition ($\phi_{syngas}/air = 0.7$, N= 750 RPM).	131
Figure 73: Effect of the CH ₄ addition on the apparent Heat Release Rate (HRR) of dual-fuel operation of the compositions ($\phi_{syngas}/air = 0.7$, N= 750 RPM).....	131
Figure 74: Example of Heat-Release Rate of Downdraft syngas as a function of ammonia shared quantity, ignition by decane pilot injection.....	136

RESUMÉ SUBSTANTIEL DE LA THESE EN FRANÇAIS

Chapitre 1 : Introduction

Du 19^{ème} au 21^{ème} siècle, des inventions comme les turbines à gaz et les moteurs à combustion interne ont permis de répondre aux besoins croissants de l'humanité en matière d'électricité, de transport et de commerce. Cependant, cette dépendance à la combustion de combustibles fossiles, tels que le charbon et le pétrole, a conduit à une augmentation massive des émissions de dioxyde de carbone (CO₂), principal contributeur au réchauffement climatique. Les conséquences potentielles de l'élévation des températures terrestres sont présentées.

En fait, différents gaz à effet de serre (GES) émis par les activités humaines, en plus du CO₂, tels que le méthane (CH₄), le protoxyde d'azote (N₂O) et les gaz fluorés (HFCs, PFCs, SF₆, et NF₃) ont des potentiels de réchauffement global différents mais non négligeables. Leur impact est souvent évalué sur une période de 100 ans, en utilisant le CO₂ comme référence.

Le premier chapitre met en évidence l'engagement mondial à limiter le réchauffement climatique à 1,5 °C au-dessus des niveaux préindustriels. Pour atteindre cet objectif, il est nécessaire de réduire de moitié les émissions de GES d'ici 2030 et de viser une neutralité carbone d'ici le milieu du siècle. Les engagements de l'Union européenne (UE) pour réduire les émissions de GES de 20 % en 2020 ont été atteints, mais de nouveaux objectifs plus ambitieux pour 2030 nécessitent une intensification de l'utilisation des énergies renouvelables.

La bioénergie et le syngas :

Les sources d'énergie renouvelables, en particulier la biomasse, font partie des solutions potentielles pour réduire les émissions de CO₂. La combustion de la biomasse, qui inclut le syngas, est présentée comme "neutre en carbone" car le CO₂ émis est compensé par le carbone capturé par les plantes pendant leur croissance. Le syngas, ou gaz de synthèse, est un combustible gazeux produit par la gazéification de la biomasse, contenant des mélanges variables d'hydrogène (H₂), de monoxyde de carbone (CO) et de méthane (CH₄), et des diluants (N₂ et CO₂). L'introduction détaille l'histoire de l'utilisation du syngas, notamment pendant la Seconde Guerre mondiale, où les pénuries d'essence ont entraîné la conversion des véhicules au gaz dérivé de la gazéification du bois.

Importance des technologies de gazéification :

La gazéification est une méthode efficace pour transformer divers types de déchets de biomasse en combustible gazeux. Le processus comprend plusieurs étapes, notamment la pyrolyse et l'oxydation partielle, pour produire du syngas. Le chapitre présente les différents types de gazéifieur, comme ceux à lits fixes et à lits fluidisés. Les gazéifieurs à lit fluidisé sont particulièrement adaptés aux grandes installations industrielles, tandis que les gazéifieurs à lit fixe conviennent mieux aux petites applications.

Défis liés à l'utilisation du syngas :

Bien que le syngas soit considéré comme une source d'énergie prometteuse, son utilisation dans les moteurs à combustion interne présente des défis, en particulier liés à la variabilité de la

composition du syngas qui peut influencer les performances de combustion et les émissions de polluants. Le syngas produit par la gazéification de déchets municipaux solides est également exploré comme une forme de biocarburant de deuxième génération, permettant de convertir des matériaux nuisibles en énergie utile.

Utilisation du syngas pour la production d'électricité :

Le syngas peut être utilisé dans diverses technologies de production d'électricité, telles que les turbines à gaz ou les moteurs à combustion interne, souvent dans des centrales de cogénération (CHP : « Combined Heat and Power ») qui génèrent à la fois de l'électricité et de la chaleur. Les centrales CHP sont courantes dans des pays comme le Danemark et la Suède, où le chauffage urbain est largement répandu. Dans le tableau ci-dessous sont résumés les avantages et les inconvénients majeurs selon le type de gazéifieur.

Type de gazéificateur	Avantages	Limitations
Lits fixes	<ul style="list-style-type: none"> ▪ Le plus simple et le process le plus robuste ▪ Economique à petite échelle ▪ Tolérant à l'origine de la biomasse 	<ul style="list-style-type: none"> ▪ Non uniforme en température ▪ Beaucoup de résidus de goudrons ▪ Faible efficacité à faible température
Lits fluidisés	<ul style="list-style-type: none"> ▪ Température uniforme ▪ Peu de goudrons et de résidus ▪ Faible temps de résidence ▪ Très bonne capacité du process 	<ul style="list-style-type: none"> ▪ Non rentable à petite échelle ▪ Forte fraction de suies dans le syngas
Ecoulement entrainé	<ul style="list-style-type: none"> ▪ Très faible teneur en résidu ▪ Economique à grande échelle ▪ Bonne qualité du syngas 	<ul style="list-style-type: none"> ▪ Non adapté pour toutes types de biomasse ▪ Non-tolérant aux particules/graines ▪ Problème avec le refroidissement des gaz

La conclusion de ce chapitre amène le travail de thèse proprement dit, décrit selon le plan suivant. Dans le but d'analyser la combustion dans des moteurs de type dual-fuel syngas/diesel, la détermination des caractéristiques de la combustion laminaire pour trois compositions de syngas représentatives des principales technologies 'Fluidbed' (lit fluidisé), Downdraft ou Updraft (pour les lits fixes) et spécifiées dans le tableau ci-dessous est réalisée avant l'étude proprement dite sur banc moteur monocylindre opaque de divers paramètres liés en particulier à la composition sur les performances et les émissions ; en dernier lieu, l'étude des caractéristiques du développement de la combustion dans un moteur à accès optiques est réalisée à partir de la chimiluminescence.

	H ₂	CO	CO ₂	CH ₄	N ₂	Richesse	LHV	Vitesse Laminaire Maximale (à 298 K 1 bar)
	%Vol	%Vol	%Vol	%Vol	%Vol	mol/mol (stœchiométrique mass/mass)	MJ/m ³	cm/s
Fluidbed (Fluidized Bed)	9	14	20	7	50	1.21 (1.25)	4.2	15.4
Updraft	11	24	9	3	53	1.12 (1.24)	4.4	30.7
Downdraft	17	21	13	1	48	1.00 (1.13)	4.8	36.7

Chapitre 2 : État de l'art des moteurs dual-fuel syngas/diesel : performances et recherches sur les émissions

L'utilisation du syngas dans les moteurs à combustion interne présente certains avantages, comme son potentiel à réduire les émissions de CO₂ lorsqu'il est produit à partir de biomasse ou de déchets. Cependant, il présente également des défis, notamment des émissions plus élevées de CO et d'hydrocarbures imbrûlés dans certaines conditions de fonctionnement.

Le syngas, en raison de sa température d'auto-inflammation élevée (>500°C), ne peut pas facilement être utilisé seul dans un moteur à allumage par compression (CI). Pour surmonter cette difficulté, l'une des solutions est d'injecter une petite quantité de carburant très réactif (tel que le diesel) près du point mort haut (TDC) du cycle pour initier la combustion. Ce concept est appelé « MCCI » (Mixing Controlled Compression Ignition). Cette technique permet de combiner l'efficacité thermique élevée d'un moteur diesel avec une réduction des émissions de NO_x et de particules, lorsque les bons paramètres sont sélectionnés (notamment le ratio entre l'énergie amenée par le carburant dit pilote et l'énergie totale, ainsi que le phasage de son injection).

Propriétés physico-chimiques des carburants :

Quelques propriétés physico-chimiques sont présentées (**Tableau 5 - Chapitre 2**) selon les compositions de syngas, avec d'autres carburants, tels que l'hydrogène, le méthane, le diesel et le biogaz. Plusieurs compositions de syngas sont analysées, qui sont des mélanges variés d'hydrogène (H₂), de monoxyde de carbone (CO), de méthane (CH₄), de dioxyde de carbone (CO₂) et d'azote (N₂). Ces compositions influencent directement les performances et les émissions des moteurs dual-fuel. On peut déjà ainsi constater qu'une teneur plus élevée en H₂ permet d'augmenter la réactivité du syngas avec des vitesses et des températures de flammes plus élevées. Le contenu énergétique des syngas, PCI (Pouvoir Calorifique Inférieur), est quant à lui bien plus faible que celui des hydrocarbures conventionnels, indiquant ainsi que l'utilisation de syngas entraînera une consommation plus élevée qu'avec les hydrocarbures afin de produire la même quantité d'énergie.

Plusieurs stratégies permettent d'optimiser ce type de moteur dual-fuel syngas/diesel :

- Paramètres d'injection du diesel : la pression, le phasage et la durée de l'injection du carburant pilote. Il s'avère que ces paramètres sont cruciaux afin de gérer la qualité de la combustion, notamment l'allumage et le phasage dans le cycle qui impacteront le rendement mais aussi la quantité de travail récupéré sur le piston selon la quantité de carburant type diesel utilisé.

- Composition du syngas : cela affecte la vitesse de la combustion et donc la durée de combustion dans le cycle moteur et la formation d'émissions polluantes, selon la teneur en carbone et le taux de diluant (CO_2 et N_2).
- Rapport de compression (CR) et le régime du moteur qui impacteront directement le rendement indiqué du moteur

Analyse des études expérimentales de la littérature :

Le chapitre 2 répertorie plusieurs études expérimentales réalisées sur des moteurs dual-fuel avec du Syngas (Tableau 6 – Chapitre 2). Par exemple, des précédentes recherches ont montré que l'ajout d'hydrogène dans le syngas augmente la température de flamme, ce qui améliore la puissance du moteur mais peut entraîner l'augmentation des émissions de NO_x [1,2]. D'autres études examinent l'effet de la dilution du syngas avec du N_2 ou du CO_2 pour réduire les émissions de NO_x . En général, pour les articles cités, l'augmentation du taux de compression du moteur réduit les émissions, augmente le rendement du moteur et permet d'augmenter le taux de remplacement du Diesel par le syngas, comme Sharma et Kaushal [3] l'ont démontré. L'augmentation du taux de compression peut en revanche favoriser l'apparition de combustion anormales [4], mais cela demeure peu probable du fait de la forte dilution présentes dans les syngas [3].

A la lumière de cette revue, l'objectif de la thèse est de contribuer à une meilleure identification de l'impact des différents paramètres qui vont affecter la combustion dans les moteurs dual fuel alimentés avec du syngas tels que la composition du syngas, le ratio d'énergie de la pilote Diesel / syngas, et l'importance des paramètres d'injection du carburant pilote sur les performances et les émissions des moteurs dual-fuel. Pour cela, Il est nécessaire de réaliser une caractérisation sur banc moteur aussi bien optique qu'opaque afin de caractériser la combustion et les émissions avec pour objectif de minimiser la quantité de Diesel introduite mais aussi de caractériser des propriétés fondamentales de la combustion comme la vitesse de flamme laminaire qui impactera le déroulement de la combustion dans le cycle moteur.

Chapitre 3 : Caractéristiques expérimentales de la flamme prémélangée laminaire syngas/air

Ce chapitre commence par un rappel des concepts clés de la théorie de la flamme prémélangée laminaire en particulier sur la vitesse fondamentale, qui décrit la vitesse à laquelle les gaz frais sont consommés lors de la combustion, et qui dépend fortement des conditions initiales (température, pression) du mélange. A partir de l'étude bibliographique, on en conclut que de nombreuses études sur les vitesses de flammes se concentrent sur des mélanges H_2/CO avec éventuellement l'ajout d'une espèce supplémentaire comme le CO_2 ou le CH_4 mais très peu d'étude s'intéressent à des compositions « complètes » de syngas à l'exception des travaux de Monteiro et al. [5,6] et Oliveira et al. [7]. Le travail réalisé a pour objectif entre autres d'étendre la base de données proposée par Monteiro et al., à partir de trois compositions de syngas représentatives, étudiées selon les conditions de richesse et de pression et température initiales. Une comparaison avec des mécanismes cinétiques les plus prédictifs est réalisée pour identifier les plus à même de prédire les propriétés de combustion dans les conditions de fonctionnement du moteur.

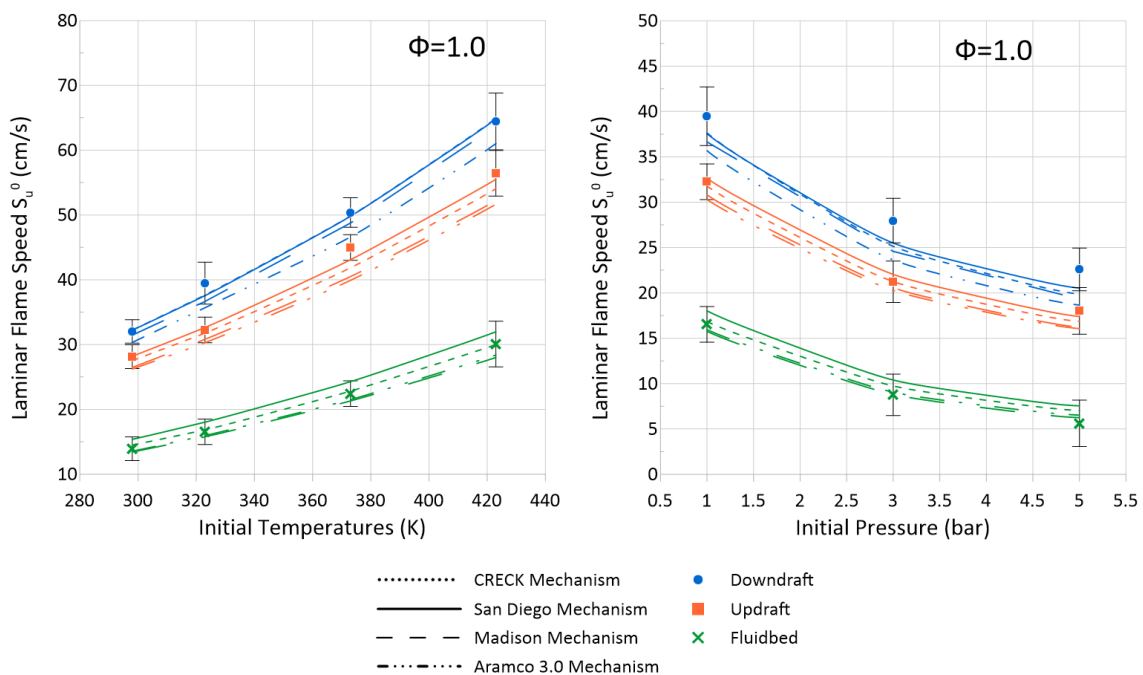
Dispositif expérimental

Le dispositif utilisé pour les expériences est une enceinte sphérique à accès optiques d'un volume de 4.2 L, entourée d'éléments chauffants pour contrôler la température. Le mélange syngas/air est créé à l'aide de débitmètres, et un système optique de type Schlieren couplé à une caméra à haute vitesse est installé pour capturer le front de flamme et suivre sa propagation. La vitesse de combustion laminaire est mesurée pour 3 types de compositions de syngas qui seront utilisées tout au long de ce travail, représentant les compositions type selon une gazéification de type 'Fluidbed, Downdraft ou Updraft (cf tableau 4 du chapitre 1) et ce, pour différentes richesses et conditions de pression et de température.

Résultats expérimentaux

Les résultats montrent que la composition du syngas influence directement la vitesse de combustion laminaire de la façon suivante : les mélanges contenant plus d'hydrogène (comme le Downdraft) ont des vitesses de combustion plus élevées, tandis que les mélanges plus dilués avec du CO₂ et de l'azote (comme le cas du Fluidbed) ralentissent la combustion. Les flammes sont également plus instables avec des compositions riches en hydrogène, ce qui entraîne une augmentation des instabilités thermo-diffusives. La longueur de Markstein, qui caractérise la réponse de la flamme à l'étirement, est également mesurée. Les résultats montrent que les mélanges pauvres en syngas ont une longueur de Markstein négative, ce qui indique que ces flammes sont instables. Les résultats sont en accord avec la littérature et sont étendus par rapport à celle-ci avec l'utilisation d'un modèle d'extrapolation de la vitesse de flamme, dit « non linéaire », plus adapté à ces mélanges que le modèles dit linéaire qui avait été utilisé jusqu'à lors.

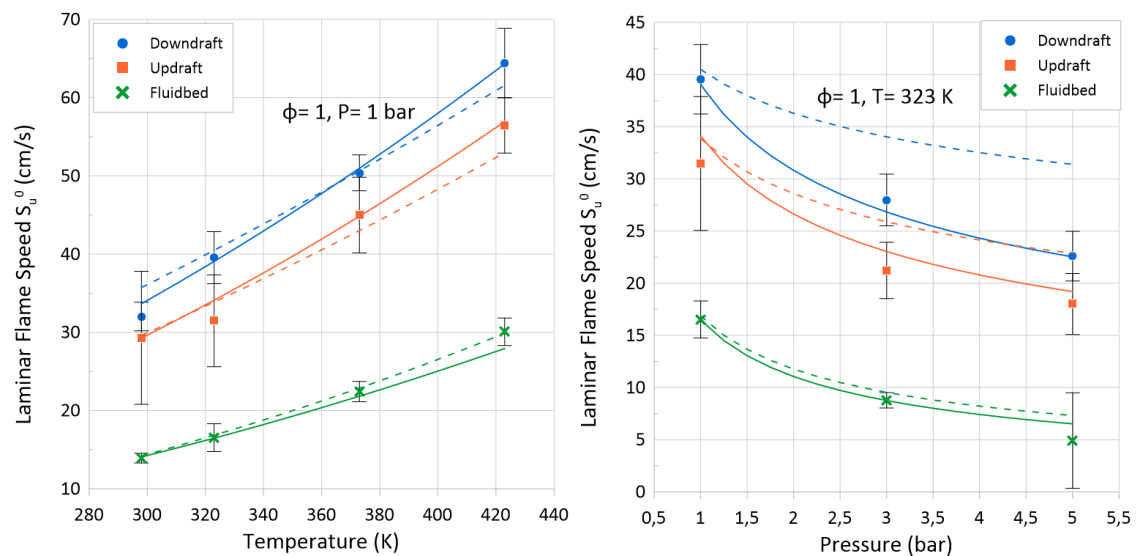
Le chapitre discute également des effets de la pression et de la température sur la propagation de la flamme, montrant que l'augmentation de la température initiale accélère la combustion, comme l'on peut voir sur la figure ci-dessous (gauche) tandis que l'augmentation de la pression tend à ralentir la vitesse de flamme (droite).



Simulations numériques et corrélations empiriques

Pour évaluer la validité des modèles cinétiques, les résultats expérimentaux sont comparés à des simulations utilisant plusieurs mécanismes chimiques (San Diego, CRECK, Madison, Aramco 3.0). Dans l'ensemble, tous les mécanismes prédisent les évolutions quelle que soit la composition du syngas, mais certains prédisent mieux le Downdraft, comme le mécanisme de Madison et le San Diego ou au contraire le Fluidbed et l'Updraft, comme le Creck et Aramco 3.0.

Des corrélations empiriques sont également proposées pour prédire la vitesse de combustion laminaire en fonction de la richesse, de la température et de la pression initiales, corrélations utiles pour des simulations de moteurs à combustion interne à faible coût (0D/1D). La figure ci-dessous montre les résultats de la corrélations obtenue (trait plein) et comparée à celle de Monteiro et Rouboa (trait pointillé) [6]. L'amélioration obtenue de la prédictibilité de cette corrélation est ainsi notable. La dernière section de la partie résultats de ce Chapitre présente l'effet de l'ajout décane, représentatif du Diesel, sur la vitesse de flamme laminaire. La comparaison avec les données expérimentales a montré que le mécanisme de Madison prédit raisonnablement la vitesse de combustion laminaire des mélanges de syngas lorsque de petites quantités de décane (jusqu'à 5 % en masse) sont ajoutées.



En conclusion, cette partie de l'étude a montré/confirmé l'impact de la composition du syngas a un impact significatif sur la vitesse de combustion laminaire et la stabilité de la flamme, et a enrichi la faible base de données existante dans la littérature sur le sujet. La composition Fluidbed, en raison de sa forte dilution, présente des vitesses de combustion plus faibles, ce qui pourrait limiter ses performances dans des applications moteur.

Chapitre 4 : Analyse multiparamétrique des performances et émissions des moteurs dual-fuel syngas/diesel avec trois compositions de syngas

Le chapitre commence par rappeler l'intérêt de l'utilisation du syngas dans un moteur à allumage par compression (CI) en mode dual-fuel pour un système énergétique polyvalent ('de type 'groupe électrogène'), notamment pour des applications stationnaires hors réseau. Cependant, la variabilité de la composition du syngas, due à la source de biomasse et au procédé de gazéification, pose des défis pour l'optimisation des performances du moteur. Ce chapitre se consacre ainsi à l'étude de l'influence des trois compositions de syngas (Fluidbed, Updraft, et Downdraft) précédemment définies sur les performances du moteur et les émissions, avec une attention particulière sur la richesse du mélange (syngas/air) et de la quantité de carburant pilote apportée.

Dispositif expérimental et méthode de post-traitement

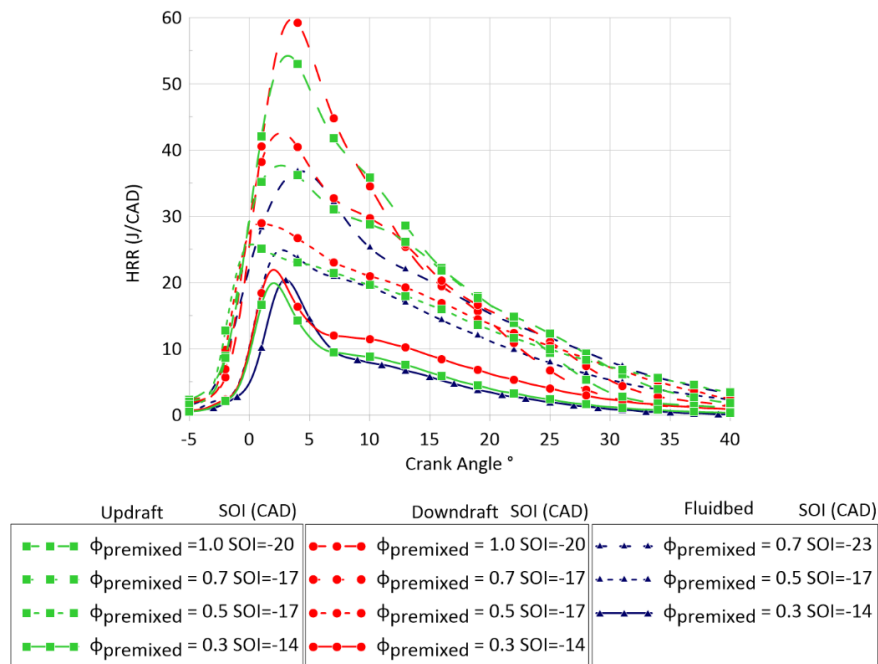
Le moteur utilisé pour les expériences est un moteur PSA DW10 4-temps, modifié pour fonctionner sur un seul cylindre (0.5 l de cylindrée). Le régime moteur est fixé à 1200 tr/min. Le syngas et l'air sont prémélangés dans un plénum avant d'être introduit dans le cylindre. La richesse du mélange syngas/air est contrôlé à l'aide de débitmètres. L'injection du carburant pilote (ici le décane, substitut du diesel) est réalisée par un injecteur de type Common-Rail Bosch CRI 2.2, la pression d'injection a été fixée à 200 bar, afin de pouvoir varier le plus facilement la quantité par la durée d'injection. La pression cylindre enregistrée permet de déterminer les paramètres d'analyse moteur tels que le taux de dégagement de chaleur (HRR), le rendement thermique, les durées spécifiques de la combustion. Une baie d'analyse a permis de mesurer les émissions de NO_x, CO, HC imbrûlés.

Résultats

Effet de la richesse

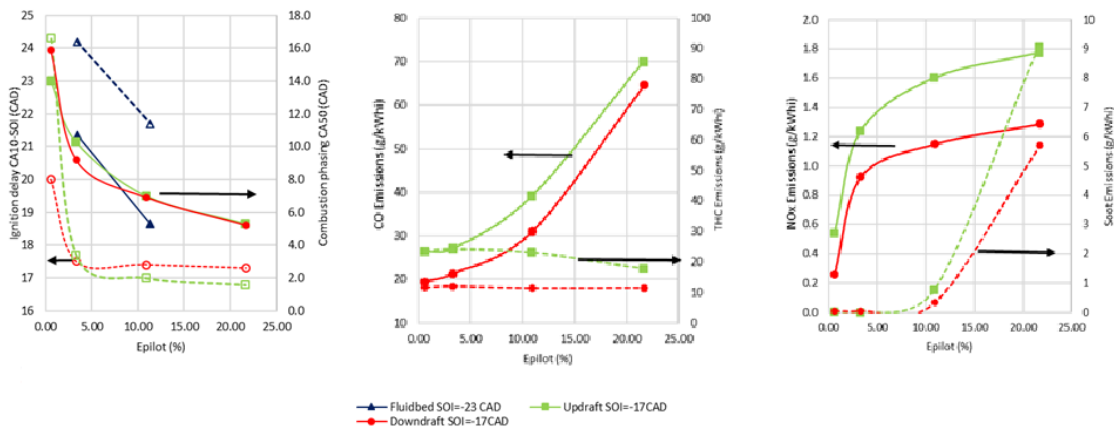
L'étude montre que l'augmentation de la richesse syngas/air entraîne une transition de la combustion en deux phases distinctes (une de prémélange et une de diffusion) à une combustion en une seule phase, où la charge de syngas est directement enflammée par le carburant pilote. Le chapitre explore comment des richesses élevées augmentent la pression maximale dans le cylindre et augmentent le délai du début d'inflammation. La figure suivante présente l'effet de la richesse du prémélange, pour les trois compositions, sur le dégagement de chaleur. Les compositions Downdraft et Updraft présente des dégagements de chaleurs, et donc des performances similaires, avec un léger avantage pour le Downdraft du fait de sa teneur en H₂ plus élevée et donc de sa réactivité. La composition Fluidbed présente des dégagements de chaleur bien moins élevés à cause de sa plus grande dilution. Par ailleurs, la stabilisation du point de fonctionnement de la composition Fluidbed est rendu plus difficile du fait de sa plus grande dilution. Un point de fonctionnement avec une richesse de prémélange de 0,7 se présente pour les 3 compositions puisqu'il permet d'obtenir les meilleurs rendements indiqués et de combustion pour les 3 syngas (pour une quantité de décane fixé à 0.61 mg). En ce qui concerne les émissions, les compositions Updraft et Downdraft présentent des résultats similaires avec un léger avantage à nouveau pour le Downdraft qui présente des émissions les plus faibles en

hydrocarbures imbrûlés (HC), monoxyde de carbone (CO) et oxyde d'azote (NO_x). Le Fluidbed présente les émissions les plus élevées en HC et CO mais les plus faibles en NO_x du fait de sa dilution plus importante.



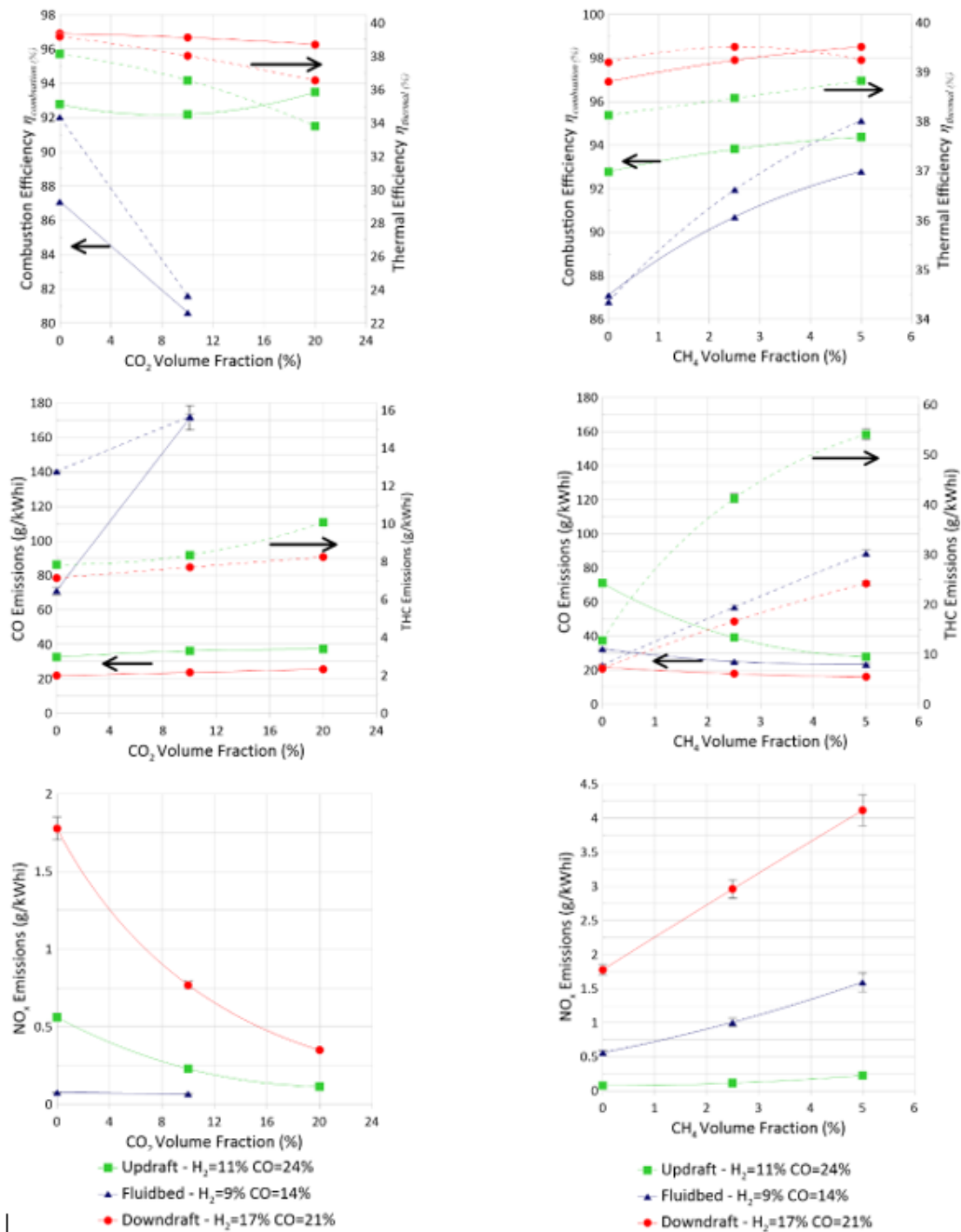
Effet de la quantité de carburant pilote

L'impact de la quantité de carburant pilote est également analysé. Une augmentation de la quantité de carburant injecté réduit le délai d'inflammation et avance la phase de combustion, en raison de la réactivité plus élevée du décane par rapport au syngas. Cependant, une injection excessive de carburant pilote peut entraîner des émissions accrues de suie et de CO, tandis que les émissions de NO_x augmentent en raison de températures de combustion plus élevées, comme le montre le graphe ci-dessous. Malgré la variation de la quantité de décane, la stabilisation du point de fonctionnement la composition fluidbed est toujours plus difficile. Il apparaît qu'un compromis est nécessaire sur la quantité de décane injectée afin de maximiser le rendement et garantir la stabilité tout en évitant une augmentation des émissions. La figure suivante présente les effets de l'augmentation de la quantité de décane sur les durées de combustions et les émissions.



Effet de la concentration en CH_4 et CO_2

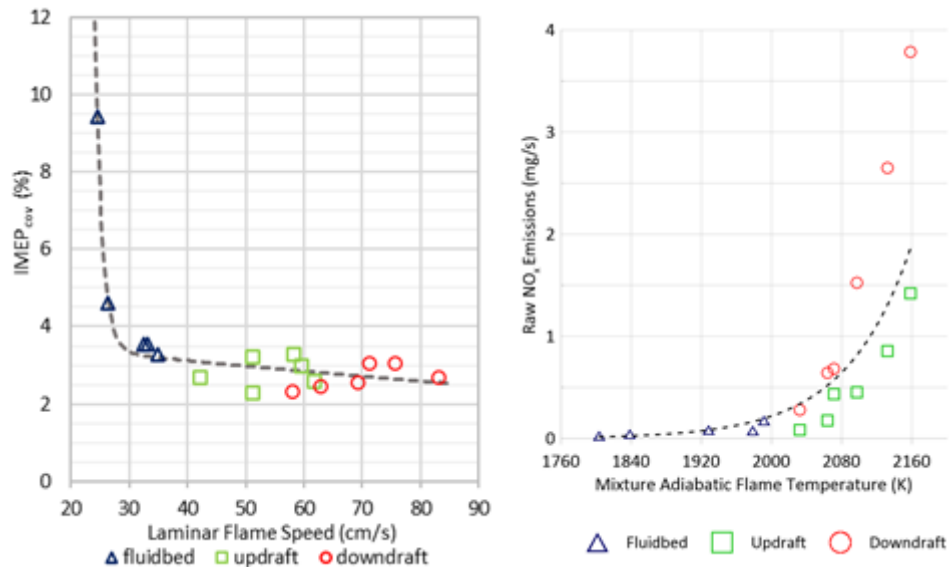
Afin d'évaluer individuellement les effets du CH_4 et du CO_2 , les compositions ont été simplifiées sur une base $H_2/CO/N_2$ avec les mêmes teneurs en H_2/CO que les compositions complètes de départ. Le N_2 est ensuite partiellement remplacé soit par le CH_4 soit le CO_2 , selon le composant que l'on souhaite évaluer. Globalement, l'ajout de CO_2 dans le syngas ralentit la combustion et réduit les émissions de NO_x , tandis que l'ajout de CH_4 améliore l'efficacité de la combustion mais augmente les émissions d'hydrocarbures non brûlés (THC) et les NO_x dans le cas des compositions Fluidbed et Downdraft (voir la figure suivante). Par ailleurs le niveau de dilution déjà très important du Fluidbed ne permet de remplacer plus de 10% du N_2 par du CO_2 . On peut néanmoins constater, que l'ajout de CH_4 a un effet très positif sur la composition $H_2/CO/N_2$ similaire au Fluidbed. Ainsi la teneur en CH_4 plus élevée de la composition originale Fluidbed par rapport aux 2 autres permet de compenser partiellement ses plus faibles performances.



Relations entre propriétés fondamentales et performances du moteur

Les relations entre les propriétés fondamentales des mélanges de syngas (vitesse de flamme laminaire, température de flamme adiabatique) et les performances du moteur ont été évaluées dans la figure ci-dessous afin d'identifier les paramètres les plus impactants S_u^0 . Par exemple,

une vitesse de flamme laminaire inférieure à 30 cm/s est associée à une instabilité de fonctionnement accrue du moteur avec le coefficient de variation de la Pression Moyenne Indiqué (IMEP_{cov}) qui excède 5%, tandis que des températures de flamme plus élevées, obtenus avec les compositions Updraft et Downdraft, qui sont moins diluées, augmentent les émissions de NO_x, comme le montre la figure suivante.



En résumé, il a ainsi été possible d'obtenir un rendement thermique indiqué du moteur supérieur à 38 %, avec richesse prémélangé de 0,7 et pression moyenne indiquée (IMEP) de 6 bar, pour toutes les compositions de syngas, avec moins de 10 % de l'énergie totale fournie par le carburant pilote. L'influence du contenu en H₂ et CO₂ dans le syngas est particulièrement notable sur la durée et le phasage de combustion, ainsi que sur les émissions. Le syngas riche en CO₂, bien qu'utile pour réduire les NO_x, peut diminuer l'efficacité de la combustion, nécessitant plus de carburant pilote pour maintenir la stabilité du moteur.

Chapitre 5 : Visualisation de la combustion dans un moteur dual-fuel syngas/diesel à accès optique

Dans ce chapitre, la combustion d'un mélange dual-fuel (syngas/diesel) est analysée à l'aide de la visualisation rapide naturelle de la combustion : la chimiluminescence, dans un moteur à accès optiques. La chimiluminescence permet de visualiser les radicaux chimiques actifs durant le processus de combustion, comme les radicaux OH*, CH*, et l'espèce CH₂O, qui sont représentatifs de différentes étapes de la combustion. Ce type d'analyse permet de mieux comprendre les mécanismes d'auto-inflammation, la propagation de la combustion, et l'influence des différentes compositions du syngas sur la combustion.

Le moteur utilisé pour ces expériences est similaire à celui du chapitre précédent, mais il est équipé d'accès optiques pour permettre une observation directe de la combustion. Un système

d'imagerie à haute vitesse avec des caméras monochromes à haute cadence, munies d'un intensificateur sont utilisées pour capter les émissions des radicaux chimiques à différentes longueurs d'onde. Les longueurs d'onde d'intérêt sont : le 308 nm, pour OH^* , 330 et 430 nm pour CH_2O^* et CH^* , respectivement. Les trois compositions de syngas (Downdraft, Updraft, et Fluidbed) ont été de nouveau testées. Les expériences ont pour but de comparer les émissions de chimiluminescence, qualitativement à différentes étapes de la combustion et de corrélérer ces signaux avec le taux de dégagement de chaleur (HRR) obtenu à partir de la pression cylindre.

Résultats

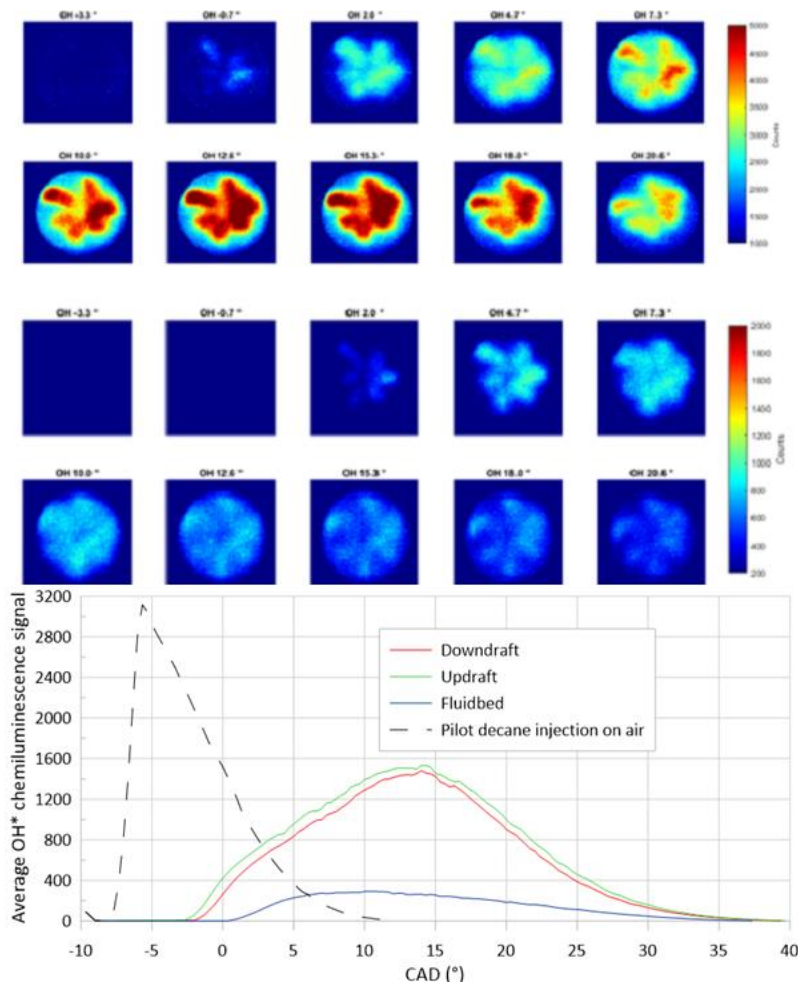
Combustion du seul carburant pilote

Les premières expériences se concentrent sur l'injection seule du carburant pilote (décane), sans syngas. Les images montrent que l'allumage se produit autour des six jets d'injection, mais la combustion reste limitée à de petites flammes localisées, sans développement global de la flamme. Ces résultats sont utilisés comme référence pour comparer les expériences avec syngas.

Comparaison des compositions de syngas

L'expérience avec les trois compositions de syngas révèle que les mélanges Downdraft et Updraft présentent des développements de combustion similaires, avec des délais d'inflammation plus longs que ceux du décane seul. En revanche, la composition Fluidbed montre une intensité beaucoup plus faible des émissions de chimiluminescence en raison de sa teneur plus élevée en CO_2 , ce qui dilue le mélange et ralentit la combustion.

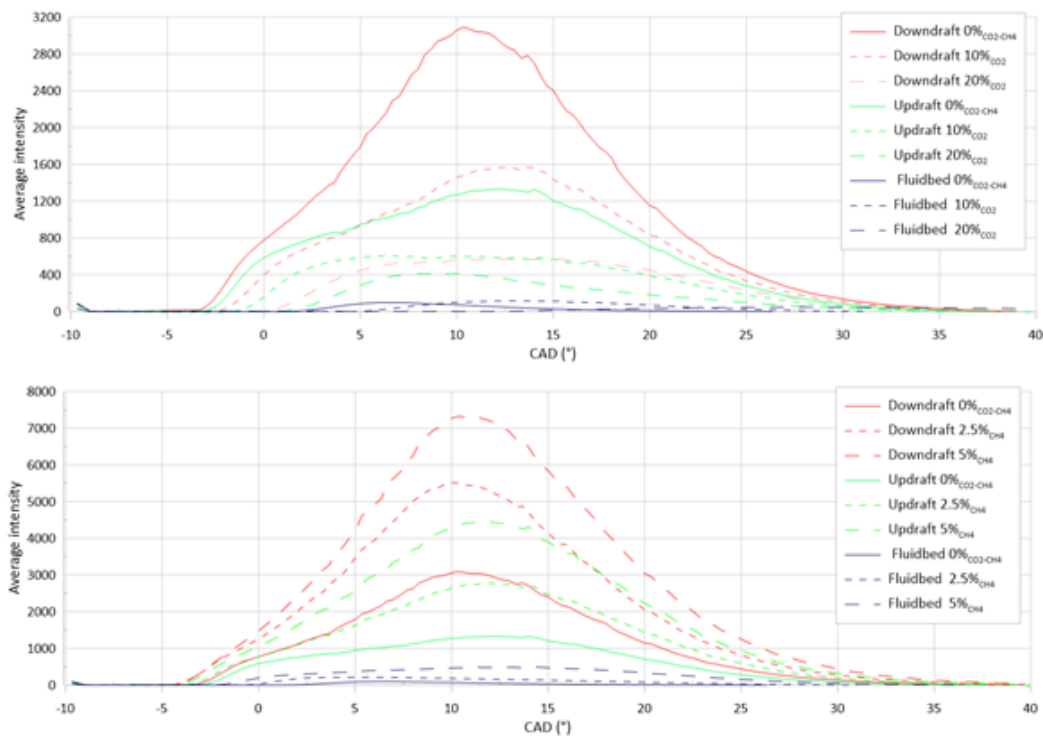
Les résultats montrent également que la concentration en H_2 dans le syngas influence fortement l'intensité de la chimiluminescence du radical OH^* , un indicateur clé de l'intensité de la combustion. Les compositions riches en H_2 produisent des flammes plus rapides et plus chaudes, alors que les mélanges dilués en CO_2 ou N_2 montrent des flammes plus lentes et moins intenses. La figure suivante présente un exemple d'images moyennées du radical OH^* pour le Downdraft (haut), plus riche en H_2 , et le Fluidbed (bas), plus dilué. Il est intéressant de remarquer que sur la première image de flamme visible, la forme est très proche pour les 2 compositions avec des sites d'allumage qui sont en moyenne similaires : le long des plumes du spray de l'injection pilote. Le graphique présente quant à lui l'intensité moyenne des trois compositions ainsi que pour le cas où la même injection pilote de décane est effectuée dans l'air, mettant ainsi en évidence l'intensité lumineuse plus faible pour les mélanges avec syngas que pour le décane seul dans l'air (avec la même quantité). Les syngas Updraft et Downdraft présentent des signaux OH^* similaires tandis que le Fluidbed est bien moins intense. La différence de délai d'allumage est également notable avec le Fluidbed qui est bien plus tardif que les 2 autres compositions, elles-mêmes s'allumant plus tard dans le cycle que le décane seul dans l'air.



Effet du CO_2 et du CH_4

L'effet du CO_2 comme diluant est également étudié. L'ajout de CO_2 dans le syngas retarde l'allumage et réduit l'intensité globale de la combustion, ce qui est visible sur les images de chimiluminescence, vu que les sites d'allumage deviennent plus espacés dans le temps. Par ailleurs, avec l'augmentation du CO_2 , les premiers sites d'allumage semblent en moyenne se concentrer sur la zone entre les 2 soupapes d'échappement, probablement du fait de la température plus élevée dans cette zone. L'augmentation de la concentration en CO_2 conduit à une combustion moins énergétique et un délai d'allumage plus long. L'effet du méthane est également analysé. L'ajout de CH_4 accélère l'allumage et augmente l'intensité de la combustion, en raison de sa réactivité plus élevée mais ne semble pas modifier les localisations des sites d'allumage en moyenne qui se trouvent toujours le long des plumes du spray. Le graphique ci-dessous présente les intensités des images OH^* : en haut les compositions où le CO_2 remplace

l'azote et en bas les intensités des images OH* : en haut les compositions où CO₂ remplace l'azote et en bas le CH₄ le CH₄ remplace l'azote.



Conclusion Générale :

Ce mémoire se termine par une conclusion générale sur ces travaux ainsi que des perspectives de recherche. Les principales lignes sont résumées ci-dessous :

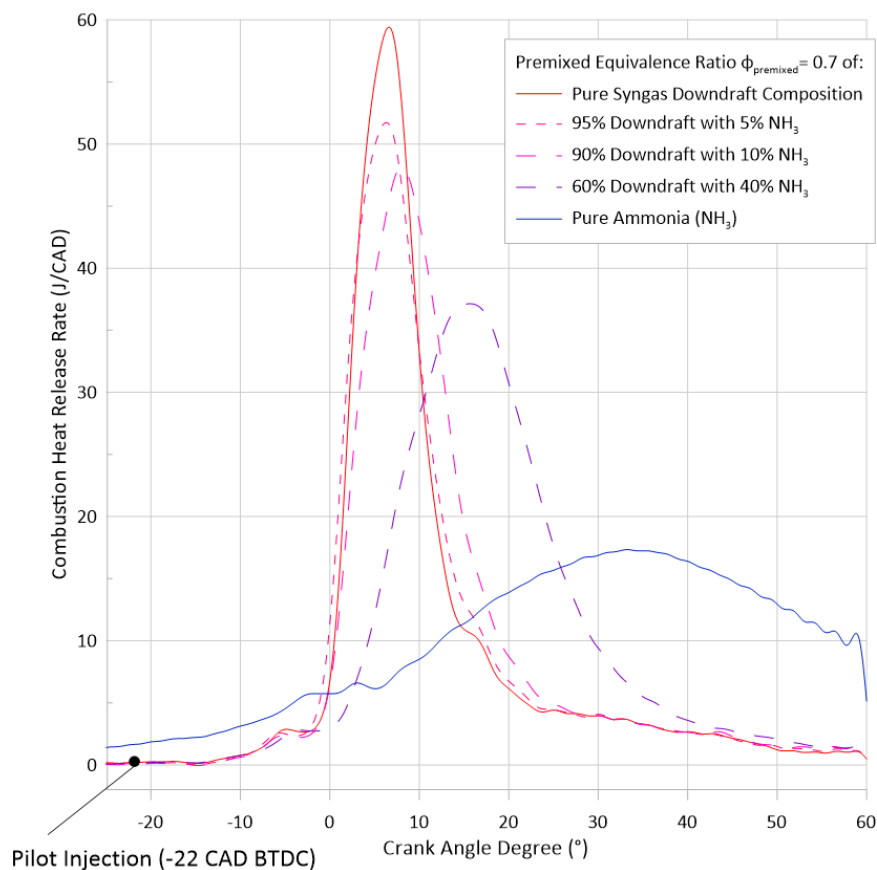
- Les moteurs à bi-carburant tels que le gaz synthétique et le diesel, peuvent utiliser différentes compositions de syngas, contenant de l'hydrogène (H₂), du monoxyde de carbone (CO), du dioxyde de carbone (CO₂), du méthane (CH₄) et de l'azote (N₂) avec une grande flexibilité.
- La performance du moteur est affectée par la composition du syngas, en particulier par la teneur en H₂ et de composés diluants, notamment le CO₂.
- Les moteurs dual-fuel syngas/diesel affichent de meilleures performances avec des taux de compression plus élevés, bien que des problèmes cliquetis puissent survenir avec certaines compositions.
- Les expériences ont montré que, sans modification importante du moteur, des rendements indiqués supérieurs à 38 % peuvent être atteints avec une contribution énergétique du Diesel limitée (moins de 10 %), ce qui représente une perspective intéressante pour la décarbonation des groupe électrogène.

- La quantité de carburant pilote, le decane (remplaçant le Diesel dans les expériences), injectée joue un rôle crucial dans la gestion des émissions et des performances du moteur. Une trop grande quantité de carburant pilote peut entraîner des émissions de suie et de NO_x plus élevées tandis qu'une trop faible quantité peut conduire à une instabilité de fonctionnement.
- L'effet du CO_2 et du CH_4 sur les performances et les émissions du moteur a également été étudié. Le CO_2 réduit les émissions de NO_x mais diminue l'efficacité de combustion, tandis que le CH_4 améliore l'efficacité mais peut augmenter les émissions d'hydrocarbures imbrûlés.
- Des études de chimiluminescence ont été menées pour observer la combustion dans un moteur à accès optique. Les images ont révélé que les radicaux OH^* , CH^* et CH_2O^* fournissent des informations cruciales sur l'initiation et le développement de la combustion et sur les délais d'allumage. Les signaux de chimiluminescence du CH_2O^* et du CH^* sont plus en accord le dégagement de chaleur apparent, que ceux du radical OH^* , mais ceux du CH^* sont davantage affectés par les émissions des suies.
- Les compositions riches en CO_2 ont montré des signaux plus faibles de chimiluminescence, indiquant une combustion moins intense.

En perspective, plusieurs investigations pourraient être menées pour compléter l'étude de l'effet de la composition sur la combustion du syngas. Concernant la vitesse de propagation laminaire et la longueur de Markstein de la flamme, une validation théorique de la longueur de Markstein obtenue pourrait être entreprise afin de valider l'extrapolation de la vitesse de flamme et la gamme de rayon utilisée pour la réalisation des mesures dans certaines conditions. Le calcul de plusieurs paramètres fondamentaux tels que les énergies d'activation, les nombres de Zel'dovich ou les nombres de Lewis reste cependant complexe en raison des multiples composants présents dans le syngas. Pour mieux comprendre l'effet de la composition sur la combustion et limiter le nombre de compositions testées, une approche basée sur des plans d'expériences pourrait être intéressante pour prédire la vitesse de flamme laminaire ainsi que les performances du moteur. Les compositions testées dans le présent travail sont dans certains cas très diluées mais ne contiennent pas de vapeur d'eau. Or selon les procédés, le syngas peut contenir de la vapeur d'eau et étudier et quantifier son impact pourrait être intéressante. De plus, lorsqu'il s'agit de mélanges très dilués, notamment contenant du CO_2 et de la vapeur d'eau, un effet de rayonnement important peut apparaître avec une possible réabsorption de la chaleur par les gaz frais conduisant ainsi à un préchauffage de ces derniers et donc modifiant la propagation de la flamme. Lorsque la vitesse de flamme laminaire devient très faible dans certaines conditions, cet effet radiatif doit être pris en compte, car il impacte la mesure de la vitesse de propagation et donc la valeur non étirée obtenue à partir du modèle d'extrapolation.

Enfin, pour élargir le champ d'étude des carburants neutres en carbone voire « zéro-carbone » sur les moteurs à bi-carburant, nous pouvons envisager la co-combustion de ces carburants, comme avec de l'ammoniac par exemple. En effet, l'utilisation du syngas, à l'époque appelé gazogène, avec de l'ammoniac dans les moteurs à combustion interne a été présentée pour la première fois en 1945 par Emeric Kroch [8]. De plus, comme indiqué dans l'introduction du manuscrit, l'ammoniac peut être présent dans la composition du syngas en tant qu'impureté,

selon s'il résulte de la gazéification de matières premières riches en azote telles que le fumier ou les boues d'épuration. Cet ammoniac est généralement retiré du syngas en raison de sa corrosivité mais avec un coût supplémentaire. Depuis ces 10 dernières années, l'ammoniac comme carburant a suscité un intérêt important, montrant un vrai potentiel pour les moteurs à allumage commandé ou les moteurs à allumage par compression via une injection pilote. Un mélange syngas/ammoniac pourrait être un atout pour un moteur, bien que les propriétés de combustion de ce type de mélange soient peu caractérisées, ce qui peut certainement poser un défi. Pour mieux illustrer cela, la figure ci-dessous présente le taux de dégagement de chaleur (HRR), obtenu dans le même moteur, pour un mélange de la composition de syngas Downdraft en fonction de la quantité d'ammoniac (NH_3) l'injection pilote de carburant le décane restant fixée à 2,1 mg), ce qui entraîne une variation de la part d'énergie apportée par le décane selon le pouvoir calorifique du mélange ammoniac/syngas. Comme on peut le constater sur la figure ci-dessous, la réactivité du mélange diminue à mesure que la teneur en ammoniac augmente, de part, le délai à l'inflammation et la durée de combustion plus longue. Un tel résultat est attendu, vu la plus faible réactivité de l'ammoniac. Cependant, si on le considère comme une impureté (c'est-à-dire en dessous de 5%_{vol.} de la composition du syngas), la présence d'ammoniac n'influence pas le HRR résultant et donc les performances du moteur. Les émissions d'un tel mélange restent à caractériser. Puisque le syngas peut être défini comme un carburant à faible émission de NO_x (comme illustré au chapitre 4), l'ajout d'ammoniac pourrait fortement modifier cela, en raison du chemin réactionnel appelé « fuel- NO_x » résultant de la combustion du NH_3 elle-même. Enfin, on peut aussi noter que l'ajout de syngas dans un moteur dual fuel (ammoniac/diesel) peut être un atout permettant une meilleure optimisation de la combustion. La meilleure des solutions restera la disponibilité locale de telle ou telle ressource énergétique.



1. Introduction

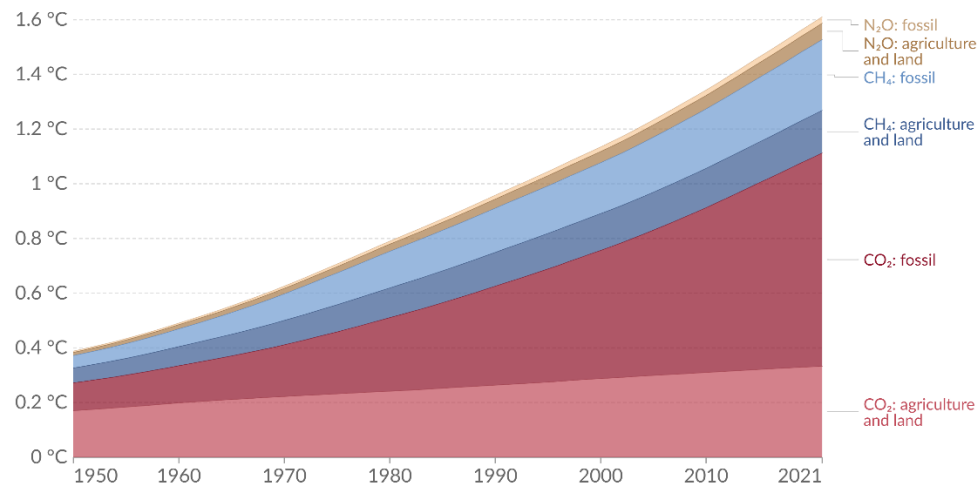
The control and use of the combustion of hydrocarbon materials is deeply intertwined with the development of mankind. The use of combustion for cooking food, metallurgical and chemical processes, and many centuries later for power production and propulsion of vehicles by means of the steam engine, were the key inventions that allowed an enormous production of wealth. In more recent centuries, the development of gas turbines and internal combustion engines unleashed new technologies to fulfill mankind's needs for electricity, trade of goods and mobility.

On the flip side, the world's economy based on the combustion of coal and petroleum products has released an enormous amount of carbon dioxide into the atmosphere - the main cause of global warming. The projected consequences of the increase of earth's temperatures can be as immense as the benefits derived from the use of combustion by humanity, but on the negative side.

In Figure 1, the global warming evolution from 1950 to 2021 and the different Green-House Gases (GHG) contribution in this evolution are presented. The global commitment to prevent the catastrophic consequences of global warming requires limiting warming to 1.5 degrees Celsius from pre-industrial levels [9,10]. The baseline of world temperatures, defined as 'pre-industrial levels', dates back from the years 1850 to 1900, since there are no accurate measurements before this period. Achieving this goal, according to the IEA "A Roadmap for the global energy sector" report [9], means cutting Green-House Gases (GHG) emissions in half by 2030 and reaching net-zero carbon dioxide (CO₂) emissions by mid-century. If the world fails to regain control of the temperatures, it may face a 10% total economic value loss by the 2050's [11]. Therefore, the challenge to the policy makers is to regulate human activities that emit GHG's, without stifling economic activities. For that reason, the European Commission [12] has set a goal to reduce GHG emissions by 20% by 2020, together with having 20% of the European Union (EU) energy sourced from renewables and a 20% improvement in energy efficiency [13]. The GHG emitted by human activity includes carbon dioxide (CO₂), methane (CH₄), nitrous oxide (N₂O), and fluorinated gases, hydrofluorocarbons (HFC's), perfluorocarbons (PFC's), Sulphur hexafluoride (SF₆) and nitrogen trifluoride (NF₃). They have different Global Warming Potentials (GWP) that must be evaluated on a time basis, usually 100 years, and CO₂ is used as a reference [14].

Global warming contributions by gas and source, World, 1950 to 2021

The global mean surface temperature change as a result of the cumulative emissions of three gases – carbon dioxide, methane, and nitrous oxide.



Data source: Jones et al. (2023). National contributions to climate change due to historical emissions of carbon dioxide, methane and nitrous oxide.

Note: This does not include cooling impacts from sulphur dioxide and aerosols, so the net warming can be lower.

OurWorldInData.org/co2-and-greenhouse-gas-emissions | CC BY

Figure 1: Global warming contributions by gas and source, World, 1950 to 2021 (adapted from [15] with data from Jones et al. [16]).

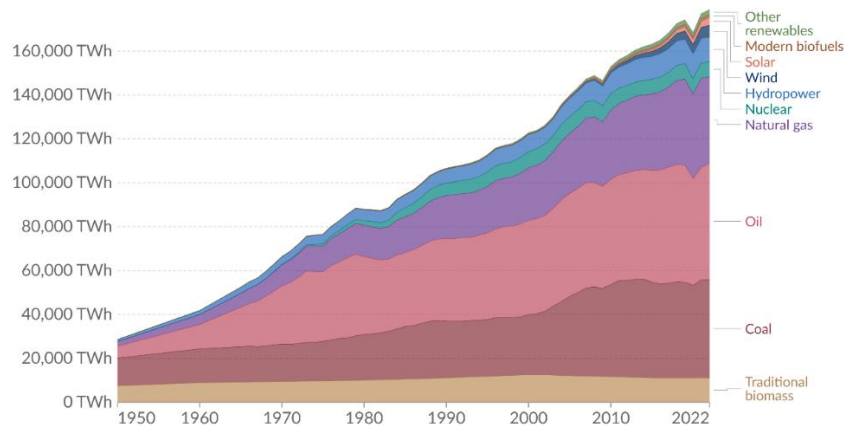
The EU commitments for the year 2020 were achieved [17]. The GHG emissions reached 78.9% of what it was in 1990 in 2018 and the share of renewable energy sources reached 22% in 2020 [17]. But, with the new commitments set for the year 2030, i.e. 40% GHG emissions reduction, 32% renewable energy, and 32.5% energy efficiency improvement, the implementation of renewable energy sources must be intensified. Renewable sources of energy are the ones that can be replenished (or renewed), as hydro, solar, wind, geothermal, ocean, and biomass sources. The availability of most of them is region-dependent, except the potential use of biomass as an energy source, the biomass root will be different. Even if the combustion of biomass emits CO₂ and other GHG, since carbon is captured in the growth of the plants, the energy extracted can be considered 'carbon-neutral'.

In Figure 2, we can see the global energy matrix along the years. There, it is clear that the role of modern biofuels, growing from 700 TWh in 2010 to 1200 TWh in 2022, is still far from well-established fossil fuels (coal and oil) which represent more than half the total consumption. The group defined by 'Traditional biomass' refers to consumption of fuelwood, forestry products, agricultural wastes, understood as raw materials without further refinement.

Global primary energy consumption by source

Primary energy is calculated based on the 'substitution method' which takes account of the inefficiencies in fossil fuel production by converting non-fossil energy into the energy inputs required if they had the same conversion losses as fossil fuels.

Our World
in Data



Data source: Energy Institute Statistical Review of World Energy (2023); Vaclav Smil (2017)
OurWorldInData.org/energy | CC BY

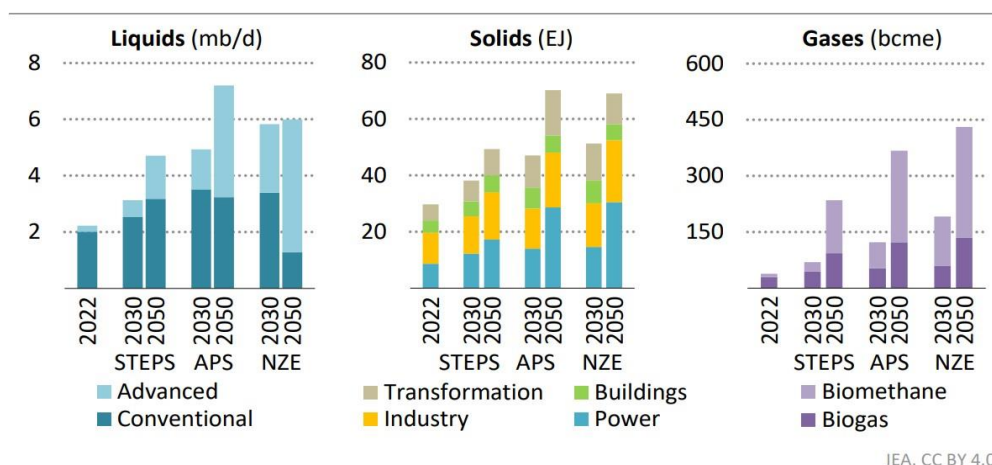
Figure 2: World energy consumption by source (from [17] with data of Vaclav Smil [18])

Another topic of major concern for mankind is the production of waste. Human waste is the byproduct of wealth and consumption habits allowed by income, without further mitigation. Nevertheless, the treatment and recycling of waste is mostly in its infancy. Garbage dump sites of all materials, managed or completely unmanaged, can be seen even in developed economies. The negative impacts of poor waste management practices include GHG emissions, water and ground pollution, among others.

Bioenergy can take many forms: liquid biofuels, including ethanol (produced by fermentation of sugar cane, corn, or other cellulosic feedstocks [19]) and biodiesel (extracted from oily grains, animal fat, and others [20] through transesterification), and gaseous fuels, such as biogas [21] and Synthesis Gas, also known as syngas [22]. As solids we have the example of biochar, produced from crop residues, that can be cofired with traditional fuels in electricity generation power stations [23].

In Figure 3 we can see different forecasts following three scenarios for 2030 and 2050, taking as reference the year 2022. The figure can be misleading because the 'solids' were transformed into gas through gasification or other methods. This solids account for the majority of what was supplied in 2022 and include Municipal Solid Waste (MSW) and forestry residues.

Stated Policies Scenario (STEPS), Announced Pledges Scenario (APS) and Net Zero Emissions by 2050 (NZE)



Full sustainable potential of bioenergy of around 100 EJ is fully exploited in the APS and NZE Scenario, with its different forms used across the clean energy economy

Figure 3: Global bioenergy supply by type and scenario, 2022-2050 (adapted from the IEA World Energy Outlook [24]).

There is an important distinction among biofuels. The first generation uses feedstocks that could otherwise be used for food production for human and animal consumption. For example, ethanol produced from corn that competes with human and animal nutrition and may incentivize deforestation [25]. Another classification that can be made is the sourcing of biofuels. The primary sources are directly harvested/collected of agriculture crops, the secondary sources are the residues of the food industry, and the tertiary sources are the post-consumer residues, that normally end up in landfills [26]. The final source includes the gases from anaerobic digestion of Municipal Solid Waste (MSW) and animal manure (biogas). Table 1 presents an overview of several biofuels with the compositions, means of production, and combustion properties.

Table 1: Biofuels: composition, production and fundamental combustion properties.

	Composition	Production	Usability: properties of combustion, emissions...
Syngas	H ₂ /CO at various ratios, a smaller portion of CH ₄ , and N ₂ and CO ₂ diluents. NH ₃ can be present when the feedstock is Nitrogen-rich [27]. – Gas.	From feedstocks with carbon-hydrogen bonds, mostly by gasification, but other methods exist such as steam reforming, partial oxidation, and auto-thermal reforming.	Usable as a fuel in gas turbines and ICE's (single- and dual-fuel engines [28]). Since the composition is highly variable, the same can be said about the combustion properties [29]. The LHV of syngas from gasification, when air is used as the gasifying agent, ranges from 4 to 6 MJ/m ³ [29] and overall slow combustion and low LHV, depending on the H ₂ /CO ratio and the amount of N ₂ +CO ₂ dilution [30].
Biogas	CH ₄ (50-70%vol.) and CO ₂ (30-50%vol.) – Gas.	Anaerobic digestion of wet animal manure and/or sewage sludge.	Usable as a fuel in gas turbines and ICE's (single- and dual-fuel engines [31]). The combustion properties and the flammability limit strongly depends on the dilution ratio [32]. After the biogas is dried and the H ₂ S contaminant is removed, it can be used in a CHP unit or upgraded to biomethane [33].
Ethanol	C ₂ H ₅ OH – liquid at ambient conditions.	Fermentation of sugar cane or beet molasses or grains feedstocks (e.g. Corn).	Easy conversion of gasoline-fueled SI engines and fully miscible with gasoline, higher octane rating than standard gasoline [34], lower LHV compared to gasoline.
Methanol	CH ₃ OH – liquid at ambient conditions.	From synthesis of syngas which comes of natural gas, coal, coke-oven gas, biomass, and others [35].	Miscible with gasoline and diesel. Greater octane number than gasoline. Possible to run on a PFI or DI SI engine, and in a CI engine, blended with diesel/biodiesel or dual-fueling with diesel (fumigating methanol on the intake plenum and injecting diesel near the TDC) [35,36].
Biodiesel	Mono-alkyl esters of long chain fatty acids derived from animal fats or vegetable oils – liquid at ambient conditions.	Alkyl esters- produced from transesterification reaction between the oil or fat and an alcohol (methanol or ethanol producing Methyl- and ethyl- esters, respectively).	Miscible with petroleum diesel. The emissions of biodiesel fueled CI engines shows a decrease of HC, CO, and PM, but a slight increase of NO _x emissions [37].

- LHV Lower Heating Value, SI Spark-Ignition, CI Compression Ignition, ICE Internal Combustion Engine, EGR Exhaust Gas Recirculation, PFI Port-Fuel Injection, DI Direct Injection, HC Hydrocarbons, CO Carbon Monoxide, PM Particulate Matter, NO_x Nitrogen Oxides, TDC Top-Dead Center.

1.1. Synthesis gas (Syngas)

Syngas utilization in Internal Combustion Engines (ICE) dates to the second World War, when gasoline shortages stimulated the conversion of vehicles to a fuel derived from wood gasification [8,38]. Syngas is a gaseous fuel derived from materials with carbon-hydrogen bonds and it can be produced by gasification or by other alternatives, such as steam reforming, partial oxidation, and auto-thermal reforming [28]. The first of the five steps of the gasification process, is *drying* of the feedstock followed by *pyrolysis* where the solid hydrocarbons, also known as tars, are exposed to temperatures of around 240 °C. After that, there is a partial oxidation, or *combustion*, that provides the thermal energy to gasify the rest of the feedstock, or with an external source of heat. *Cracking* then turns heavier hydrocarbons into simpler molecules and finally, *reduction*, where the H₂O and CO₂ from *combustion*, are partially transformed back into H₂ and CO [39]. This gasification process needs a gasifying agent, such as air or oxygen, and produces, on the fuel side, a mixture of Hydrogen (H₂), Carbon monoxide (CO) and a smaller portion of methane (CH₄). It also contains diluents, such as Carbon dioxide (CO₂), and Nitrogen (N₂) and some contaminants, such as tars, Particulate Matter (PM), ammonia (NH₃), Hydrogen Sulfide (H₂S), halides, and other trace elements present to complete the composition [40]. Among them, the ammonia volumetric concentration is strongly dependent on the nitrogen content of the feedstock and can reach 6 %_{vol/vol} content, when sewage sludge is used as feedstock [27] and, despite its toxicity, it can be burned without emitting CO₂. This effect on producer gas composition was studied by Brequigny et al. [41] applied in a Spark-Ignition (SI) engine.

Air is the more widespread and cost-effective gasifying agent, and when it is used the syngas produced is named as producer gas [42]. The syngas compositions tested in this thesis belong to that category, and compositions derived from steam or CO₂ as gasifying agent are then not considered. To understand what influences the final composition of syngas, the following sections will present a brief overview of feedstock types and gasifier technology.

1.1.1. Feedstock types

Any carbon-based material can be gasified, but gasifying plants run predominantly on non-renewable feedstocks [43,44]. Solid (like wood chips, saw dust, etc.), liquid (petroleum, etc.), and gaseous (methane, etc.) feedstocks can be gasified, but solid feedstocks are more easily fed into a gasifier. The gasification of biomass gained a renewed interest with the push into renewable energy sources [45]. This is relevant when the solar radiant power input, that rovers around 10¹⁷ Watts (W), is considered to be partially stored by plants by photosynthesis (0.02%) resulting in the availability of 10²¹ Joules (J) of energy per year [46]. To give some perspective to this numbers, total electricity consumed in the world in 2019 was about 10¹⁹ J [47].

Gasification is also an efficient process for transforming feedstocks into a gaseous fuel, feedstocks that otherwise would be sent to a landfill and, consequently, emitting methane (CH₄), which has a Global Warming Potential (GWP) 28 times greater than CO₂ [48]. 'Biomass wastes' is a very general term that could take the form of wood derivatives (chips, branches, saw dust...), agriculture waste (manure, crop residue...), and domestic or industrial sewage. Up to today, as a function of the country, crop residues could be wasted or burned, polluting the atmosphere (e.g., wheat and rice residues [49]). The challenge is that biomass wastes come in different sizes and/or shapes, affecting the gasification feeding process, with also different moisture contents. Therefore, before the gasification process, the biomass feedstock

must be dried to reach a moisture content around 15%_{w/w} and ground or filtered into a uniform size [49]. Additionally, the availability of these wastes is sparsely distributed geographically and seasonal [49,50].

One feedstock that is attracting increasing attention is municipal/industrial solid waste [51,52]. When syngas is produced from Municipal Solid Waste (MSW) it can be considered a second-generation biofuel [53]. Gasifying MSW can reduce the overall land area occupied to process 30 Mt of MSW (1 Mt/year during 30 years) by 30-fold [52,54]. When syngas is produced from carbonaceous materials derived from waste, the resulting fuel has the additional benefit of the conversion of deleterious materials into useful energy products.

In this work, we are interested in the use of syngas in a Waste-to-Energy plant. This conversion can be accomplished in several thermal machines, such as gas turbine, gas engine or a steam turbine. Each of these machines exhibits a wide range of energy efficiencies, requiring a specific cleaning of syngas, and produce different power outputs [52,55].

In conclusion, the gasification of biomass has advantages and drawbacks:

- advantages → it is inexhaustible, it can be considered carbon-neutral, with possible implementation all around the world
- drawbacks → the variable heat and moisture content of the feedstock, the scale of the operation, which may turn out to be too small to operate efficiently, and the energy lost in the extraction process [49].

1.1.2. Types of gasifiers

There are several types of gasifiers. The first major distinction is its mode of operation: fixed bed, fluidized bed, or entrained-bed. There are different modes of operation regarding how and in which direction the feedstock and air flows inside the gasifier, and the overall temperature curves of the reactants. For example, for the 'Updraft' gasifier, or 'counter-flow' gasifier, the flow of feedstock is opposed by the syngas production, whereas in 'Downdraft' gasifiers these flows are co-current. This allows for the tar generated at the top of the Downdraft gasifiers to be cracked when it goes through the hot biomass and the grate [56], resulting in a 1% tar yield [57]. Whereas in Updraft gasifier, it is common to observe higher tar levels in the produced gas, around 10-20% [57], that needs to be cleaned to a certain level depending on the final application [50]. The second distinction is the exit-gas temperatures, Updraft gasifiers present lower temperatures than Downdraft ones [58].

In Figure 4, we can see the schemes of the four main air-fed gasifiers. The second major distinction is how the heat necessary for the gasification process is provided. The heat may derive from the partial-combustion of the feedstock (direct, autothermal gasification), or from an external source (indirect, allothermal gasification).

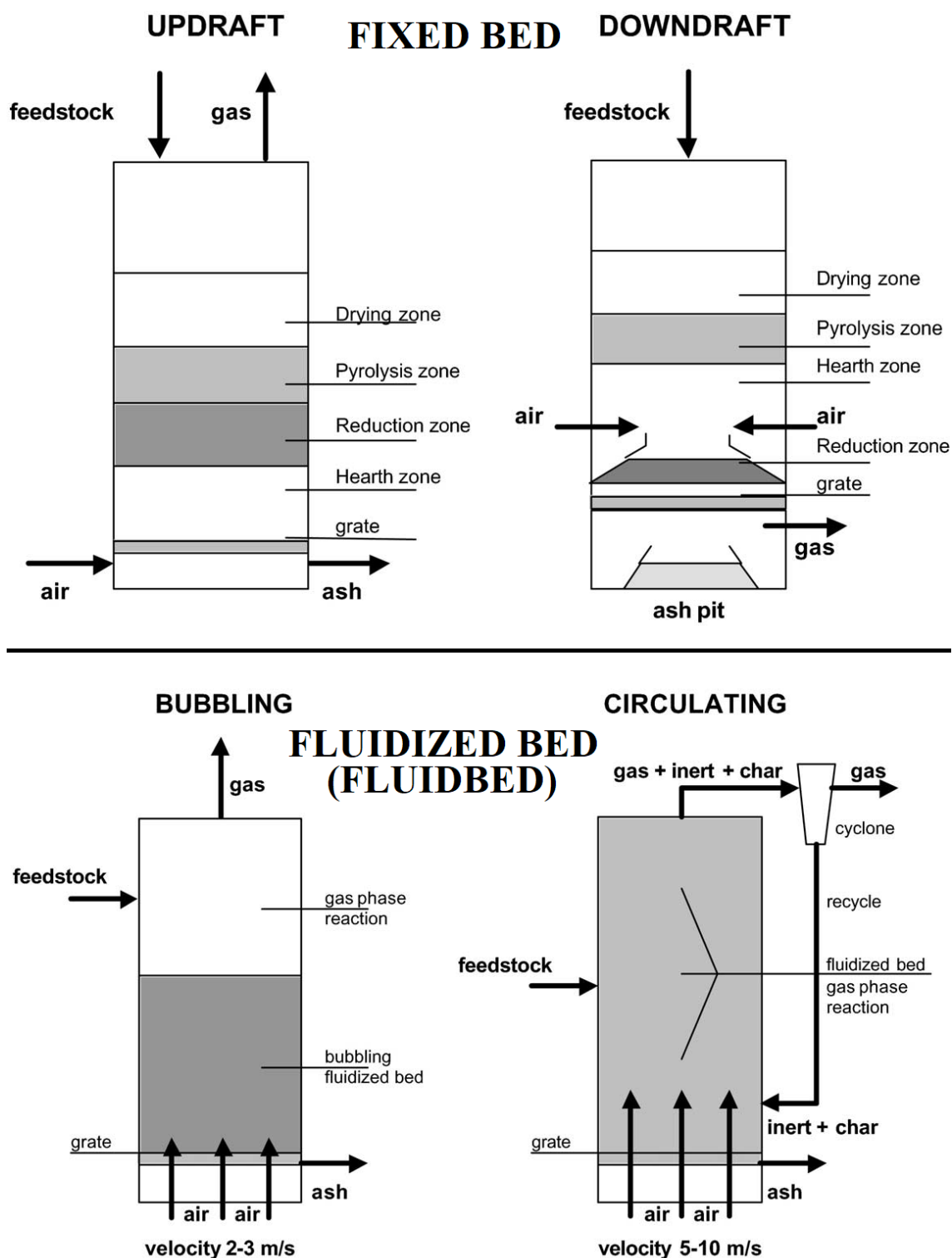


Figure 4: Common types of fixed and fluidized bed autothermal gasifiers (adapted from V. Belgiorno et al. [59]).

In Figure 5, we can see the results of the different approaches to gasification of biomass. Generally, the fixed-bed gasifiers are suited to smaller power outputs associated with autothermal gasification, whereas in larger installations fluidized-bed gasifiers are more usual. Nevertheless, the use of steam as a gasifying agent is gaining attention due to its end-gas composition rich in H_2 and higher calorific value. However, the chemical reactions associated with steam gasification are on average endothermic, requiring an external source of heat.

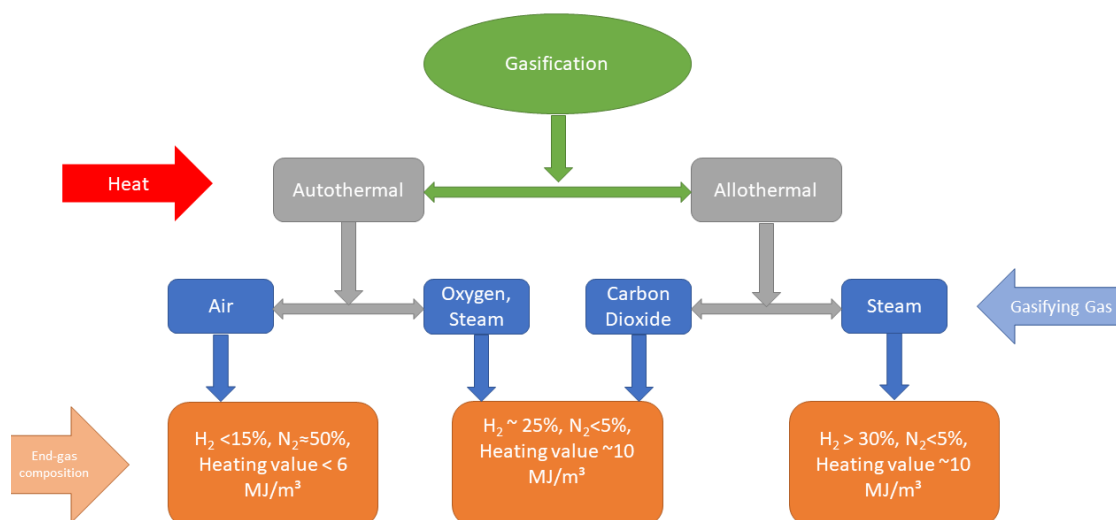


Figure 5: Product characteristics of allothermal and autothermal biomass gasification (adapted from R. Thomson et al. [50]).

In small-scale gasifiers the main goal is to improve the heating value of the producer gas. This is generally dependent on reducing the nitrogen by using an Air Separation Unit (ASU) or by externally heating the process. For the latter the process is named as allothermal, requiring an external source of heat through a heat exchanger inside the gasifier or through the circulation of a material acting as a heat carrier [60]. With both methods, the increased cost and additional complexity may turn the system unfeasible, especially for small-scale gasifiers.

Table 2 presents the major advantages and drawbacks of gasifiers presented in Figure 4. In autothermal gasification, the necessary heat for the endothermic reactions is provided by the partial oxidation of the feedstock. If air is used as the gasifying agent the gas produced has a heating value between 4 to 7 MJ/Nm³, which is suitable for power applications [60]. For other applications, like the conversion into methanol and other liquid biofuels, pure O₂ is preferred. Nonetheless, the operating costs will increase due to the costs of producing O₂ in the ASU.

Table 2: Advantages and drawbacks of gasifier design (adapted from Sikarwar et al. [61])

Gasifier design	Major advantages	Major limitations
Fixed bed/moving bed gasifier	<ul style="list-style-type: none"> • Simplest and robust design <ul style="list-style-type: none"> ○ Economical at small scale ○ Tolerant to large range of biomasses 	<ul style="list-style-type: none"> • Non-uniformity in temperature <ul style="list-style-type: none"> ○ High tar and char yields
Fluidized bed gasifier	<ul style="list-style-type: none"> • Uniformity in temperature distribution <ul style="list-style-type: none"> ○ Low tar and char yields • Shorter residence time <ul style="list-style-type: none"> ○ High capacity for raw material processing 	<ul style="list-style-type: none"> • Uneconomical for small scale <ul style="list-style-type: none"> ○ High PM fraction in syngas
Entrained flow gasifier	<ul style="list-style-type: none"> • Very low tar yield <ul style="list-style-type: none"> ○ Economical for large scale ○ High quality syngas 	<ul style="list-style-type: none"> • Unsuitable for biomass <ul style="list-style-type: none"> ○ Non-tolerant for coarse particles ○ Issue with raw gas cooling

The third distinction concerns the pressure of the operation of the gasifying system: atmospheric or pressurized. The overall cost of the pressurized system can reach four times the cost of an atmospheric gasifier (for a 20 MWe installation [58]). On the other hand, it has the advantage of turning unnecessary a gas compressor for feeding a gas turbine afterwards, and of having a relatively high tar acceptance [58]. For biomass gasification, since the biomass is more reactive than coal, there are fewer advantages for pressurized systems, in terms of a chemical kinetics point of view.

1.1.3. Syngas cleaning methods

After the syngas is produced by gasification, several contaminants must be eliminated. The contaminants are tars (i.e. condensable hydrocarbons), Particulate Matter (PM), alkali metals, nitrogen molecules (NH_3 , HCN), sulfides (H_2S , COS), hydrogen chloride (HCl), and other trace elements [57,61].

The cleaning levels required for power generation applications (i.e. ICE and Gas Turbines) are presented in Table 3. Like for the final composition of the syngas, the feedstock has an influence on the contaminants [57]. Depending on the final application of the gas and its emissions standards, some contaminants must be removed [52,57,60]. The cleaning methods are classified by their operating temperature: hot (above 300°C), cold (under 100°C) and warm gas (between those two temperatures). The cold gas techniques often employ water sprays and the low outflow temperatures that allow water to condense. The contaminants will serve as nucleation sites for water condensation, or be absorbed by the water droplets [57]. Warm cleaning occurs in temperatures above the boiling point of water, but cold enough for the condensation of ammonium chloride (NH_4Cl). The hot gas cleaning techniques are

aimed at alkali metals removal. The sulfur contaminants (H_2S and COS) must be separated, to not interfere with the Selective Catalytic Reduction (SCR) system operation [43].

Table 3: Typical syngas cleaning requirements per application [57].

Contaminants	IC engine	Gas Turbine
Particulate Matter (PM)	<50 mg/m ³	<30 mg/m ³
Tars	<100 mg/m ³	---
Sulfur (H_2S , COS)	---	<20 μ L/L
Nitrogen (NH_3 , HCN)	<25 mg/Nm ³ [62]	<50 μ L/L
Alkali	---	<0.024 μ L/L
Halides (primarily HCl)	---	<1 μ L/L

1.1.4. Choice of different syngas compositions during this study

The syngas compositions can be varied, with the five main components with various shares, not to mention the contaminants. The choice of the syngas composition tested must be representative as well as possible, of real gasifiers to identify how each component influences the performance and emissions of the engine/turbine. Three compositions were defined following the suggestions of Bridgwater [58] to represent the typical compositions of three types of air-fed gasifiers: Fluidbed (Fluidized Bed), Updraft and Downdraft (see Table 4).

Table 4: Selected syngas compositions and resulting properties.

	H_2	CO	CO_2	CH_4	N_2	Stoichiometric Fuel Ratio	Air	LHV	Maximum flame speed
	%Vol	%Vol	%Vol	%Vol	%Vol	mol/mol (mass/mass)		MJ/m ³	(at 298 K 1bar) cm/s
Fluidbed (Fluidized Bed)	9	14	20	7	50	1.21 (1.25)		4.2	15.4
Updraft	11	24	9	3	53	1.12 (1.24)		4.4	30.7
Downdraft	17	21	13	1	48	1.00 (1.13)		4.8	36.7

The compositions also present different H_2/CO ratios, 0.46, 0.64 and 0.80 for Updraft, Fluidbed and Downdraft, respectively. This is one of the important parameters for syngas combustion [63]. The choice made for air-fed gasifiers, implying high nitrogen concentration on the product, is justified by the little number of allothermal power plants or with an ASU [64]. This is shown by the high nitrogen concentration on the product in Table 4.

1.2. Syngas as a fuel for power generation

Renewable energy sources cannot supply all fluctuating electricity demand for all countries. Therefore, multiple solutions must be explored. Future energy supplies must emit as little GHG as possible, and also be renewable, and be dispatchable [65]. The use of syngas as a solution for providing power is extensive, with variety of sizes, efficiencies, and technology maturity. The following subsections will provide a brief overview of the uses of syngas, obtained from gasification of biomass and waste, in power applications.

1.2.1. Gas turbines: Integrated Gasification Combined Cycle (IGCC)

In IGCC, the syngas produced by gasification of coal, biomass, among others, is introduced into a Gas Turbine (GT), as the unique fuel or co-fired with Natural Gas (NG) or fuel oil [66]. The main challenge in operating GT, originally designed for NG, is that the heating value of syngas is four to eight times lower than natural gas.

As shown in Figure 6, the gasifier in the IGCC set-up feeds directly the GT. A careful balance of the N_2 content already present in the syngas and the N_2 added by the Air Separation Unit (ASU), must be considered to comply with the NO_x emissions regulations. The heat from the exhaust gases can be recovered with a Heat Recovery Steam Generator (HRSG), increasing the overall efficiency of the system. Also, the steam generated in the HRSG can be injected in the combustor for NO_x control of the GT.

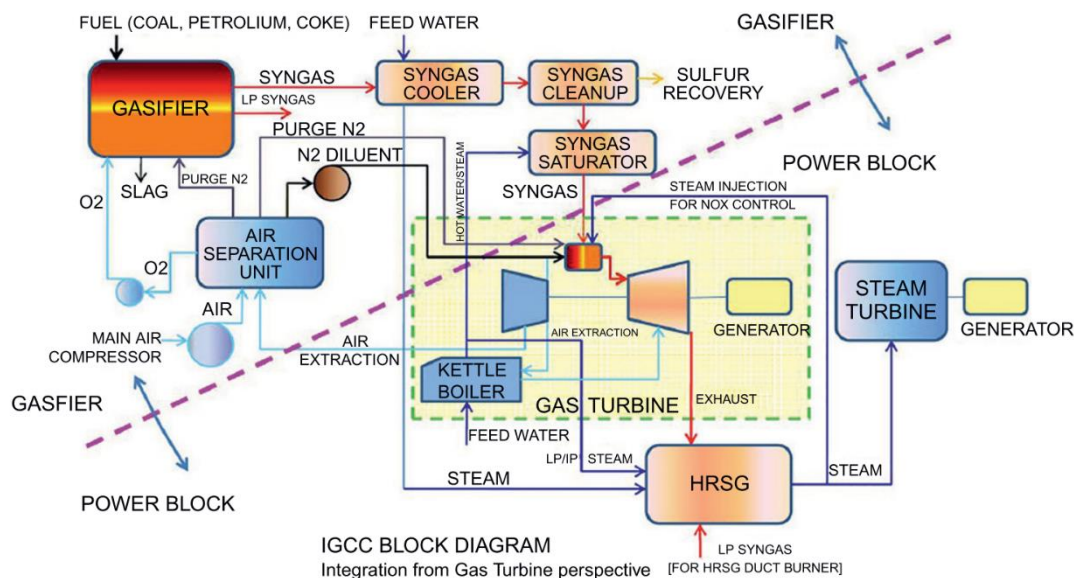


Figure 6: Diagram of IGCC (adapted from Ganjikunta [67])

With the intend to compare both thermal machines, i.e. ICE and micro-GT, Fatiguso et al. [68] simulated both machines applied in an CHP of an electrical power of 240 kW_{el} (originally designed for NG), with the syngas produced by a Downdraft gasifier. They concluded that, considering hot and cold days, the ICE is more resilient to the impact of ambient temperatures on both thermal and electrical efficiency.

However, in low electrical loads, between 20 to 50%, the micro-GT is slightly more efficient than the ICE.

1.2.2. Internal Combustion Engines (ICE)

Syngas fueled Internal Combustion Engines (ICE) exists since the 1920s, when the French inventor Georges Imbert developed a first wood gas generator for automotive use [28]. Due to fossil fuel rationing during the WWII, the use of syngas for fueling Internal Combustion Engines (ICE) was a common practice, at the time usually named the 'wood-gas'. Nowadays, syngas can be used as a fuel in Combined Heat and Power (CHP) plants, which are common in Denmark and Sweden [64,69] where district heating is widespread [70].

Figure 7 presents a schematic design of a CHP plant, which uses an ICE coupled with a generator. There, the heat is extracted from the hot syngas after the gasifier and the engine exhaust. The efficiency of the CHP plant can be calculated by considering the net electrical efficiency or the overall efficiency, which is the electrical power and the added heat in the water divided by the heating value of the fuel. Therefore, the energy of the hot syngas produced by the gasifier and exhaust gases of the engine are partially recovered, contributing to the high overall efficiency of the CHP that ranges from 70% to 90% [64].

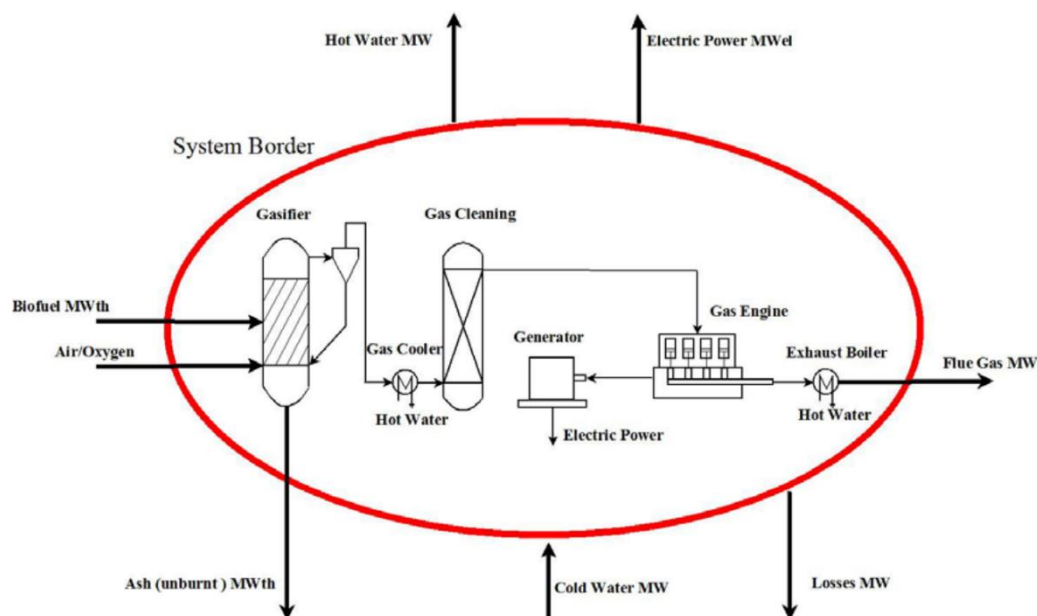


Figure 7: Schematic of a Combined Heat and Power (CHP) plant that uses an Internal Combustion Engine (ICE) (adapted from Brandin et al. [64])

As for any fuel, a syngas ICE can be Compression Ignition or Spark-Ignition engine. But in fact, the use of syngas in Compression Ignition (CI) engines is possible following two combustion modes : Homogenous-Charge Compression Ignition (HCCI) [71,72] or Dual-Fuel Compression Ignition, where the ignition is allowed due to the pilot injection of a high-reactivity fuel. Bhaduri et al. [71] investigated HCCI operation with three syngas compositions feeding a mono-cylinder air-cooled engine with a Compression Ratio (CR) of 12:1. They investigated the effect of water content and tar presence on

syngas, and the intake pressure and temperature of the manifold. They achieved almost 98% combustion efficiency with the hydrogen-rich syngas composition, despite the overall high CO emissions which were always above 5%.

The limiting factor in syngas HCCI operation is the low load due to the small knock-limited Equivalence Ratio (ER), and the hard combustion phasing tuning. This is hard combustion phasing tuning is exacerbated by the syngas composition uncertainty. To better control the engine behavior other routes need to be explored, such as dual-fuel or spark-ignited engines.

In Spark-Ignition (SI) engines, the injection strategy could be homogenous (in port-fuel) or stratified with direct injection. However, there are only a few published papers regarding direct-injection of syngas [73]. Sridhar et al. [74,75] found for that syngas composition there was no sign of abnormal combustion, 'knock', even at the higher CR (17:1).

With the intent of comparing both modes of operation on the same engine, Shashikantha and Parikh [4] experimented on a diesel engine: first on diesel-only to establish a baseline, then on Syngas-Diesel dual-fuel. A spark-plug was inserted on the cylinder head, after a reduction of the Compression Ratio (CR) of the engine, optimized to 11.5:1 (originally at 17:1) with also a change of piston design. From the spark-ignited experiments, with syngas and natural gas, lower NO_x and CO emissions were obtained than in diesel-only and dual-fuel operation, with the caveat that the injection timing in dual-fuel operation was not optimized and the CR was changed. The difference between Shashikantha [4] and Sridhar [74] works, regarding the appearance of abnormal combustion in the case of Shashikantha [4], may be explained by the different H_2 content of the syngas composition. When Sridhar et al. [74] varied the CR, it was clear that the efficiency of the engine dropped when the CR is reduced.

To summarize, the advantages of dual-fuel operation include the minimal engine modifications and also the flexibility, of increasing the pilot fuel amount if the supply of syngas fluctuates in production flowrate and/or in its composition. Additionally, the expected knocking-tendency of syngas, due to the H_2 presence, is attenuated by the presence of diluents. Therefore, the dual-fuel engine can operate with a high Compression Ratio, taking advantage of the efficiency benefit.

1.3. Plan of this manuscript

This manuscript is composed of six chapters. Following this introduction, we present an analysis of the literature review of syngas/diesel dual-fuel engines. The main parameters relevant to these engines, such as syngas-to-diesel energy share, diesel injection parameters and syngas composition. We highlight the effects of these parameters on engine performance and exhaust emissions. The third chapter is dedicated to the study of fundamental laminar combustion of syngas, as a function of three compositions selected for engine-relevant conditions. For this purpose, we determine and analyze two combustion properties: laminar flame speeds and Markstein lengths. In Chapter 4, the dual-fuel engine performance and the related emissions for the selected syngas compositions and the other engine operating parameters are presented. These are measured in a single cylinder compression engine. In Chapter 5, we provide a combustion analysis in an optically accessible single-cylinder engine. In this analysis, we select specific engine conditions by fixing the syngas/air equivalence ratio and pilot fuel injection parameters, then we analyze the combustion images. The manuscript is then finished by discussing the main conclusions and some possibilities for future work and new perspectives.

2. State of the art in syngas/diesel dual-fuel engine: performance and emissions research

The use of syngas as a fuel in a Compression Ignition engine (CI) present some challenges, due to their high auto-ignition temperature ($>500^{\circ}\text{C}$) [28]. For this reason, a successful operation of this biofuel in a CI engine necessitates an injection of a high cetane number (high reactivity) fuel, as for example, close to Top Dead Center (TDC) of the cycle [76,77]. This concept is known as a Mixing Controlled Compression Ignition (MCCI) engine [78] where the main low-reactivity fuel combustion is primed by a small injection of a high-reactivity fuel, known as the pilot fuel. Figure 8 presents the schematic of a Reactivity-Controlled Compression Ignition (RCCI) engine, a particular case of MCCI, but provides the general concept of the dual-fuel engine. Those engines can combine the high thermal efficiency of a diesel engine, related to their higher Compression Ratios (CR), together with lower NO_x and PM emissions, when the right parameters are selected, like the ratio of energy of the pilot fuel and the phasing of its injection [77]. The low-reactivity fuels used in MCCI engines can be Syngas [79], Natural Gas (NG) [80], Hydrogen (H_2) [81], Methanol [82] or Ammonia (NH_3) [83], all of them are low-carbon or, in the case of ammonia and hydrogen, zero-carbon fuels. They are combined with a high-reactivity fuel that can be either conventional diesel, dimethyl ether or biodiesel, where the important factor is the reactivity of the fuel, represented by its cetane number and its aromatic content [76,84]. Table 5 presents the physicochemical properties of several fuels, renewable, reference and fossil, with five different syngas compositions presented along common fuels. The syngas composition, referred to as 'Syn4', is the most representative of the three compositions tested in the manuscript, resulting in similar heating values.

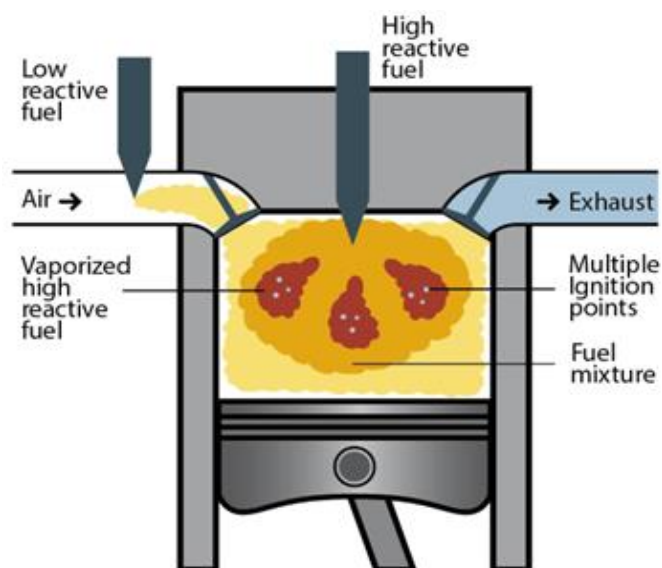


Figure 8: Illustration of the dual-fuel engine operation (image adapted from [186])

Table 5: Physicochemical properties of a typical syngas mixtures compared to other fuels (adapted from the work of Paykani et al. [28])

Properties	Syn1	Syn2	Syn3	Syn4	Syn5	Biogas	H ₂	CO	Methane	Gasoline	Diesel
Density (kg/m ³) (at NTP)	0.54	0.67	0.68	1.05	1.04	1.11	0.0824	1.145	0.656	719.7	832
Molecular weight (kg/kmol) (at NTP)	13.91	15	15.2		23.2	34.4	2	28	16.04	103	200
Stoichiometric air/fuel ratio (kg/kg)	5.3	4.58	7.23	1.4	2.07	5.67	34.2	2.5	17.2	14.7	14.7
Flammability limits (vol.% in air)	24-60	6.06-74.2	5.8-41.4	7-21.6	13.4-58	7.5-14	4-75	12.5-74	5-15	1.4-7.6	0.6-7.5
Flammability limit [ϕ]	0.2-7.2	-	-	-	-	-	0.1-7.5	0.3-6.8	0.4-1.6	0.7-4.3	1.0-6.5
Autoignition temperature [K]	980	873-923	873-923	898	898	923	858	882	813	550	589
Minimum ignition energy [mJ] *ST	-	-	-	-	-	-	0.02	-	0.28	0.24	-
Laminar flame speed [m/s] *ST	1	1.8	-	0.5	0.5	0.25	1.8-2.8	0.4	0.38	0.37-0.43	-
Adiabatic flame temperature [K] *ST	2584	2385	2400	-	2200	2145	2390	2214	2214	2580	-
Quenching distance [mm] *ST	-	-	-	-	-	-	0.64	1.6	2.1	2.84	-
Lower heating value [MJ/kg]	15.7	17.54	24.4	5	7.47	17	119.7	10.1	50	43.4	42.6
Volumetric energy content [MJ/m ³]	8.47	11.75	16.59	5.25	7.84	18.87	9.86	11.56	32.8	31235	35443
Syn1:57/43:H ₂ /CO, Syn2:50/50:H ₂ /CO, Syn3:40/40/20:H ₂ /CO/CH ₄ , Syn4: 22.6/24.3/2.2/9.3/41.2:H ₂ /CO/CH ₄ /CO ₂ /N ₂ , Syn5: 19.6/29.6/5.27/5.41/40.56: H ₂ /CO/ CH ₄ /CO ₂ /N ₂ and Biogas: 55.6/42.3/2.1: CH ₄ /CO ₂ /N ₂ (by volume).; NTP normal temperature (T=298.15 K) and pressure (p=1 bar); ST at stoichiometry ($\phi=1$)											

There are several parameters to optimize in a MCCI engine in the case of a syngas/diesel dual-fuel experiment such as the syngas/diesel energy ratio, the diesel injection parameters (injection pressure, timing...), the composition of syngas itself, and other general engine parameters (engine speed, load, Compression Ratio...). Table 6 provides a review of dual-fuel experimental studies performed with a syngas (H₂/CO + diluents), whose composition is similar to a producer gas and primed by the injection of a high-reactivity fuel (pilot fuel). Azimov et al. [1] explored a dual-fuel combustion method called PREMIER (Premixed Mixture Ignition in the End-gas Region), where the combustion starts with the auto-ignition of the pilot fuel, and subsequently the main fuel premixed flame propagation towards the cylinder wall, that increases the unburnt-gas temperature to the point of its auto-ignition. In this combustion mode, the Heat-Release Rate (HRR) is divided in two stages and can be observed in several other studies [85–87]. presents the scheme of Reactive Controlled Compression Ignition (RCCI) engine operation, one particular case of MCCI engine. The main difference between RCCI and conventional dual-fuel that in RCCI the high-reactivity fuel injection occurs early in the cycle, this may turn unfeasible in high-load operation, since the Maximum Pressure Rise Rate (MPRR) and the maximum in-cylinder pressure can exceed the designed limits of the engine [88].

Roy et al. [2] tested two producer gas compositions, only by changing H₂ and N₂ mole fractions, and with similar Energy Share of Syngas (ESS) to Azimov et al. [1]. They also obtained two-stage HRRs, when the certain Injection Timing (IT) and syngas/air equivalence ratio are used, i.e. $\phi \approx 0.6$ and slightly advanced IT (See Figure 9). The dual-fuel engine with the high-H₂ composition produced more NO_x emissions than with the low-H₂ composition, for all syngas/air equivalence ratios, due to the higher flame temperature inducing higher thermal NO_x.

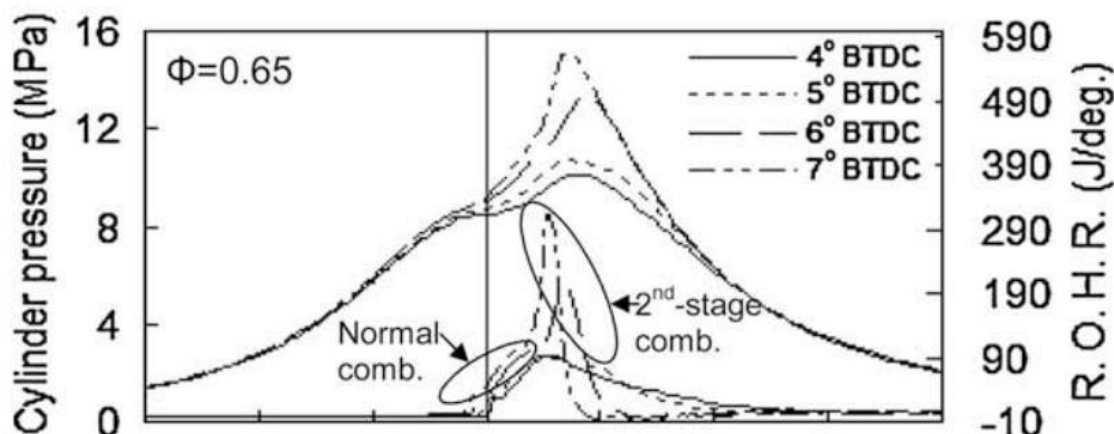


Figure 9: Example of a two Heat-Release Rate (HRR), reproduced from the work of Roy et al. [2].

Regarding the effects of Compression Ratios (CR), Sharma and Kaushal [3] tested a low calorific value (~ 6.6 MJ/Nm³) producer gas in a dual-fuel engine with CR's ranging from 12:1 to 18:1. The higher ESS are possible with higher CR, inducing a decrease of NO_x, HC and CO emissions at high-load, due to a more complete combustion. The increase of CR also decreases the exhaust temperatures and, by doing so, increases the engine efficiency. However, it must be noted that in dual-fuel mode the engine produces four to six times the HC emissions and 1.3 to 1.5 times the CO emissions of the same engine running on pure diesel on full-load [3]. Some of these results of Sharma and Kaushal [3] are depicted in Figure 10. Balakrishnan and Mayilsamy [89] also tested an even more N₂-diluted producer gas (N₂ = 58.8%) and, even with a small ESS (5-20%), the CO emissions decreased linearly with the increase of CR, when the engine is running at full-load.

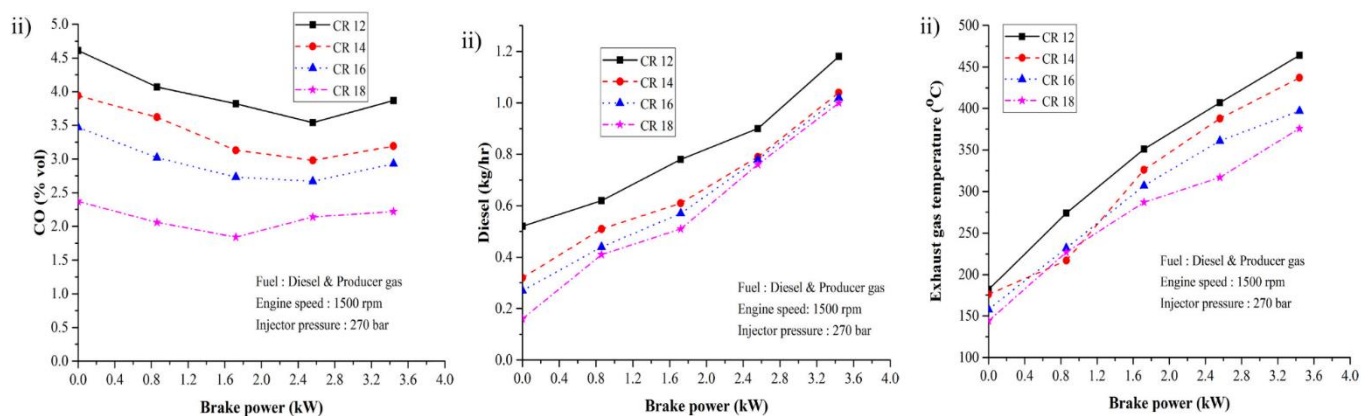


Figure 10: Results of Sharma and Kaushal [3] in dual-fuel producer gas/Diesel.

Another very important factor is the nature of the pilot fuel and the injection parameters (Injection Timing, Injection Pressure...), affecting the range of achievable operating conditions [76,84]. Carlucci et al. [90] tested three different ESS and biodiesel as the pilot fuel (cetane number of 52), of the same syngas composition (20/20/60:H₂/CO/N₂ by volume), and determined that it does not influence the overall engine efficiency, but the choice of Injection Timing (IT) does. They concluded that the lower Injection Pressure and the IT slightly advanced in relation to the Top-Dead-Center (TDC) provides a more complete combustion, i.e. lower HC and CO emissions, higher thermal efficiency and in-cylinder temperatures, and consequently higher NO_x emissions. Figure 11 presents the fuel conversion efficiency (η_f = engine brake power/ total provided chemical power) of the engine for two Injection Pressures (IP), 500 and 100 bar, and for the three ESS. In the second part of the study, they analyzed the effect of splitting the pilot fuel injection into two smaller injections (where the total volume of the pilot fuel injection is kept constant), on engine performance and emissions. Splitting the pilot injection is an effective strategy the improve fuel conversion efficiency at low-to-mid engine loads.

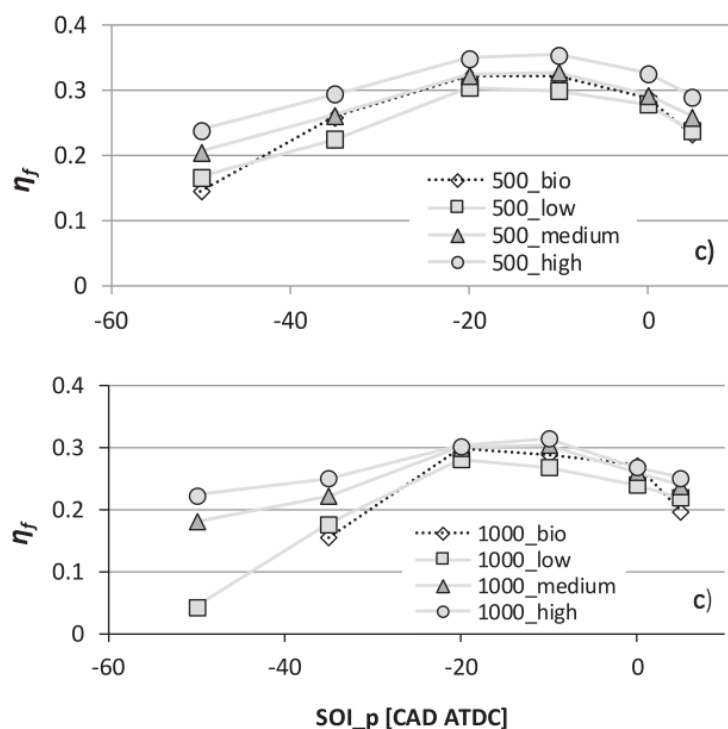


Figure 11: Fuel conversion efficiency (η_f) of the dual-fuel, comparing the 3 ESS (35/50/65%:low/medium/high) and pilot fuel injection only (dashed line-'_bio'), with two injection pressures, 500 and 1000 bar (adapted from the work of Carlucci et al. [90]).

After this review of dual-fuel experimental studies performed with a syngas, we proceed to determine the effects of the syngas composition, ESS and the injection parameters of the pilot fuel, on the dual-fuel engine performance and emissions. To keep this analysis realistic, three syngas air-gasified compositions were selected [58] and the combustion dynamics between the premixed air-syngas mixtures and the diesel-surrogate, decane, are presented in the following chapters.

Composition(s) Tested	Equivalence Ratios/ Energy Share of Syngas	Pilot Fuel Type, Injection Parameters	Engine Parameters (CR, Engine Speed...)	Emissions/Performance	Comments	
Azimov et al. [1]	7 compositions: H ₂ (%) / CO (%) / CH ₄ (%) / N ₂ (%) / CO ₂ (%) / LHV (MJ/kg): 13.7/22.3/1.9/16.8/45.3/4.13 20.0/22.3/1.9/16.8/39.0/4.99 56.8/22.3/1.9/16.8/2.2/13.64 13.7/22.3/1.9/23.0/39.1/3.98 13.7/22.3/1.9/34.0/28.1/3.74 56.8/5.9/29.5/2.2/5.6/38.69 56.8/29.5/5.9/2.2/5.6	$\phi = 0.3-0.95$ / total energy input: 2300 J/cycle \rightarrow 94 % ESS	Diesel, IP = 800 bar, 3 mg/cycle, IT $\uparrow\downarrow$.	CR 16:1, N = 1000 rpm, IP = 2 bar.	When \uparrow H ₂ in composition, IMEP \uparrow η \uparrow and CD \downarrow , but NO _x emissions \uparrow . Whereas when \uparrow CO ₂ in composition, IMEP \downarrow η \downarrow , but NO _x emissions \downarrow .	100% H ₂ also tested.
Roy et al. [87]	13.7% H ₂ , 22.3% CO, 1.9% CH ₄ , 16.8% CO ₂ and 45.3% N ₂ LHV \sim 5.0 MJ/m ³	$\phi_{\text{Global}} = 0.63$ / ESS 83-96.6%	Diesel, IP = 400-800 bar, 2-10 mg/cycle, IT 8 to 13.5 BTDC.	CR 16:1, N = 1000 rpm, Intake pressure = 2 bar.	The lower NO _x emissions for retarded injection timing and injection pressures, but with a small penalty for HC/CO emissions. In general IP \uparrow \rightarrow power \uparrow	
Roy et al. [2]	2 compositions: Low-H ₂ \rightarrow 13.7% H ₂ , 22.3% CO, 1.9% CH ₄ , 16.8% CO ₂ and 45.3% N ₂ LHV \sim 5.0 MJ/m ³ High-H ₂ \rightarrow 20% H ₂ , 22.3% CO, 1.9% CH ₄ , 16.8% CO ₂ and 39% N ₂ LHV \sim 5.65 MJ/m ³	Low-H ₂ syngas \rightarrow $\phi=0.40-0.95$ / ESS \approx 93.5-96.1% High-H ₂ syngas \rightarrow $\phi=0.42-0.99$ / ESS \approx 93.8-96.3%	Diesel, IP = 800 bar, 3 mg/cycle, IT depends on ϕ .	//	Low-H ₂ syngas \rightarrow \downarrow NO _x High-H ₂ syngas \rightarrow \uparrow power and faster combustion	
Sharma and Kaushal [3]	16.12% H ₂ , 17.58% CO, 5.83% CH ₄ , 15.88% CO ₂ , 40.67% N ₂ , 0.87% H ₂ S and 3.02% O ₂ Heating value 6.61 MJ/Nm ³	ESS 0-46.7% (depending on CR)	Diesel, CN 51.2, IP = 270 bar.	CR 12:1 to 18:1, N = 1500 rpm, Load $\uparrow\downarrow$.	Diesel consumption \downarrow with \uparrow of CR. Exhaust T° \uparrow and NO _x emissions \downarrow in Dual-Fuel mode. NO _x , CO, HC \downarrow with CR \uparrow at higher loads.	Syngas from Downdraft gasifier fed with pistachio shells

Rinaldini et al. [91]	9.4% H ₂ , 22.4% CO, 3.4% CH ₄ , 5.4% CO ₂ and 59.4% N ₂ , LHV ~5. MJ/m ³	ESS 0-57% (depending on load)	Diesel, IP = 1600 bar.	CR 17.5:1, Turbocharged and EGR present but not used, N = 3000 rpm, Load 50-100-300 Nm.	CA ₉₀₋₁₀ ↑ and CA ₁₀ ↓ with ↑ of ESS. Engine brake η ↑ with ESS (~36% for pure diesel and ~40% with ESS= 27%)	Syngas from Downdraft gasifier.
Guo et al. [92]	3 compositions: H ₂ (%)/CO(%)/CO ₂ (%)/N ₂ (%)/LHV(MJ/kg) 18.0/21.0/13.0/48.0/4.06 29.0/10.0/13.0/48.0/4.38 34.0/48.0/12.0/6.0/10.29	ESS 0-60% (depending on load)	Diesel, CN 45.4.	CR 16.25:1, Int. Pressure ↓ and EGR not used, N = 910 rpm, Load ↓.	NO _x ↓ only with syngas with higher N ₂ content (i.e high dilution). In general, ESS ↑ → ID ↑ η ↓ Soot ↓.	
Carlucci et al. [93]	3 compositions: Type - H ₂ (%)/CO(%)/N ₂ (%) A - 15/25/60 B - 20/20/60 C - 25/15/60	Gaseous fuel injection pressure p _{gf} = 3–5–7 bar	Biodiesel, CN 52, IP 500-750-100-1250 bar, IT 2.5 – 7.5 BTDC	CR 17.1:1.	IP ↑ → η ↑, NO _x ↑, HC↓ and CO↓.	
Carlucci et al. [90]	H ₂ (%)/CO(%)/N ₂ (%)/LHV(MJ/kg) 20/20/60/26.2	ESS 35/50/65 %	Biodiesel, CN 52, IP 500 and 1000 bar, 11 mm ³ /cycle, Single and split injection with ↓ IT.	CR 17.1:1, Int. Pressure= 1.29 bar, N = 1500 rpm, Load ↓.	ESS not changed the overall η, but IT does. By splitting the pilot fuel injection, η↑ and THC, CO and NO _x ↓, for all IT.	Study of injection parameters (IP, IT and split injection).
Balakrishnan and Mayilsamy [89]	12.3% H ₂ , 10.1% CO, 1.5% CH ₄ , 58.8% N ₂ , 14.6% CO ₂ , 2.7% O ₂ , 3.56 MJ/m ³ .	ESS 5-20%, depending on load and CR.	Diesel B23 (23 % biodiesel, by volume in diesel fuel), IP = 200 bar, Load 0-100%.	CR 14:1, 16:1, 18:1 and 20:1, N ≈ 1400-1600 rpm.	↑ CR → NO _x , smoke, Exhaust Temperature ↓ and η ↑.	

- ↓ Variable, ↓ Decrease, ↑ Increase, → Results/leads in/to, CN Cetane Number, ESS Energy Share of Syngas, IP Injection Pressure, IT Injection Timing, CA₁₀ first part of the combustion process, CA₉₀₋₁₀ main part of the combustion process, EGR Exhaust Gas Recirculation, NO_x Nitrogen Oxides, CO Carbon Monoxide, HC Hydrocarbons, ID Ignition Delay, η efficiency, HOME Honge Oil Methyl Ester, BTDC Before Top Dead Center

Table 6 : Literature review on syngas/diesel dual-fuel engine.

3. Experimental characteristics of laminar syngas/air premixed flame

3.1. Introduction

We open this chapter presenting the key concepts of the laminar premixed flame theory, to provide a theoretical background to the experimental set-up employed in the determination of the laminar flame speed and Markstein length.

Premixed flames consist of a combustible mixture of fuel and oxidizer that when ignited, produce heat and burnt gases, where several chemical kinetics, thermodynamics and transport phenomena are involved. The following exothermic chemical equation presents the overall concept of combustion:



where the letters F, O and P represents the fuel, oxidizer and products of the combustion, respectively, and ν represents the stoichiometric coefficients of each component. This process involves several elementary and intermediate chemical reactions. The equivalence ratio, commonly noted with the Greek letter phi, ϕ , is defined as follows:

$$\phi = \frac{\left(\frac{X_F}{X_O}\right)}{\left(\frac{X_F}{X_O}\right)_{st}} \quad (3-1)$$

Where X_F and X_O are the fuel and oxidizer mole fractions, present in the said mixture, and the *st* subscript relates to the stoichiometric ratio of the reactants. When a mixture has an equivalence ratio under 1, $\phi < 1$, the mixture is considered to be 'lean' and thus the oxidizer is in excess; whereas in a 'rich' mixture the fuel is in excess equating to $\phi > 1$.

A laminar flame can be split into different zones. Figure 12 illustrates the evolution of temperature, reactant concentration and heat release of a premixed flame. A laminar flame is composed of a preheating zone governed by mass and heat diffusion, represented by thickness δ_p , and a reaction zone, δ_r . Numerous definitions have been proposed in literature to evaluate the flame thickness [94]. The first definition, referred to as the kinetic (or diffusion) thickness (δ_k) often corresponding just to the length of reaction zone, is:

$$\delta_k = \frac{\lambda_u}{\rho_u C_{p,u} S_L^0} \quad (3-2)$$

Where λ_u is the thermal conductivity, ρ_u is the density of the unburnt gases, $C_{p,u}$ is the constant pressure heat capacity by mass and S_L^0 is the laminar flame speed, as defined by Zel'dovich [95]. A second definition, relying on the extraction of the gradient of the temperature profile as a function of the axial distance through the flame is proposed [94], and defined as:

$$\delta_G = \frac{T_{ad} - T_u}{\left(\frac{dT}{dx}\right)_{max}} \quad (3-3)$$

This approximation relies upon the application of a linear gradient as the tangent of the inflection, which corresponds to $(dT/dx)_{max}$, from unburnt (T_u) to burnt conditions (T_{ad}), numerically modelled using the CHEMKIN-Pro software.

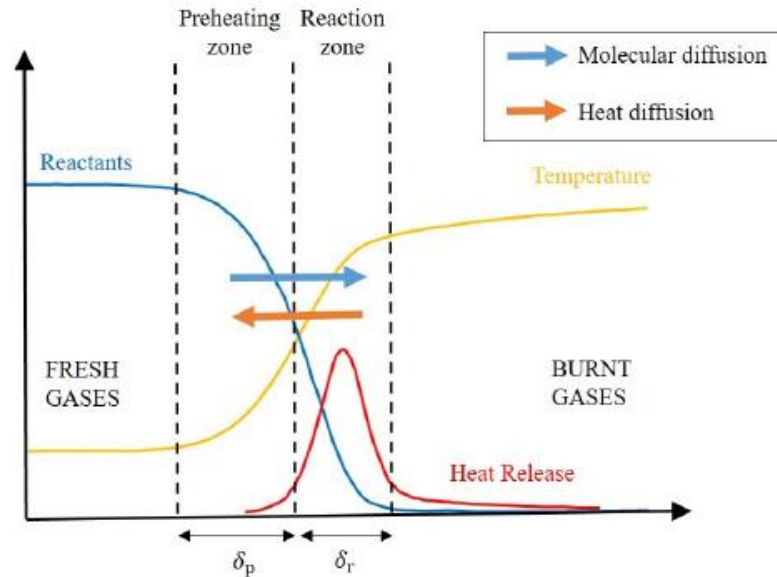


Figure 12: Schematic of a premixed flame (reproduced from [96]).

3.1.1. Laminar flame propagation

The consumption speed of the fresh, unburnt gases is described as the laminar burning velocity, S_L^0 , and it can be defined with the reaction rate, $\dot{\omega}_k$, of all the chemical reactions participating in combustion. For a 1D unstretched adiabatic laminar flame we have the following equation:

$$S_L^0 = \frac{1}{\rho_u (Y_{k,b} - Y_{k,u})} \int_{-\infty}^{+\infty} \dot{\omega}_k dz \quad (3-4)$$

Where $Y_{k,b}$ and $Y_{k,u}$ are the mass fractions of species 'k' on the unburnt and burnt side, respectively, far from the flame front. S_L^0 depends on the initial thermodynamic state, temperature and pressure, of the mixture. In practical terms, to measure S_L^0 we need to determine a local flame velocity. Figure 13 presents the schematic of the measurement of the

estimate flame propagation, where the local velocity of the flame can be defined for each infinitesimal volume of the flame.

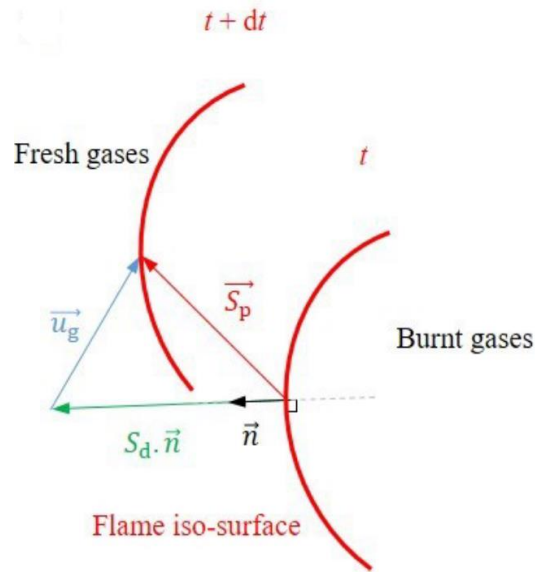


Figure 13: Schematic of the contours of local propagation and displacement speed of a premixed laminar flame (adapted from [96]).

Considering an iso-temperature surface of the flame, the local propagation speed of the flame can be defined by the following equation:

$$\vec{S}_p = S_d \cdot \vec{n} + \vec{u}_g \quad (3-5)$$

Where S_d is the flame speed displacement speed, that is multiplying by the normal component to the flame surface, and \vec{u}_g is the velocity of the fresh gases at this point. In practice, since the fresh gases in experimental set-up (described in 3.2 Experimental set-up) are considered at rest, the \vec{u}_g component is zero because the burnt gases are assumed to be quiescent ($\vec{S}_p = \vec{S}_b$). To define the unburnt flame speed, S_u , assuming measurement on the burned side, we can simply multiply the normal value of S_b by the ratio of the gas densities of the burnt and unburnt gases, assuming an infinitely thin flame front and using mass conservation:

$$S_u = \frac{\rho_b}{\rho_u} S_b \quad (3-6)$$

Where $\frac{\rho_b}{\rho_u}$ is the volumetric density ratio, obtained by means of equilibrium calculations, and S_u and S_b are the speeds of the unburnt and burnt gases, respectively.

In practical systems, the flames are submitted to stretch that modifies the flame propagation. The stretch rate was defined by Williams [97] from the surface flame area (A) as:

$$K = \frac{1}{A} \frac{dA}{dt} \quad (3-7)$$

Where K , the flame stretch whose unit is s^{-1} , can be decomposed as $K = K_c + K_s$ where K_s is the strain and K_c is the component caused by the curvature. To determine the unstretched unburnt laminar flame speed, various correlations between flame stretch and unstretched flame speed have been proposed. The first extrapolation as defined by Wu and Law [98], assumed a linear relationship, based on the assumption of a weakly stretched flame and near equi-diffusion of mass and heat [99,100]:

$$S_b^0 = S_b - L_b \cdot K \quad (3-8)$$

Where S_b^0 is the unstretched burned laminar speed and the L_b factor is the Markstein length, which can be defined as the stretch sensitivity. As such S_b^0 can be derived by extrapolation of equation (3-8) to a corresponding intercept value ($K = 0$). It should be noted that the Markstein length is related to the Lewis number, which is defined as the ratio of thermal to mass diffusivity of the deficient reactant ($Le = \frac{D_{th}}{D_m}$, with D_{th} and D_m are the thermal and mass diffusivities, respectively).

The second extrapolation, non-linear, allows for arbitrary Lewis number, and takes into consideration deviations in adiabatic and planar assumptions, such as flames heavily influenced by stretch. Kelley and Law proposed the following relationship [101]:

$$\left(\frac{S_b}{S_b^0}\right)^2 \ln\left(\frac{S_b}{S_b^0}\right)^2 = -\frac{2L_b K}{S_b^0} \quad (3-9)$$

A quasi-steady nonlinear association between S_b and K is employed, rearranged with the error used for least squares regression to obtain an extrapolated unstretched flame speed. In their study, Kelley and Law [101] compared both extrapolation methods and concluded that the non-linear method provided better accuracy for higher hydrocarbon fuels, due the nonlinearity of its flame response. The model is then more able to account for Lewis number far from unity.

Figure 14 presents the relationship between Le and stretch, the overall flame stability and the dependence of the unstretched unburnt laminar flame speed (S_u^0) to the stretched laminar flame speed (S_u). Once extrapolated to zero stretch, $S_u = S_u^0$ is considered equal to the unstretched unburnt laminar flame speed (S_u^0). As illustrated in Figure 14, the mass diffusion (or 'Molecular diffusion') from the fresh gases to the reaction zone is enhanced by positive curvature towards the fresh gases. Mixtures with $Le > 1$ are generally ruled by the thermal diffusion and the flame speed is faster in the portions with strengthened thermal diffusion and slowed down in the portions with enhanced molecular diffusion, which leads to a reduction of the flame curvature and a stabilization of the flame. Mixtures with $Le < 1$ behaves in the opposite direction. These thermal-diffusive instabilities can induce small cellular structures in the flame, increasing flame surface area, and thus flame speed.

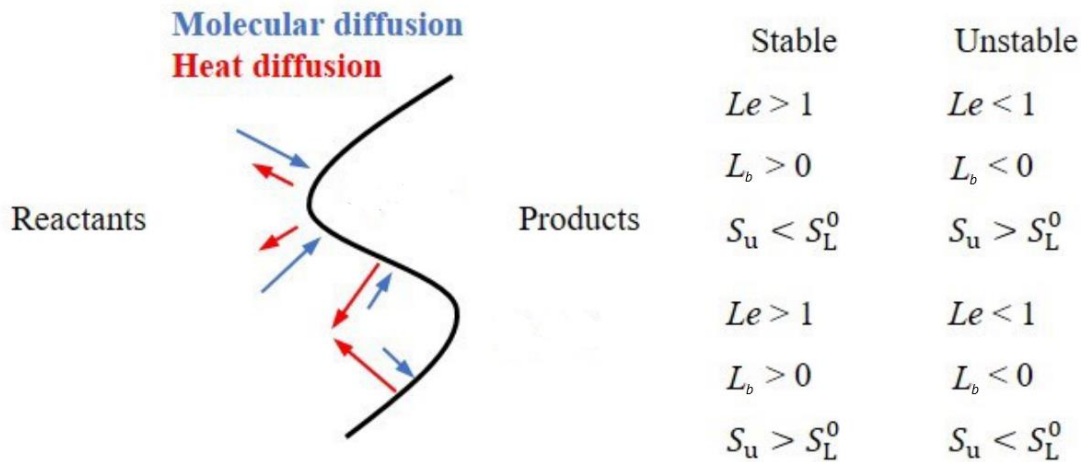


Figure 14: Relation of the Lewis number (Le) and the Markstein length (L_u , related to the burned L_b by the expansion ratio) with the flame stability (adapted from [96]).

These parameters affect the flame propagation in Internal Combustion Engines (ICE), since the S_L^0 is directly related to the consumption speed of the fuel and, therefore, the overall efficiency of the engine. Coupling this parameter with optimized conditions and ignition energy, the higher this parameter is, the lower the Cycle-to-Cycle Variation of the engine is [102]. Moreover, the flame stretch sensitivity properties, such as the Le and the L_b , are strongly related to the ignition and, subsequently, the development of the early flame inside the engine, as demonstrated by Brequigny et al. [103] and in his PhD thesis [104], as well as Aleiferis et al. [105], with different fuels on a SI engine. With these fundamental properties discussed and their importance highlighted, we shall now introduce the experimental set-up employed as well as data acquisition and processing techniques.

3.2. Experimental Set-up

The set-up used in the determination of laminar flame speeds consists of an optically accessible spherical vessel, with a lab scale system to reproduce syngas compositions using flowmeters and a Schlieren optical set-up coupled with a high-speed camera to capture the flame front. The set-up main characteristics are presented here, and more fully described in previous works [106–108].

The spherical vessel is a 4.2 L, stainless steel sphere with a 200 mm inner diameter and optical access is granted by four quartz windows of 70 mm in diameter. For initial temperature control, heating elements are placed around the combustion chamber and in the intake tube, allowing for unburnt temperatures up to 473 K. Initial pressure is measured by a piezoelectric pressure transducer with an associated uncertainty of $\pm 2\%$, with the set-up enabling unburnt pressures up to 10 bar.

In between each run, a vacuum pump depletes the sphere of gases dropping the pressure to below ~ 10 mbar. For gas mixtures, six flowmeters (Brooks 5850S ($\pm 1\%$)) are connected to the intake of the sphere and insure that, by the end of the filling process, the specified mixture composition and initial pressure are obtained. For liquids, a Coriolis flowmeter introduces the specified amount of liquid fuel. To ensure the vapor state of the fuel (decane, as a surrogate for Diesel) the inlet tube was heated to around 100°C , and introduced in a mixing valve to be mixed with the other gases. For all tested cases, the quantities of decane are well under its saturation pressure. During this filling process a fan spins, guaranteeing homogeneity, stopping 20 s before the ignition, allowing quiescence to be achieved.

The ignition system is composed of an automotive coil-on-plug (DELPHI-GN10632-12B1) connected to two 0.5 mm thick tungsten electrodes with a 1.5 mm spark gap. The tungsten electrodes are mounted at 90° to avoid too many interferences in the field of view. Ignition charge time is set at 3 ms resulting in ~ 80 mJ of discharge energy. A simultaneous TTL signal to the data-acquisition and ignition systems trigger the experiments.

The high-speed Schlieren set-up used was as schematized in Figure 15. The light from the LED (CBT120) passes through a parabolic mirror that produces a parallel beam. The second parabolic mirror focuses on the cutoff point placed between lenses L1 and L2 (see Figure 15), which focuses the beam on the camera sensor. The camera used on the experiments is a High-Speed Phantom V1610, set to record at 7000 frames-per-second with a resolution of 640×800 pixels² and a spatial resolution of 0.11 mm/pixel. This recording speed allows us to capture, at least, 30 frames for the fastest flame in our study.

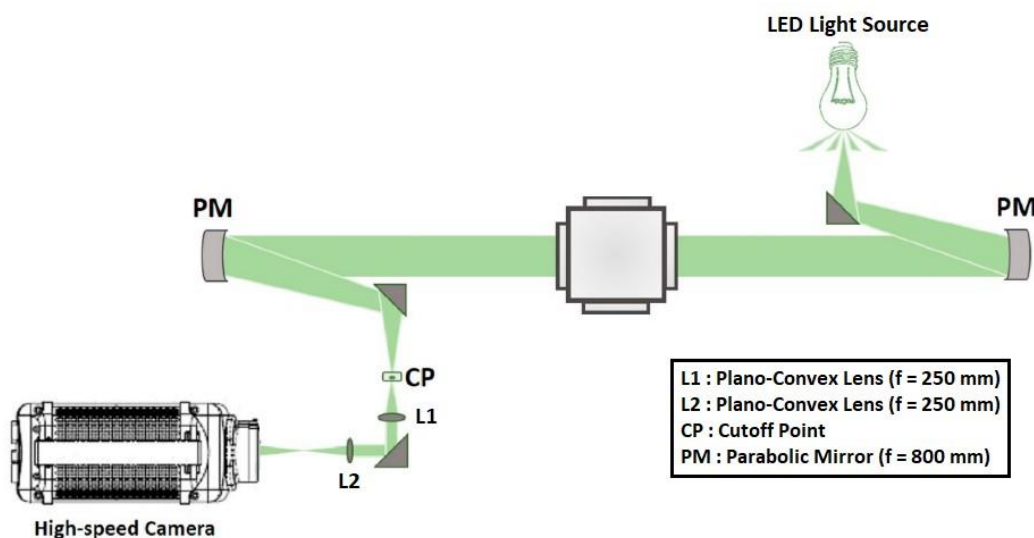


Figure 15: Schlieren Optical Set-up.

One aim of this study was to generate a database of syngas laminar flame speeds at different temperature and pressure, across a wide range of equivalence ratio. The test conditions are detailed in Table 7, based on three types of syngas composition (see Section 3.3) and thermodynamic conditions. Three repetitions are made for each condition.

Table 7: Experimental test conditions.

Syngas Composition	Downdraft, Updraft	Fluidized Bed
Equivalence Ratio (ϕ)	0.6 - 1.4	0.6 - 1.2
Pressure (bar)	1,3 and 5	
Temperature (K)	298, 323, 373, 423	

The post-processing method, performed in the Matlab environment, was fully described in Di Lorenzo et al. [109]. First, the images are subtracted from the background, binarized by a specific chosen threshold, and filtered by a low-pass filter to reduce noise on the contour of the flame front. For each frame, a contour is defined by “filling” the empty areas with the dilation/erosion technique. Figure 16 is an example of the results of the contour detection routine.

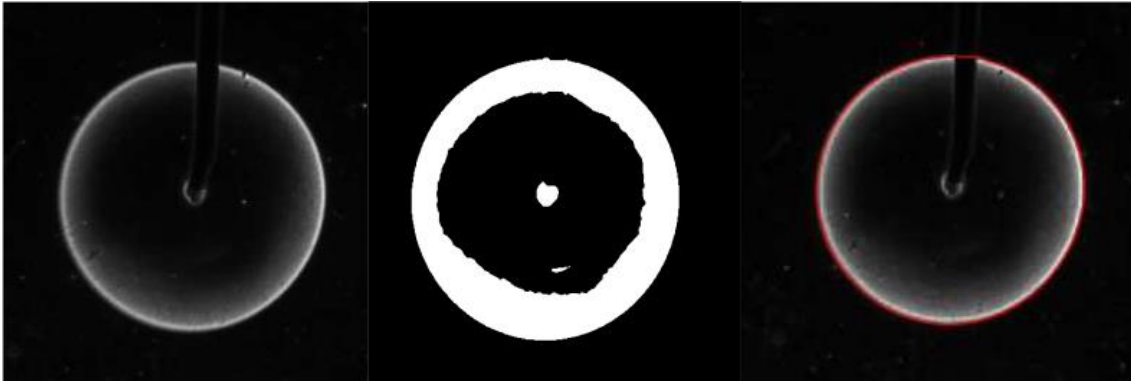


Figure 16: Post-processing steps illustrated by the unprocessed image (left), the binarized image (center) and the resulting flame contour traced over the unprocessed image (right).

The corresponding radius is given by Equation (3-10):

$$R_f = \sqrt{\frac{A}{\pi}} \quad (3-10)$$

Once the flame radius over time profile is obtained, the speed and stretch profiles can be calculated as follows [106]:

$$S_b = \frac{dR_f}{dt} \quad K = \frac{2}{R_f} \frac{dR_f}{dt} \quad (3-11)$$

Using the stretch and displacement profiles, the stretched flame speed (S_b^0) can be extrapolated to unstretched laminar flame speed (S_b^0), using a non-linear quasi-steady extrapolation (Equation (3-9)) proposed by Kelley and Law [101] and validated by Halter et al. [110] for methane/air and isooctane/air flames. Gong et al. [111] evaluated the accuracy of four extrapolation methods for H₂/CO mixtures by comparing extrapolation results to DNS_{mapping}. The non-linear quasi-steady extrapolation used here (Equation (3-9)) was more accurate than the linear extrapolations based

on stretch and curvature. Differences between both extrapolation models are illustrated in Figure 17. We can notice that both extrapolation methods provide similar estimations, with a deviation less than 10%. The radius limits for the extrapolation were chosen in a shot-by-shot basis following the guidelines proposed by Han et al. [112]. At early flame propagation (small radii) the flame is heavily influenced by ignition energy, so the minimum radius must be selected to ensure minimum influence in the extrapolation. To limit pressure effects a maximum radius of 25 mm was considered, within the 30% of chamber radius as proposed by Burke et al. [113].

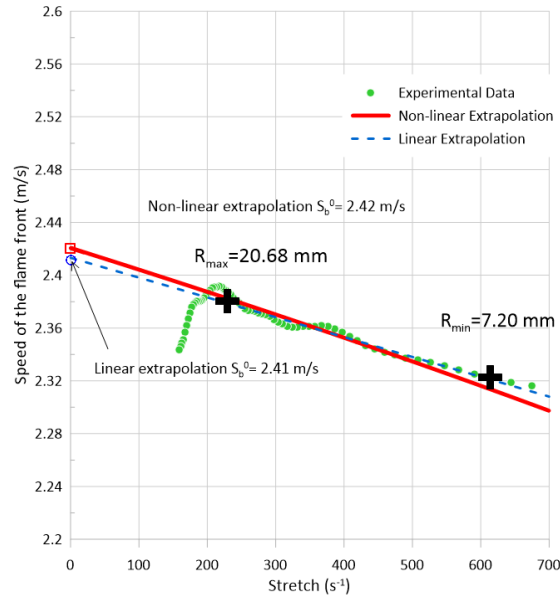


Figure 17: Example of flame speed evolution as a function of stretch - downdraft composition at 1 bar, 373 K and $\phi = 1.2$.

Furthermore, laminar flames tested in this chapter are susceptible to flame instabilities. Indeed, very slow flames are prone to buoyancy, whereas hydrogen rich compositions are susceptible to thermodiffusive instabilities. Figure 18 presents two examples of the two instabilities that should be avoided in post-processing to ensure measurement accuracy. To do so the flame radii considered for the extrapolation were adjusted. The case of the Fluidbed composition at 5 bar and $\phi = 0.6$ results were not considered for this reason, whilst in the other case, the radii used for the extrapolation ranged from 6 to 10 mm.

Table 8 presents the average minimal-maximum radii, between the three shots, used in initial temperature of 323 K and 1 and 5 bar of initial pressure, for each composition and equivalence ratio. It is evident that when the initial pressure increases, the flames become susceptible to these types of instability sooner, and this is why the maximum radii shrinks as the pressure increases. Therefore, in the worst cases, the range of radii can be around 3 mm long, which is very short. However, the number of points used for the extrapolation remains always higher than 30 thus ensuring a good correlation between the extrapolation model and the experimental data.

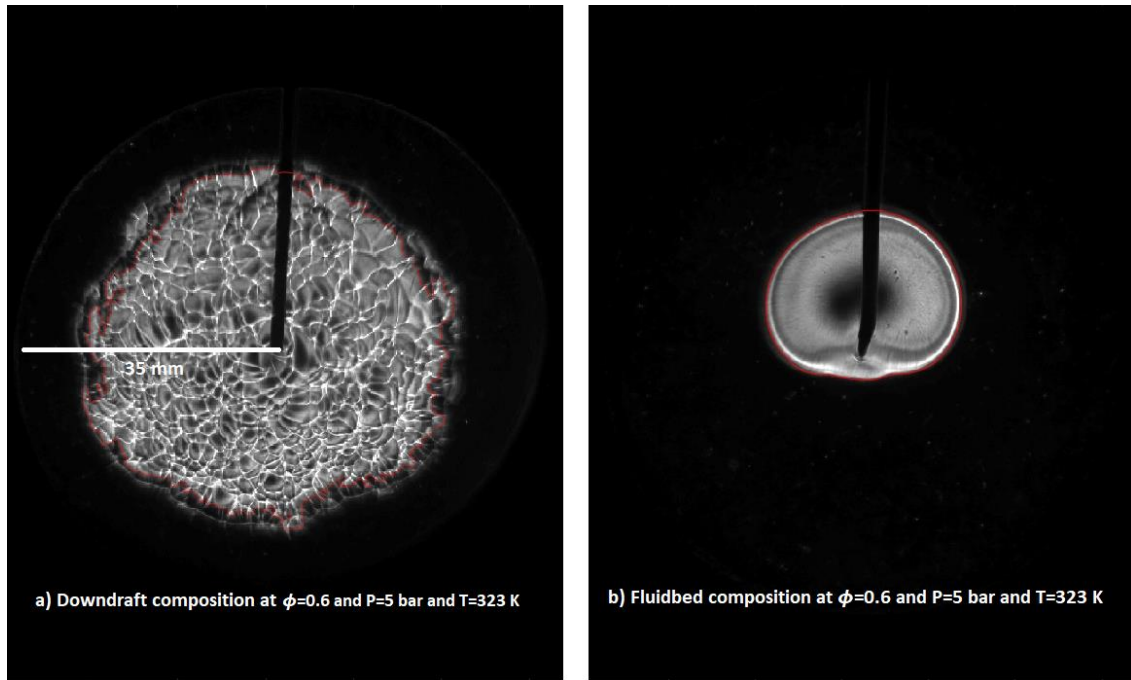


Figure 18: Example of the instabilities, thermal-diffusive (left) and buoyancy (right), we can obtain in this study.

Table 8: Flame radiuses used to extrapolate the S_u^0 .

Equivalence Ratio (ϕ)	Downdraft				Updraft				Fluidbed			
	1 bar		5 bar		1 bar		5 bar		1 bar		5 bar	
	R_{min} (mm)	R_{max} (mm)										
0.60	6.6	18.0	5.9	9.7	7.3	17.5	6.1	13.1	8.7	18.9	-	-
0.70	8.8	19.5	5.7	8.4	6.3	15.1	5.8	11.4	9.3	22.5	5.7	11.3
0.80	6.5	18.7	6.6	9.2	10.3	23.8	6.8	16.4	10.1	22.2	6.9	15.2
0.90	6.8	17.0	6.1	9.6	9.0	25.0	6.3	16.5	7.3	20.6	6.5	15.2
1.00	7.2	18.1	5.9	11.3	11.2	22.5	6.7	14.9	8.0	21.2	5.3	12.2
1.10	7.4	18.7	5.2	10.4	9.2	22.3	6.8	19.3	8.3	19.5	5.2	12.4
1.20	8.2	14.5	5.9	15.0	7.7	21.0	6.6	15.6	9.0	19.2	-	-
1.30	6.8	15.1	4.3	10.3	6.3	16.4	7.4	14.4	-	-	-	-
1.40	7.0	15.3	3.7	7.6	6.8	16.0	6.1	13.1	-	-	-	-

The unstretched laminar flame speed, S_u^0 , is plotted over the global equivalence ratio calculated following Equation (3-12).

$$\phi = \frac{AFR_{st}}{\frac{Air\%_{vol}}{Syn\ gas\%_{vol}}} \quad (3-12)$$

Finally, the unburned laminar flame speed is given by $S_u^0 = \frac{\rho_b}{\rho_u} S_b^0$, where ρ_b and ρ_u are the burned and unburned gas densities, respectively calculated by the equilibrium model in Ansys CHEMKIN-Pro.

3.2.1. Uncertainty Analysis on the experimental value of S_u^0

Based on the work of Moffat [114], adjusted for the current set-up by Brequigny et al. [115], the overall uncertainty $B_{S_u^0}$, can be estimated as:

$$B_{S_u^0} = \sqrt{\left(\frac{\Delta S_u^0}{S_u^0}\right)_{P,T,\phi}^2 + \left(\frac{\Delta S_u^0}{S_u^0}\right)_{imaging}^2 + \left(\frac{\Delta S_u^0}{S_u^0}\right)_{statistical}^2} \quad (3-13)$$

The three components on Equation (3-13) represent, from left to right, experimental hardware errors, imaging errors and statistical errors. Given the fact that in this experiment there are six flowmeters (BROOKS 5850S 2 NL/min for air and N₂, 1.2 NL/min for CO and 0.5 NL/min for the other gases), with an error of ±1% of full scale, the uncertainty for the equivalence ratio is estimated to be around ±0.02. The temperature of the gases in the vessel is measured by a K-type thermocouple and the deviation from the set temperature can be up to 1% for the 298 K case, where the effect of hot burnt gases heating the vessel is more pronounced. Pressure before ignition is measured by a piezoelectric pressure transducer with an associated uncertainty of ±2%. Overall hardware related uncertainty can be calculated by Equation (3-13). Considering that the worst-case scenario for the coefficients α and β are 3.33 and -0.6 the hardware related uncertainty is 3.50%.

$$\left(\frac{\Delta S_u^0}{S_u^0}\right) = \sqrt{\left(|\alpha| \frac{\Delta T}{T}\right)^2 + \left(|\beta| \frac{\Delta P}{P}\right)^2} \quad (3-14)$$

The global imaging error was previously determined by Brequigny et al. [115] and Lhuillier et al. [106] to be 2.5% for the same experimental set-up. Statistical error varies from below 1% to above 10% when conditions are not ideal (slow flame and low equivalence ratios). Regarding the uncertainty related to radiation losses, it can be concluded, based on Chen's [116] work and the concentration of CO₂ on the tested syngas compositions, that the effects of radiation can be neglected in most cases. However, in some cases, the laminar burning velocity reaches values below 10 cms/s typically for lean Fluidbed mixtures at high pressure where radiation effect could be at stake, especially considering the composition of the syngas which could lead to reabsorption and therefore pre-heating of the fresh gases. For the worst case of this work, i.e. a high pressure lean Fluidbed experiment leading to a S_u^0 of about 4 cm/s, a CHEMKIN simulation using the Optically Thin Model (OTM) was conducted to assess the maximum potential error due to radiation. Knowing that OTM does not account for reabsorption but only the heat losses from the burnt gases, it gives a maximum relative error of about 12%. The consideration of radiation effect and especially reabsorption would require further investigation.

3.2.2. Laminar flame speed simulation

The Ansys CHEMKIN-Pro PREMIX code is used to obtain 1-D adiabatic unstretched laminar flame speeds at the different test conditions, to assess the validity of chemical kinetic mechanisms. The model consists of a freely propagating premixed laminar flame with adaptive grid and mixture-average transport properties. The Soret effect (thermal diffusion) was considered due

to the presence of H₂ in the compositions. Final GRAD and CURV parameters were set to 0.1. A preliminary analysis was conducted, by which several kinetic mechanisms were appraised and the ones that showed the most promising results were San Diego's [117], CRECK [118], Madison [119] and Aramco 3.0 [120]. In Table 9, a description of the selected mechanisms is presented.

Table 9: Mechanisms description

Mechanism	Type	Fuel	Number of Species-Reactions	Validation by (Temperature and Pressure range)
CRECK [118]	Detailed	Syngas C ₀ -C ₃	114-1999	Ignition delay (1350-2000 K; 0.76-3.77 atm), S_u^0 (300-373 K; 1-3 atm)
San Diego [117]	Short	C ₁ -C ₄	47-257	Ignition delay (1050-1400 K; 10-30 atm), S_u^0 (298 K; 1 atm)
Madison [119]	Reduced	C ₁₀ -C ₁₆	178-758	Ignition delay (700-1250 K; 10-30 atm), S_u^0 (353-443 K; 1-10 bar)
Aramco 3.0 [120]	Detailed	C ₀ -C ₁₀	581-3037	Ignition delay (990-1781 K; 1-40 atm), S_u^0 (295-399 K; 1-5 atm)

Most of the available kinetic mechanisms for syngas are validated for the main components of syngas but individually and not for the syngas mixture itself. This is the case for the NUI Galway [121] mechanism that, despite being thoroughly validated with measured flame speeds of H₂ and CO mixtures, did not perform well when predicting S_u^0 for the compositions tested here, even though methane (CH₄) is present in the mechanism. This is because, mixtures containing CH₄ were not validated specifically on flame speed in the mechanism designing process. This is highlighted in Figure 19, where both experimental and simulation results for an initial temperature of 323 K and 1 bar of pressure are presented. Another common limitation of the

mechanisms is that they are usually validated with laminar flame speeds for a narrow temperature and pressure range.

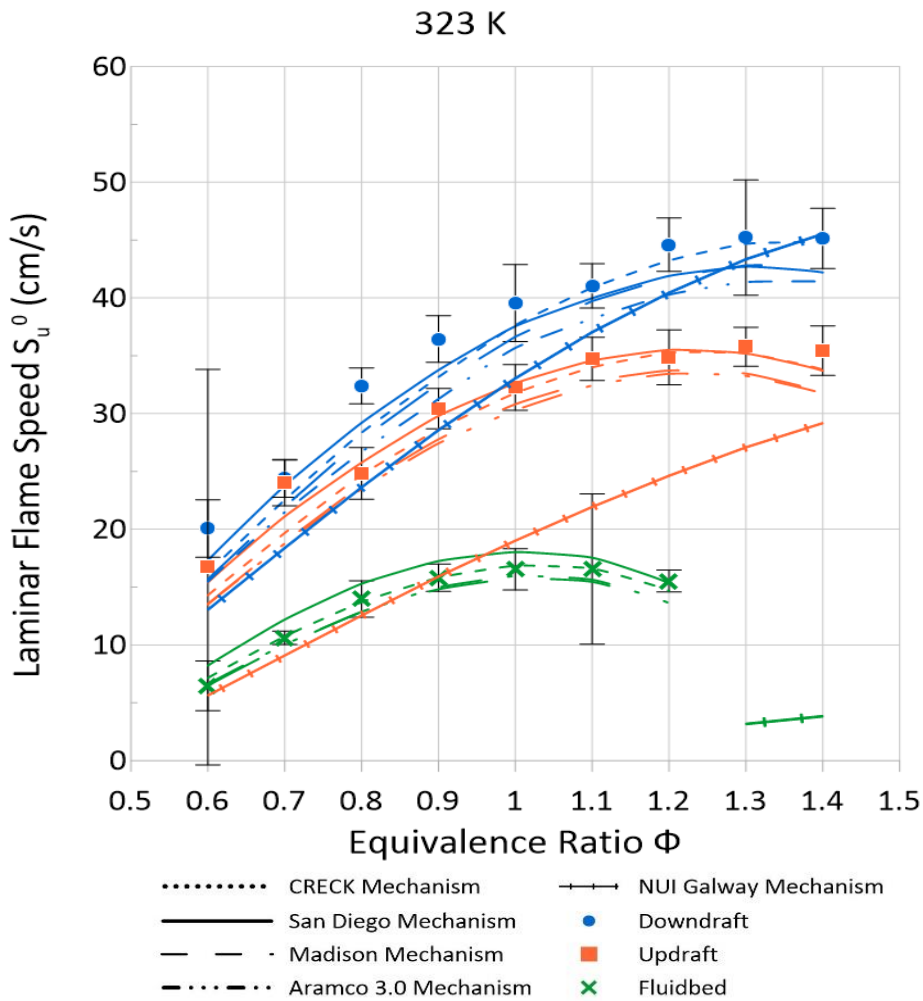


Figure 19: Example of experimental and simulated S_u^0 results for 3 syngas compositions at 1 bar and 323 K.

Additionally, to visualize the behavior of each tested mechanism, the difference between the experiments and the simulation results was estimated employing Equation (3-15), as validated by Kawka et al. [122], and discussed in the results section of this chapter.

$$E_i = \left(\frac{S_{u_{sim}}^0 - S_{u_{exp}}^0}{\sigma(S_{u_{exp}}^0)} \right)^2 \quad (3-15)$$

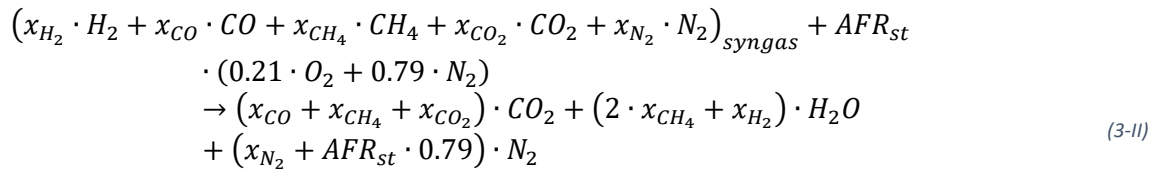
Where $S_{u_{sim}}^0$ is the simulation result, $S_{u_{exp}}^0$ is the average experimental result and $\sigma(S_{u_{exp}}^0)$ its uncertainty value, all of them evaluated in that specific condition (P, T, ϕ).

The availability of S_u^0 data for real-world syngas compositions, at a wide range of thermodynamic conditions, is necessary to confirm that a mechanism can be used for CFD simulation.

3.3. Background Literature: the case of syngas

As discussed previously, syngas composition varies with the biomass source and the gasification process used [63,123], but its main components are CO, H₂, N₂, CO₂ and CH₄. The change in the composition will affect the combustion process itself and the pollutant species produced.

The complete chemical equation of the combustion of syngas reads as follows:



Where x_{xxy} is the mole fraction of each syngas component and AFR_{st} is the stoichiometric Air-to-Fuel Ratio (in moles) of the syngas composition.

Most of previous studies on laminar flame speed of syngas have been focused on H₂/CO mixtures with diluents [63,124–127]. The ratio between H₂ and CO mole fractions is one of the major parameters for determining the overall quality of the fuel. Bouvet et al. [63] measured laminar flame speeds of mixtures with H₂/CO ratios ranging from 0.052 to 1, using shadowgraphy of spherically propagating flames. Their results showed that, by increasing hydrogen content from 0.052 to 1, the mixture's maximum flame speed ($S_{u,max}^0$) increases from around 60 to 180 cm/s.

Other articles included CH₄ and CO₂ addition [30,128,129], highlighted their importance for S_u^0 . Lapalme et al. [128] tested the effect of CH₄, CO and CO₂ addition in spherically propagating flame stability, with H₂/CO ratios ranging from 0.33 and 7.5. Zhou et al. [30] studied the effect of the dilution of a H₂/CO/CH₄ fuel mixture with CO₂ and N₂ separately for varying pressures. Zhou concluded that elevated pressures induced an early onset of flame instabilities (wrinkles) and that flame stretch sensitivity increased with N₂ and CO₂ dilution. Considering the dilution effects on the flame speed outcome, they also observed a stronger effect for CO₂ than with N₂, due its chemical dissociation, participating directly in the reaction CO+OH ↔ CO₂+H, and its higher thermal capacity [30,130].

Different from the work mentioned above, the study done by Monteiro et al. [5,6] investigated three compositions representing the typical production of the following types of gasifiers (see 1.1.2):

- Downdraft: fixed-bed gasifier, where the product flow is recovered on the bottom of the reactor, following the same direction as the downward-moving biomass introduction.
- Updraft: fixed-bed gasifier, where the product is recovered on the top of the reactor, flowing in the opposite direction to the downward moving biomass.
- Fluidbed gasifier: where biomass is mixed in an inert solid (sand for example).

Monteiro et al. [5] used the spherically propagating flame method to measure laminar flame speeds for the three compositions, at normal temperature and pressure conditions and equivalence ratios ranging from 0.6 to 1.2. They found that, on average, S_u^0 values for Downdraft and Updraft mixtures are, respectively, 14 and 8 cm/s higher than those of Fluidbed mixtures. Figure 20 presents an example of their results for S_u^0 , where one can note how the high dilution of the Fluidbed mixture induces a decrease of S_u^0 and shortens its flammability limit. Monteiro

and Rouboa [6] expanded on their previous work by including initial pressure variation from 1 to 20 bar but with limited variation on the equivalence ratio (0.8, 1.0 and 1.2).

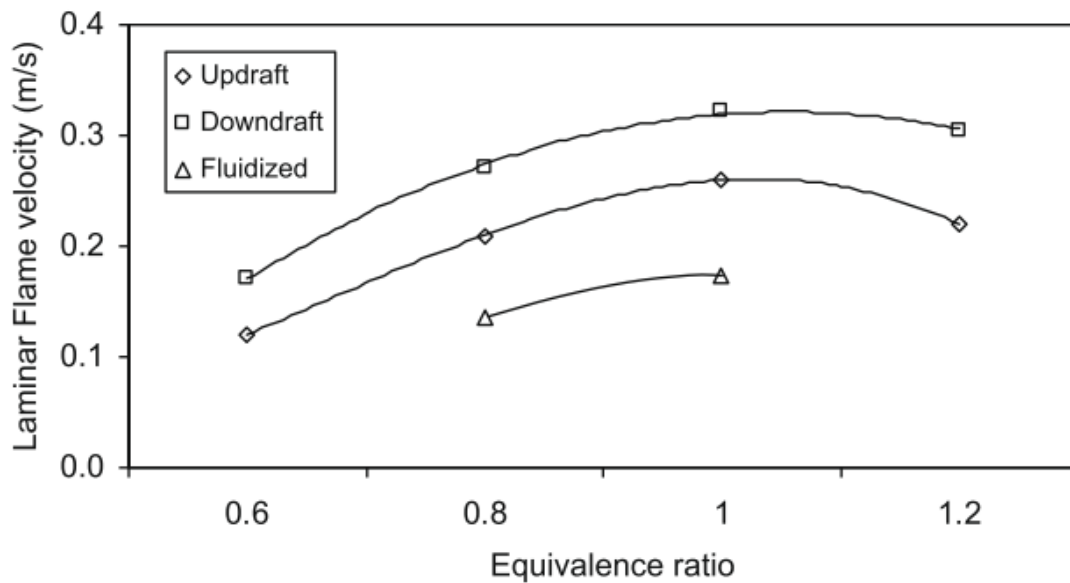


Figure 20: Unstretched laminar flame speed (S_u^0) versus equivalence ratio (ϕ) plot of the 3 reference compositions at 293 K and 1 bar ((reproduced from the work of Monteiro et al. [5])

In this chapter, we will enhance the database of laminar speeds for a wide range of temperatures, pressures and equivalence ratios for each syngas composition, and the effect of the addition of a high-reactivity fuel will be studied for the first time. This database will help to validate reaction mechanisms for syngas combustion. The syngas composition selected for this study reflect real end-gas produced by air-fed gasifiers, and are presented in Table 10, alongside fundamental combustion properties. It is important to underline that Monteiro et al. [5] and Monteiro and Rouboa [6] also analyzed these same compositions, thereby facilitating comparison.

From the results, the dependency of the laminar flame speed, on temperature, pressure and equivalence ratio is evaluated and compared to the Metghalchi and Keck [131] flame speed correlation, as well as the correlations from Monteiro and Rouboa [6], based on the Metghalchi and Keck [131] formalism. Furthermore, the selected reaction kinetic mechanisms were compared and appraised. The stretch behavior of the evaluated syngas compositions is also analyzed with respect to their Markstein lengths. Additionally, the influence of small amounts of decane (up to 5% by mass) on the laminar burning velocity of the syngas compositions was investigated.

Table 10: Typical syngas properties of syngas compositions from selected gasifiers.

	H ₂ (%)	CO (%)	CO ₂ (%)	CH ₄ (%)	N ₂ (%)	LHV (MJ/m ³)	Air fuel ratio (AFR _{st})	$\frac{\rho_u}{\rho_b}$	Flame Thickness (mm)	Maximum Flame Speed S _{u⁰} (cm/s)	Maximum T _{ad} (K)
Fluidized Bed (Fluidbed)	9	14	20	7	50	4.2	1.21	0.18	0.651	15.4	1780
Updraft	11	24	9	3	53	4.4	1.12	0.18	0.375	30.7	1900
Downdraft	17	21	13	1	48	4.8	1	0.18	0.364	36.7	1870

3.4. Results and discussion

In this section all results obtained during this study are compared to the results available in the literature and to predictions obtained from simulation with the four kinetics mechanisms.

3.4.1. Laminar flame speed

In Figure 21 the laminar flame speed is plotted as a function of the equivalence ratio for the three syngas compositions, alongside literature data, at 1 bar and 298K. With respect to the Downdraft composition (highest H₂ content), S_{u⁰} peaks at around $\phi = 1.3$, although similar S_{u⁰} are measured between $\phi = 1.1$ and 1.4, with flame speeds in that range comparable to the S_{u⁰}_{max} of CH₄ ($\phi = 1.1$ S_{u⁰} ~ 37 cm/s). It is observed that this same behavior of S_{u⁰}_{max} plateauing is apparent for the other syngas mixtures but shifted to slower flame speeds with decreasing H₂ content. Over the tested range, the compositions exhibit no clear S_{u⁰} max, unlike traditional Hydrocarbons, as CH₄, with a clear peak at $\phi = 1.05 - 1.1$. Furthermore, it can be noticed that the Updraft and Downdraft compositions produce flames that are around two and three times faster, respectively, than those of the Fluidbed composition for the same conditions. Again, this is consistent with the higher H₂ and CO contents in those two compositions. The flame speed of the Downdraft composition is slightly higher than the Updraft and is very similar to the flame speed of methane/air mixtures ($\phi = 0.8 - 1.1$).

Only two studies focused on the determination of laminar flame velocity for the typical syngas compositions, as defined by Bridgwater [58]. Monteiro et al. [5] measured S_{u⁰} of three main syngas compositions using schlieren imaging of a flame, expanding in a rectangular constant volume chamber. Oliveira et al. [7] tested the Downdraft composition on a Bunsen burner set-up coupled with OH PLIF imaging. Only Oliveira et al. [7] included simulation results to compare with their experimental data.

Figure 21 shows that the results of Monteiro et al. [5] are in a very good agreement for Downdraft and Updraft lean mixtures but strong divergence can be noted in the rich side, with a similar plateau region observable ($\phi = 1.1 - 1.4$). In the case of the Updraft, good agreement is observed at and below stoichiometry, however, important discrepancies are noticed on the rich side, with an important decrease in S_u^0 measured by Monteiro et al. [5]. However, in the case of Fluidbed, the limited measurements from Monteiro et al. [5] are higher than from this study. On the other hand, results from Oliveira et al. [7] for the Downdraft exhibit a similar trend in S_u^0 values but a noticeable shift towards lower S_u^0 . It has to be underlined that the Bunsen burner technique, used by Oliveira et al. [7], is strongly dependent of the inlet stream velocity and, even when well calibrated, the results are only accurate to around 6% [132]. Therefore, this first comparison with the few results available in literature indicates the discrepancy with the present results but also the lack of data for laminar flame speed in the case of syngas.

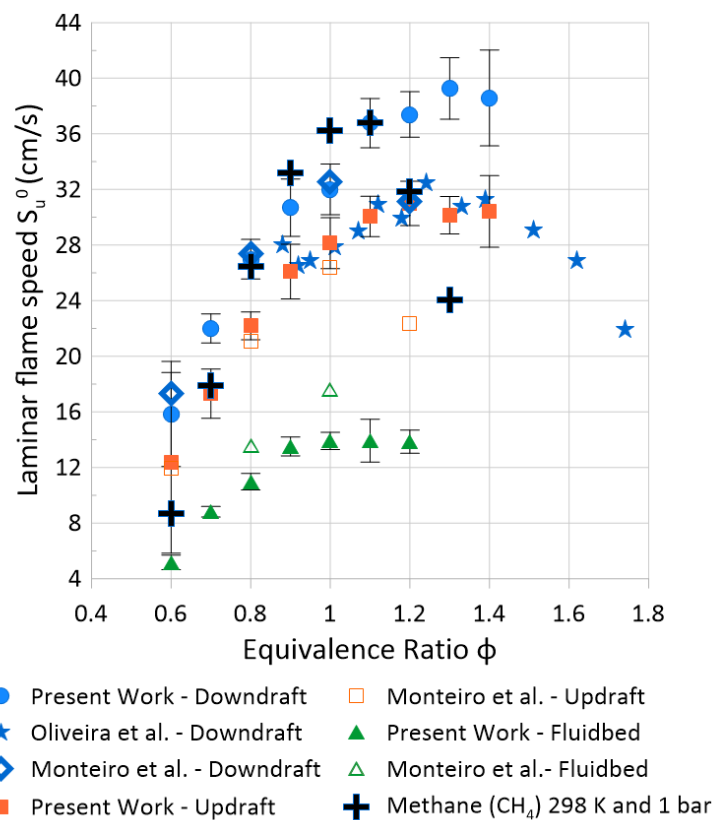


Figure 21: Comparison of S_u^0 results at 1 bar 298 K with results from Monteiro et al. [5] (1 bar 293 K) and Oliveira et al. [7] (0.954 bar 298 K); methane S_u^0 results provided by [133].

In Figure 22, the experimental results are compared to simulated results from the aforementioned kinetics mechanisms. The influence of equivalence ratio and unburnt temperature ($T_{in} = 298 - 423$ K) on the flame speed are also depicted below. As expected, the increase of T_{in} increases the S_u^0 , and is well captured by the appraised reaction mechanisms. It is noted that an increase in T_{in} does not drastically change the prediction accuracy of the mechanism.

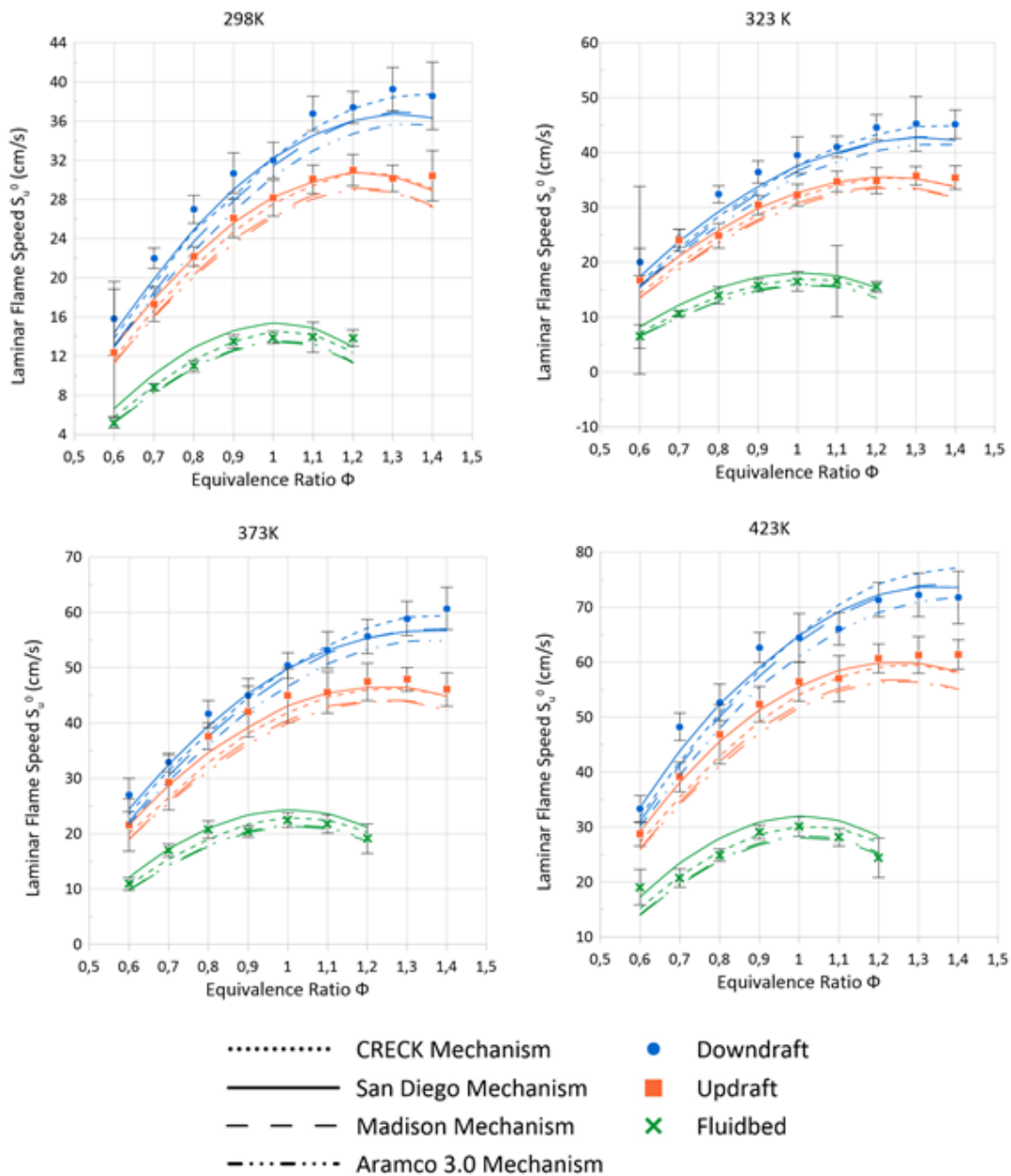


Figure 22: Experimental and simulated S_u^0 results at 1 bar for four initial temperatures (298, 323, 373 and 423 K).

The equivalence ratios corresponding to the maximum S_u^0 values are also well predicted, within the experimental uncertainty intervals. However, it is noticed that no plateauing in S_u^0 is simulated by the reaction mechanisms for any of the tested blends, although observed in these measurements and literature data. The S_u^0 values for the Downdraft and Fluidbed compositions are best predicted by the CRECK mechanism, whereas in the case of the Updraft, the experimental results seem to be closer to the San Diego's predictions. A detailed analysis between the simulated data and experimental measurements are presented later in this subsection.

Figure 23 presents the evolution of S_u^0 as a function of initial temperature for three equivalence ratios condition ($\phi = 0.8, 1.0$ and 1.2). With respect to the Fluidbed composition, all the appraised simulations fall within the uncertainty levels of the experimental data, from lean to

rich conditions. However, good agreement is observed for the Downdraft across stoichiometric and rich conditions, with simulations underpredicting the flame speed under lean conditions across the evaluated temperature range. With respect to the Downdraft, under lean conditions, discrepancy is observed at higher temperatures, whilst at richer conditions better agreement is seen. Moreover, we can see that all mechanisms correctly predict the gradient increase of S_u^0 for all compositions.

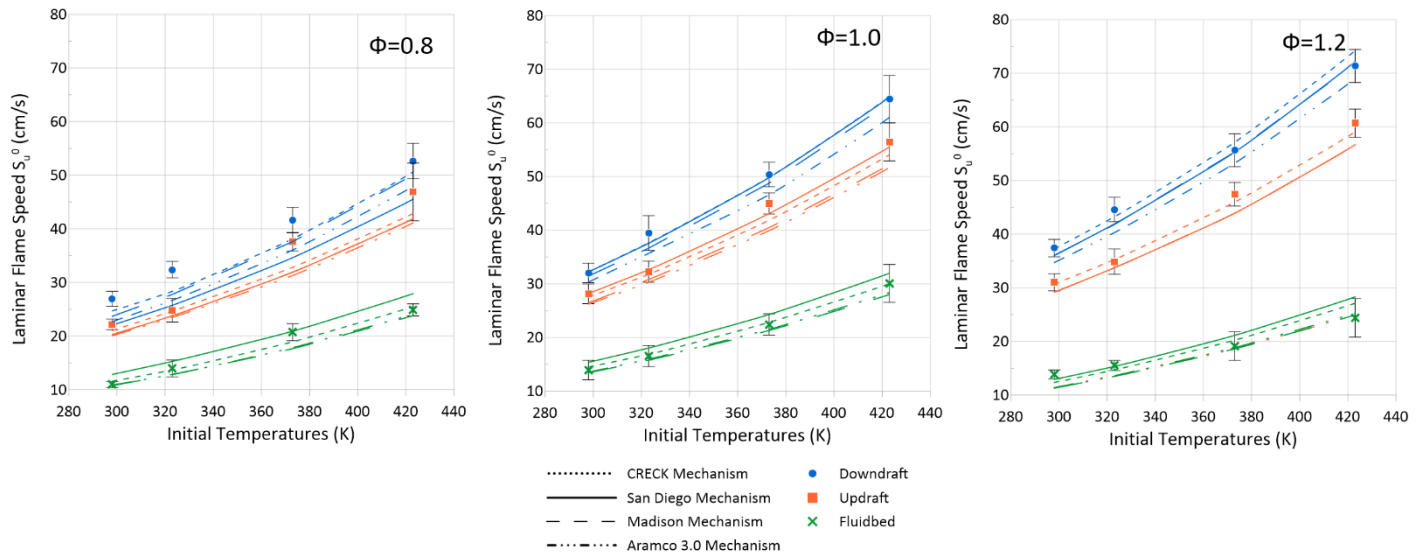


Figure 23: Kinetics mechanisms performances with varying the initial temperatures at three equivalence ratios.

The effect of initial pressure is shown in Figure 24, at 323 K for 3 and 5 bar. It can be noted that all mechanisms agree in the effect of the initial pressure, considering the experimental data, at least within a confidence interval. At higher pressures, the buoyancy effect, which slows flames for Fluidbed mixtures, and thermo-diffusive instabilities, induced in the case of high hydrogen content as for Downdraft mixture, are more pronounced thus increasing shot-to-shot variability and consequently, the statistical uncertainty. Those effects are minimized in the post-processing phase by reducing the range of radii considered to post-process the data and estimate the flame speed to avoid the high radii where cellularity instabilities and flame deformations tend to appear. Therefore, an attempt is made to limit the radius range employed for the extrapolation. Thus, the minimum radius is selected with care to minimize the influence of the ignition energy, whilst the maximum radius is chosen to avoid cellularity and buoyancy (to consider the assumption of a spherical flame). However, by doing so, uncertainty in the extrapolation increases since less data points are available as described in [132,134], with Table 8 summarizing the range of radii employed in this study for selected conditions. Indeed, the upper radius limit used for the extrapolation can drop down to values less than 10 mm at high pressure making the extrapolation more uncertain, as shown by Wu et al. [114]. This enhanced uncertainty, is clearly visible particularly at 5 bar, and for the Fluidbed composition at rich conditions.

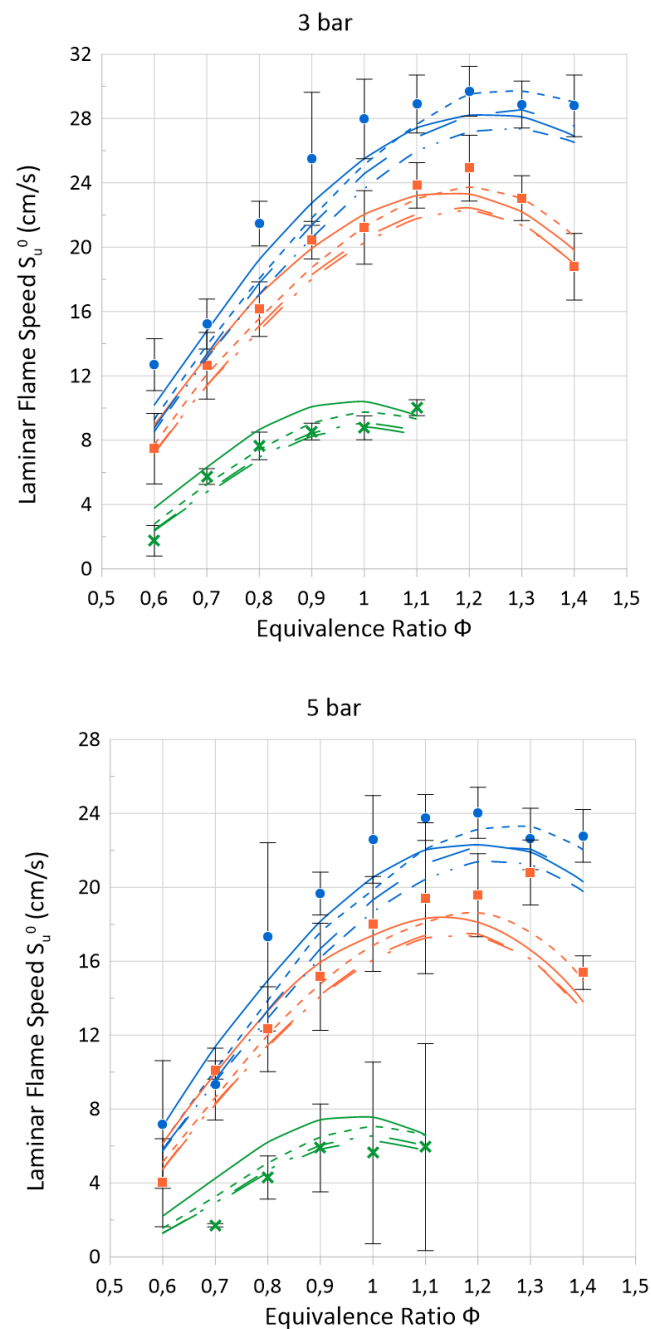


Figure 24: Experimental and simulated S_u^0 results at 323 K initial temperature for 3 and 5 bar.

To highlight the effect of pressure on S_u^0 , Figure 25 presents the evolution of S_u^0 at three different ϕ , 0.8, 1.0 and 1.2, for the three compositions. As one can see, S_u^0 for lean and stoichiometric Downdraft/air mixture is underpredicted, but the overall tendency is well captured. Other than that, all mechanisms predict well the effect of the pressure variation for the tested experimental conditions. This was to be expected since all the reaction mechanisms employed were validated

against high pressure data, aside from the notable exception of San Diego, nevertheless also demonstrating good agreement.

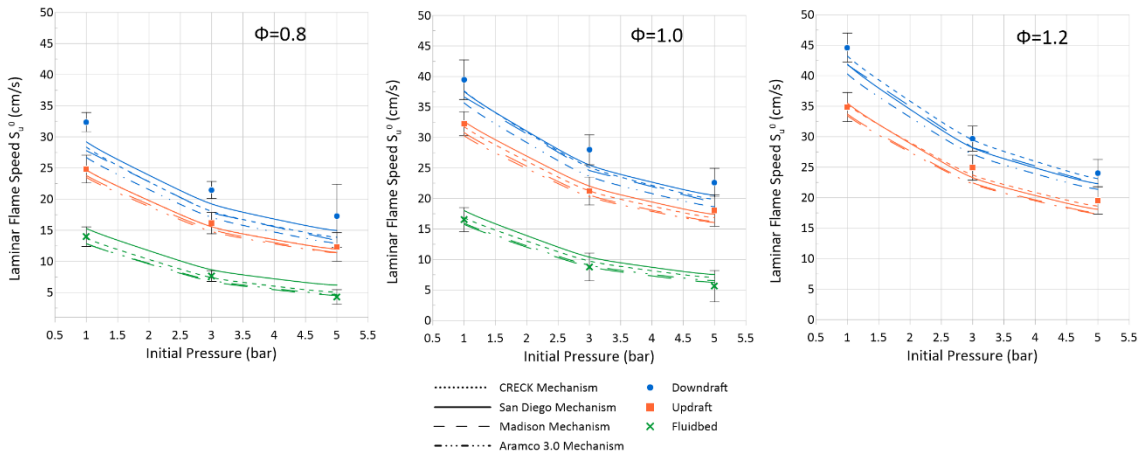


Figure 25: Comparison of the effect of pressure on the S_u^0 for the three compositions at three equivalence ratios at $T_{in}=323\text{ K}$ ($\phi=0.8, 1.0$ and 1.2)

In order to better visualize the differences between the experimental results and the simulations, the average, median and maximum difference was calculated using the Kawka method [122] (detailed in Section 3.2.2). Table 11 confirms that the San Diego and CRECK mechanisms provide the best agreement with the Downdraft experimental data, exhibiting identical average differences, and Aramco 3.0 displays the poorest one, with a factor of six on the average difference with San Diego and CRECK.

Table 11: Difference between mechanism predictions and experimental results for Downdraft.

Mechanism	Average Difference	Median Difference	Maximum Difference
CRECK	0.32	0.45	6.92
San Diego	0.32	0.71	4.32
Aramco 3.0	1.52	2.53	13.79
Madison	0.76	0.95	9.00

In general, average and median difference for Updraft mixtures are smaller than those obtained for Downdraft mixtures, as displayed in Table 12. However, the maximum differences are in general higher for the Updraft than for the Downdraft.

Table 12: Difference between mechanism predictions and experimental results for Updraft.

Mechanism	Average Difference	Median Difference	Maximum Difference
CRECK	0.19	0.24	9.09
San Diego	0.12	0.13	5.70
Aramco 3.0	1.08	1.64	13.21
Madison	0.89	1.33	14.40

Table 13 confirms that the CRECK mechanism best predicts the burning velocity for Fluidbed mixtures. The San Diego mechanism, which predicts well S_u^0 for Updraft and Downdraft, cannot provide accurate values in the case of Fluidbed mixtures.

Table 13: Difference between mechanism predictions and experimental results for Fluidbed.

Mechanism	Average Difference	Median Difference	Maximum Difference
CRECK	0.15	0.18	12.62
San Diego	1.02	1.33	33.41
Aramco 3.0	0.22	0.48	8.73
Madison	0.21	0.56	12.00

Overall, for the three syngas compositions, the CRECK and Aramco 3.0 mechanisms are the most and least accurate, respectively, of the kinetics mechanisms tested here.

Table 14 presents the complete visualization of the differences between simulated and experimental values of laminar flame speed as a function of (P, T, ϕ) , allowing to see in which parameter the mechanisms fails to provide close enough results for each syngas composition. There, we can observe that the CRECK mechanism is globally in good agreement for all three compositions, even though the San Diego mechanism agrees more with the experiment for both the Downdraft and Updraft on average, but fails to reproduce the experimental data for the Fluidbed composition. The Aramco mechanism, contrary to the San Diego mechanism, agrees well for the Fluidbed composition but much less for the Updraft and, especially, Downdraft compositions. This different approach to visualize the discrepancies is enlightening, since just looking the average, median and maximum difference cannot paint the correct picture of the validation of each mechanism. The Madison mechanism also provides acceptable predictions of flame speed for the three syngas compositions, despite being developed for heavier fuels, and this can be useful for future experiments, which will use a highly reactive fuel. Globally, all mechanisms can predict the effect of initial pressure and temperature on the S_u^0 .

Table 14: Difference between simulation ($S_{u_{sim}}^0$) and experimental result ($S_{u_{exp}}^0$) (Kawka et al.[122])

CRECK	Downdraft							CRECK	Updraft							CRECK	Fluïbed						
	1 bar - 298K	1 bar - 323K	1 bar - 373K	1 bar - 423K	3 bar - 323K	5 bar - 323K	1 bar - 298K		1 bar - 323K	1 bar - 373K	1 bar - 423K	3 bar - 323K	5 bar - 323K	1 bar - 298K	1 bar - 323K		1 bar - 373K	1 bar - 423K	3 bar - 323K	5 bar - 323K			
0.6	0.272	2.385	1.314	0.350	4.466	0.087	0.008	0.020	0.772	0.485	0.012	0.224	1.259	0.096	0.053	1.448	1.215	-					
0.7	6.704	1.341	0.732	6.809	0.745	0.159	0.111	4.709	3.006	1.881	0.071	9.089	0.038	0.048	2.005	0.037	1.006	12.629					
0.8	2.641	6.924	2.125	0.381	6.211	0.459	1.275	0.004	7.518	0.558	0.116	0.019	1.111	0.032	1.249	0.296	0.075	0.444					
0.9	1.387	2.702	0.017	2.340	0.797	3.385	0.528	1.062	1.406	0.978	2.090	0.018	0.011	0.000	1.660	0.033	0.973	0.059					
1.0	0.015	0.321	0.057	0.012	1.338	1.345	0.107	0.061	2.524	0.462	0.000	0.207	0.870	0.030	0.086	0.002	1.719	0.084					
1.1	0.835	0.006	0.051	2.262	0.509	1.981	0.189	0.156	0.154	0.002	0.363	0.105	0.019	0.037	0.170	0.963	2.036	0.013					
1.2	0.007	0.364	0.245	0.872	0.018	0.446	0.037	0.028	0.431	0.376	0.340	0.180	3.270	0.788	0.180	0.573	-1.000	-					
1.3	0.149	0.012	0.003	0.973	0.336	0.164	0.063	0.118	0.247	0.313	0.001	3.428	-	-	-	-	-	-					
1.4	0.003	0.015	0.122	1.314	0.014	0.286	0.275	0.586	0.184	1.631	0.805	0.210	-	-	-	-	-	-					
San Diego																							
San Diego	Downdraft							San Diego	Updraft							San Diego	Fluïbed						
	1 bar - 298K	1 bar - 323K	1 bar - 373K	1 bar - 423K	3 bar - 323K	5 bar - 323K	1 bar - 298K		1 bar - 323K	1 bar - 373K	1 bar - 423K	3 bar - 323K	5 bar - 323K	1 bar - 298K	1 bar - 323K		1 bar - 373K	1 bar - 423K	3 bar - 323K	5 bar - 323K			
0.6	0.148	1.248	0.723	0.008	2.431	0.001	0.009	0.006	0.000	0.029	0.441	0.813	7.728	0.649	1.004	0.327	4.593	-					
0.7	4.317	0.147	0.064	3.255	0.076	1.104	0.080	2.128	0.121	0.139	0.079	0.139	4.996	7.479	0.035	2.645	1.415	39.410					
0.8	2.223	4.316	0.838	0.011	2.651	0.216	0.019	0.175	2.913	0.063	0.275	0.183	10.298	0.693	0.016	7.270	1.389	2.658					
0.9	0.687	1.808	0.008	1.825	0.443	1.736	0.063	0.134	0.727	0.114	0.187	0.073	2.517	1.481	8.499	0.398	8.836	0.408					
1.0	0.013	0.354	0.064	0.008	1.015	0.766	0.001	0.036	0.919	0.071	0.127	0.058	5.501	0.678	1.988	1.158	4.809	0.154					
1.1	1.636	0.223	0.000	1.139	0.697	2.082	0.035	0.007	0.006	0.124	0.201	0.072	0.348	0.002	1.325	3.616	1.048	0.014					
1.2	0.746	1.404	0.012	0.076	0.952	1.626	0.042	0.072	0.216	0.110	0.626	0.427	1.281	0.043	0.577	1.185	-	-					
1.3	1.369	0.258	0.595	0.122	0.291	0.189	0.013	0.118	0.187	0.212	0.370	5.704	-	-	-	-	-	-					
1.4	0.443	1.303	1.109	0.153	0.991	3.112	0.345	0.660	0.208	1.403	0.238	2.980	-	-	-	-	-	-					
Madison																							
Madison	Downdraft							Madison	Updraft							Madison	Fluïbed						
	1 bar - 298K	1 bar - 323K	1 bar - 373K	1 bar - 423K	3 bar - 323K	5 bar - 323K	1 bar - 298K		1 bar - 323K	1 bar - 373K	1 bar - 423K	3 bar - 323K	5 bar - 323K	1 bar - 298K	1 bar - 323K		1 bar - 373K	1 bar - 423K	3 bar - 323K	5 bar - 323K			
0.6	0.543	3.129	2.505	0.852	5.961	0.152	0.027	0.035	2.290	1.537	0.018	0.095	0.000	0.000	1.109	2.494	0.431	-					
0.7	11.590	2.339	2.024	8.123	1.466	0.016	0.443	6.592	4.562	2.897	0.359	14.409	1.080	1.372	6.288	0.559	4.910	6.895					
0.8	5.521	8.999	2.826	0.621	7.195	0.609	3.600	0.215	10.708	0.857	0.371	0.141	0.121	0.501	3.660	0.851	1.024	0.049					
0.9	1.902	3.736	0.184	3.679	0.994	6.815	1.248	2.316	2.435	1.933	3.364	0.117	2.083	0.717	0.041	0.697	0.335	0.001					
1.0	0.099	0.761	0.512	0.028	1.914	1.926	0.827	0.539	5.181	1.442	0.085	0.492	0.651	0.181	0.750	1.384	0.004	0.017					
1.1	2.178	0.337	0.032	0.748	1.330	4.172	1.259	1.074	1.274	0.186	1.639	0.244	0.299	0.136	0.307	0.149	11.995	0.001					
1.2	0.712	1.526	0.010	0.021	0.954	1.767	1.329	0.231	2.534	2.314	1.461	0.886	9.460	4.618	0.032	0.023	-	-					
1.3	1.126	0.233	0.447	0.175	0.052	0.112	0.895	1.896	1.226	1.950	1.328	7.135	-	-	-	-	-	-					
1.4	0.274	0.768	0.946	0.292	0.430	2.212	1.444	2.813	1.765	5.624	0.002	5.910	-	-	-	-	-	-					
Aramco																							
Aramco	Downdraft							Aramco	Updraft							Aramcb	Fluïbed						
	1 bar - 298K	1 bar - 323K	1 bar - 373K	1 bar - 423K	3 bar - 323K	5 bar - 323K	1 bar - 298K		1 bar - 323K	1 bar - 373K	1 bar - 423K	3 bar - 323K	5 bar - 323K	1 bar - 298K	1 bar - 323K		1 bar - 373K	1 bar - 423K	3 bar - 323K	5 bar - 323K			
0.6	0.597	3.463	3.049	1.595	6.705	0.172	0.022	0.035	2.246	1.621	0.013	0.101	0.014	0.004	0.929	2.340	0.516	-					
0.7	14.383	3.340	4.038	12.821	1.901	0.004	0.569	6.876	5.493	3.466	0.346	13.081	0.745	1.029	5.652	0.394	3.893	7.719					
0.8	9.303	13.794	5.440	2.072	10.211	0.751	4.461	0.363	13.206	1.145	0.613	0.168	0.026	0.525	3.260	0.477	0.659	0.118					
0.9	3.692	6.711	0.950	7.067	1.426	9.263	1.767	2.968	3.065	2.704	4.264	0.132	1.660	0.510	0.001	0.516	0.037	0.003					
1.0	0.875	1.375	2.756	0.604	3.126	2.780	1.091	1.000	6.612	1.848	0.174	0.580	0.381	0.100	0.498	0.917	0.150	0.034					
1.1	4.725	1.578	0.573	0.017	2.743	7.543	1.884	1.507	1.809	0.305	2.150	0.280	0.201	0.117	0.145	0.023	8.574	0.000					
1.2	2.798	3.582	0.609	0.581	2.753	3.812	1.599	0.360	2.695	2.778	1.665	0.989	8.727	4.031	0.009	0.062	-	-					
1.3	2.714	0.603	1.790	0.112	1.126	0.730	1.133	2.239	1.328	2.222	1.465	7.117	-	-	-	-	-	-					
1.4	0.751	2.078	2.352	0.000	1.429	4.563	1.561	3.002	1.880	5.883	0.004	5.222	-	-	-	-	-	-					

- Color grading as follows: Green if difference is under 1, yellow if it is over 1 and under 5, red if it's over 5.

3.4.2. Laminar Flame Speed Dependence on Initial Pressure and Temperature

Based on the above experimental results the correlation adapted from Metghalchi and Keck [131], given by Equation (3-16), is considered in the case of the three syngas compositions. This kind of correlation remains useful in the case of low-cost 0D/1D engineering simulations and analysis tool for IC engine as well as for CFD models requiring the laminar burning velocity.

$$S_u^0 = S_{u_{ref}}^0 \left(\frac{T}{T_0}\right)^\alpha \left(\frac{P}{P_0}\right)^\beta \quad (3-16)$$

With $S_{u_{ref}}^0$, α and β , based on 2nd-degree equation, and determined from the experiments, as presented in Table 15.

Table 15: Summary of different empirical correlation for S_u^0 .

Syngas composition	$S_{u_{ref}}^0$	α	β
Downdraft	$-39.38\phi^2 + 107.06\phi - 34.02$	$1.34\phi^2 - 3.25\phi + 3.76$	$-1.12\phi^2 + 2.44\phi - 1.66$
Updraft	$-50.09\phi^2 + 121.88\phi - 42.52$	$3.28\phi^2 - 7.25\phi + 5.87$	$-1.61\phi^2 + 3.51\phi - 2.26$
Fluidbed	$-40.60\phi^2 + 87.14\phi - 32.47$	$3.87\phi^2 - 9.62\phi + 7.71$	$-4.64\phi^2 + 9.31\phi - 5.24$

Given the coefficients obtained from the equations above (Table 15), S_u^0 was calculated for each experimental data point. Figure 26 shows a comparison of the correlation presented above and the one proposed by Monteiro and Rouboa [6], for the same syngas compositions (at $\phi = 1$). In general, good agreement is observed between the present correlation and Monteiro and Rouboa [6], with differences augmenting with increasing temperature, notably for Updraft and Fluidbed. Much bigger differences are witnessed with increasing pressure, particularly with increasing Hydrogen content within the syngas compositions. Table 16 presents the error of the correlation predictions for all data points. Overall the correlation works best for Downdraft mixtures, and worst for the Fluidbed.

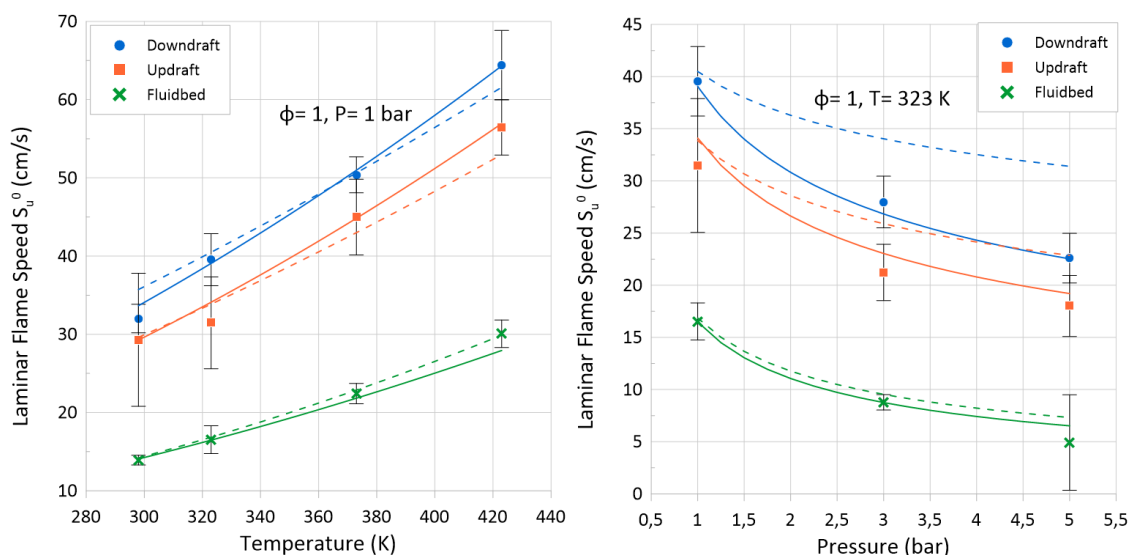


Figure 26: Comparison of current work correlation (solid line) and Monteiro and Rouboa [6] (dashed line) agreements with experimental data.

Table 16: Errors for correlation predictions and experimental measurement.

Syngas Composition	Average Error (%)	Median Error (%)	Maximum Error (%)
Downdraft	3.64	2.16	22.42
Updraft	4.07	2.57	23.75
Fluidbed	6.42	3.06	36.8

Table 17 presents the α and β coefficients calculated from experimental data and from the kinetic mechanisms. A few key conclusions can be drawn from these results:

- for Downdraft mixtures the temperature effect seems overestimated by all mechanisms;
- the temperature effect on the Fluidbed mixture decreases sharply with the increase in equivalence ratio;
- the Aramco 3.0 and CRECK mechanisms present similar coefficients for Downdraft and Updraft mixtures, this is consistent with the fact that both mechanisms are based on the mechanism of Metcalfe et al. [135] for the reactions involving C1 hydrocarbons and oxygenated fuels;
- the effect of pressure is almost two times stronger for the Fluidbed composition, for all three equivalence ratios, than the other two compositions and this will be of great importance in an engine use.

Table 17: Temperature and pressure dependence coefficients for different equivalence ratios fitted on experimental and mechanism data.

		α			β		
	Data	$\phi=0.8$	$\phi=1.0$	$\phi=1.2$	$\phi=0.8$	$\phi=1.0$	$\phi=1.2$
Downdraft	Experimental	2.02	1.85	1.79	-0.43	-0.34	-0.35
	CRECK Mechanism	2.13	1.98	1.92	-0.45	-0.38	-0.38
	UCSD Mechanism	2.15	1.98	1.94	-0.42	-0.37	-0.38
	Aramco 3.0	2.16	1.99	1.93	-0.45	-0.38	-0.38
	Madison	2.18	2	1.94	-0.46	-0.39	-0.38
Updraft	Experimental	2.17	1.9	1.89	-0.48	-0.36	-0.36
	CRECK Mechanism	2.1	1.87	1.84	-0.45	-0.38	-0.39
	UCSD Mechanism	2.09	1.9	1.88	-0.42	-0.37	-0.41
	Aramco 3.0	2.07	1.92	1.89	-0.45	-0.38	-0.4
	Madison	2.09	1.92	1.88	-0.46	-0.38	-0.41
Fluidbed	Experimental	2.49	1.96	1.74	-0.77	-0.58	-0.76
	CRECK Mechanism	2.25	2.09	2.22	-0.62	-0.53	-0.6
	UCSD Mechanism	2.22	2.08	2.23	-0.56	-0.53	-0.66
	Aramco 3.0	2.28	2.11	2.26	-0.63	-0.54	-0.64
	Madison	2.27	2.1	2.25	-0.64	-0.55	-0.66

3.4.3. Markstein length

As described earlier and in several studies [103,104], the sole parameter S_L^0 is not sufficient to describe the process of the flame propagation in the engine. The Markstein length (L_b) is another important fundamental parameter that can be extracted from the laminar flame study. Its value can help to characterize the response of the flame to stretch, mainly influenced by the thermal and the mass diffusivities, and their ratio, named the Lewis number [94], defined in detail in the introduction of this chapter. Early experimental investigations, underline that preferential diffusion (i.e. Le deviating from unity), can strongly influence the burning rates of stretched flames – which undergo the combined effects of strain, curvature, and flame motion. This is of importance to understand the flame dynamics in thermal applications based on combustion, such as Internal Combustion Engines (ICE) and Gas Turbines (GT). As demonstrated by Brequigny et al. [103], engine global parameters such as the combustion phasing in the engine cycle can be correlated to the Lewis number and hence to some extent to the Markstein length. Indeed, their results showed that increasing the Lewis number (for $Le > 1$) could lead to a delay of the combustion in the cycle.

In Figure 27, the Markstein length, measured at 1 bar and 298 K, are compared to those of Monteiro et al. [5] at 293K (empty symbols), as well as pure hydrogen [133]. Considering that Monteiro et al. provided only limited data, it was only possible to verify qualitative trends. It should be noted that, a negative Markstein length means that the flame is thermo-diffusively unstable ($Le < 1$) leading to an

acceleration of the flame with increasing stretch level thus implying a faster early flame development. The opposite holds true for positive Markstein lengths ($Le > 1$). Generally, for all compositions, the Markstein length increases with equivalence ratio, with negative values for lean mixtures and a transition to positive near $\phi = 1 - 1.1$, unlike hydrogen which shifts at slightly leaner conditions ($\phi = 0.8$). These analogous trends support the idea that it is the presence of H_2 that is dictating the global stretch response. Noteworthy, irrespective of the syngas composition, the stretch response above stoichiometry is identical to that of H_2 . However, on the lean side, negative Markstein lengths are enhanced in comparison to pure H_2 . Furthermore, there is an important difference between Fluidbed and the two other mixtures with a more pronounced drop at low equivalence ratios for Fluidbed due to the high N_2 and CO_2 content (See Table 10) as underlined by Zhou et al. [30].

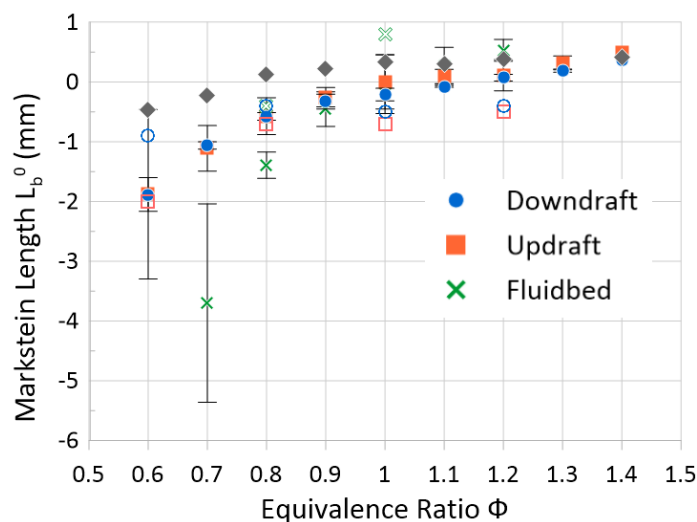


Figure 27: Present work experimental Markstein length results at 1 bar 298 K (filled symbols) compared to Monteiro et al. [5] results at 1 bar 293 K (empty symbols). Diamonds - Hydrogen at 1 bar and 298 K from [133].

Anggono et al. [136] also found that high CO_2 dilution rates can increase significantly stretch sensitivity of CH_4/CO_2 /air flames. This is also confirmed by Lapalme et al. [128] who showed that the addition of CO_2 into a H_2/CO mixture with a H_2/CO ratio of 1.2 leads to a decrease of the Lewis number from 1.02 at 0% CO_2 down to 0.61 for 35% vol. of CO_2 , with the H_2/CO ratio being kept constant. Figure 28 presents the evolution of the Markstein length near the transition between negative to positive for the Downdraft and Fluidbed compositions, for different ranges of temperature at atmospheric pressure. We can see that, with the increase of temperature, the Markstein length on the lean side is higher, then closer to zero for both compositions, i.e. Downdraft and Fluidbed. For stoichiometric mixtures, it

seems that the temperature increase leads to an increase of Markstein Length, thus having a stabilizing effect. On the other hand, no major trend is observed for rich mixtures with the temperature increase.

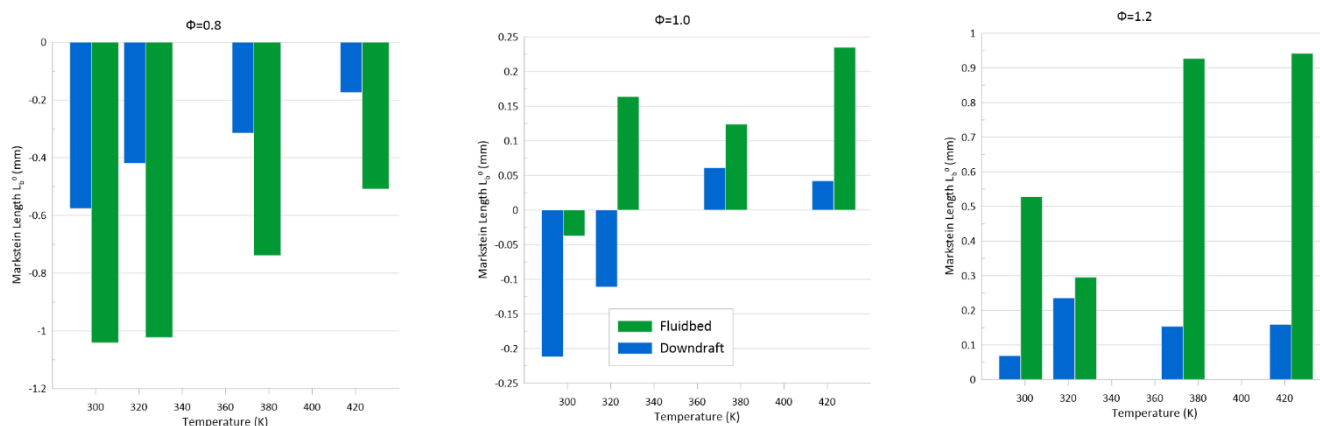


Figure 28: Markstein length results of the Fluidbed and the Downdraft compositions, for different temperatures and 3 equivalence ratios.

It is important to note the difference in behavior between Fluidbed and the two other mixtures: the drop in Markstein length at low equivalence ratios is considerably more pronounced. This behavior is consistent with the findings of Zhou et al. [30], which showed a reduction in Markstein length with higher CO_2 dilution and is partly related to the Lewis number as shown by Lapalme et al. [128]. The Fluidbed composition differentiates itself from the other two compositions by the higher CO_2 and CH_4 mole fractions (see Table 10). The CH_4 being equi-diffusive ($Le \approx 1$) within the H_2/CO mixtures, the CO_2 has higher impact on the stretch sensitivity of the blend.

Bouvet et al. [63] studied the effect of the H_2/CO ratio on the Markstein length and S_u^0 . Even if the mixtures here are more complex, some of their conclusions can be useful for this work. For a 50/50% H_2/CO mixture, they measured a minimum Markstein length of about -3 mm at $\phi = 0.4$ at ambient pressure and a temperature higher than the one observed for the Fluidbed composition at $\phi = 0.7$ (see Figure 27). This could possibly be explained by the important CO_2 content as developed below. Bouvet et al. [63] also shows that the transition from negative to positive Markstein length lies around $\phi = 0.95 - 1.1$ for H_2/CO ratio of 0.33 and 1.0. In Figure 29 only the results for Updraft and Downdraft compositions are plotted to highlight that despite the H_2/CO ratio difference, i.e. 0.46 for the Updraft and 0.81 for the Downdraft, Markstein length are very similar across the range of equivalence ratio. Also, since the H_2/CO ratio is about 0.64 for the Fluidbed composition, this confirms that the large difference in Markstein length between these two and the Fluidbed compositions on the lean side might be related to the total dilution, N_2 and CO_2 , which is similar for Updraft and Downdraft, 62% and 61%, respectively, but larger for Fluidbed (70%). Besides, for a constant CO_2 content of 25% vol., Lapalme et al. [128] shows that increasing the H_2/CO ratio from 0.5 to 2.0 only decreases the Lewis number from 0.65 to 0.57. Considering the syngas compositions, and their H_2/CO ratios, used in the present study, this seems to make the H_2/CO ratio, a less impacting parameter on the Lewis number in comparison to the CO_2 content.

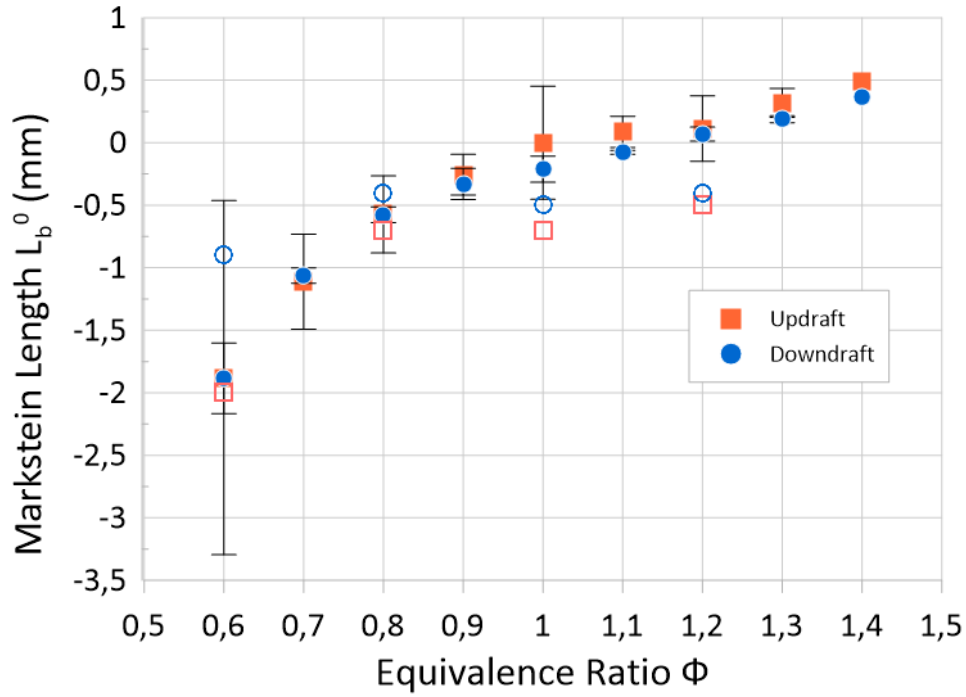


Figure 29: Zoom of the previous figure; experimental Markstein length results at 1 bar 298 K (filled symbols) compared to Monteiro et al. [5] results at 1 bar 293 K (empty symbols).

Other important parameters are directly related to the Markstein length relation with the Lewis and Zel'dovich numbers as in the following model suggested by Chen [137]:

$$L_b = \left[\frac{1}{Le} - \left(\frac{Ze}{2} \right) \left(\frac{1}{Le} - 1 \right) \right] \cdot \frac{\rho_b}{\rho_u} \delta_\kappa \quad (3-17)$$

Where Ze is the Zel'dovich number, $\frac{\rho_b}{\rho_u}$ the burned/unburned density ratio and δ_κ the flame thickness, defined as $\delta_\kappa = \lambda / (\rho_u \cdot c_p \cdot S_u^0)$ [138], with c_p the specific heat at constant pressure. The Zel'dovich number is defined as $Ze = \frac{E_a}{R \cdot T_b} \cdot \frac{T_b - T_u}{T_b}$, where E_a is the activation energy, R is the universal gas constant, T_b is the burned gas temperature and T_u is the unburned gas temperature.

As the Fluidbed composition, due to its diluent content, induces a higher activation energy and a lower Lewis as shown by Lapalme et al [128], a lower Markstein length is to be expected compared to the Downdraft and Updraft composition. Figure 30, reproduced from Lapalme et al [128], presents the effect of the addition of CO_2 (diamond symbol) and CH_4 (square symbol) on the critical radius of the appearance of instabilities on the flame front. This figure highlights the effect of the addition of CO_2 should promote mixture instability (showed by a slight decrease of the critical radius) through the diffusional-thermal mechanism, since effective Lewis (Le_{eff}) strongly decreases, thus, as already mentioned, making the extrapolation model more uncertain for the Fluidbed.

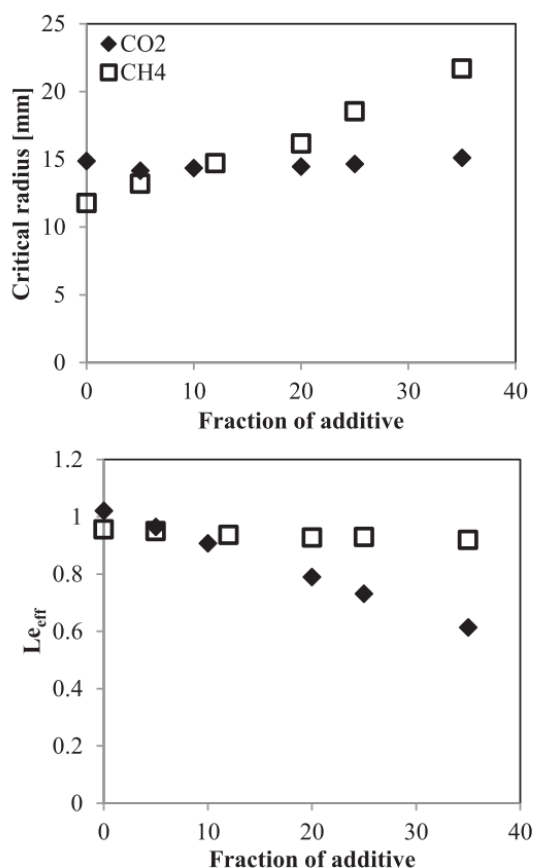


Figure 30: Effect of the addition of CO₂ and CH₄ on the effective Lewis number (Le_{eff}) and the critical radius of the appearance of flame instabilities (adapted from Lapalme et al [128])

Finally, from Figure 29, it can be seen that, in terms of stretch response the Downdraft and Updraft composition does not behave differently, and it is assumed that they will do the same in engine. As already underlined, the Fluidbed composition shows a slightly different behavior but mostly on the very lean side where measurement remains uncertain as highlighted by the error bars. As a conclusion, in this comparison of various syngas compositions, it appears that the laminar burning velocity may be a much more influencing parameter driving the flame propagation in engine than the stretch sensitivity. This in view of the fact that the syngas compositions show very different S_u^0 but very similar trends in Markstein length. Nonetheless, further study on the effect of each syngas component on Markstein length is needed to explain this phenomenon, as well as a detailed study of the various fundamental combustion properties (Le , Ze , δ , and σ) and their respective influence on the stretch-behavior measured.

3.4.4. Laminar speed of syngas/decane mixtures

Once the S_u^0 is determined for the different syngas compositions, on several initial temperatures and pressures and equivalence ratios, the interaction of syngas and the high-reactivity fuel must be examined as the syngas will be used as fuel for a dual-fuel engine ignited by a pilot diesel fuel injection. For this reason, in this subsection we explore the effect of the addition of a small portion of decane, as a surrogate for Diesel, on the S_u^0 . The decane, $C_{10}H_{22}$, fractions are given as the ratio between decane

and total fuel, i.e. decane + Syngas, in the vessel as given in Equation (3-18). The syngas/decane oxidation reaction equation is presented in Equation (3-III).

$$\text{Decane}_{\%} = 100 \cdot \frac{\text{Decane}_{\text{mass/vol/energy}}}{\text{Decane}_{\text{mass/vol/energy}} + \text{Syngas}_{\text{mass/vol/energy}}} \quad (3-18)$$

$$\begin{aligned} & (x_{H_2} \cdot H_2 + x_{CO} \cdot CO + x_{CH_4} \cdot CH_4 + x_{CO_2} \cdot CO_2 + x_{N_2} \cdot N_2)_{\text{syngas}} \\ & + \left(AFR_{st\text{-}syngas} + \frac{15.5}{0.21} \cdot x_{C_{10}H_{22}} \right) \cdot (0.21 \cdot O_2 + 0.79 \cdot N_2) + x_{C_{10}H_{22}} \\ & \cdot C_{10}H_{22} \\ & \rightarrow (x_{CO} + x_{CH_4} + x_{CO_2} + 10 \cdot x_{C_{10}H_{22}}) \cdot CO_2 \\ & + (2 \cdot x_{CH_4} + x_{H_2} + 11 \cdot x_{C_{10}H_{22}}) \cdot H_2O \\ & + \left(x_{N_2} + \left(AFR_{st\text{-}syngas} + \frac{15.5}{0.21} \cdot x_{C_{10}H_{22}} \right) \cdot 0.79 \right) \cdot N_2 \end{aligned} \quad (3-III)$$

The temperature was maintained above 400 K to avoid condensation of the decane fuel. Regarding simulation, as the Madison mechanism [119] includes higher hydrocarbons, it was considered for this study. Table 18 summarized the different mixtures tested by considering 2.5% or 5% of decane in mass content.

Table 18: Different tested mixtures of the three syngas compositions with two different amounts of decane.

Syngas + Decane content (mass %)	Decane content (vol.%)	Decane content (energy %)	Syngas/air Equivalence Ratio	Global Equivalence Ratio range
Downdraft + 2.5%	0.45	19.0	0.5- 1.2	0.67– 1.6
Updraft + 2.5%	0.46	17.6	0.5- 1.2	0.65– 1.57
Fluidbed + 2.5%	0.49	17.8	0.5– 1.0	0.65– 1.3
Downdraft+ 5%	0.90	32.4	0.5– 1.0	0.83– 1.66
Updraft + 5%	0.92	30.5	0.5- 1.0	0.8– 1.57
Fluidbed + 5%	0.98	30.7	0.5- 0.9	0.8– 1.44

S_u^0 was also determined for pure decane and compared with literature data, from Munzar et al. [139] and Ji et al. [140], alongside simulations employing the Madison mechanism as highlighted in Figure 31. These experimental data are globally within the present uncertainty intervals but with less accuracy for richer mixtures. Maximum flame speeds are all within 5% of each other and are reached at around 1.05-1.1. The simulation results are globally close to experimental data, but the present data is closer for rich mixtures.

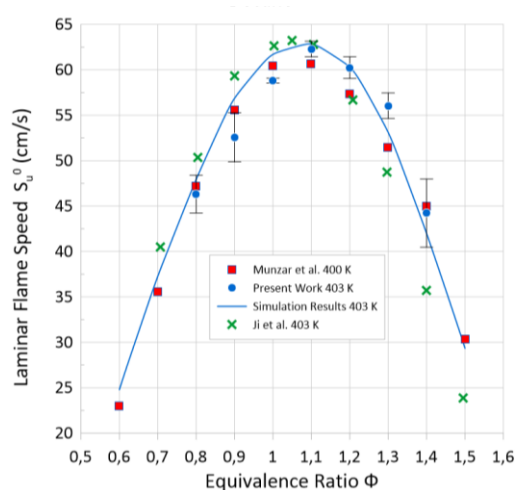


Figure 31: S_u^0 of pure decane of the present work compared with simulation results [119] and literature data [139,140].

From the measurements presented for syngas/decane mixtures in Figure 32, several key conclusions can be drawn:

- The addition of decane in syngas/air flames can increase S_u^0 especially for lean mixtures, even surpassing the maximum pure syngas values on a wider range of equivalence ratio, in the case of Fluidbed composition.
- Higher H_2 content on the Downdraft composition produces faster flames whereas, low H_2 and CO combined with high CO_2 content (in the case of Fluidbed) produces slower flames (almost half of the speed).
- Madison mechanism [119] predict globally the laminar flame speed values but the agreement is worse for Updraft and at higher pressures where S_u^0 is underpredicted (see the effect of pressure also in Figure 24, for pure syngas).

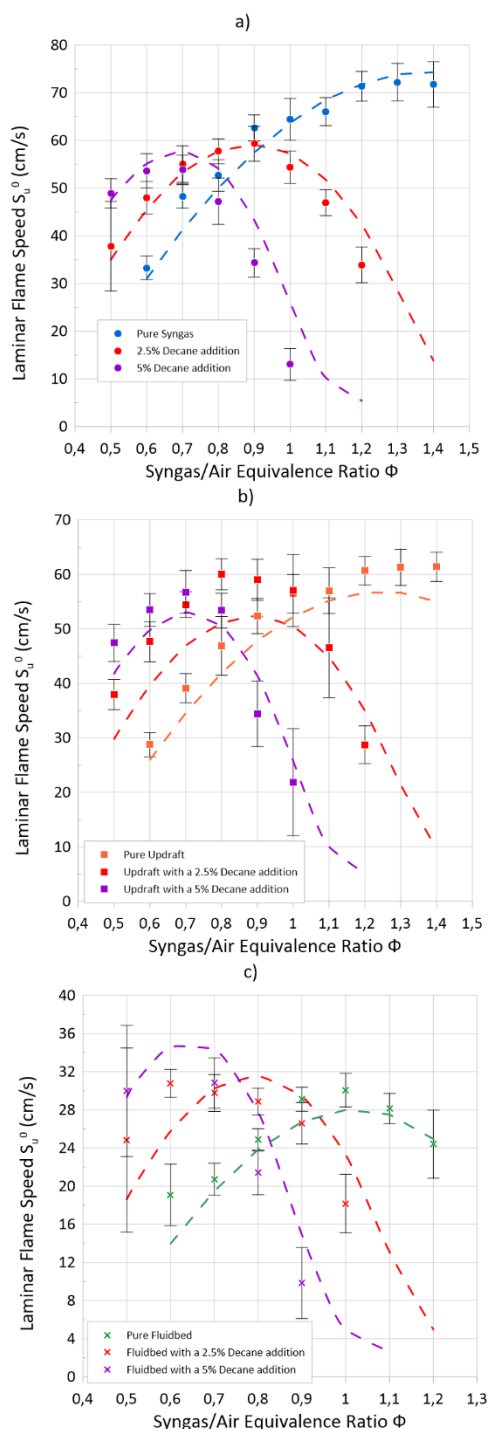


Figure 32: Evolution of laminar flame speed as a function of syngas/air equivalence ratio for three decane contents at 1 bar and 423 K. a- Downdraft composition, b- Updraft, c- fluidbed syngas composition, simulation results, using the Madison mechanism [119], in the dashed line.

As previously said and showed in Figure 32, for a fixed equivalence ratio of the syngas/air, the addition of decane to a lean syngas/air mixture can increase the S_u^0 whereas no benefits are showed for higher equivalence ratio. Therefore, the lean syngas/air mixture could be of interest for a dual fuel engine use as investigated in the following chapter. Therefore, in Figure 33, we can see the effect of pressure on the S_u^0 with the addition of the two Mass Fractions (MF). It must be noted that we did not test the effect of pressure for pure syngas at higher pressure at this initial temperature of 423 K, this is the reason for presenting a single cross measured at 1 bar and 423 K. From this graph we can see that the

Downdraft and Updraft present the same values of S_u^0 with the decane addition, that correspond to a global ϕ_{global} of around 0.9 and 1.1 for 2.5 and 5% MF decane addition, respectively. The increase of S_u^0 for a fixed lean equivalence ratio of the syngas/air mixtures with the decane addition is also clearly visible for the three compositions and holds true when the pressure increases. The relative increase in S_u^0 due to decane addition seems similar for the three compositions.

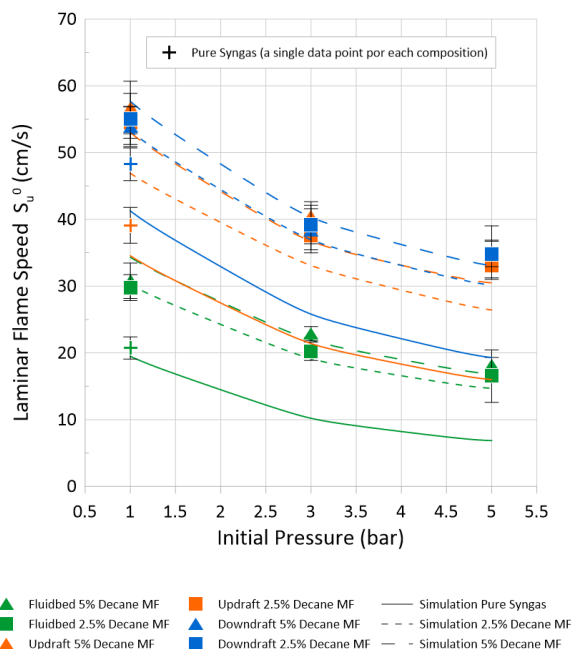


Figure 33: Effect of pressure and the decane addition for a fixed equivalence ratio ($\phi_{syngas/air} = 0.7$) on the laminar flame speed (S_u^0) (MF \rightarrow Mass Fraction).

3.5. Conclusion

In this chapter, the first complete database of laminar flame speed is provided for the three typical syngas compositions as a function of equivalence ratio, initial temperature (up to 423 K) and initial pressure (up to 5 bar), with also a comparison with the only two literature available data and the data obtained from four kinetic mechanisms. The presence of the decane in the mixture due to dual fuel operating conditions was also studied. The main conclusions that can be drawn from these results are:

- The experimental data obtained show good global agreement with the only two literature results especially for lean mixtures.
- As expected, due to the presence of high content of dilution by CO_2 and N_2 in the Fluidbed composition, the flame speed is lower than for the Downdraft and Updraft. For example, at 298 K and 1 bar, Fluidbed, Updraft and Downdraft laminar flame speeds peak at 14, 31 and 37 cm/s, respectively.
- The effect of pressure on the laminar burning velocity is stronger for the Fluidbed composition. This indicates that in internal combustion engines this syngas mixture can be less suitable in terms of performance.
- A classical correlation, based on the work of Metghalchi and Keck [131] and useful for 0D/1D simulation, indicated an acceptable agreement for the laminar burning velocity (less than 5% of discrepancies on average).

- The comparison with results from simulation based on four kinetics mechanism allows to conclude that best agreement is obtained with CRECK and San Diego mechanisms rather than with Aramco and Madison mechanisms.
- Markstein lengths tend to negative values for lean mixtures with a transition to positive around the stoichiometry, indicating that the flames are more and more unstable due to the curvature in the lean mixture and this is accentuated with the Fluidbed due to the higher dilution.
- In the case of decane ignition of syngas mixture, the comparison with the experimental data indicated that the Madison mechanism can predict very well laminar burning velocity of syngas mixtures when small amounts of decane (up to 5% in mass) are added. This is useful for dual-fuel engine investigations explored in the next chapters.

In the next chapter, we analyze how these fundamental combustion properties affect the results obtained in this chapter, in terms of performance and emissions of a syngas/diesel dual-fuel engine.

4. A multiparameter analysis of syngas/diesel dual-fuel engine performance and emissions with three syngas compositions

4.1. Introduction

The challenge when fueling an internal combustion engine with syngas is the inherent variability in composition, due to the biomass origin and the gasification process, as already described in the first chapter. From the literature study in Chapter 2, it is evident that the use of syngas in a Compression-Ignition (CI) engine in dual-fuel mode has the advantage to be a flex-fuel energy system, especially for off-grid stationary application. In dual-fuel mode, due to the pilot injection of reactive fuel (as Diesel fuel), the physicochemical interactions of the gaseous syngas combustion interactions with the liquid pilot fuel spray add complexity, poorly studied and understood. Currently, even if natural gas or methane dual-fuel operation are well covered by the literature [80,141–144], it is less the case for syngas fuels. Moreover, to correctly optimize dual-fuel syngas CI engines, the effects of the fluctuation of the composition, needs to be better understood. The challenge, addressed in this chapter, when studying the influence of syngas composition on dual-fuel engine performance is that the engine is not fed with ‘real’ syngas but a controlled composition of syngas, representative of what is possible to produce from gasification. In parallel, a special attention will be done to identify the impact of each gas component on performance and emission parameters. Therefore, the novel approach chosen for this study is to consider the three compositions already chosen for Chapter 3, as Fluidbed, Updraft and Downdraft. In Table 19, the compositions are reminded with also the Air/Fuel ratio at the stoichiometry, the energy provided from these gases and the maximum laminar flame speed, experimentally determined in Chapter 3.

Table 19: Syngas Compositions.

	H ₂	CO	CO ₂	CH ₄	N ₂	Stoichiometric Air/ Fuel ratio	LHV (MJ/m ³ of gas)	Maximum laminar flame speed at 298K and 1bar (cm/s)
	(%Vol)	(%Vol)	(%Vol)	(%Vol)	(%Vol)	(mol/mol) (mass/mass)		
Fluidbed	9	14	20	7	50	1.21 (1.25)	4.2	15.4
Updraft	11	24	9	3	53	1.12 (1.24)	4.4	30.7
Downdraft	17	21	13	1	48	1.00 (1.13)	4.8	36.7

Previous studies as indicated above, are mainly conducted with a unique syngas composition or are numerical studies [102,145–147]. In most of these studies, the diesel substitution ratio is quite low, under 60%, except for some studies (see Table 6). Here, the global objective of this study is to identify what are the fundamental combustion and physical properties of syngas that determine engine performance and operating limits in dual-fuel mode, by considered lowest content of diesel to ignite syngas charge. For that, the effects of the pilot fuel quantity and equivalence ratio of premixed syngas/air on engine performance and emissions are analyzed as a function of syngas composition.

Moreover, to highlight the contribution of CH₄ and CO₂ contents, an additional analysis is carried out with ternary mixtures of H₂/CO/N₂.

4.2. Experimental set-up and post-processing

In this section the engine characteristics, experimental method and the post-processing method are described.

4.2.1. Experimental Set-up

The engine characteristics are described in Table 20 It is based on Research 4 stroke PSA DW10 engine, converted to single-cylinder operation with three cylinders not fueled. As it was not possible to reach 1500 rpm, to represent the engine speed for genset application, with our set-up due to important vibrations of the intake/exhaust pipes and bench, the constant engine speed of 1200 rpm was selected. To set the desired intake charge compositions a series of flowmeters, as specified in Table 21, are used. The resulting uncertainty for the premixed syngas/air equivalence ratio, $\phi_{premixed}$ (Equation 4-1) of the intake charge is $\pm 2\%$. The mixing of the syngas/air charge is ensured by the intake plenum as schematized in Figure 34, which also enables to damp pressure oscillations inside the intake port.

Table 20: Engine Characteristics.

Displaced Volume	499 cm ³
Bore	85 mm
Stroke	88 mm
Rod length	145 mm
Compression Ratio	17:1
Piston Bowl Type	“Mexican hat”
Firing TDC position	0 CAD
Intake Valve Opening	351 CAD ATDC
Intake Valve Closure	157 CAD BTDC
Exhaust Valve Opening	140 CAD ATDC
Exhaust Valve Closure	366 CAD ATDC
Oil and Coolant Temperature	85 °C

Table 21: Flowmeter Controllers.

Gas Type	Flowmeter Controller	Full Scale	Uncertainty
Air	Emerson F025S	1100 NL/min	$\pm 0.5\%$
N ₂	Brooks 5851S	100 NL/min	$\pm 0.9\%$
CO	Brooks 5851S	100 NL/min	$\pm 0.9\%$
H ₂	SLA5850	50 NL/min	$\pm 1,0 \%$
CO ₂	SLA5850	37 NL/min	$\pm 1.0\%$
CH ₄	SLA5850	5 NL/min	$\pm 1.0\%$

The pilot injection of the diesel surrogate is obtained by means of a Bosch CRI 2.2 six-holes common-rail injector operating at the reduced pressure of 200 bar to guarantee minimal injection quantities with sufficient injection duration. The injector was characterized by means of an IAV type-K flow rate analyzer to provide the injection rate profiles and injection quantities as a function of the injection duration (see subsection 4.2.3 for further details). Decane ($C_{10}H_{22}$) was used as the surrogate of diesel fuel to facilitate kinetics simulations (see the previous subsection Laminar speed of syngas/decane mixtures).

Therefore, as the premixed equivalence ratio, $\phi_{premixed}$, is defined as the air/syngas molar ratio at the stoichiometry divided by the real air/syngas molar ratio, a global equivalence ratio, ϕ_{global} can be also calculated as a function of the pilot fuel amount and the stoichiometric mass air/fuel ratio of decane (i.e. 15.03) as indicated in Equation (4-2).

$$\phi_{premixed} = \frac{0.5\dot{V}_{CO} + 0.5\dot{V}_{H_2} + 2.0\dot{V}_{CH_4}}{0.21\dot{V}_{Air}} \quad (4-1)$$

$$\phi_{global} = \phi_{premixed} + \frac{15.03}{\dot{m}_{air}/\dot{m}_{pilot}} \quad (4-2)$$

Additionally, the energy share of the pilot fuel (decane) energy of the total supplied energy is defined as follows:

$$E_{pilot} = 100 \cdot \frac{\dot{m}_{inj}LHV_{C_{10}H_{22}}}{\dot{m}_{inj}LHV_{C_{10}H_{22}} + \dot{m}_{syngas}LHV_{syngas}} \quad (4-3)$$

A MEXA 7100D-EGR HORIBA gas analyzer was used to measure O_2 (magneto-pneumatic detector), CO and CO_2 , (non-dispersive infrared absorption analyzer), NO_x (chemiluminescence analyzer) and total unburnt Hydrocarbons (THC) (flame ion analyzer) concentrations. Additionally, an AVL 415S smoke-meter, with a detection limit of 0.02 mg/m^3 was used to provide soot emission data. The full experimental set-up is schematized in Figure 34.

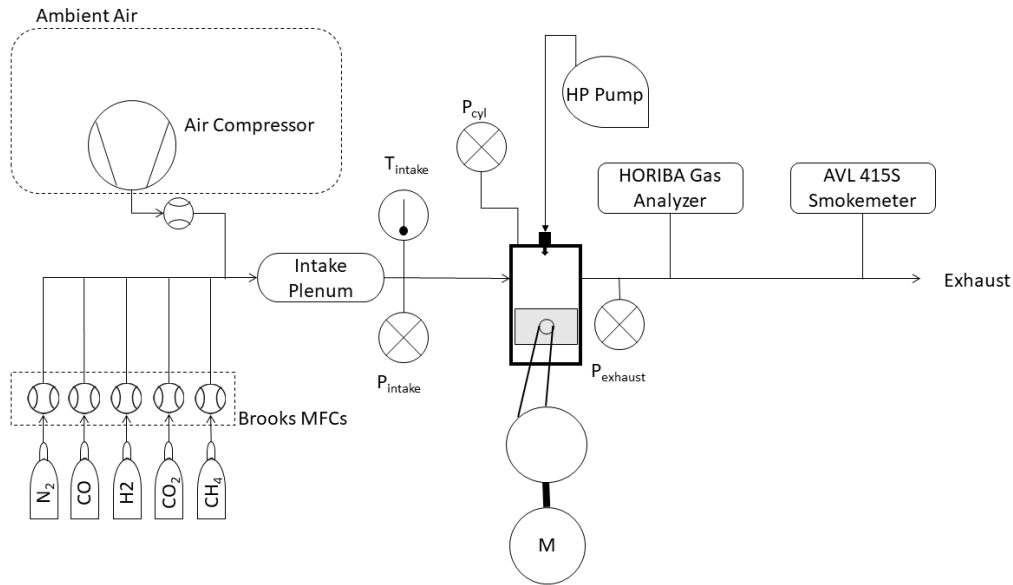


Figure 34: Experimental Set-up scheme

4.2.2. Post-processing method

From the in-cylinder pressure, measured by a Kistler 6043A piezo-electric pressure transducer (accuracy of $\pm 2.0\%$) and averaged over 100 consecutive cycles, the gross Heat Release Rate (HRR) is estimated with the following equation:

$$HRR \left(\frac{J}{CAD} \right) = \frac{\gamma}{\gamma-1} P \frac{dV}{d\theta} + \frac{1}{\gamma-1} V \frac{dP}{d\theta} + \frac{dQ_{wall}}{d\theta} \quad (4-4)$$

$$\frac{dQ_{wall}}{d\theta} \left(\frac{J}{CAD} \right) = w \cdot S \cdot (T - T_{wall}) \quad (4-5)$$

$$w \left(J \cdot K^{-1} \cdot m^{-2} \right) = 3.26b^{-0.2} P^{0.8} T^{-0.55} \nu^{0.8} \quad (4-6)$$

The heat transfer coefficient h is determined using the correlation proposed by Woschni [148]. The integrated value of $dQ_{combustion}$ is used to determine the mass of fuel burnt (MFB). Cylinder wall temperature, T_{wall} , is estimated at 423 K. The calculation is first done with a constant heat capacity ratio, γ , to obtain a first estimate of MFB. Then, γ is reassessed from the MFB with the mole fractions of all six components (N_2 , O_2 , CO , H_2 , CO_2 , CH_4) for the unburnt and for the burnt gases, from the gas analyzer, using NASA polynomials equation. Equations (4-4)-(4-6) are then recalculated with this variable γ and the definitive MFB value is obtained.

The thermal efficiency is calculated with the following equation:

$$\eta_{thermal} = \frac{IMEP \cdot V_{cyl} \cdot \dot{m}_{total}}{LHV_{CO} \cdot \dot{m}_{CO} + LHV_{H_2} \cdot \dot{m}_{H_2} + LHV_{CH_4} \cdot \dot{m}_{CH_4} + LHV_{C_{10}H_{22}} \cdot \dot{m}_{C_{10}H_{22}}} \quad (4-7)$$

The combustion efficiency is calculated by doing the oxygen balance between intake and exhaust related to the total equivalence ratio, given by Equation (4-8).

$$\eta_{combustion} = \frac{0.21\dot{m}_{air-intake} - \dot{m}_{O_2-exhaust}}{\dot{m}_{O_2-theoretically\ burning}} \quad (4-8)$$

4.2.3. Determination of the injected decane mass

In Chapters 4 and 5, the same six-holes Bosch CRI 2.2 injector was used, with the characteristics described in Table 22. The Common-Rail pressure is reduced to 200 bar, from the specified 1600 bar, aiming to reduce the injected mass with good repeatability.

Table 22: Characteristics of the Bosch CRI 2.2 used in the experiments.

Injector Type	Solenoid-Valve Injector
Number of Orifices (#)	6
Orifice Diameter (μm)	0.13
Injector Angle ($^\circ$)	149
Common-Rail Pressure (bar)	200

The injector is controlled by an EFS IPOD 8532 to phase the beginning of the injection and the closing. The injection rate was characterized using an IAV type-K flow rate analyzer, to provide the injection rate profiles and injection quantities as a function of the injection duration.

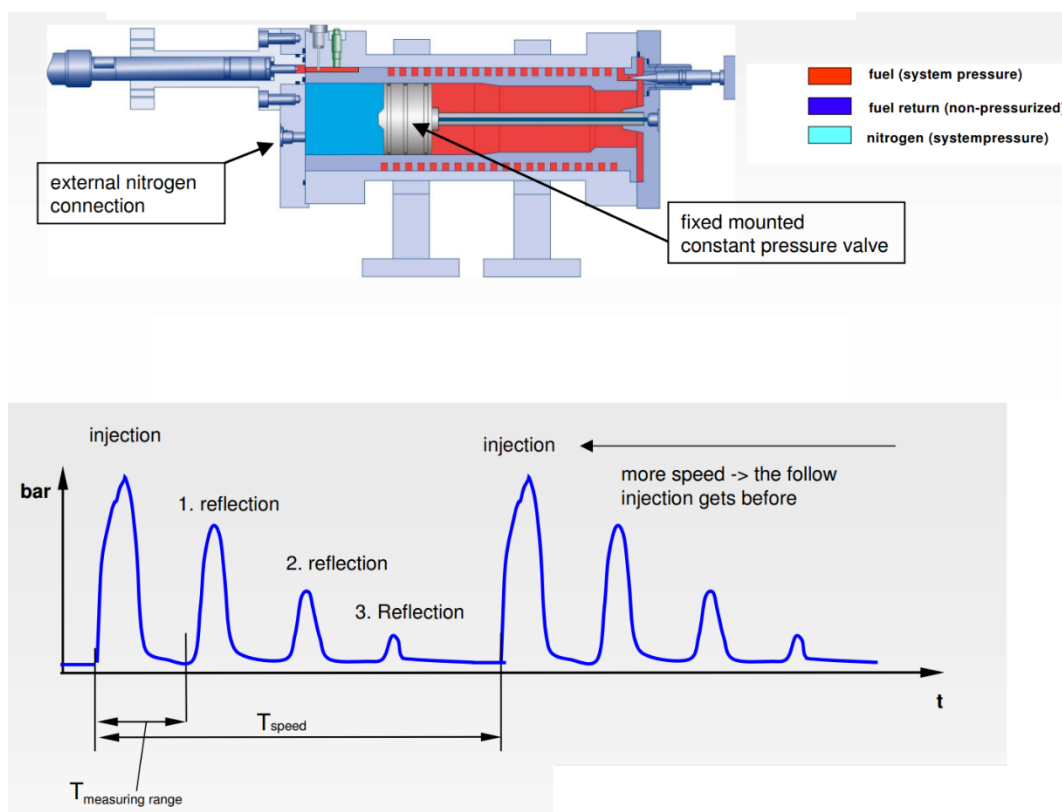


Figure 35: Schematic of the IAV injection analyzer used along with an example of the fuel of interest pressure trace (reproduced from the IAV GmbH. brochure).

The principle of the IAV injection analyzer is to measure the fluid pressure oscillations when the injection occurs. In Figure 35, the scheme of the device and an example of fluid pressure oscillations, that determine the injected mass for a given injection duration, is displayed.

Equation (4-9) presents how the injected mass is determined, where \dot{m} is mass flow rate of the injection, L_t is the length of the fluid that is placed in and SS is the sound speed of the fluid at the specified counter-pressure of the fluid, set by the system pressure. The influence of the counterpressure on the fluid sound speed must be characterized and the counter-pressure must be representative of the in-cylinder pressures where the injection will occur.

$$\dot{m} = \frac{L_t}{SS} \cdot \Delta p \rightarrow \Sigma \rightarrow m = \frac{L_t}{SS} \cdot \int p(t) dt \quad (4-9)$$

The fluid of interest is decane and for all the range of counter-pressure, to represent the in-cylinder pressure, from 12 to 50 bars, the injection durations is varied from 170 to 1000 μ s. Table 23 presents the injected mass for different injection durations and counter-pressures, system pressures, that allowed to interpolate the injected decane mass used in the engines experiments.

Table 23: Injected decane mass (mg) for the selected injector on different injection durations and system pressures.

Injection duration (μ s) \rightarrow	170	190	210	230	250	275	300	350	400	500	750	1000
Counterpressure (bar) \downarrow												
12	0.051	0.068	0.095	0.093	0.098	0.106	0.129	0.175	0.235	0.410	1.522	3.733
22	0.052	0.078	0.105	0.111	0.108	0.112	0.147	0.216	0.305	0.535	1.865	4.482
26	0.054	0.079	0.117	0.121	0.110	0.122	0.151	0.233	0.311	0.597	2.126	4.856
32	0.056	0.082	0.129	0.124	0.115	0.128	0.158	-	0.334	0.632	2.223	4.869
38	0.057	0.078	0.116	0.116	0.120	0.144	0.187	0.266	0.376	0.684	2.276	5.224
52	0.074	0.118	0.114	0.110	0.121	0.159	0.247	0.325	0.484	0.816	2.565	5.588

4.3. Results and discussion

4.3.1. Effect of premixed equivalence ratio

To study the effect of syngas/air equivalence ratio, the injection duration of decane was kept constant at 500 μ s, which corresponds to 0.61 mg, when the syngas amount only varied. The Start Of Injection (SOI) was optimized to guarantee maximum IMEP. Premixed equivalence ratio, ϕ_{premixed} was varied to 0.3, 0.5, 0.7 and 1.0 for all three compositions except for Fluidbed at $\phi_{\text{premixed}} = 1.0$, very unstable combustion was induced, i.e. $\text{IMEP}_{\text{cov}} > 10\%$. Moreover, increasing ϕ_{premixed} leads not only to a syngas

mass flowrate increase but also an air mass flowrate decreases to keep constant the intake pressure (i.e. 1 bar).

In Figure 36 the HRR plots show that, for all syngas compositions, the increase of ϕ_{premixed} induces a transition from a two-phase combustion mode to a single-phase one. This is linked to the reduction of the ignition delay of the syngas/air mixtures with ϕ_{premixed} increase, as the ignition of syngas simultaneously with decane charge, instead of having the first auto-ignition of the decane charge followed by a slow flame of syngas/air mixture. When the pilot injection occurs, i.e. 20 CAD BTDC, the liquid fuel is atomized and has enough time to mix with the nearest surrounding syngas/air premixed mixture. Therefore, the ignition of the liquid pilot spray will also ignite the surrounding premixed charge of syngas especially if the syngas is in sufficient quantity as for the stoichiometric syngas/air case.

When ϕ_{premixed} is lower, the decane is introduced later, so less time to obtain a mixing with syngas/air, and less syngas is also available. Therefore, the decane will first ignite before the ignition of the premixed syngas charge. It should also be noted that the maximum HRR increases with ϕ_{premixed} but the delay does not seem to be affected after $\phi_{\text{premixed}} \geq 0.5$ for Downdraft and Updraft. Higher H_2 concentrations in the syngas composition induce higher peak of HRR. This is consistent with the findings of Dhole et al. [149] and Roy et al. [2].

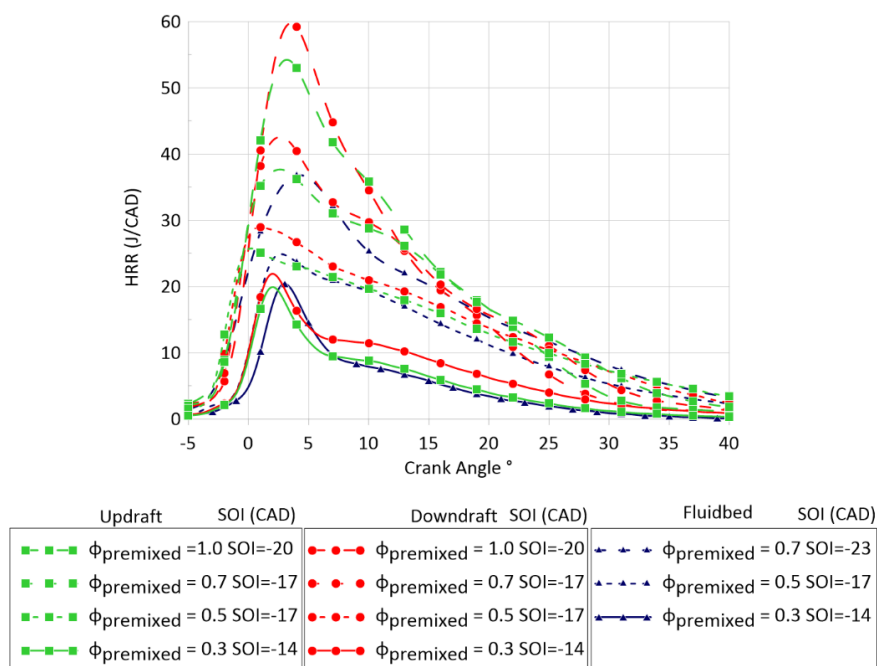


Figure 36: Evolution of Heat Release Rate for all premixed equivalence ratios and the three compositions ($N=1200$ RPM, $P_{\text{intake}} = 1$ bar, $T_{\text{intake}} = 300K$).

For the same equivalence ratio, the overall evolutions of HRR are not so affected by the syngas composition. But the ϕ_{premixed} increase leads to a higher pressure peak and a longer combustion tail for Downdraft, as highlighted in Figure 37, where the average in-cylinder pressure is presented. For $\phi_{\text{premixed}}=0.7$, Updraft and Downdraft compositions present similar pressure evolution while the pressure peak remains a bit lower for Fluidbed, as expected due to its lower energy content.

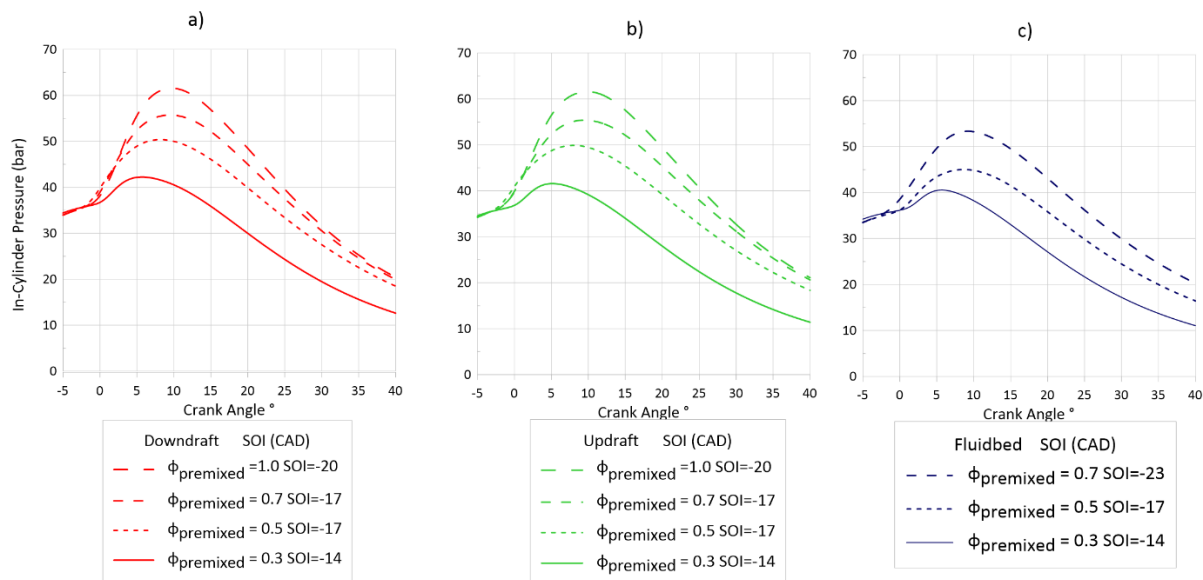


Figure 37. Evolution of In-Cylinder Pressure for all premixed equivalence ratio. ($N=1200$ RPM, $P_{\text{intake}} = 1$ bar, $T_{\text{intake}} = 300$ K).

Figure 38a displays the corresponding IMEP, with also the part of energy due to the decane pilot injection, E_{pilot} . First, in agreement with HRR and in-cylinder pressure evolutions, IMEP increases with ϕ_{premixed} since more energy is introduced. Then it is worth noticing that, in all cases, the energy share of the pilot remains below 7% of the total energy amount. Since the injected quantity of decane is maintained constant, the pilot energy share decreases with ϕ_{premixed} .

Figure 38b shows the IMEP_{cov} as well as the maximum pressure rise rate, i.e. MPRR, as a function of ϕ_{premixed} . For premixed equivalence ratio greater than 0.5, the combustion is quite stable for all compositions, with IMEP_{cov} below 6%, except for Fluidbed (8%). For $\phi_{\text{premixed}} = 0.3$, the combustion is more likely to be unstable (up to 13% of IMEP_{cov} for Downdraft) even if it remains possible to operate the engine. The maximum pressure rise rate is a good noise indicator, it increases with ϕ_{premixed} because of energy input increase and also the H_2 content in the syngas composition. The syngas compositions can be ranked, as Fluidbed, Updraft to Downdraft from lower to higher maximum pressure gradient. For Downdraft and Updraft at stoichiometric premixed equivalence ratio, it should be mentioned that the MPRR is at the limit of excessive combustion noise (4 bar/CAD) [150].

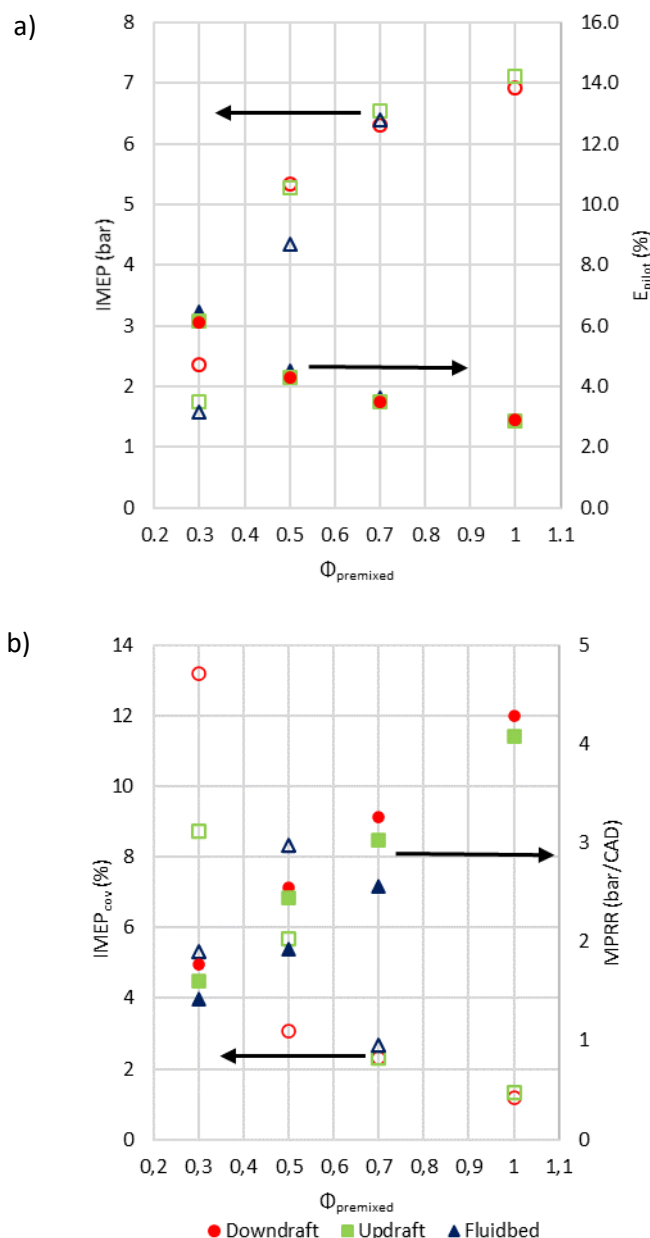


Figure 38. a) IMEP (empty symbols) and E_{pilot} (filled symbols) and b) IMEP_{cov} (empty symbols) and MPRR (filled symbols) as function of $\phi_{premixed}$.

In Figure 39, both the ignition delays from the pilot injection timing, estimated as the difference between the crank angle when 10% of MFB is reached (CA10) and the timing of the start of injection (SOI) and the first part of the combustion development, i.e. CA50 - CA10, are plotted as a function of the equivalence ratio. First, it can be noted that the increase in premixed equivalence ratio increases the ignition delay. It is probably explained by the fact that the SOI is advanced, as it can be seen in Table 24, with the increase in premixed equivalence ratio, to guarantee maximum IMEP with minimum IMEP_{cov} and a relatively constant CA50, to guarantee also a good thermal efficiency. This is especially applied for the Fluidbed composition, which the increase is more linear and stronger than for the Downdraft and Updraft ones. This is probably explained by the higher CO₂ content (20%) of Fluidbed composition that contributes to delay the autoignition. Yet, the duration of the first half of the combustion strongly decreases from $\phi_{premixed} = 0.5$ onwards, due to the increased reactivity of the premixed charge and the increase of the flame propagation speed.

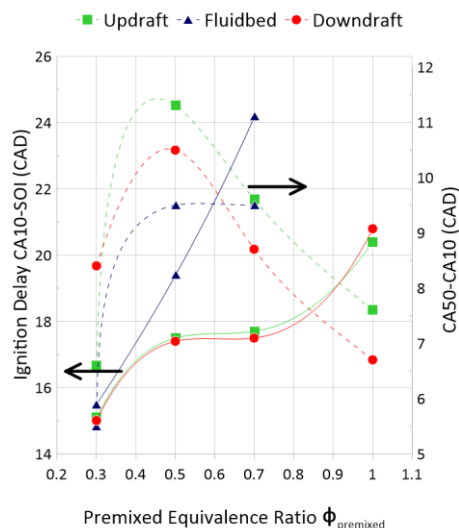


Figure 39: Effect of premixed equivalence ratio on ignition phasing (continuous lines) and first half of combustion (dotted lines) ($N = 1200$ RPM $P_{intake} = 1$ bar $T_{intake} = 300K$).

Table 24: Start Of Injection (SOI) configuration.

Premixed Equivalence Ratio ($\phi_{premixed}$)	Downdraft and Updraft (CAD BTDC)	Fluidbed (CAD BTDC)
0.3	-14	-14
0.5	-17	-17
0.7	-17	-23
1.0	-20	--

To better demonstrate the effect of the $\phi_{premixed}$ on the combustion phasing, Figure 40 presents the CA10-50-90, the CAD that the MFB reaches 10, 50 and 90%, respectively, and the SOI's values for the three compositions, on equivalence ratios ranging from 0.3 to 1.0. The CA50 and CA90 are reduced for the Downdraft and Updraft compositions, and since the CA10's values are similar, one can conclude that first and second phase, represented as CA50-CA10 and CA90-CA50, are shortened.

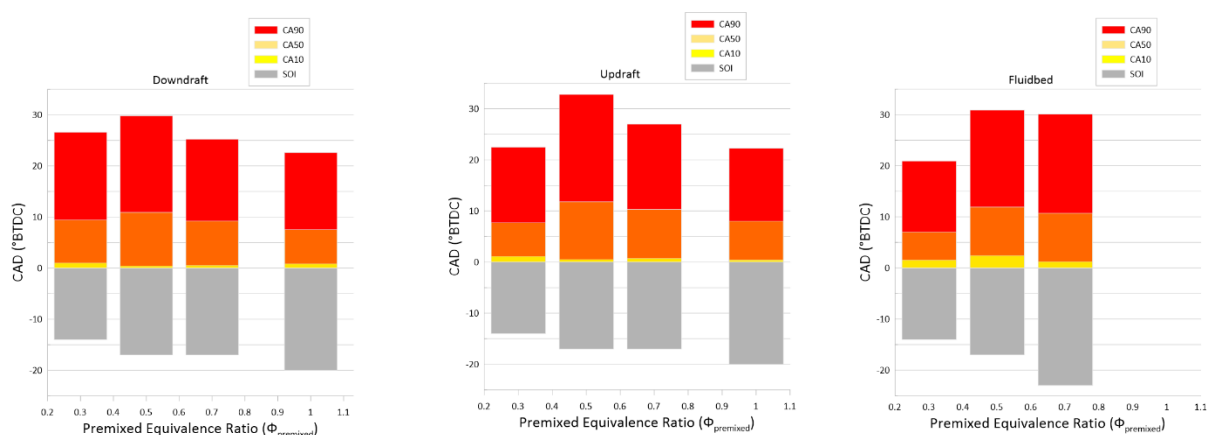


Figure 40: The effect of $\phi_{premixed}$ on the combustion phasing (1200 RPM, $P_{intake} = 1$ bar, $T_{intake} = 300K$).

Figure 41 presents the thermal and combustion efficiencies and emissions as a function of premixed equivalence ratio for the three Syngas compositions. Both combustion and thermal efficiencies are bell-

shaped reaching peak values around 98% and 39%, respectively, for both the Downdraft and Updraft compositions.

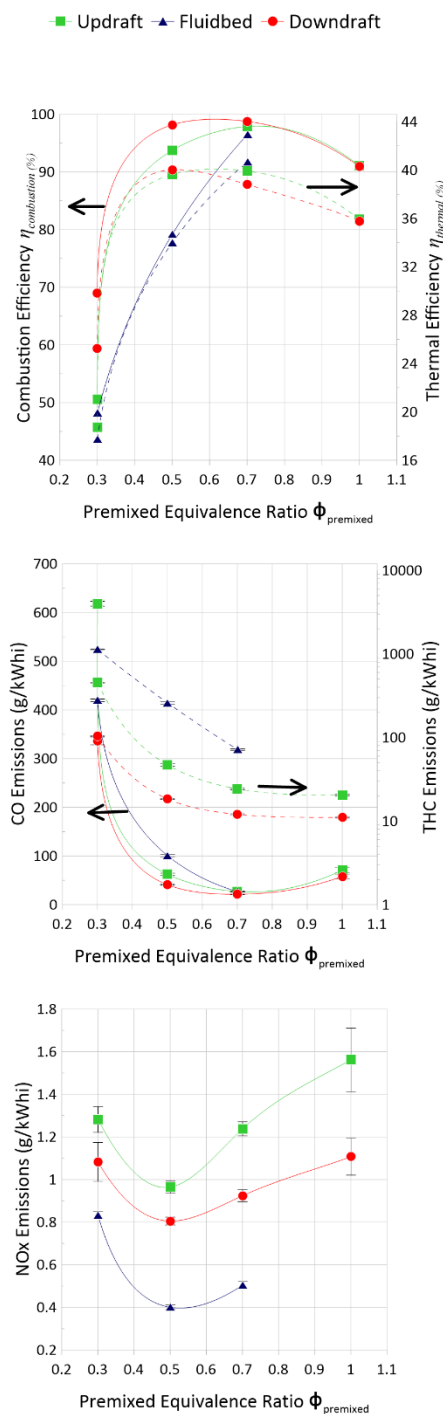


Figure 41: Efficiencies and exhaust gases emissions as a function of premixed equivalence ratio for the three Syngas compositions (1200 RPM, $P_{intake} = 1$ bar, $T_{intake} = 300$ K, Optimum SOI).

For Fluidbed, efficiencies continuously increase but the curves start to bend. Since premixed stoichiometric equivalence ratio was not achievable, it is not possible to forecast for which equivalence ratio efficiencies will start to decrease. The lowest combustion efficiency, reached for the ultra-lean premixed charge, induces, as expected, the highest CO and THC emissions. The minimum CO and THC emissions are obtained when $\phi_{premixed}$ is between 0.5 – 0.7 and as expected where efficiencies are the highest ones. Overall, this effect of the premixed equivalence ratio on the CO and THC emissions confirms the ones observed by Roy et al. [2]. For NO_x emissions, also the lowest values are obtained

at $\phi_{premixed} = 0.5$, with the highest ones reached at the stoichiometric syngas/air mixture. This evolution is not expected as the NO_x emission peak is reached in lean side in classical SI engine. It is indeed surprising to observe that minimum NO_x coincides with minimum CO, but since syngas is a highly diluted fuel (about 50% N_2 , 10 to 20% CO_2), its combustion temperature is very low leading to low NO_x levels even in lean mixtures where CO emission is also minimum. Similar trends were observed numerically for NO_x emission but not for the ones of CO (Kousheshi et al. [151]). For all operating conditions, soot emissions were below the detection limit of the measurement device.

4.3.2. Effect of pilot fuel injection quantity

In the previous section, since the optimal premixed equivalence ratio was found to be around $\phi_{premixed} = 0.7$, the effect of the pilot injection was evaluated at this particular value, while the injection duration was varied from 250 μs to 1000 μs , i.e. corresponding to 0.11 to 4.86 mg of decane injected per cycle (see Table 25). First, to evaluate the contribution of the pilot amount in the combustion development, the pilot fuel is first injected in air (without syngas) and then in air plus 5%_{vol} CO_2 and 20%_{vol} N_2 concentrations (equivalent charge dilution as the Downdraft case).

Table 25: Experimental conditions to study the effect of pilot fuel injection quantity.

Case	Injection Duration (μs)	Decane injected mass (mg)	ϕ_{global}	Pilot fuel energy share (%)	IMEP (bar)	SOI (CAD) ATDC
Downdraft/Air	250	0.11	0.71	0.6	5.7	-17
	500	0.61	0.74	3.3	6.3	
	750	2.16	0.83	10.9	6.8	
	1000	4.86	1.0	21.7	7.4	
Air	500	0.61	0.02	100	0.4	-11
	750	2.16	0.08		1.2	
	1000	4.86	0.17		2.8	
Air/Diluents	750	2.16	0.1	100	0.7	-16
	1000	4.86	0.22		2.0	

In Figure 42, it can be clearly seen that the ignition delay of the reactive fuel, decane from pilot injection, is similar in air with diluents as with the presence of syngas. However, it can be noted that for the highest quantity of liquid pilot injection, i.e. 4.86 mg, an earlier heat release can be observed between -5 and -2 CAD before TDC, smaller than the main HRR peak due to the syngas combustion. This low-temperature heat release could indicate a two-stage ignition process that does not occur when the decane injection is done in non-reactive medium (i.e. air or air/diluent). In these cases, the combustion occurs in two phases: the main combustion phase due to the premixing of decane with air and a second one, slower due to the diffusion-controlled combustion. The distinction between the phases is less clear when syngas is premixed with the intake charge but there is still an inflexion point after the peak in HRR for 0.61 and 2.16 mg quantity injected at around 7 and 9 CAD ATDC respectively.

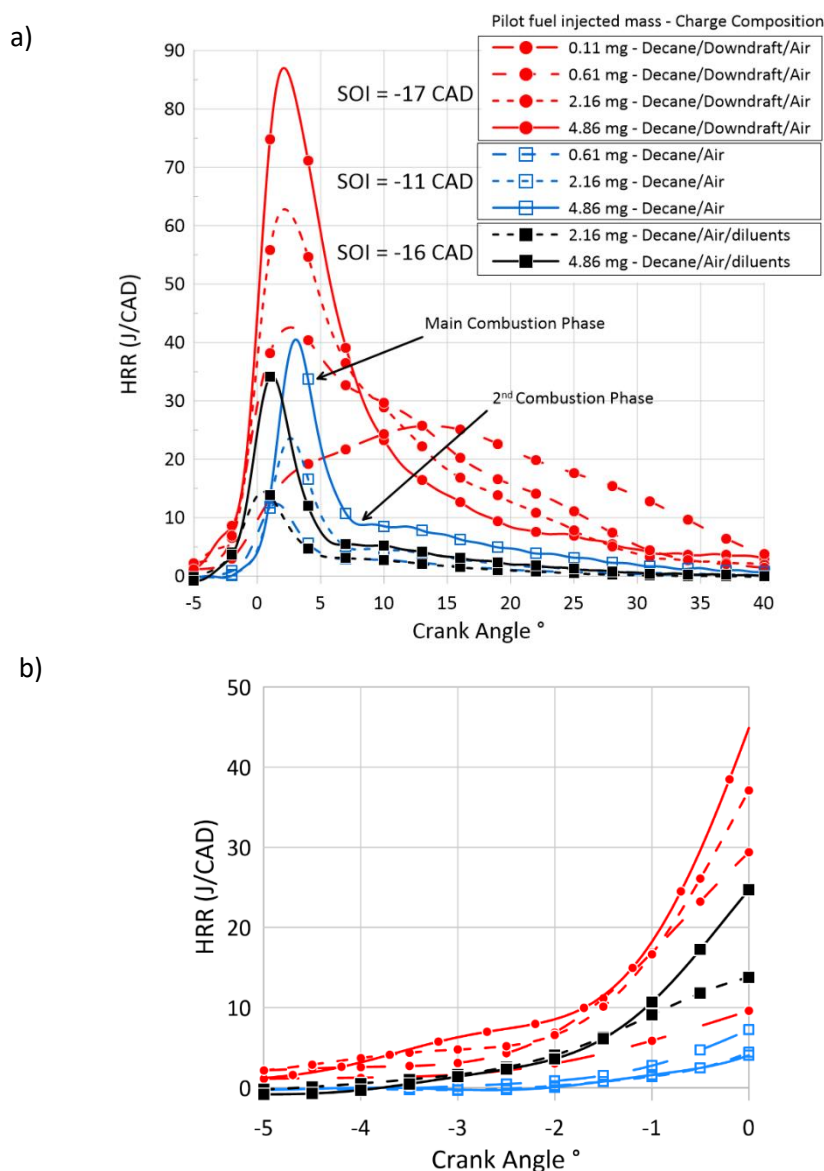


Figure 42: a- Heat release rate from the fuel pilot injection in air and air with diluents compared to Downdraft dual-fuel. ($\phi_{premixed} = 0.7$) and b- zoom between -5 and 0 CAD.

In Figure 43, the effect of decane addition on the ignition timing and the combustion phasing (CA50) is presented for the three syngas compositions. For the Fluidbed composition, stable combustion could not be achieved at the lowest and highest pilot fuel injection durations therefore only two data points

are presented. This behavior can be attributed to the high CO_2 concentrations of Fluidbed combined with the comparatively low H_2 and CO contents. For Updraft and Downdraft ones, the ignition delay seems to stabilize once enough decane is injected (over 10% of the total available energy). But, the combustion phasing is monotonically advanced with the addition of decane, as expected from the HRR profiles presented in Figure 42 for the Downdraft composition. Basically, increasing the energy share from the more reactive fuel will reduce the ignition delay of the whole fuel charge as observed on CA10-SOI, the decane being easier to auto-ignite. This will lead to a shift of the CA50 and globally of the whole combustion earlier in the cycle. For Downdraft, IMEP_{cov} decreases from 2.4 down to 1.1 % and MPRR increases from 1.2 up to 6.9 bar/CAD as E_{pilot} increase. For Updraft, the trends and values are very similar to Downdraft. However, for Fluidbed, IMEP_{cov} decreases from 2.6 down to 2 % and maximum pressure gradient increases from 2.6 up to 4.8 bar/CAD with E_{pilot} increases. Hence, and as expected, ranking in terms of combustion stability and noise is the same as the one observed in the previous section.

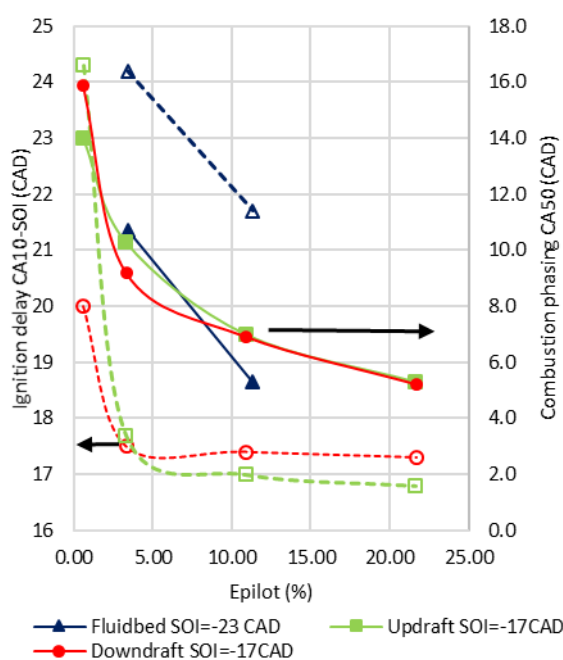


Figure 43: Effect of pilot fuel energy share on ignition delay (empty symbols, dashed lines) and combustion phasing CA50 (filled symbols, continuous lines) for three Syngas compositions (1200 RPM, $P_{\text{intake}} = 1 \text{ bar}$, $T_{\text{intake}} = 300\text{K}$, $\phi_{\text{premixed}} = 0.7$).

In Figure 44a, for Updraft and Downdraft compositions, it could be noted that the combustion and thermal efficiencies are bell shaped with a maximum value, reached around 10% pilot fuel energy share. Fluidbed results are not plotted here as only two conditions provide stable combustions. It must be noted that the Updraft composition induces a lower combustion efficiency than Downdraft but a better thermal one. This is observed even though CA50 is very similar between the two compositions for the same pilot fuel amount (Figure 43). Due to the higher H_2 content, Downdraft syngas has a greater flame speed (Table 19) thus leading to a better consumption of fresh gases. On the other hand, this higher H_2 content could lead to higher combustion temperature and therefore more heat losses thus a strong reduction of the thermal efficiency as highlighted numerically by Kousheshi et al. [151]. The emissions data show that CO and soot emissions are negatively affected by the increase in decane quantity, without any bell or inverse bell shape: more diesel-type fuel induces more unburnt carbonaceous exhaust gases, i.e. a slight reduction seems to occur with decane addition for the Updraft

composition. The level of soot was so low that no value could be measured, for fuel amount lower than 12% energy share as previously observed by Papagiannakis et al. [141] in the case of methane/diesel dual-fuel engine. Yet when reaching 20% for E_{pilot} , soot emissions rise significant value up to 6-9 g/kWh. It is also clear that NO_x emissions strongly increase as a function of decane amount, due to the increase of in-cylinder temperatures. It is interesting to notice that, both CO and NO_x are minimum for the same E_{pilot} and increase with E_{pilot} increase. Not only the syngas due to its strong diluent content is globally a low NO_x fuel, with a combustion temperature lower to usual hydrocarbon fuels but also since the global equivalence ratio remains lean for all conditions the CO and HC emissions are also low. Yet, when increasing decane quantity both NO_x and CO increase simultaneously due to the combustion temperature increase leading to higher NO_x . Moreover, an increase of decane injection leads to a decrease of the evaporation rate and of local air/fuel/syngas mixing, inducing higher CO and HC. The effects of CO_2 on NO_x emissions will be discussed further on the final part of this work.

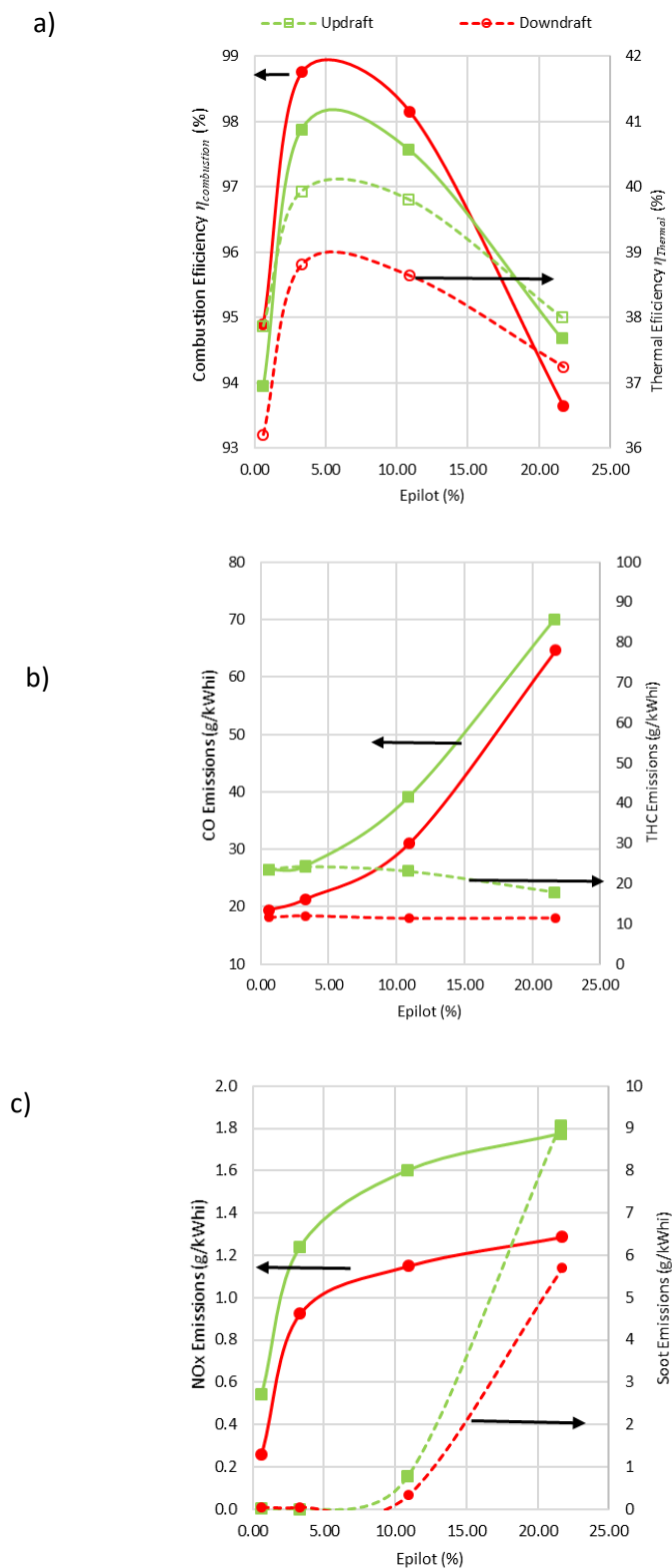


Figure 44: Efficiencies and emissions as a function of decane energy share for the three Syngas compositions. Filled symbols/continuous lines: a) Combustion efficiency, b) CO, c) NO_x emissions. Empty symbols/Dashed lines: Thermal Efficiency, THC and Soot emissions for a, b and c respectively (1200 RPM, $P_{intake} = 1$ bar, $T_{intake} = 300$ K, $\phi_{premixed} = 0.7$).

Figure 45, NO_x and CO emissions are presented as a function of CA50 and ϕ_{global} . Regarding the relationship between emissions and combustion phasing, for this premixed equivalence ratio, CO emissions reach a plateau for CA50 > 9 CAD ATDC while NO_x emissions decrease almost linearly with CA50, as the in-cylinder temperature is higher for shorter combustion phasing. The NO_x emissions as

function of the global equivalence ratio follows the decane share and seems to reach a plateau when the global equivalence ratio tends to 1. Meanwhile, the increase in CO emissions seems not to reach a plateau as usually in SI engines: CO increases with the global equivalence ratio increase.

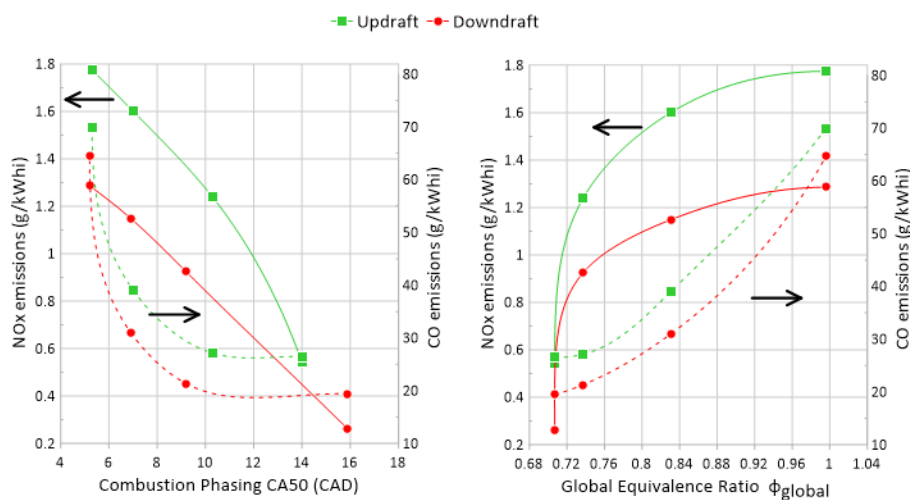


Figure 45: Specific emissions of NO_x (continuous line) and CO (dashed line) as a function of combustion phasing (left) and global equivalence ratio (right) (1200 RPM $P_{intake} = 1 \text{ bar}$, $T_{intake} = 300\text{K}$, $\phi_{premixed} = 0.7$).

4.3.3. Effect of CH₄ and CO₂ concentration

To give further insight on the roles of CH₄ and CO₂ on performance and emissions, complementary measurements were performed with the composition variations as in Table 26. The variation consists of maintaining H₂ and CO volume fractions constant while adjusting the N₂ volume fraction to compensate CO₂ or CH₄ variations. The variations are designated by the composition (FB, UD, DD for Fluidbed, Updraft, Downdraft respectively), from which the H₂ and CO content is kept, followed by an index that refers to the CO₂ or CH₄ content. The variation FB–20_{CO2} is greyed out as no stable operation could be obtained. The Madison kinetics mechanism [119] was selected in combination with the PREMIX and EQUIL CHEMKIN-Pro Ansys codes to estimate laminar flame speed and adiabatic flame temperature of the syngas fuel respectively, by considering initial conditions equal to those in the cylinder at the start of injection, i.e. 864 K and 30 bar, for $\phi_{premixed} = 0.7$. The effect of the decane injection was not considered since it is impossible to characterize the local decane/syngas fraction without an optical engine and with an optimized optical technique. This mechanism was validated for laminar flame speed in Chapter 3. Premixed equivalence ratio was kept constant at 0.7 and the injection with a duration of 400 μs , i.e. $E_{pilot} \approx 1.65\%$, started at -18 CAD BTDC.

Table 26: Variations on the original Syngas compositions.

Variation	H ₂ (%vol)	CO (%vol)	CO ₂ (%vol)	CH ₄ (%vol)	N ₂ (%vol)	Adiabatic Equilibrium Flame Temperature (K) @ 864K & 30 bar	Laminar Flame Speed (cm/s) @ 864K & 30 bar
FB – 0 _{CO₂-CH₄}	9	14	0	0	77	1868	32.3
FB – 10 _{CO₂}			10	0	67	1834	24.3
FB – 20 _{CO₂}			20	0	57	1802	14.9
FB – 2.5 _{CH₄}			0	2.5	74.5	1955	33.0
FB – 5 _{CH₄}			0	5	72	2016	35.0
FB - Reference			20	7	50	2004	26.4
UD – 0 _{CO₂-CH₄}	11	24	0	0	65	2092	61.5
UD – 10 _{CO₂}			10	0	55	2059	51.1
UD – 20 _{CO₂}			20	0	45	2028	41.9
UD – 2.5 _{CH₄}			0	2.5	62.5	2131	59.5
UD – 5 _{CH₄}			0	5	60	2160	58.2
UD - Reference			9	3	53	2112	51.1
DD – 0 _{CO₂-CH₄}	17	21	0	0	62	2120	83.0
DD – 10 _{CO₂}			10	0	52	2088	69.1
DD – 20 _{CO₂}			20	0	42	2057	57.9
DD – 2.5 _{CH₄}			0	2.5	59.5	2154	75.4
DD – 5 _{CH₄}			0	5	57	2178	71.2
DD – Reference			13	1	48	2095	62.7

In Figure 46, the effect of CO₂ and CH₄ content on HRR is highlighted. CO₂ addition to syngas delays the onset of combustion and extends the combustion duration. This effect has been well described by Xiang et al.[152] and Halter et al.[153] for CH₄/CO₂/Air mixtures where the dilution, thermal and chemical contributions of CO₂ to the reduction of laminar flame speed have been quantified. Since the total dilution amount, i.e. N₂ + CO₂ quantity, is kept constant, the effect seen here is both related to the thermal (increased heat capacity of the charge → reduction of charge temperature) and chemical effects. Moreover, the two combustion stages obtained for Downdraft and Updraft without any CO₂ (DD – 0_{CO₂-CH₄} and UD – 0_{CO₂-CH₄} respectively), are less evident with CO₂ addition. On the other hand, the addition of CH₄ advances the start of combustion and makes it easier to distinguish the two combustion phases. This could indicate that the H₂ in the syngas might be consumed first, contributing to the initial rise in HRR, followed by the slower-burning CO and CH₄.

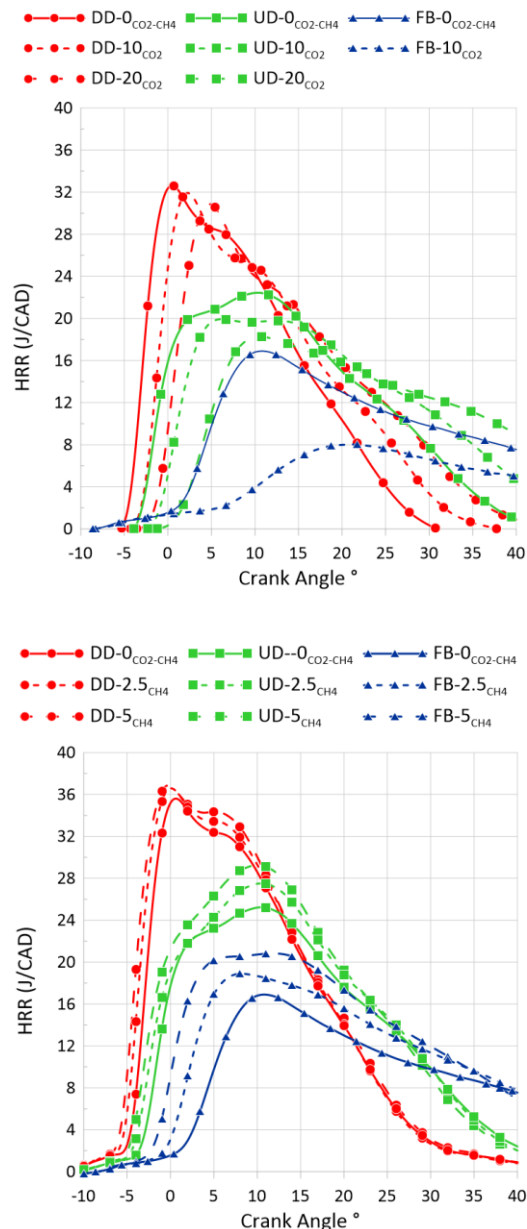
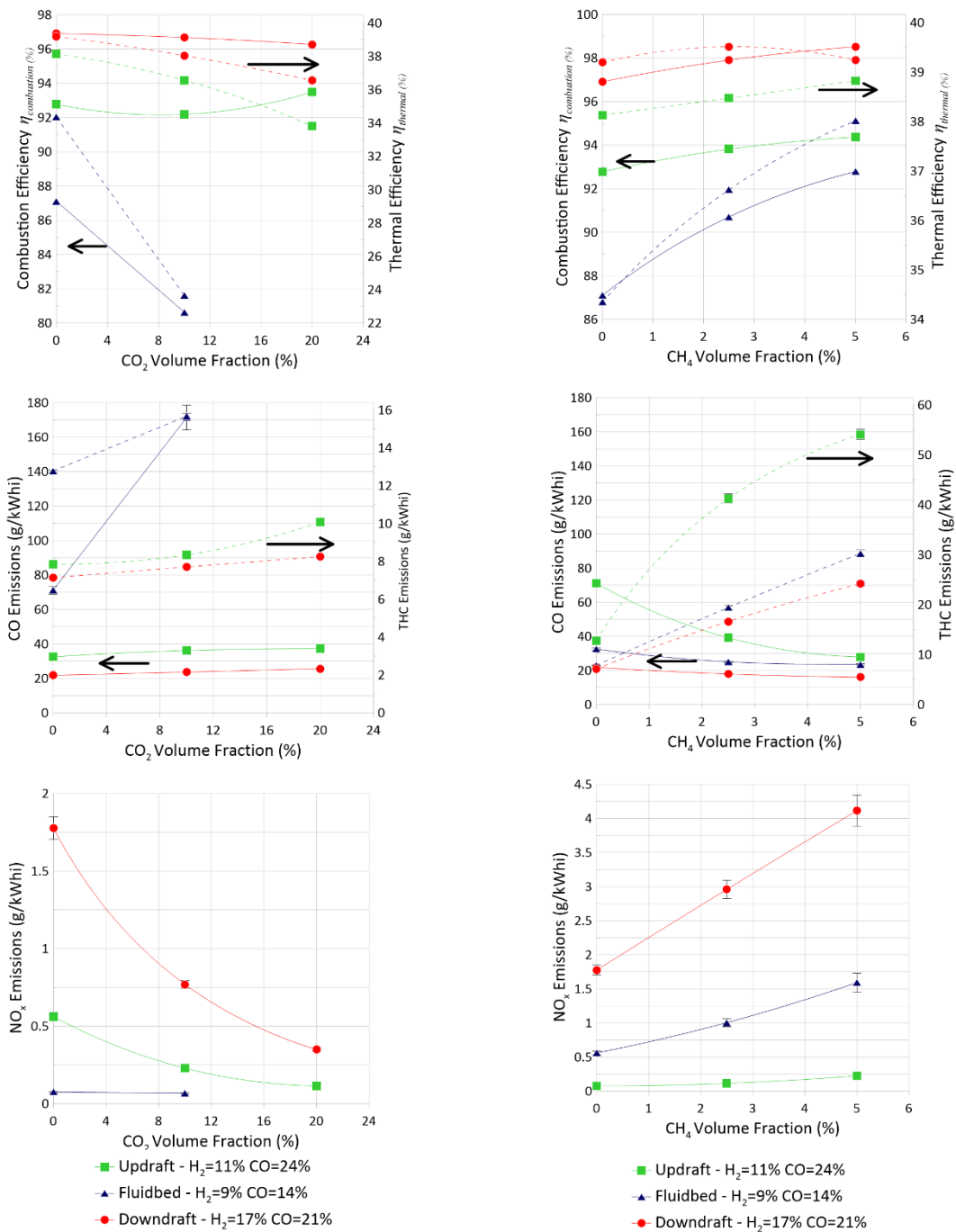


Figure 46: Heat Release Rate profiles for varying CO_2 (top) and CH_4 (bottom) contents (1200 RPM $P_{\text{intake}} = 1 \text{ bar}$, $T_{\text{intake}} = 300\text{K}$, $\phi_{\text{premixed}} = 0.7$ SOI = -18 CAD BTDC)

The resulting efficiencies and emissions from the variations tested are presented in Figure 47. Soot emissions are not presented because they are always under the detection limit. By replacing N_2 with CO_2 , the decrease of combustion efficiency induces CO and THC to increase and a reduction of NO_x emissions. It should also be mentioned the effect of the delay of the combustion phasing, as the start of injection was maintained constant and not optimized.

Figure 47b indicates that CH_4 addition increases both thermal and combustion efficiencies resulting in lower CO emissions. Despite the overall higher combustion efficiencies, THC emissions increase with CH_4 addition due to the increase of unburned CH_4 itself. Even if the amount of CH_4 added remains low, the increase of the CH_4 constant induces an increase of NO_x emissions, mainly due to higher in-cylinder temperatures, as predicted by the higher adiabatic temperature values Table 26. Due to the higher H_2 content, Downdraft composition provides a faster combustion development thus leading to a better

consumption of fresh gases. On the other hand, this higher H₂ content could lead to higher combustion temperature and therefore more heat losses thus depleting the thermal efficiency.



a) Effect of CO₂ content

b) Effect of CH₄ content

Figure 47. Effect of Syngas components a) CO₂ and b) CH₄ on engine efficiencies and exhaust emissions (1200 RPM, P_{intake} = 1 bar, T_{intake} = 300K, φ_{premixed} = 0.7, SOI = -17 BTDC).

4.3.4. Relationship between fundamental composition properties and engine operation

In order to predict the effect of syngas composition, it is important to highlight the relationship between the fundamental properties of the composition (such as laminar flame speeds, LFS, or adiabatic flame temperature, T_{ad}) and the resulting engine performance and emissions, as presented in Figure 48, where some empirical correlations are suggested to identify better the effect of properties variations, summarized in Table 26 to the combustion duration and stability and NO_x , THC and CO emissions. The first flame development stage duration (CA50-CA10) and the total combustion duration (CA90-CA10) clearly decrease with the laminar flame speed with a clear transition when the flame speed goes under a certain level probably due to the engine instabilities linked to the low value of LFS in the case of Fluidbed. A similar behavior was observed by Lhuillier et al. [154] for NH_3/H_2 mixtures in a SI engine. Nevertheless, while the trend is clear for the whole of the 17 compositions tested, two groups can be identified as a function of H_2/CO contents for LFS lower than 40 cm/s. Similar tendency can be noticed in Figure 48b, when the composition of a syngas/air mixture induces a laminar flame speed lower than 40 cm/s, as it is for Fluidbed composition, IMEP_{cov} rises sharply as function of Laminar Flame Speed decreases. Yet, for $\text{LFS} > 40$ cm/s, the stability is not affected by any laminar flame speed change.

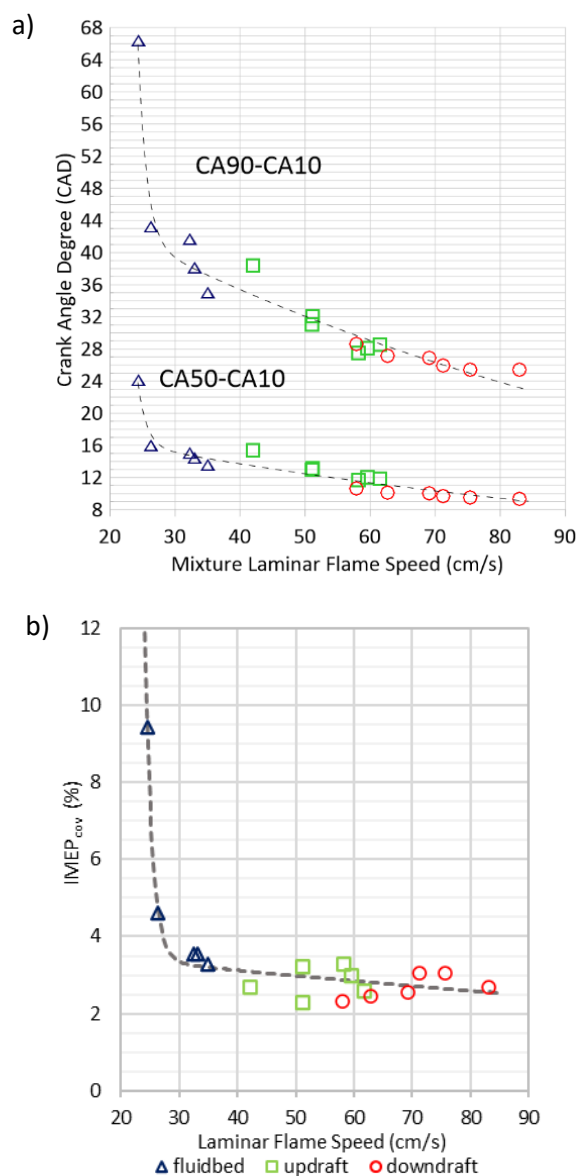


Figure 48: Relationship between a- combustion duration and b- stability ($IMEP_{cov}$) as a function of syngas Laminar Flame Speed. (1200 RPM , $P_{intake} = 1\text{ bar}$, $T_{intake} = 300\text{ K}$, $\phi_{premixed} = 0.7$ $SOI = -18\text{ CAD BTDC}$)

The effect of CH_4 content is not studied as a function of LFS but by considering the total hydrocarbon (THC) emissions. As it can be seen in Figure 49a, the linear evolution of HC indicates that the part of intermediate CH due to the decane oxidation (or to crevice trapping) is very low in comparison to the part due to the CH_4 content, without any effect of the syngas composition. In the case of CO emissions (Figure 49b), similar linear dependency can be noted for Downdraft and Updraft compositions but the exhaust CO values are less than 10% of the CO quantity introduced. This is caused by the good oxidation of the CO during the combustion process. Yet, the high $IMEP_{cov}$ for Fluidbed induces higher instabilities, which also leads to higher CO emissions (15%).

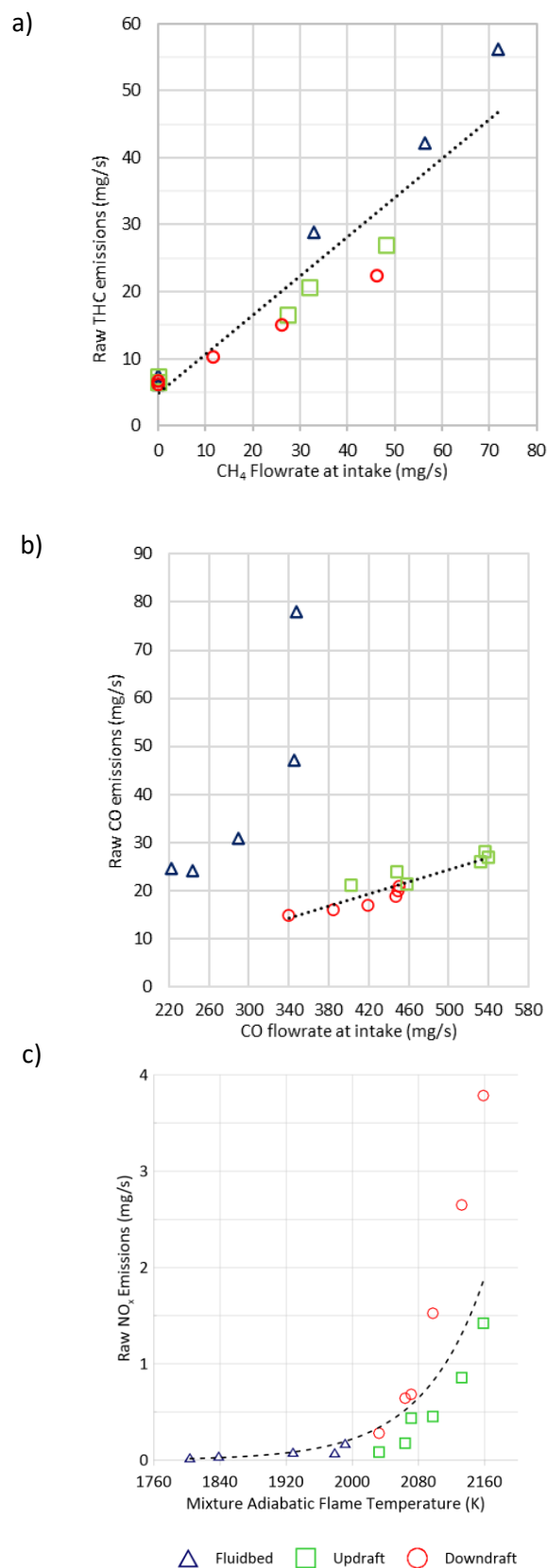


Figure 49: Relationship between THC emissions and intake CH₄ (a), Exhaust and Intake CO (b), NO_x and T_{ad} (c) (1200 RPM, $P_{intake} = 1$ bar, $T_{intake} = 300$ K, $\phi_{premixed} = 0.7$ SOI = -18 CAD BTDC).

As the main source of NO_x for these fuels is the thermal Zel'dovich mechanism, NO_x emission at the exhaust increases exponentially with the adiabatic flame temperatures as shown in Figure 49c. The increase of H₂ contents as in Downdraft induces an exponential evolutions of NO_x emissions. Notably,

for very similar adiabatic flame temperatures, the Downdraft compositions produce more NO_x than the Updraft compositions. Last, as highlighted by Rakopoulos et al. [155], the oxygen content has a significant effect on performances and emissions. When comparing Updraft and Fluidbed, they exhibit very similar H_2 content but different CO content for Updraft. Rakopoulos et al. [155] showed that NO emissions increase with the degree of oxygenation which could explain the higher NO_x levels for Updraft mixtures compared to Fluidbed.

4.4. Conclusion

In this chapter, the syngas/decane dual fuel engine was successfully operated with the three compositions of syngas. As a function of the syngas compositions, the injection parameters, i.e. injection timing and mass, were optimized and the effect on the engine performance and emissions was quantified. The following remarks following these dual-fuel experiments with syngas can be concluded:

- With a minimum of adaptation and no engine geometry optimization, indicated thermal efficiencies of over 38% were obtained with all syngas compositions, with less than 10% of the total energy supplied by the decane, surrogate of the Diesel fuel.
- Heat release rate profiles showed a strong influence of H_2 content in the syngas composition on combustion duration and phasing.
- The presence of CO_2 also plays an important role as diluent to reduce NO_x emissions in dual-fuel operating mode. While this can be interesting for complying with emission regulations, too much CO_2 on Syngas can lead to poor combustion efficiency. This requires more reactive fuel in the pilot injection to ensure stable engine operation, resulting in a potential increase of CO_2 and soot emissions.
- The development of the in-cylinder combustion can be well predicted based only on known fundamental properties of the syngas composition as the laminar flame speed. The emissions also can be predicted as a function of the different components in the syngas. This could be useful for live tuning of the engine's control strategy to as a function of the composition fluctuations of the gasifier product gas. Accurate predictions would require a better knowledge of secondary chemical and physical effects of varying syngas compositions such as chemical pathways and species rate of production.

In the next chapter, some analysis of the combustion development will be provided through some experiments, performed in another syngas/decane dual-fuel single cylinder engine with optical accesses. The objective is to provide a better understanding on different combustion steps (as diffusion phase, premixed or cool flame due to pre-ignition) and flame propagation itself, as it relates to the different compositions and their respective fundamental combustion properties.

5. Visualization of the syngas/diesel dual-fuel combustion in an optically-accessible engine

5.1. State of art of Chemiluminescence studies for syngas combustion in ICE

Chapter 3 was dedicated to determine some of the relevant fundamental combustion properties of syngas. In Chapter 4, we proceeded to evaluate the performance and emissions of the syngas/diesel dual-fuel engine, as related to these fundamental properties. To further enhance the understanding of these relations, this chapter investigates the combustion process inside the combustion chamber, in the case of syngas/diesel dual-fuel optical engine. For that purpose, several optical diagnostics can be applied as a function of the phenomena to be characterized (flow, soot formation, radicals' chemiluminescence, etc.). For example, to analyze the combustion ignition timing and spatial location, it is necessary to visualize the flame and the presence of radicals, like the OH and CH, which represent the different phases and temperatures of the combustion process [156–158]. Each radical can be detected by using different techniques: the emission of the radical due to natural excitation (chemiluminescence) or due to the laser excitation (Laser induced fluorescence). Both techniques have advantages and drawbacks: natural chemiluminescence technique is easier, requiring only intensified camera but is not quantitative and 3D integrated. On the other hand, planar laser induced fluorescence is 2D and could be quantitative but requires a dye laser. More recently, Infrared visualization has been developed by Mancaruso et al. [159]. This method is non-intrusive, and can also provide other important information for combustion analysis, as the qualitative information about fuel vapor distribution and ignition location during low and high temperature. Unfortunately, this visualization requires a specific high-speed IR camera.

The visible and near-visible electromagnetic spectrum emitted by the combustion has two separate contributing agents: soot incandescence and radical chemiluminescence. The difference between these two signals is that soot incandescence is a broadband signal, whose maximum peak power is a function of the temperature of the particle [157]. On the other hand, radical chemiluminescence is a narrow-band emission, which is a result of the photons emitted during the electronic transitions from a self-excited to a more stable molecule or species [158], overlaid on top of the broad-band emission from the CO_2^* continuum [160].

In the case of syngas/dual fuel combustion, if the quantities of the pilot-fuel are small, the Natural Luminescence signal shifts from soot incandescence to Chemiluminescence (CL) [161]. Indeed, as discussed in [162], and unlike hydrocarbon flames, in the case of syngas mixture, the most significant radical emission due to the presence of H_2 combustion comes from the hydroxyl, OH^* , chemiluminescence, which is in the UV domain and is distinguishable from chemiluminescence emissions from the CH^* . As indicated by Huang et al. [162], the addition of CO and/or CO_2 can have a significant influence on the level of OH^* intensity: as indicated in the Figure 50, the OH^* emission intensity is reduced.

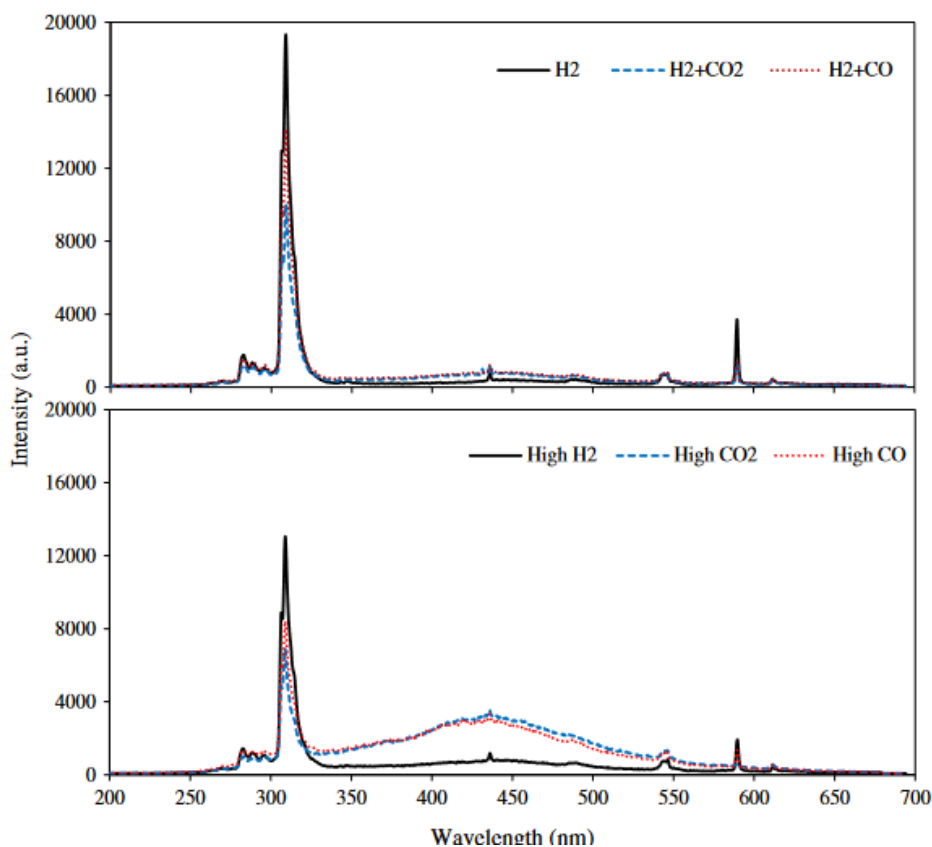


Figure 50: Example of chemiluminescence spectrum in syngas flame as a function of H_2 , CO and CO_2 concentration (reproduced from Huang et al. [162])

In the case of syngas combustion ignited by diesel type fuel pilot injection, low temperature pre-reactions can occur as a function of the injection strategy, as indicated in [142], mainly identified by formaldehyde (CH_2O), as done in HCCI combustion [163]. Therefore, in the case of dual-fuel combustion, one way to distinguish the low-temperature (low-T) and the high-temperature (high-T) ignition is to follow OH^* and CH_2O^* species. However, depending on the mixture, it could be difficult to distinguish the two phases of the combustion: one from the pilot fuel combustion itself and the other one from the premixed phase [142].

Several studies have focused on dual-fuel engines running on Natural Gas or methane ignited by Diesel pilot injection [164,165] and more recently with ammonia [166,167]. Up to today, these studies have not been performed for syngas; only a few studies have considered syngas, but in the context an optical Spark ignition engines [168,169]. Therefore, only for fully premixed flames, and mainly by performing experiments to study flame development without following specific radical or species

In the case of premixed combustion in SI engine, Solferini de Carvalho et al. [169] studied the effect of H_2 variation in a producer gas (H_2 -CO- CH_4 - CO_2 - N_2 mixture) by varying H_2 from 14%, which corresponds to the initial producer gas composition, up to 62%. The studies had been performed in an optically accessible SI engine with a CR of 9.68:1, coupled with an intensifier and a high-speed camera to follow flame development. One main conclusion was that the measured turbulent flame speed increases linearly with the increase of H_2 content, and the propagation flame speed with 24% H_2 matched very well with that obtained for pure CH_4 . Moreover, the observed flames remain more circular, i.e. less wrinkling, as the H_2 content increased. In fact, as underlined in [170], the ratio between the turbulent propagation velocity and the laminar flame velocity indicates that the increase in turbulence influences

the flame propagation acceleration less than the mass diffusivity and the reaction rate, when the enrichment is with H_2 . This results are in line with some other optical SI engine studies performed in the case of reformer gas (H_2 -CO-CO₂) compositions [170,171]. Martinez-Boggio et al. [172] also confirmed recently these results by analyzing natural luminescence images in the UV-visible spectrum along the entire cycle to follow the propagation of the flame front: for different composition of H_2 -CO-CO₂-N₂, as it can be seen in the image examples in Figure 51. Hydrogen promotes the flame propagation and reduces the engine instabilities. Despite that, the syngas having the highest values of turbulent flame speed/laminar flame speed ratio is not the one with the highest content of hydrogen but with higher methane and/or diluted gases content. In the case of syngas mixture, the turbulent flame speed/laminar flame speed ratio is around 20, because of the effect of the turbulence on slow laminar flame. For pure H_2 /CO cases, this number is around 10.

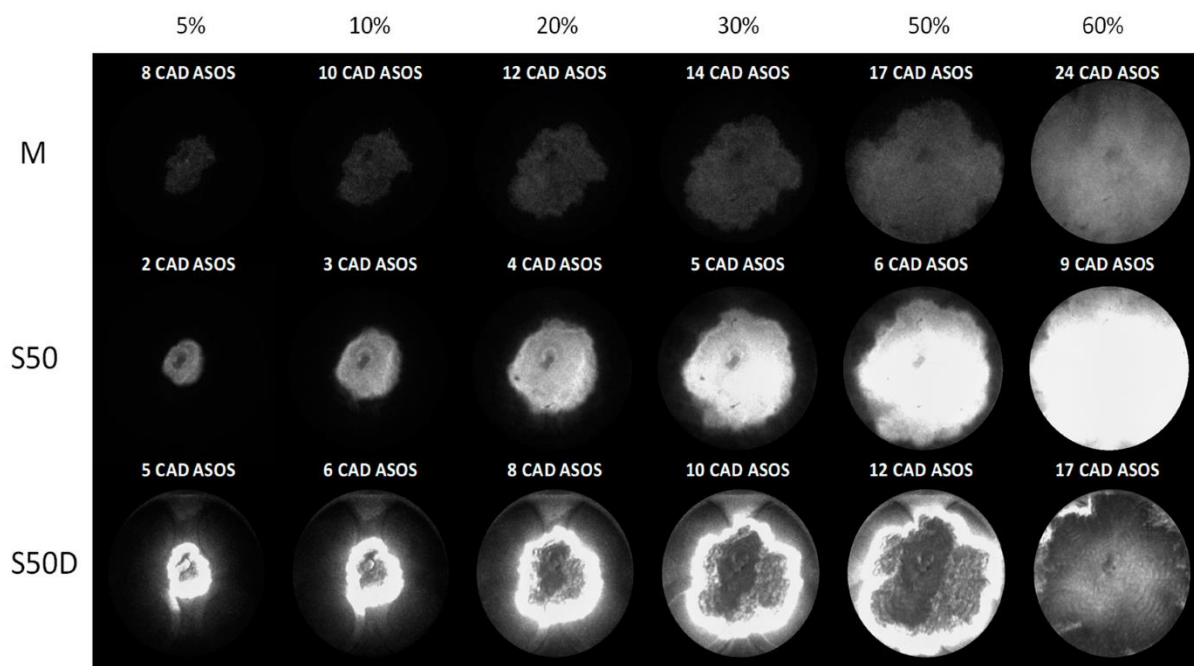


Figure 51: Example of natural luminosity of syngas stoichiometric flame for same flame area (5-10-20-30-50-60%) – M : methane, S50 : 50% H_2 -50%CO, S50D : 25% H_2 -25%CO-15%CO₂-35%N₂ (reprinted from Martinez-Boggio et al. [172]).

In the case of dual-fuel engine, Ahmad et al. [164] analyzed the effect of the equivalence ratio of the premixed methane/air, for different intake temperatures as a function of the Diesel injection share, on the ignition delay. With the low pilot share, 16.5% of the total energy, the bright spots related to soot incandescence, only appears towards the end of the combustion and limited to a few, close to the injector tip. The corresponding Ignition Delays (ID) only decreased marginally when the pilot fuel share goes from 16.5 to 27.5%.

Srna et al. [173] characterized the chemiluminescence of lean-premixed natural-gas combustion ignited by dodecane pilot in a rapid compression–expansion machine and identified the significant contributions to the natural luminosity due to soot, OH* and CH* with some broadband overlap due to the chemiluminescence of CO₂*, CHO* and CH₂O* species. One interesting conclusion was that CH* chemiluminescence can only be detected at ignition and during the pilot-fuel combustion period. Therefore, they performed complete studies by implementing also CH₂O PLIF [143]. They also revealed that as a function of the Diesel content, the analysis based on natural luminosity techniques could be affected by the soot incandescence itself, even for OH* UV chemiluminescence at 308 nm, some bright spots could be identified [164,173]. Their objective was to identify the discrepancy between the ID

estimated from the calculation HRR (based on the Pressure and Volume of the cylinder), and the ID based on the first appearance of the OH* chemiluminescence signal in dual-fuel engines. One of the conclusions was that both the increase of the methane/air equivalence ratio and the decrease of O₂ content of the charge, decreased the rate of luminosity emitted by the OH* and broadband (mostly from CHO*, CH₂O*, and CO₂*), which may pose a problem for detecting the correct ID. Cheng et al. [174] also conducted OH* and CH₂O* chemiluminescence alongside Natural Luminescence imaging in a dual-fuel methane/Diesel optical engine. They did not observe a large discrepancy between the low-temperature, associated with CH₂O* CL, and the high-temperature IDT's, associated with OH* CL. Nevertheless, the CH₂O* CL signal did rise faster. They concluded that the small injection duration was the reason for that behavior, leading to a decrease of the delay time between the two combustion phases.

In this chapter, the study of dual-fuel syngas/Diesel combustion based on chemiluminescence images is presented and analyzed for the three compositions from Bridgwater [58]. First OH* CL images and averaged signals are presented and discussed, followed by CH* and CH₂O* CL, through the excited-state formaldehyde in the low-temperature ignition, consumed during the second stage. The effect of CO₂ and CH₄ content is also analyzed, with the average OH* chemiluminescence signals, and the experimental Ignition Delay (ID) values are discussed by considering values obtained by performing OD kinetic simulations.

5.2. Experimental set-up

To study the combustion behavior of the dual-fuel syngas/Diesel engine, we have selected to evaluate the impact of the compositions, mainly of CO₂ and CH₄, while keeping the H₂/CO ratio of each of the three compositions. Meanwhile, we adjust N₂ fraction to balance-out the addition of the two components of interest, as previously presented in subsection 4.3.3 of the previous chapter. Based on the results on metal engine, the premixed equivalence ratio was set to 0.7 as the optimal one, with the minimal possible quantity of the high-reactivity fuel, decane. This limitation of decane quantity can eliminate, or at least minimize, the interference of soot-incandescence, identified by bright spots in [164].

The optical engine is based on one single cylinder PSA DW10 engine, similar to the metal one, but with a slightly lower CR, as shown in Table 27. Unlike for the previous experiments, the engine speed was maintained at 750 RPM (1500/2) but the engine only fires once every three cycles, to avoid mechanical stress on the transparent piston. A scheme of the global set-up is plotted in Figure 52.

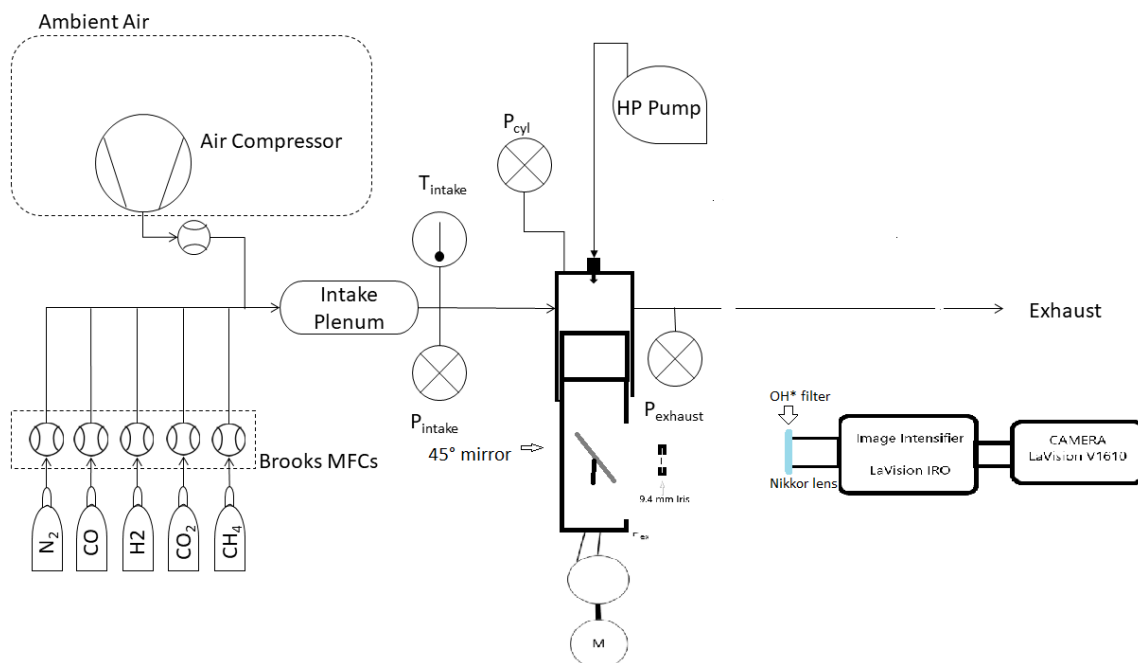


Figure 52: scheme of the optical engine set-up.

Air is compressed and dehumidified before being fed into the Brooks mass flow controller. The flowmeters set-up is very similar as the previous one (section 4.2.1), with same uncertainty level of $\pm 2\%$ of the intake charge equivalence ratio, $\phi_{premixed}$, as presented in Table 28. The only difference from the metal engine set-up is due to the different air controller.

Regarding the decane ($C_{10}H_{22}$) fuel, the same Bosch CRI 2.2 common-rail injector, previously characterized on an IAV type-K flow injector, was used on the same 200 bar rail pressure (see 4.2.3 Determination of the injected decane mass for further details). The injection timing (SOI) was kept constant at -15 CAD before Top Dead Center with a duration of 400 μs . Therefore, the injected mass is ± 0.32 mg, i.e. less than 2% of the total fuel energy and the $\phi_{decane/air}$ is ± 0.02 .

The intake temperature was maintained at 25°C. Temperatures were recorded at the intake and the exhaust of the engine, as well as the intake and exhaust pressures. The in-cylinder pressure traces were recorded by an AVL GH15D sensor and coded every 0.1 CAD. The post-processing method is similar to the previous one (see 4.2.2 Post-processing method), but from the 100 recorded Cycles, only 33 are fired cycles and 67 non-fired cycles. The apparent Heat-Release Ratio (HRR) will be plotted, instead of the combustion HRR, because the calculation of the thermal losses is less straightforward in an optical engine.

Table 27: Engine characteristics.

Displaced Volume	499 cm ³
Bore	85 mm
Stroke	88 mm
Optical Window Diameter	50 mm
Rod length	145 mm
Compression Ratio	15.6:1*
Piston Bowl Type	“Mexican hat”
Firing TDC position	0 CAD
Intake Valve Opening	351 CAD ATDC
Intake Valve Closure	157 CAD BTDC
Exhaust Valve Opening	140 CAD ATDC
Exhaust Valve Closure	366 CAD ATDC
Coolant Temperature	85 °C
Oil Temperature	80 °C

* slightly lower CR than the standard engine

Table 28: Mass Flow Controllers.

Gas Type	Controller	Full Scale	Uncertainty
Air	Brooks 5853S	500 NL/min	±0.5%
N ₂	Brooks 5851S	100 NL/min	±0.9%
CO	Brooks 5851S	100 NL/min	±0.9%
H ₂	SLA5850	50 NL/min	±1,0 %
CO ₂	SLA5850	37 NL/min	±1.0%
CH ₄	SLA5850	5 NL/min	±1.0%

5.2.1. Optical imaging set-up

Chemiluminescence images were obtained by using Phantom v1610 monochrome high-speed camera with a Nikkor 105mm lens, coupled with a high-speed intensifier (LaVision High-Speed IRO). The camera with IRO and the lens is aligned with the 45° mirror, as indicated in the scheme (Figure 52). The combustion is observed through the extended piston and the fused-silica optical window of piston, with bowl shape as the metal one (Figure 53).



Figure 53: Optical piston (bowl-type).

Different filters can be used as a function of species to observe. For the OH* chemiluminescence, two filters, Newport FSQ-UG11 BP and 20CGA-305 LP have been combined to maximize the transmittance at 308 nm and limit the other wavelengths as indicated in Figure 54.

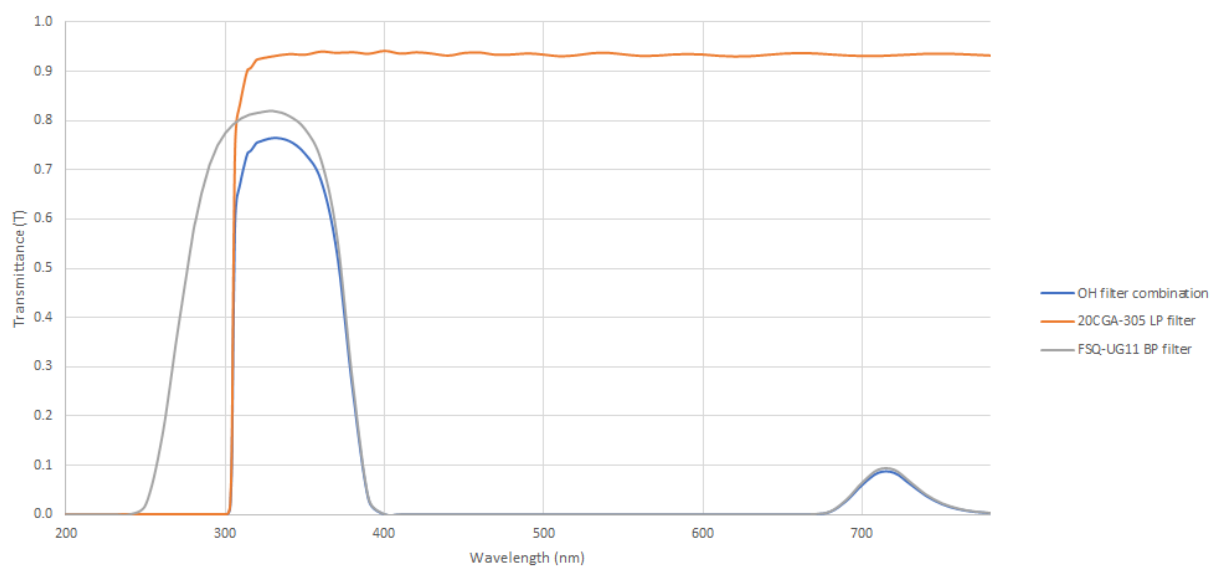


Figure 54: Filter combination used for OH* chemiluminescence imaging.

The final set-up is presented in Figure 55, with the distances between the iris, lenses and the rest of the imaging devices, are highlighted.

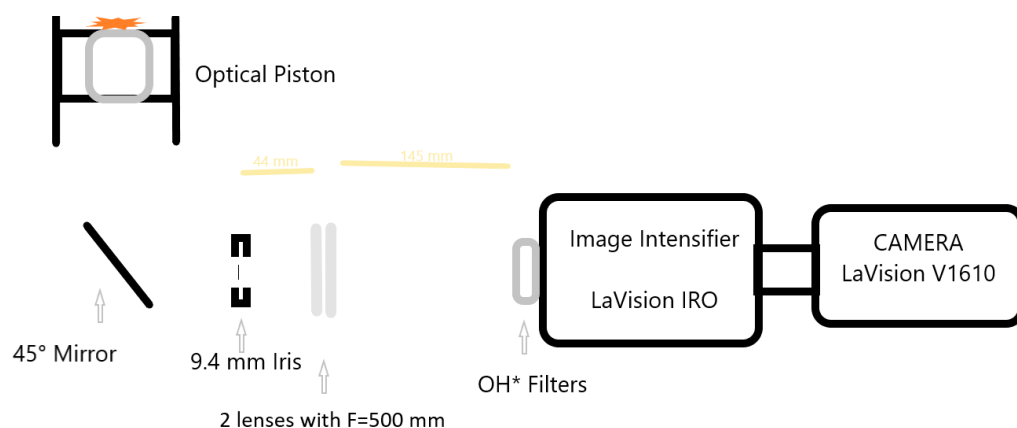


Figure 55: Optical imaging set-up for OH^* chemiluminescence.

For the OH^* chemiluminescence, the intensifier was set to a gain of 61% with a gate of 39.200 ms combined with a delay of 5 ns. The camera framerate is 16 000 fps with an exposure time of 45 μs , to record three images every CAD. During a cycle, the recording begins at -10 CAD BTDC, providing 150 images with a resolution of 768x768 pixels², with a magnification ratio of 11.5 pixels/mm.

Two other species were selected, CH_2O^* and CH^* [174,175] and recorded simultaneously using a LaVision Image Doubler. Figure 56, presents the transmittance of the filters: a BP filter from Chroma Technology centered at 431 nm and 28 nm bandwidth for CH^* chemiluminescence, and a combination of three filters (ZUL0325 LP, ZHS0385 SP and ZUS0350 SP, from Asahi Spectra) for formaldehyde (CH_2O^*) chemiluminescence. It has to be noted that the OH^* filter set-up does not avoid the CH_2O^* signals but, since the CH_2O^* signals are order of magnitude smaller than the OH^* signals, we assume that there is no strong effect on the results. The intensifier gain was set to 69%, with the same previous values for the gate and the delay. The camera lens was changed to a custom one, where the focal length can be freely adjusted, and the resolution obtained was 768x576 pixels² (7 pixels/mm), with the same exposure setting.

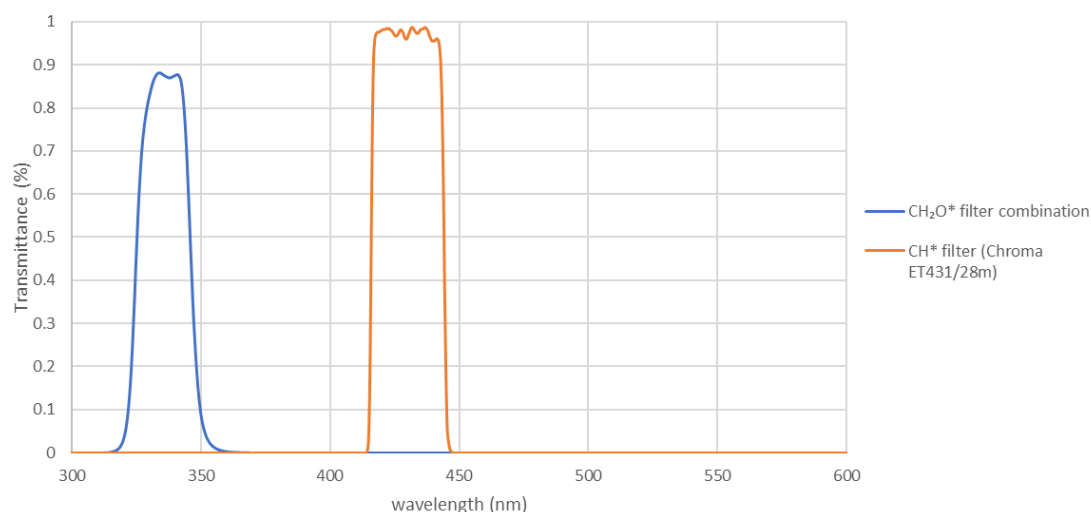


Figure 56: Filters used for the CH^* and CH_2O^* chemiluminescence

5.2.2. Imaging post-processing

The images have been processed by an in-house developed routine in MATLAB and schematized in Figure 57. This processing was used for OH*, CH* and CH₂O*:

- It starts with the application of a circular mask corresponding to the piston window to remove signals that are out of its bound. Indeed, to discriminate the light reflected by the piston and cylinder walls, a geometrical circular mask with the diameter of the effective piston window is applied to all the images, leaving only the light that passes directly through the window to be processed. Hence the pixels outside of the window's boundary are multiplied by 0 while the one inside are multiplied by 1.
- The second step consists in removing the background, i.e. the noise, by subtracting the mean images of three consecutive frames before the combustion starts. Then for each CAD, an average image is calculated over 40 cycles. Finally, the pixels intensity of this averaged imaged is computed.

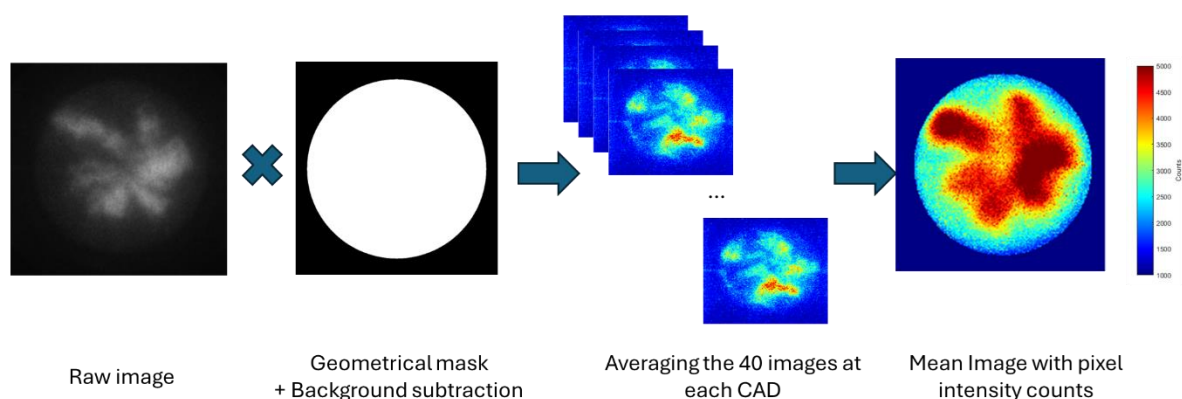


Figure 57: Schematic view of chemiluminescence image post-processing.

5.3. Results and discussion

5.3.1. The case of the decane pilot injection by itself

First, the average OH* images were recorded in the case of engine running with decane content only as presented in Figure 58 without considering an important effect of soot emission. As it can be seen in Figure 58, from -8.3 CAD BTDC until 10.6 CAD ATDC. The combustion is ignited along the six jets of the injector, not identically as a function of the injector holes physical/real geometries. The decane charge is so tiny that only six small flames can be identified without a global flame enrollment as for a conventional Diesel ignition. The maximum area occupied by natural chemiluminescence is strongly dependent on where ignition occurs, which is here along the decane spray. The total combustion requires less than 14 CAD to be finished. From these images, due to the small decane quantity, the OH* chemiluminescence spatially averaged is compared to the HRR calculated from in-cylinder pressure (see 4.2.2 Post-processing method), without considering an important effect of soot emission. As it can

be seen in Figure 59, a good qualitative agreement between the OH* signal and the apparent HRR data is observed, in the case of engine running with the pilot injection only. Due to the small HRR, the estimate of HRR from the pressure signal induces a lot of noise, very low signal-to-noise ratio. The IDT estimate from OH* chemiluminescence is around 7 CAD, which is in agreement with HRR data. As expected and well known, the OH* chemiluminescence continues after the HRR. In fact, OH* luminous intensity starts when the CO starts oxidizing into CO₂ with a longer time life as indicated in [176]. Indeed, the maximum intensity of OH* chemiluminescence appears very close to maximum oxidation rate of the CO to CO₂, so the time of maximum pressure rise rate.

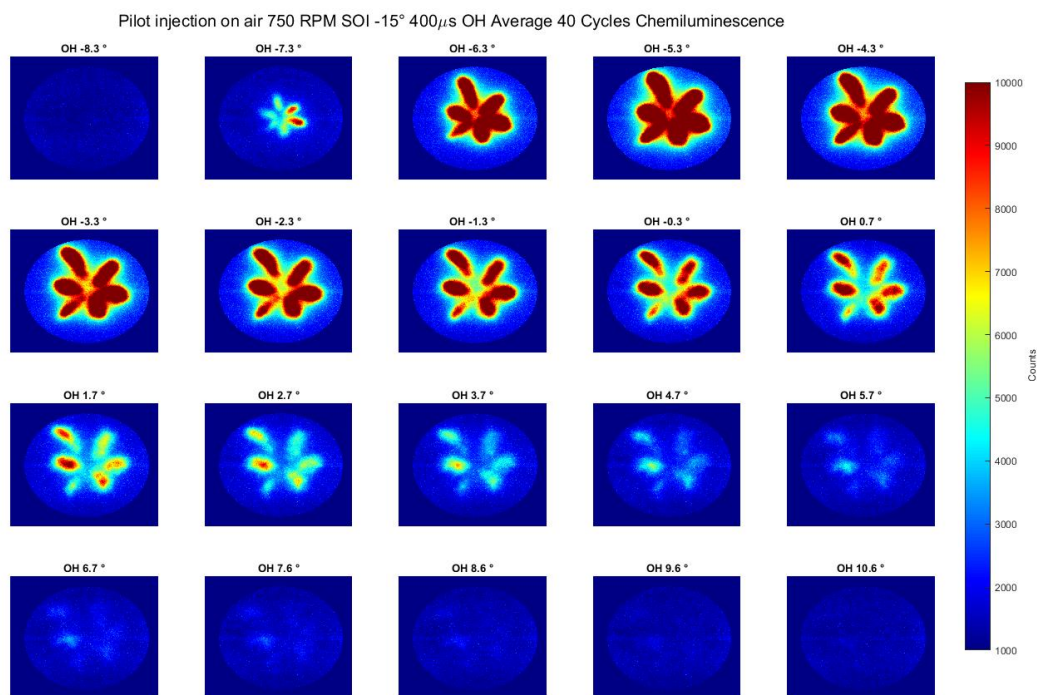


Figure 58: OH* chemiluminescence images averaged on 40 cycles and the bar plot of the corresponding average signal for the pilot decane injection on air (without syngas, $N=750$ RPM).

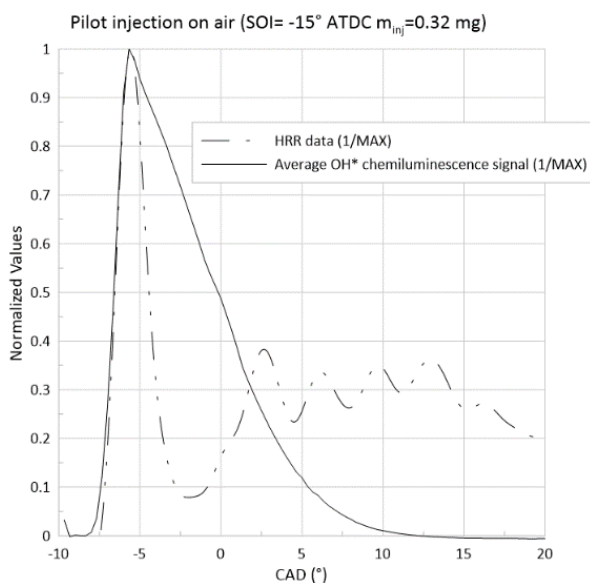


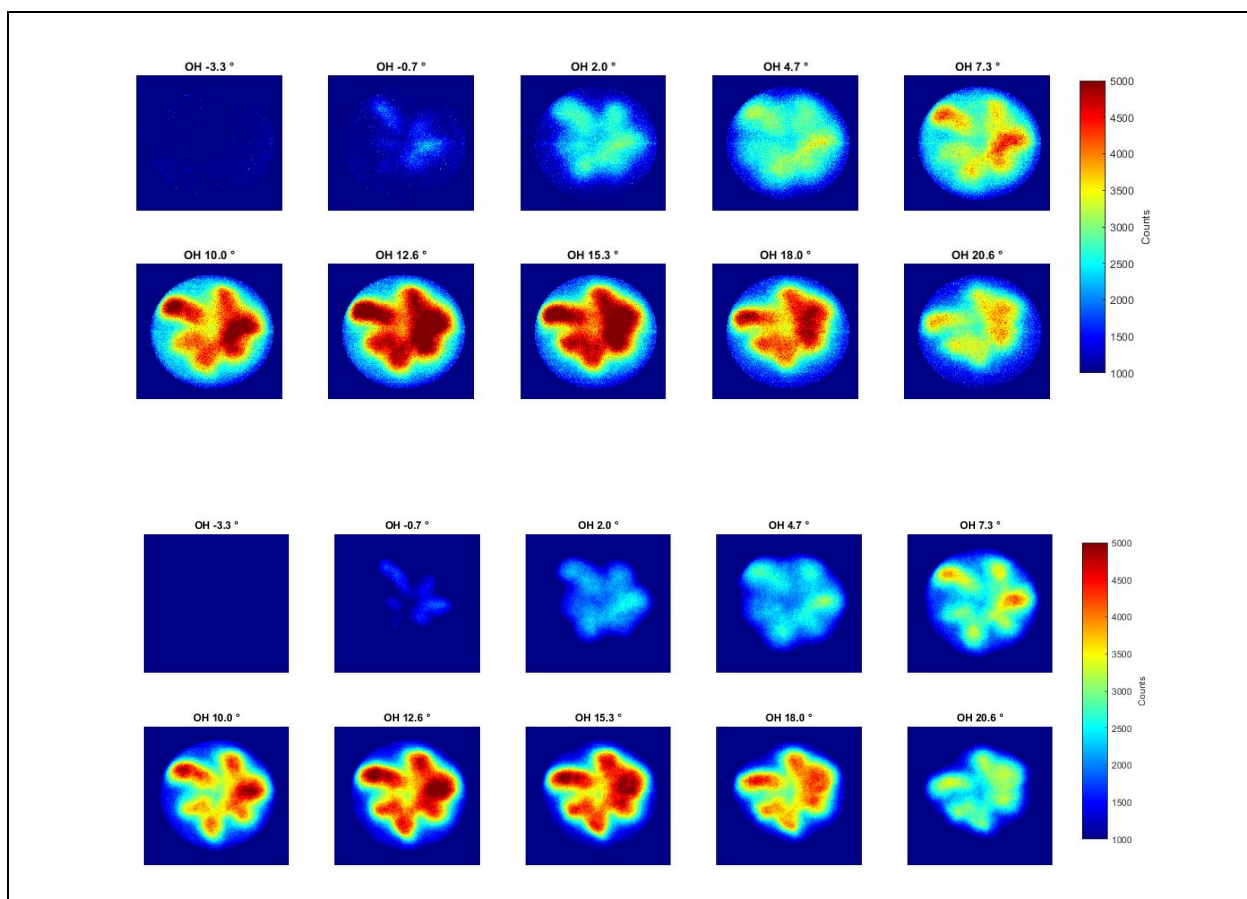
Figure 59: OH* chemiluminescence images averaged on 40 cycles and the bar plot of the corresponding average signal for the pilot decane injection on air (without syngas, $N=750$ RPM).

5.3.2. Comparison of the different syngas compositions

The OH* chemiluminescence images are presented in the case of the combustion for the three syngas compositions in Figure 60. The characteristics of these syngas compositions are reminded in Table 29. Very similar combustion development and OH* intensity is obtained in the case of Downdraft and Updraft syngas mixture: the beginning of the ignition remains along the decane spray and even if the flame propagation occurs more inside the entire bowl, the jet shape continues to be identified. In comparison to decane combustion only, the OH* emissions started 5 CAD later in the presence of syngas for Downdraft and Updraft; and 6 CAD later for the Fluidbed. In the case of Fluidbed syngas composition, the low level of OH* chemiluminescence, which required the change of intensity scale, is mainly due to two main differences: the quantity of H₂ in the fuel (H₂+CH₄) and the dilution effect due to the CO₂+N₂.

Table 29: Syngas compositions.

	H ₂	CO	CO ₂	CH ₄	N ₂	Total dilution	H ₂ /(H ₂ +CH ₄)
	(%Vol)	(%Vol)	(%Vol)	(%Vol)	(%Vol)	(%)	(%)
Updraft	11	24	9	3	53	62	0.785
Downdraft	17	21	13	1	48	61	0.944
Fluidbed	9	14	20	7	50	70	0.5625



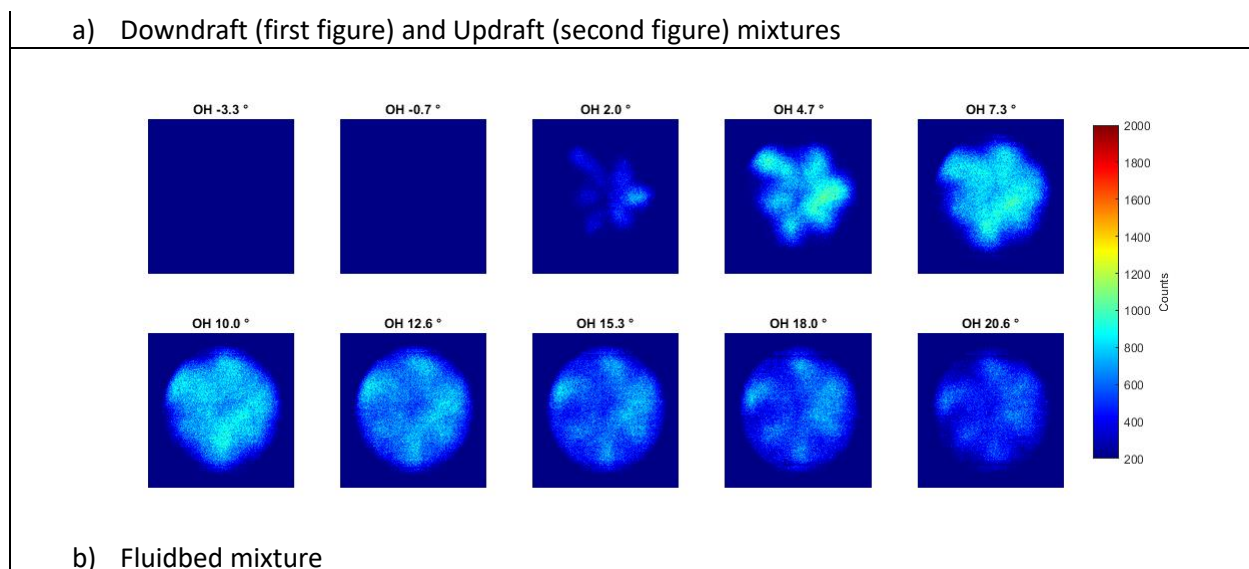


Figure 60: OH^* chemiluminescence images for the original compositions in a dual-fuel engine (a- Downdraft and Updraft and b- Fluidbed ; $\phi_{\text{premixed}} = 0.7$, $N = 750$ RPM).

Figure 61 presents the averaged OH^* chemiluminescence signal along the combustion development for the three syngas compositions and for the decane alone. The IDT is strongly increased with the syngas content and the overall intensity is decreased. In the case of Fluidbed composition, OH^* chemiluminescence intensity signal is divided by a factor of three mainly due to the dilution effect and the lower content of H_2 . On the other hand, it seems that the maximum OH^* emission occurs earlier than for the other two compositions, which is not expected due to the lower laminar flame propagation for this mixture.

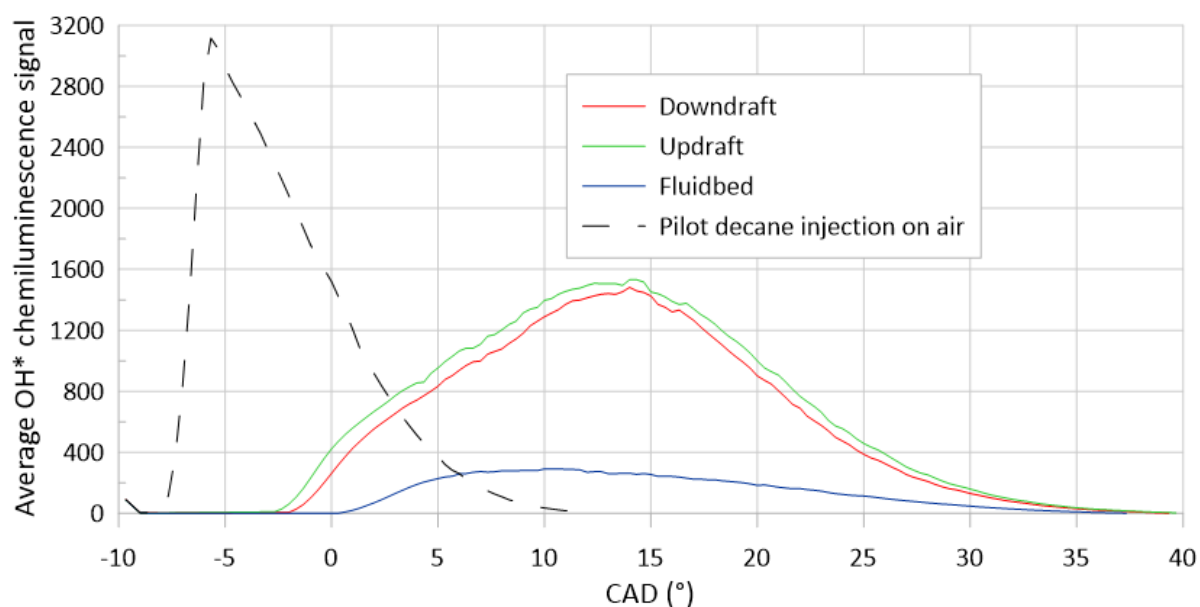
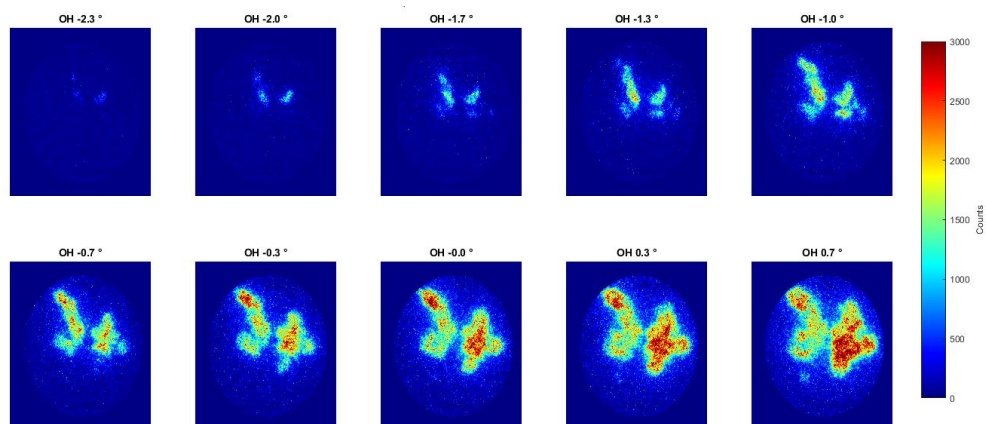


Figure 61: Average OH^* chemiluminescence signal of the compositions.

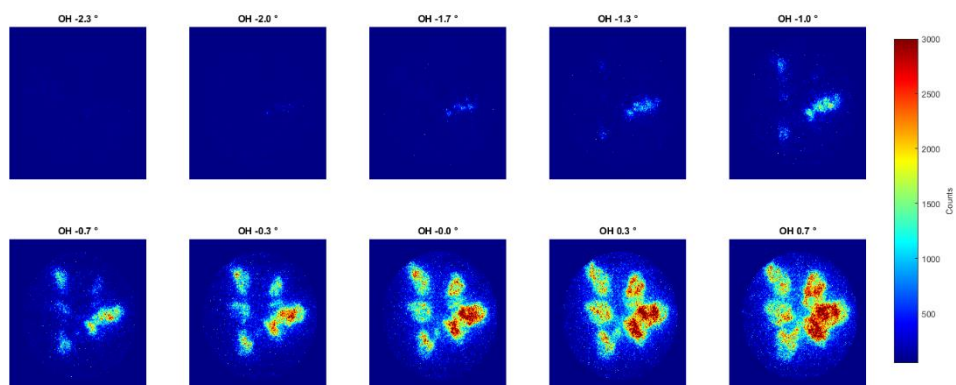
In Figure 62, instantaneous images of OH^* chemiluminescence from the same cycle are plotted to identify better the ignition sites, for all compositions. As previously for the decane only, the ignition sites are not at the same time along the six decane jets but started in one site only before being carried

in the other decane rich zones of the spray. The Fluidbed OH* CL signal is very small and only appears close to the Top-Dead-Center. It should be noted that Figure 62 only represents a single cycle, and the cycle-to-cycle variation is considerable, so we cannot reach a conclusion related to the combustion timing.

a) Downdraft



b) Updraft



c) Fluidbed

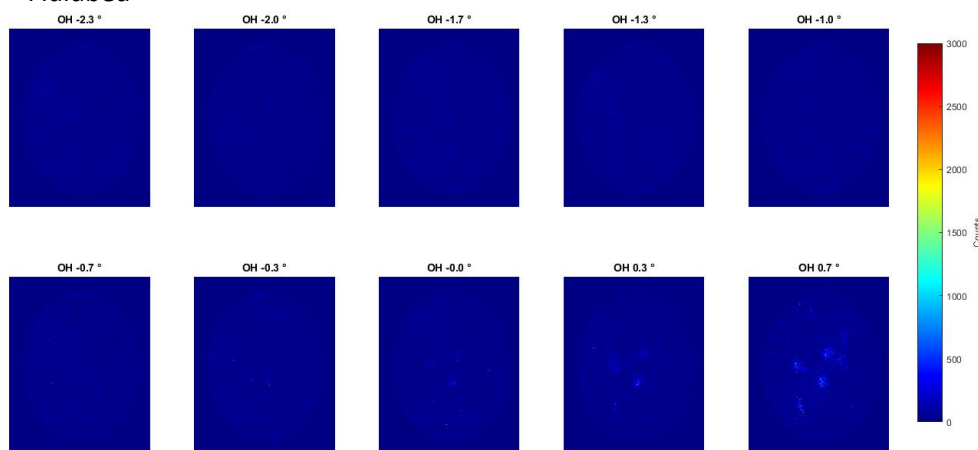


Figure 62: Instantaneous OH* Image along same combustion cycle for the 3 original compositions ($\phi_{premixed} = 0.7$, $N = 750$ RPM).

The spatially averaged OH^* intensity is compared to the average apparent HRR in Figure 63 : as expected, the Fluidbed composition presents much weaker OH^* chemiluminescence signals, because of its higher CO_2 concentration. Moreover, due to the low OH^* signal intensity, relative to the maximum one, it is not possible to determine precisely the onset of the combustion, as highlighted in the zoomed image. Besides, it seems that location of the OH^* peak does not match with the CAD of the apparent HRR peak. Similar observations were made by Srna et al. [173] and Schlatter et al. [177], when they compared the ID detected on the conventional HRR calculations or on the Schlieren images, with the IDT detected with the OH^* chemiluminescence onset, for NG/Diesel dual-fuel experiments in Rapid Compression-Expansion Machines.

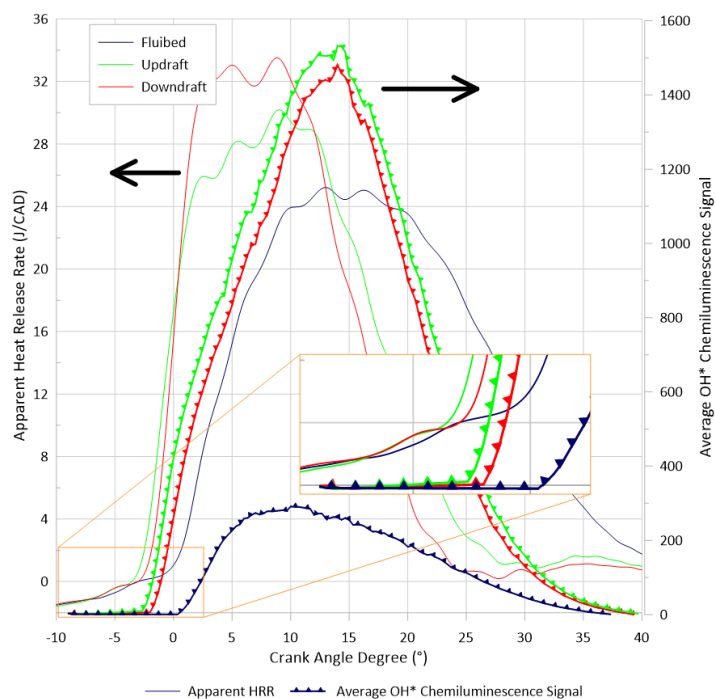


Figure 63: Comparison of the apparent Heat Release Ratio (HRR) and the OH^* chemiluminescence signals for the 3 original compositions ($\phi_{\text{premixed}} = 0.7$, $N = 750$ RPM).

To see if other chemiluminescent radicals align better with the apparent HRR of a syngas/Diesel dual-fuel engine, similar analysis is done for CH^* and CH_2O^* . As it can be seen from Figure 64, CH^* and CH_2O^* average signal intensities represent better the HRR, for the three compositions, in terms of combustion ignition and maximum of the peaks. This is similar to Cheng et al. [174] conclusion from a study in NG/Diesel dual-fuel engine, where they found the CH_2O^* chemiluminescence appears before the OH^* ones and also rises faster. The lack of a clear two-phase ignition separation, on both the HRR's and the CL's average signals, can be explained by the very small pilot-fuel injection, which decreases the induction time between these two phases [174]. It has also to be noted the CH^* CL appears just after the CH_2O^* signal but rises faster. For the Fluidbed composition, one can see the OH^* and CH_2O^* peaks are slightly before the HRR peak, but the CH^* intensity is better phased with the apparent HRR.

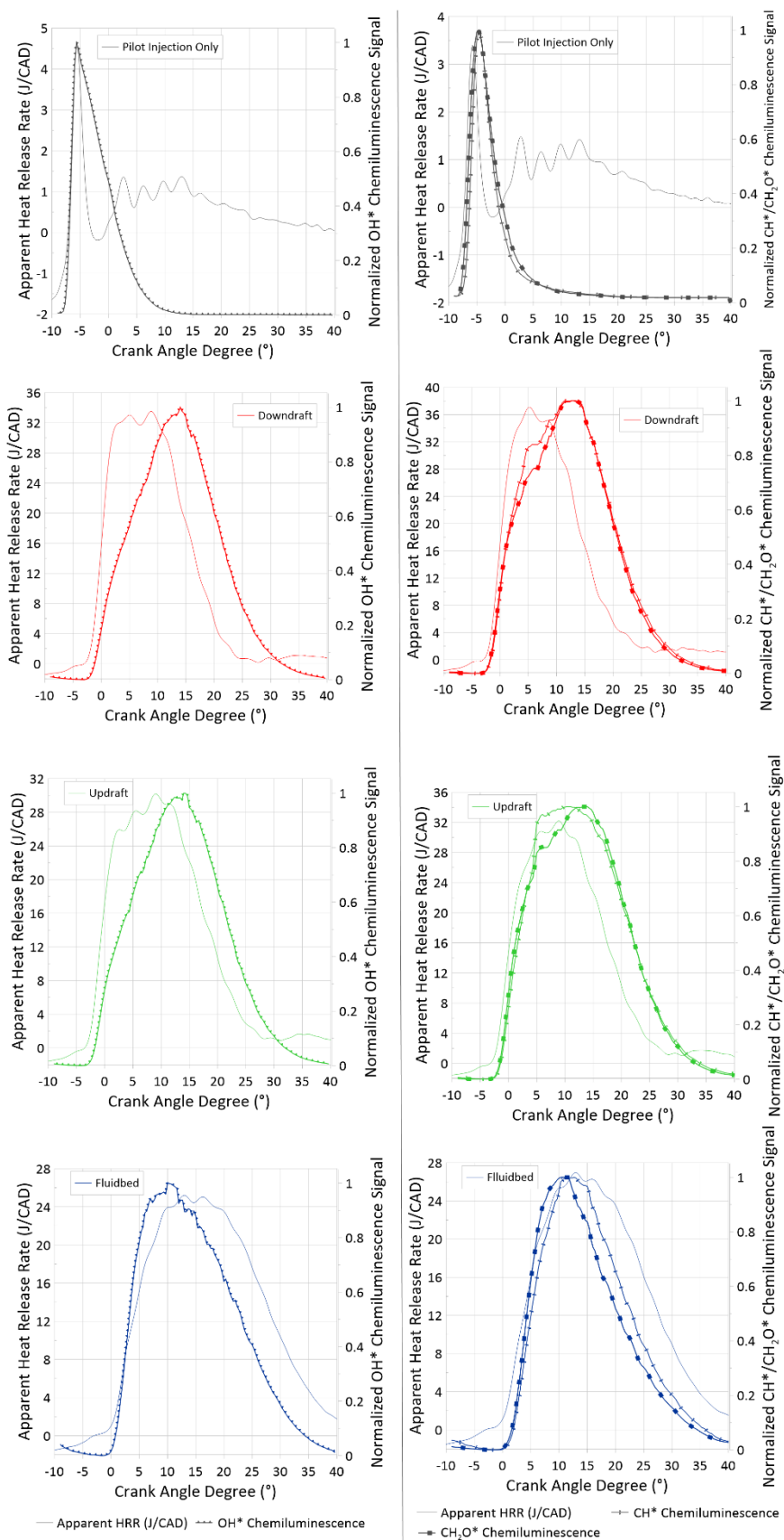


Figure 64: Comparison of the average apparent HRR with the normalized chemiluminescence of OH* (left) and CH*/CH₂O* (right) ($\phi_{premixed} = 0.7$, $N = 750$ RPM).

5.3.3. Effect of the CO₂ and CH₄ content on the syngas composition.

The syngas compositions can vary a lot in terms of CH₄ content, which is reactive molecule, and CO₂ content, which acts as diluent. In the case of dual-fuel combustion, the different content of these fuels can induce not only a difference in the flame development speed, but also in the ID itself. Indeed, for example, Rajasegar et al. [178] identified the difference on the n-heptane ignition delay as a function of the presence of CH₄ or H₂, both experimentally and with kinetics simulation. They concluded that there is a significant inhibition effect of Natural Gas on the autoignition chemistry of n-heptane pilot-fuel as characterized by increasing ignition delays with also a noticeable shift in the first-stage as a function of the premixed equivalence ratio also. In fact, it is due to the combination of reduced oxygen concentration induced by the premixed combustion and to the change of the mixture thermal capacity and last, because of CH₄ acting as a radical sink. In the case of CO₂, the effect of different amount will be mainly on the dilution rate as it can be seen in Table 30 . Moreover, the specific heat is increased by 30%, inducing a decrease of the adiabatic theoretical flame temperature (T_{ad} , in Table 30) and in the laminar flame speed itself. Therefore, as shown in Table 6 of Chapter 2, from literature studies the effect of dilution due to the presence of CO₂ is more important than the dilution effect by N₂. On the other hand, the difference in the CH₄ amount affects the overall reactivity of the syngas. Therefore, the variation of CO₂ and CH₄ amount in the gas composition affects both the adiabatic flame temperature, due to difference reactivity, and dilution level and, as expected, the laminar flame speed itself.

Table 30: Variations on the original Syngas compositions.

Variation	H ₂ (%vol)	CO (%vol)	CO ₂ (%vol)	CH ₄ (%vol)	N ₂ (%vol)	H ₂ /(H ₂ +CH ₄) (% vol.)	Diluent CO ₂ +N ₂ (%)	CO ₂ /(CO ₂ +N ₂) (%)	Tad. (K)	S _u ^o (cm/s)
FB – 0 _{CO₂-CH₄}	9	14	0	0	77	100.0	77.0	0.0	1868	32.3
FB – 10 _{CO₂}			10	0	67	100.0	77.0	13.0	1834	24.3
FB – 20 _{CO₂}			20	0	57	100.0	77.0	26.0	1802	14.9
FB – 2.5 _{CH₄}			0	2.5	74.5	78.3	74.5	0.0	1955	33.0
FB – 5 _{CH₄}			0	5	72	64.3	72.0	0.0	2016	35.0
FB - Reference			20	7	50	56.3	70.0	28.6	2004	26.4
UD – 0 _{CO₂-CH₄}	11	24	0	0	65	100.0	65.0	0.0	2092	61.5
UD – 10 _{CO₂}			10	0	55	100.0	65.0	15.4	2059	51.1
UD – 20 _{CO₂}			20	0	45	100.0	65.0	30.8	2028	41.9
UD – 2.5 _{CH₄}			0	2.5	62.5	81.5	62.5	0.0	2131	59.5
UD – 5 _{CH₄}			0	5	60	68.8	60.0	0.0	2160	58.2
UD - Reference			9	3	53	78.6	62.0	14.5	2112	51.1
DD – 0 _{CO₂-CH₄}	17	21	0	0	62	100.0	62.0	0.0	2120	83.0
DD – 10 _{CO₂}			10	0	52	100.0	62.0	16.1	2088	69.1
DD – 20 _{CO₂}			20	0	42	100.0	62.0	32.3	2057	57.9
DD – 2.5 _{CH₄}			0	2.5	59.5	87.2	59.5	0.0	2154	75.4
DD – 5 _{CH₄}			0	5	57	77.3	57.0	0.0	2178	71.2
DD – Reference			13	1	48	94.4	61.0	21.3	2095	62.7

Kinetics Simulation of Ignition Delay

To provide a better understanding of the effect of CO₂ and CH₄ amount on syngas combustion, kinetics simulations of OD closed homogenous reactor using the Ansys CHEMKIN-Pro software have been performed with the Madison kinetic mechanism [119], as it is the single one that can simulate syngas gases and decane together. The kinetics simulation results are not presented for the original compositions, since the effect of the very different CH₄ concentration (1, 3 and 7% for Downdraft, Updraft and Fluidbed, respectively) will bias the result. The initial temperature and pressure in the simulation were kept the same for all compositions, of 800 K and 30 bar, respectively, to mimic engine conditions at SOI. The setting values are given in Table 31.

Table 31: Properties of the OD homogenous reactor used.

Settings of the OD closed homogenous reactor	
Problem Type	Constrain Volume and Solve Energy Equation
End time of the simulation (s)	2.0
Initial temperature (K)	800
Initial pressure (bar)	30
Volume (cm ³)	5.0
Heat Loss	0.0
Equivalence Ratio of the selected premixed Syngas/air mixture	0.7
Added Species (fully mixed)	C ₁₀ H ₂₂ (decane)
Ignition Delay: Species Maximum Fraction	OH

Due to the direct injection of decane in the combustion chamber, the local concentration of decane in the syngas/air mixture can strongly vary as a function of the spray penetration and vaporization. Therefore, to reproduce this local effect, the initial gas composition for each simulation is set to represent local experimental conditions, even if the ratio of syngas to air is held constant, the quantities of decane are added to analyze different hypothetical local mixtures. A range of initial compositions of decane, represented by 'decane/air equivalence ratio', varying from 0.5 to 4 were therefore set.

Since decane autoignition is a two-stage process [179], as a function of the mixtures conditions, these two-stages can occur with syngas combustion, as it can be seen in Figure 66 for Fluidbed, where the shorter IDT is the low-temperature one and the longer the high-temperature one. Therefore, in Figure 66, where the ID times are presented in CAD (1 ms equals 4.5 CAD at 750 rpm), 2 IDTs are plotted (when they exist) and indicated as low or high temperature. In the presence of H₂, low temperature IDTs are predicted even if the minimum ignition delay stays relatively flat over a wide range of pilot-fuel equivalence ratios. This is like what can be observed in Figure 65: from high concentration of decane, the first and the second ignition delay are no more affected by the concentration of decane, which means that there is a competition with the premixed flame chemistry. The difference of ID between the different syngas composition is evident for Fluidbed certainly due to the dilution increase. As Rajasegar et al. [180] pointed-out, up to a decane equivalence ratio of 1.4, the main ID increases more strongly with H₂ than with CH₄. As in Fluidbed, there is less H₂ but more CH₄, these effects could be counterbalanced. The CO content of the different compositions can also be responsible for the different IDT. Indeed as pointed out by Gersen et al. [181] the addition of CO can increase the ignition delay time from a factor 2 from pure H₂ to a 50/50 H₂/CO blend as reported in [182,183]. However, this increase was not observed by Gersen et al. [181], as they measured similar ignition delay times for both pure hydrogen and 70/30 H₂/CO mixtures for pressure between 20 and 70 bar. Unlike Gersen et al. [181], Mittal et al. [182,183] also showed that increasing CO has an inhibiting effect on the H₂ chemistry. Gersen et al. [181] attributed this difference to the different specifications of the various rapid compression machines used in the literature. Thi et al. [184] showed with shock tube measurements at 20 bars similar results as Gersen et al. [181] : for a fixed equivalence ratio (0.3 and 1.0) similar ignition delays for undiluted syngas having different H₂/CO ratio, namely 2.4 and 0.5. A syngas with H₂/CO ratio of 1 and containing 30% CO₂ also showed similar ID as the undiluted mixtures. This is also confirmed by the work of Matthieu et al. [185] where CO₂ addition "did not show any appreciable effect on the ignition delay time" for lean mixtures ($\phi=0.5$) at 12.5 and 32 atm. In the study of Thi et al. [184], only the nitrogen dilution at 58% on the syngas with H₂/CO \approx 0.4 (so close to the 0.5 H₂/CO syngas) seems to have a retardant effect on the ID.

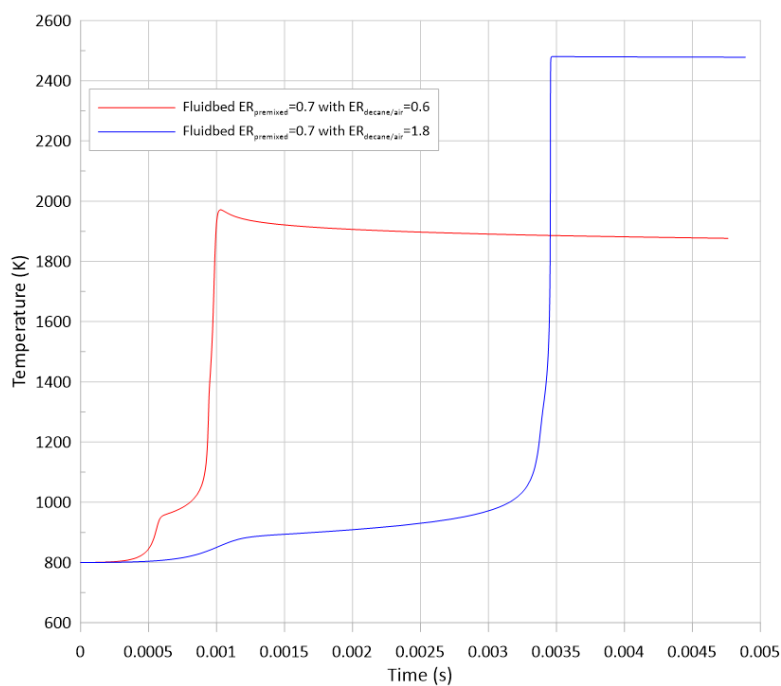


Figure 65: Temperature profiles of two $\phi_{decane/air}$, 0.6 and 1.8, mixed with a premixed charge of Fluidbed/air at $\phi_{premixed}=0.7$.

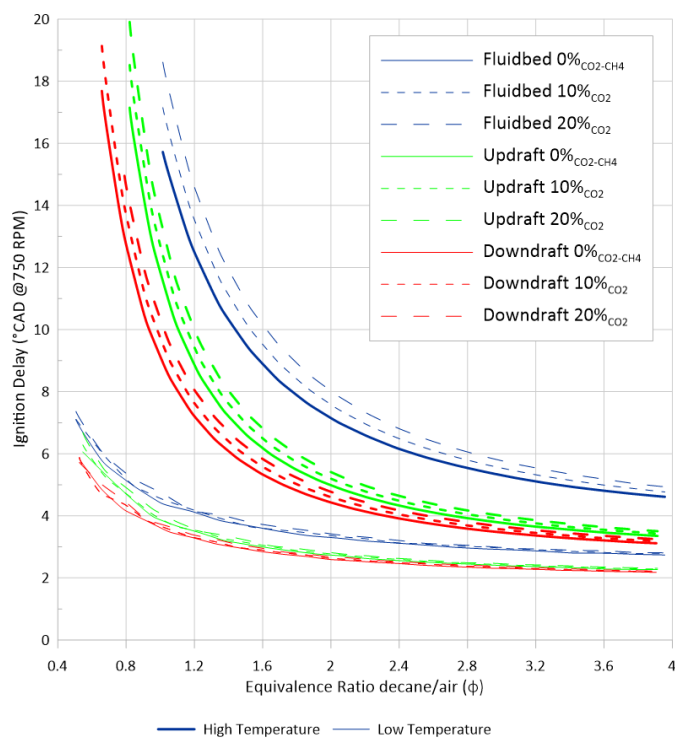


Figure 66: The effect of CO_2 amount (from 0 to 20%) on the Ignition Delays of Syngas/Decane mixture for the 3 syngas compositions ($T_{in}= 800K$, $P_{in}= 30$ bar, $\phi_{syngas/air} = 0.7$ using the Madison Mechanism).

From these ID simulations, it can be clearly concluded that the ID was ranked as follow Downdraft<Updraft<<Fluidbed, and that the CO_2 addition increases the ID.

In the case of CH_4 addition, which corresponds to a decrease of N_2 content in the fuel composition, the IDT strongly decreases, as it can be seen in Figure 67. Matthieu et al [185] showed that adding CH_4 to 50/50 H_2/CO undiluted syngas leads to an increase of the ignition delay. In the present study, the opposite is observed as we are replacing the diluent (N_2) by a reactive component (CH_4), thus leading to a decrease of the IDT.

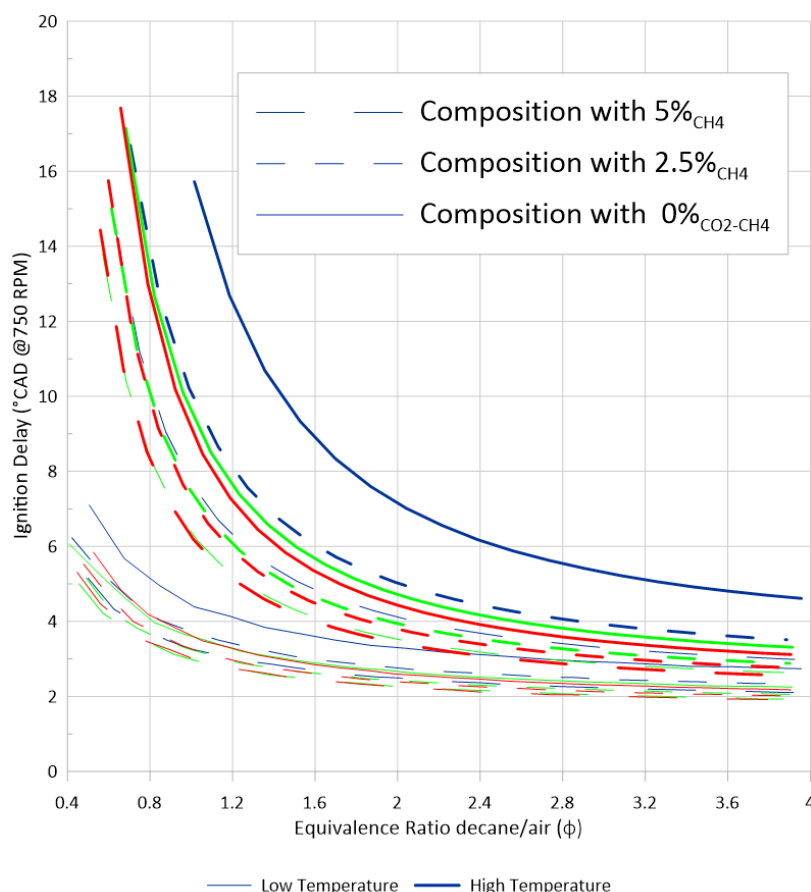


Figure 67: Effect of CH_4 variation in the reactive species in syngas on the IDT.

The CO_2 concentration effect

As an example, the effect of CO_2 is presented in Figure 68 where OH^* averaged images are plotted in the case of Updraft syngas composition only, as similar observation can be made for the two other compositions. As function of the CO_2 increase in the total dilution mixture ($\text{CO}_2 + \text{N}_2$), the beginning of the combustion is strongly shifted, and the overall intensity level strongly decreases. In the case of 20% of CO_2 , the emission becomes very low and for most of the time not observable without changing the scaling. This is highlighted by plotting the average OH^* chemiluminescence signal, as in Figure 69, the Downdraft syngas composition which presents the highest OH^* intensity is strongly affected by CO_2 content: for 10% CO_2 similar intensity level is reached than for the Updraft case without CO_2 , but with a slightly longer ignition delay. Therefore, the difference on IDT for these two syngas is mainly due to the higher CO_2 content of the Downdraft composition.

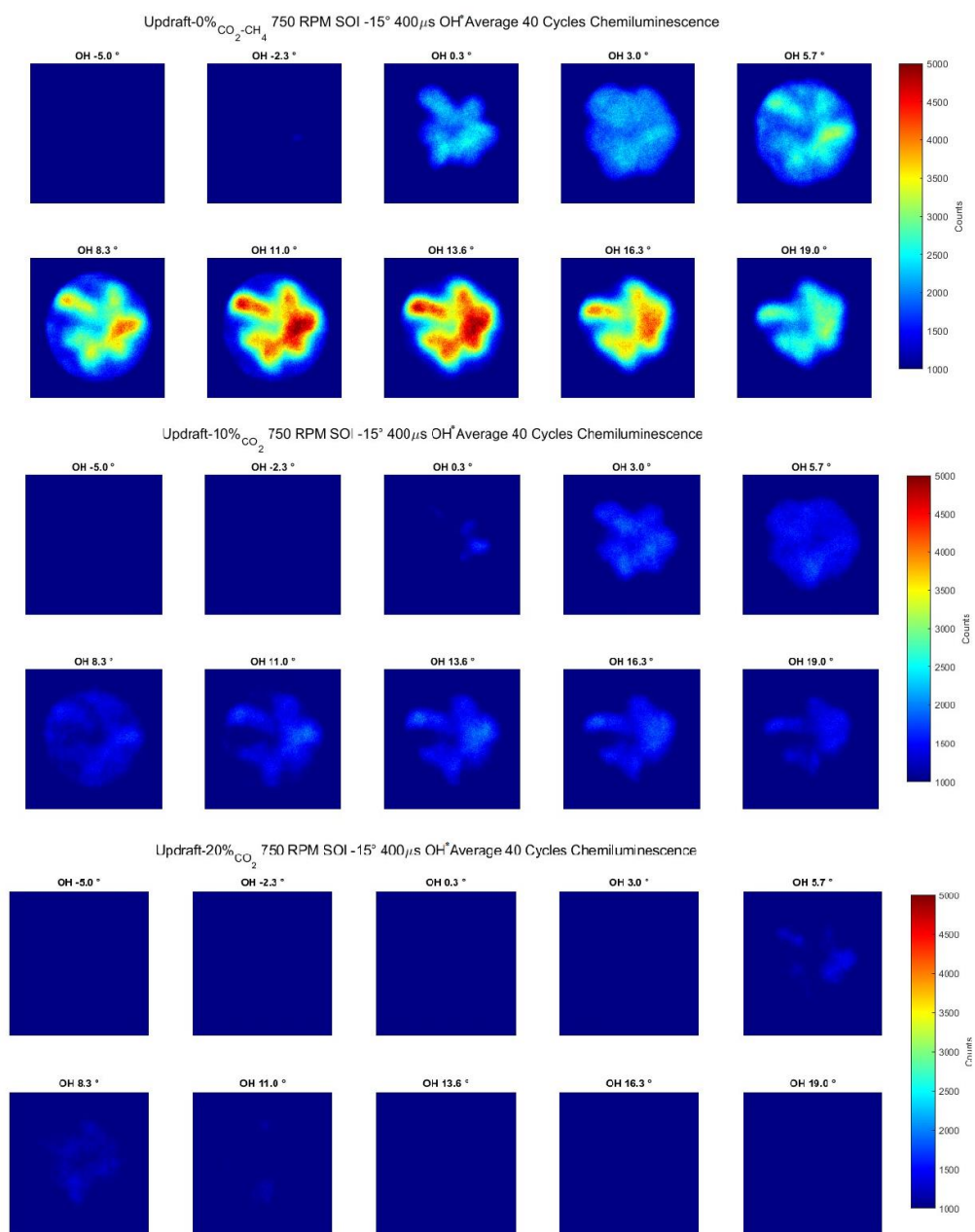


Figure 68: Effect of the CO₂ share on OH* chemiluminescence averaged images for Updraft-based compositions, ignited by the pilot injection ($\phi_{\text{syngas/air}} = 0.7$, $N = 750$ RPM).

Figure 68 presents the effect of CO₂ on the Updraft-based composition: much lower overall intensity is obtained when the N₂ portion replaced by CO₂. Since the overall effect is the same for Downdraft and Fluidbed, only the averaged intensity is plotted for all compositions.

Figure 69 presents the effect of CO₂ on the raw average OH* chemiluminescence signal (a) and a comparison with the apparent HRR, grouping by the composition on which the variation is based on (b). First, it must be noted that the recorded images of the Fluidbed composition without CO₂ or CH₄ were noisy, so further after-treatment was required. Higher intensity is obtained for composition with

10% CO₂ but the phasing of OH* signal remains unchanged. One can see that Downdraft-based compositions presents the higher intensity, the composition with 10% CO₂ matching the intensity of the Updraft without CO₂, but with a slightly larger delay. We can also see that the lower CO₂ content of of Updraft, can explain the very slightly longer IDT of the Downdraft original composition, as visible in Figure 63.

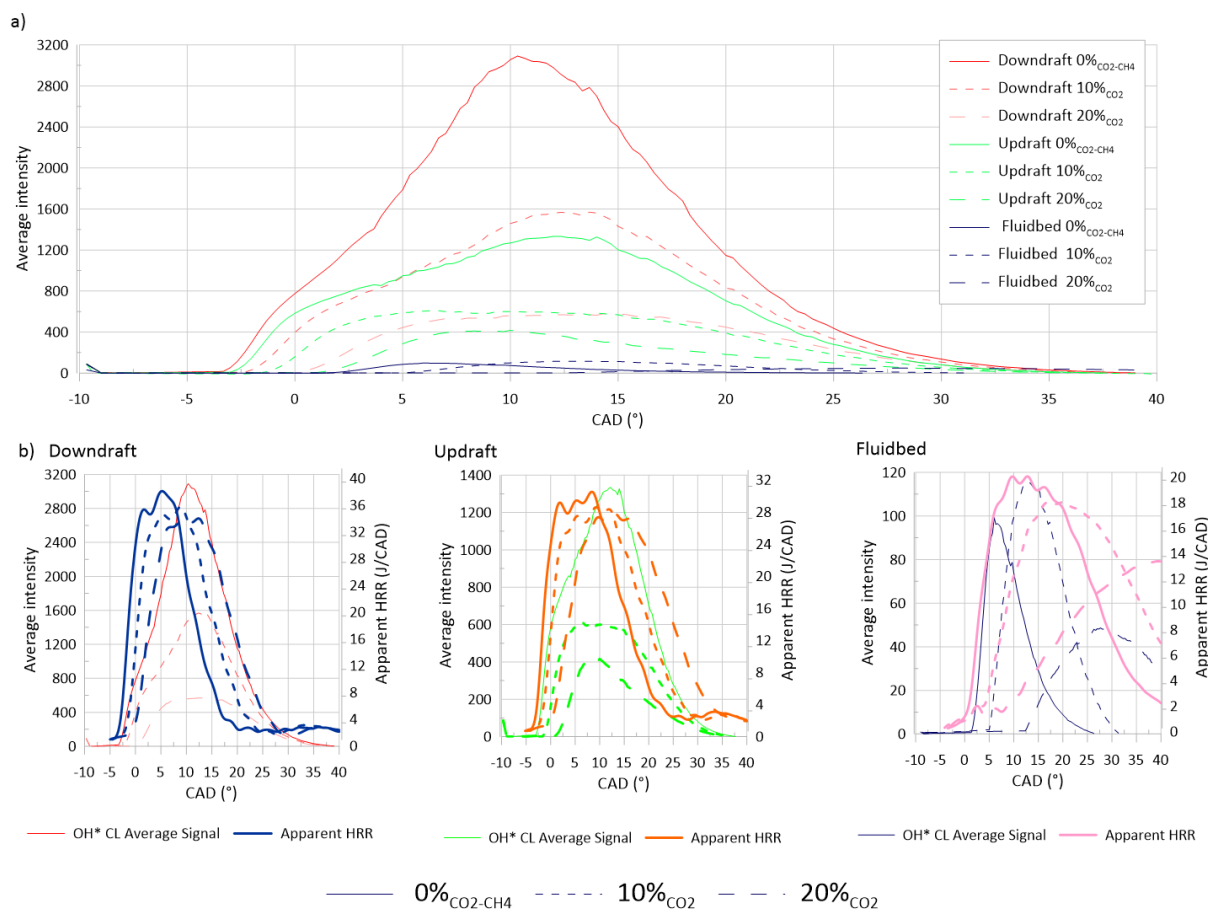


Figure 69: a- Effect of CO₂ on the average OH* chemiluminescence signal b- Comparison of the OH* average signal with the apparent Heat-Release Rate (HRR), grouped by the original composition ($\phi_{\text{syngas/air}} = 0.7$, $N = 750$ RPM).

Finally, to conclude on CO₂ impact on flame development, Figure 70 presents the apparent HRR for the three compositions when partially replacing N₂ share with CO₂. The presence of CO₂ instead of N₂ strongly delays and reduces (i.e. ‘flattens’) the apparent HRR, especially in the Fluidbed case where, as example, the IDT is delayed of 4 CAD from 0 to 10% of CO₂ and up to 8-9 CAD for 20% CO₂.

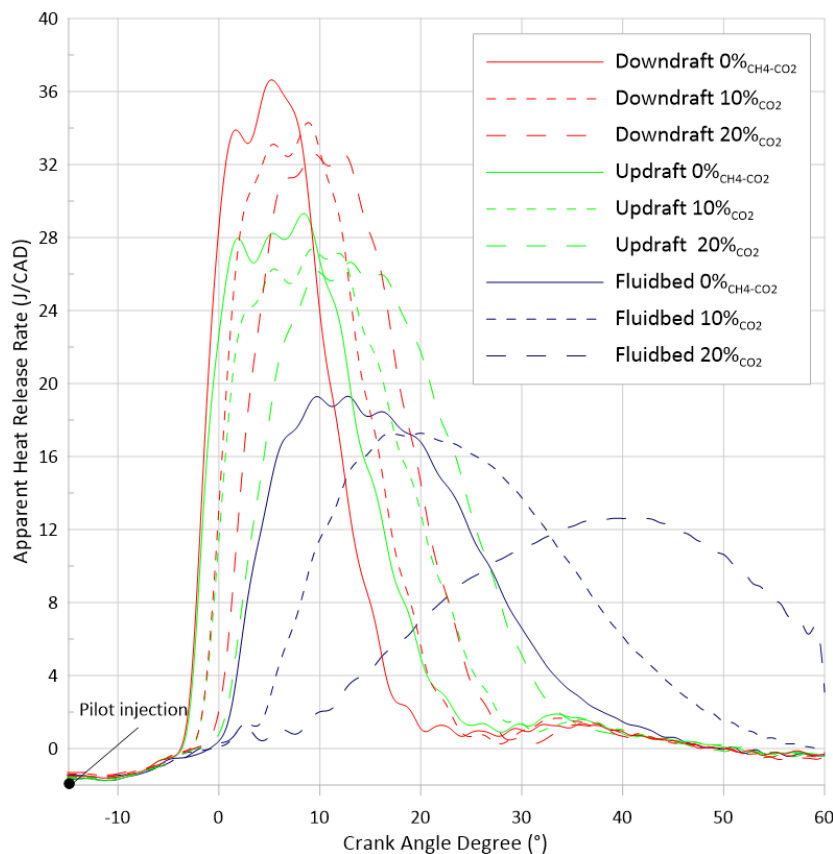


Figure 70: Effect of CO_2 addition in total amount of dilution ($\text{N}_2 + \text{CO}_2$) on Heat Release Rate (HRR) for the 3 original compositions ($\phi_{\text{syn gas/air}} = 0.7$, $N = 750$ RPM).

The CH_4 concentration effect

The effect of CH_4 is studied as well, but with smaller percentages, 2.5 and 5% only. As it can be seen in Figure 71, where the average OH^* images are presented using the Updraft composition, the combustion OH^* visualization is strongly enhanced by the presence of CH_4 . This enhancement is similar in the case of other compositions. In Figure 72, one can see the effect of CH_4 on the OH^* chemiluminescence average signal for all composition (a) and a comparison with the apparent HRR, grouping by the original composition (b). One can see how the CH_4 gives the Fluidbed composition more manageable combustion phasing.

In Figure 73, the result of changing the CH_4 concentration of the composition can be seen in the shape of the apparent HRR. When the concentration of CH_4 is increased, besides the combustion being slightly advanced, the peak HRR is also increased. This ignition advancement can be quantified in the same way as before, the CA were the HRR reach 1 J/CAD minus the SOI. With this method, we can see that the 2.5% replacement of N_2 by CH_4 advances this value by 0.4° , and the 5% replacement by 0.7° CAD.

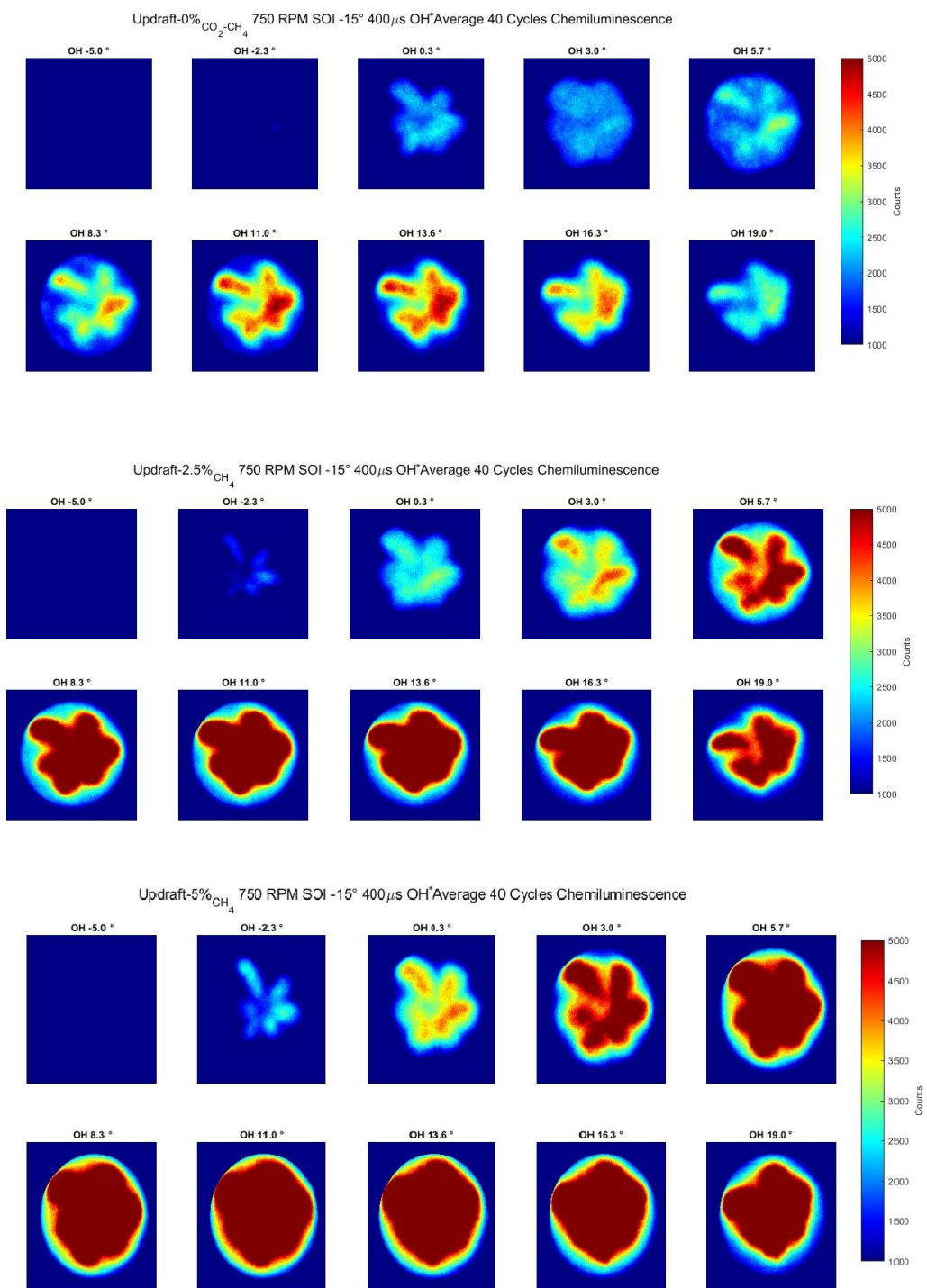


Figure 71: Effect of the CH₄ share on the OH* chemiluminescence averaged images for Updraft-based compositions ($\phi_{\text{syn gas/air}} = 0.7$, $N = 750$ RPM).

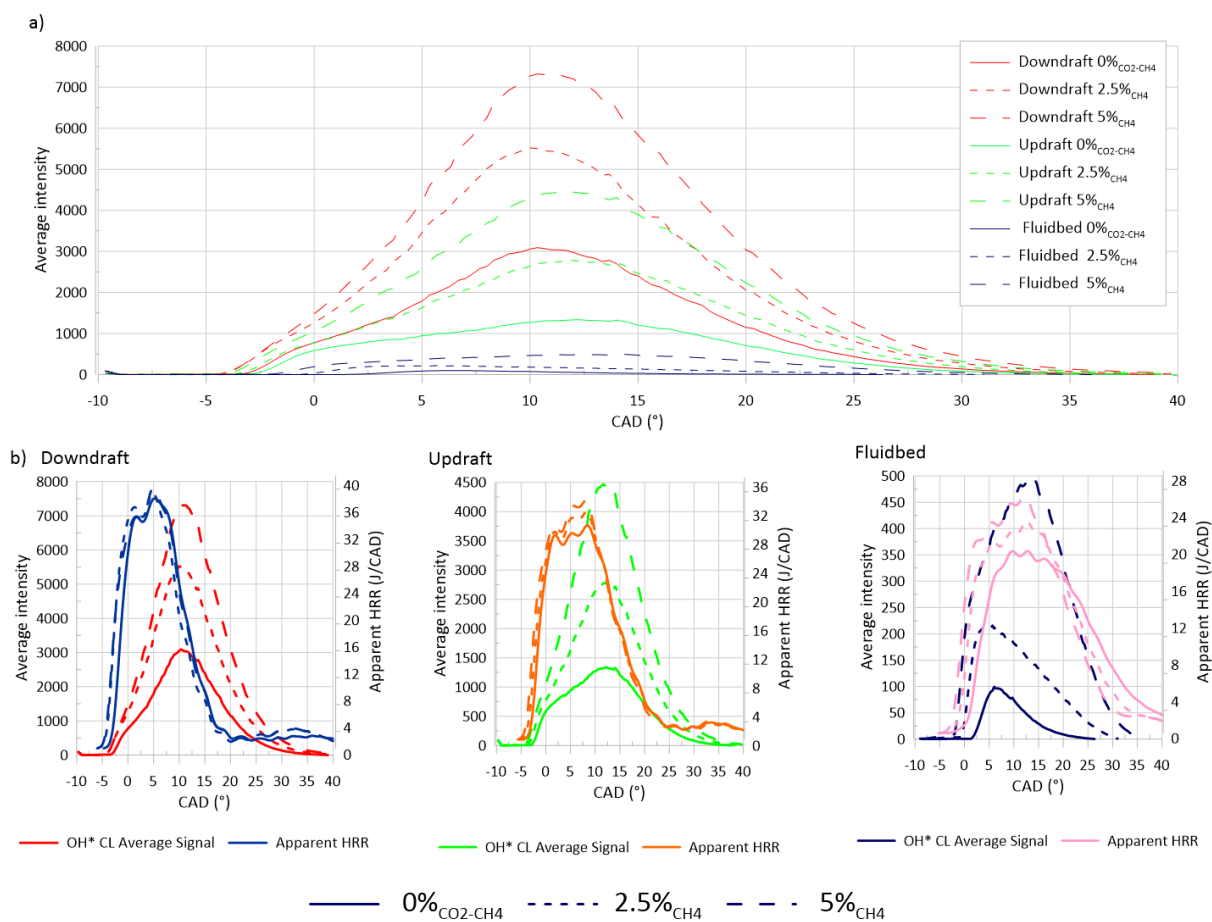


Figure 72: a- Effect of CH_4 on the average OH^* chemiluminescence signal b- Comparison of the OH^* average signal with the apparent Heat-Release Rate (HRR), grouped by the original composition ($\phi_{\text{syngas}/\text{air}} = 0.7$, $N = 750$ RPM).

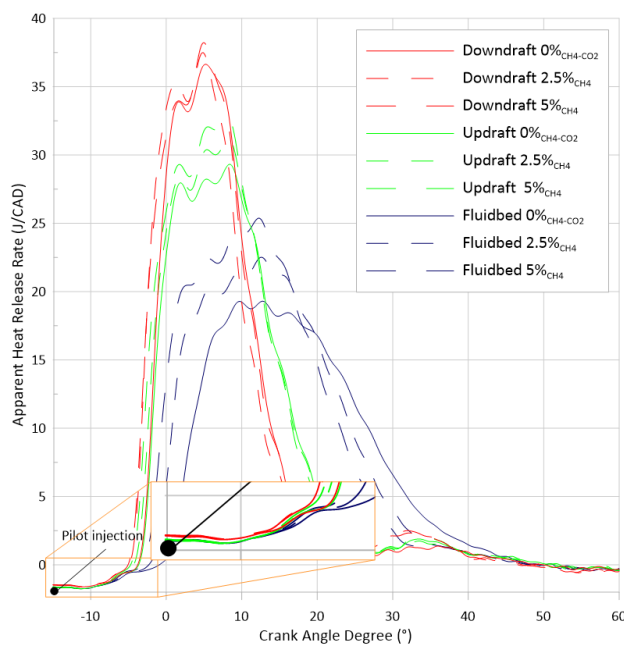


Figure 73: Effect of the CH_4 addition on the apparent Heat Release Rate (HRR) of dual-fuel operation of the compositions ($\phi_{\text{syngas}/\text{air}} = 0.7$, $N = 750$ RPM).

The zoomed portion of the graph above is there to highlight the small first-phase of the two-phase combustion, that is a result of the small pilot fuel injection as discussed in 4.3.2 Effect of pilot fuel injection quantity. Nevertheless, with the HRR results from the optical engine, is easier to distinguish the two combustion phases.

5.4. Conclusions

For an optimal pilot-fuel injection setting, chemiluminescence of OH* radical images were obtained and presented of a syngas/Diesel dual-fuel engine. Formaldehyde (CH₂O*) and CH* chemiluminescence signals were obtained and compared with those of OH*. Alongside the three compositions, set by the literature, the effect of varying the CO₂ and the CH₄ content was demonstrated and quantified. The main conclusions are as follows:

- For the tested conditions of the syngas/decane on dual-fuel operation, no signs of soot-incandescence were spotted for OH* and CH₂O* chemiluminescence, due the small injected mass of decane. However, for the CH* chemiluminescence images, whose characteristic wavelength is larger (431 nm), the soot interference was present, manifesting as a plateau of its average signal.
- The OH* chemiluminescence images of the three syngas compositions ignited by the decane injection in a dual-fuel engine were presented and the Updraft and Downdraft presented similar averages, regarding the delays and intensities.
- In contrast, the Fluidbed compositions presented the lowest signal, three times of the other two compositions, and with a larger delay.
- A comparison of the OH* chemiluminescence average signal with the apparent Heat-Release Rate (HRR) revealed a discrepancy of the location of each peak value. The CH* and CH₂O* signals average where more aligned with the HRR, despite still not capturing the initiation of the combustion development.
- The effects of the additions of CO₂ and CH₄ were studied, the results can help explaining the trend observed in the engine, since the larger content of CH₄ of the Fluidbed composition compensates its larger CO₂ content in terms of ID. Conversely, the larger CO and smaller CO₂ contents of the Updraft can help explaining the similar ID to the one of Downdraft, since the literature found no clear effect of the H₂/CO ratio on ID.

6. Final conclusions and suggestions for future work

In this PhD thesis, the use of syngas in a dual-fuel engine was evaluated. In the introduction, the general context was presented by summarizing the consensus about global warming and the goals to avoid these consequences. The role of biomass and waste energy sources was pointed-out as one promising solution and the production and usability for power generation of Synthesis gas, 'syngas', were detailed. Still in the first chapter, the different means of production of syngas were detailed, alongside the types of feedstock used and the cleaning process needed for each use case. The usability of syngas in Gas Turbines (GT) and Internal Combustion Engines (ICE) was examined, helping the selection of the dual-fuel ICE concept for further investigation. Syngas compositions were selected from the literature review, to represent as well as possible real-world gas produced by air-fed gasifiers.

After the introduction, an overview of the different parameters, driving the syngas/Diesel dual-fuel engine operation, is provided. In this chapter the effect of syngas composition, the phasing and quantity of the pilot fuel injection, and the ratio of energy provided by the syngas, on the engine performance and emissions, was clarified. It highlights the importance of the balance of the Hydrogen (H_2) content and the two major diluents: Nitrogen (N_2) and Carbon Dioxide (CO_2). The syngas/Diesel dual-fuel engine gains in efficiency with higher Compression Ratios (CR). Unfortunately, some studies identified the appearance of abnormal combustion ('knock'), which can be mitigated depending on the diluent's quantity in the syngas. Overall, most of the studies of syngas/Diesel dual-fuel engine do not achieve high Diesel substitution ratios. Moreover, the syngas compositions did not simulate real compositions, rather a combination of some of the five main components (H_2 , CO, CO_2 , CH_4 , N_2). There, this study aims to expand the field of knowledge in dual-fuel syngas/Diesel, first by measuring selected properties of three syngas compositions produced by air-fed gasifiers, then, underlining how the different parameters, related to these compositions and the engine operation, alter the emissions and performance of the engine. Finally, the combustion process is analyzed with chemiluminescence images of selected radicals recorded in an optically-accessible Compression-Ignition (CI) engine, to discuss the combustion development.

The third chapter begins by reminding the concepts of premixed flame theory. Then, the main properties, such as the laminar flame speed and the Markstein length for the 3 types of syngas were measured. The effect of the initial temperature and pressure and the presence of decane (as surrogate for Diesel), on these properties, is gaged for different equivalence ratios. The comparison with the results obtained from kinetic simulation with the four available mechanisms was provided. A correlation, between the laminar flame speed and the initial pressure (1 to 5 bar), temperature (298 to 423 K) and equivalence ratio (0.6 to 1.4), was determined for each composition. The range of equivalence ratios was enlarged from the literature, from 0.8-1.2 to 0.6-1.4, which is more relevant for very lean mixture engines. The three compositions present similar Markstein length values on a range of equivalence ratio of 0.8-1.2, whereas the Markstein length evolution in the case of Fluidbed composition presents a stronger transition towards negative values than the two other ones on the lean side ($\phi < 0.8$). Except for this condition, the results suggest that the composition of syngas are differentiated more strongly by the laminar flame speed than by the stretch sensitivity of the flame. As previously concluded from other studies, the Fluidbed composition, i.e. the composition with the highest dilution fraction, has the slowest laminar flame speed, down to twice lower than the other two compositions. This is exacerbated at higher pressures, as verified by the larger β value, i.e. the pressure exponent of the Metghalchi & Keck formulation, which indicates the pressure dependency of the laminar flame speed, and this will inevitably impact on the engine performance.

In Chapter 4, the performance and emissions of a syngas/decane dual-fuel engine are presented. The three compositions and the different operating conditions (premixed syngas-air equivalence ratio, quantity of decane share) were evaluated. The first conclusion is that, without significant adaptation or engine geometry optimization, the indicated thermal efficiencies exceed 38%, and this for all syngas compositions, and accompanied by decane contributing less than 10% of the total energy input. The injected pilot-fuel quantity plays an important role, in achieving smooth power delivery and controlling unburned gas emissions. On the other hand, a large pilot-fuel fraction could lead to higher soot emissions, reducing the possible environmental benefits.

Additionally, the effect of CO₂ and methane (CH₄) contents were quantified in H₂/CO/N₂ mixtures, from the original three compositions, where these two components were added individually. By means of the kinetic simulation with the Madison mechanism, some fundamental combustion properties were extracted especially the laminar flame speed and the adiabatic flame temperature. These fundamental properties correlated well with the combustion duration and stability, in the case of the laminar flame speeds, and for NO_x emission, with the adiabatic flame temperature. The relation between the CO₂ content and the engine emissions and performance was clearly identified, as expressed by the trade-off between the NO_x emissions and the combustion efficiency – unburnt gas emissions. The CH₄ fraction also presents a similar trade-off between unburnt hydrocarbon emissions and overall efficiency. Even though some kinetic mechanisms were validated in Chapter 3, a good suggestion for future work would be to re-run the laminar flame tests with the proposed additions of CO₂ and CH₄ on the original compositions. These further tests could better quantify the effect of these additions on these two fundamental properties: the laminar flame speed and the Markstein length.

In Chapter 5, an optical engine set-up was implemented to visualize the behavior of the main combustion radicals. A comparison between the average hydroxyl (OH*) chemiluminescence intensity obtained from images and the apparent Heat-Release Rate (HRR) was discussed., for the three syngas compositions at the same equivalence ratio ($\phi_{premixed}$) of 0.7, as previously determined as the optimum value on the previous chapter. In the dual-fuel case, due to the large divergence of the location of the peak OH* average signal with peak apparent HRR, two other chemiluminescent radicals, namely CH* and formaldehyde (CH₂O*), were also followed. The images of these two species were more aligned with the apparent HRR, despite the HRR onset not being captured by any of these species.

The considerably lower OH* signal of the Fluidbed composition was in accordance with the findings of the previous chapters, presenting OH* signals three times lower than the other syngas compositions and larger delays also. As in Chapter 4, the effects of CO₂ and CH₄ were analyzed. First, the determination of the Ignition Delay Times (IDT) as function of the local decane content from closed homogeneous reactor simulation show that the higher CH₄ content of the Fluidbed composition balances-out the inhibiting effect of higher CO₂ content. This result became evident by not being able to test the Fluidbed composition with 20% CO₂ content on Chapter 4, due to the instability of the engine, i.e. high Coefficient of Variability of Indicated Mean Effective Pressure ($IMEP_{cov}$).

As perspectives, several investigations could be conducted to complete the study of the effect of the composition on syngas combustion. Regarding the laminar burning velocity and Markstein length, a theoretical validation of the obtained Markstein length could be undertaken in order to validate the flame speed extrapolation and the range of radius used in certain conditions. The calculation of several fundamental parameters such as activation energies, Zel'dovich numbers, or Lewis numbers remains however complex due to the multiple components present in the syngas. To better understand the composition effect on combustion and limit the number of tested compositions, an approach based on Design of Experiments (DOE) could be of interest for predicting the laminar flame speed as well as

engine performances. The compositions tested in the present work are in some cases highly diluted. Moreover, when dealing with highly diluted mixtures, especially containing CO_2 and steam, important radiation effect can appear with possible reabsorption from the fresh gases thus leading to a preheating of the latter and hence modifying the flame propagation. When the laminar flame speed becomes very small in some conditions, this radiative effect needs to be considered, since it is impacting the propagation speed measurement and therefore the unstretched value obtained from the extrapolation model.

Finally, to broaden the field of study on carbon-neutral and carbon-free fuels on dual-fuel engines, we can envision the co-firing of these fuels, such as ammonia. As indicated in the introduction of the manuscript, ammonia can be already present in the syngas composition as a contaminant and the use of syngas, at the time referred as 'coal-gas', with ammonia in ICE was first presented in 1945 by Emeric Kroch [8]. Indeed, syngas can contain ammonia if it results from the gasification of nitrogen-rich feedstocks such as manure or sewage sludge. This ammonia is usually removed from the syngas due to its corrosiveness but with a supplementary cost. Nonetheless, ammonia has gained interest as a fuel in the last decade showing potential for both Spark-Ignition engines or Dual-Fuel CI engine. A syngas/ammonia blend should be therefore bearable for an engine. However, the combustion properties of this kind of mixture are still not sufficiently characterized, this can certainly pose a challenge. To better illustrate that, the Figure 74 below presents the Heat-Release Rate (HRR), obtained in the same engine, for a Downdraft mixture as a function of ammonia (NH_3) shared quantity. The pilot fuel injection remains the decane, with a fixed mass quantity (2.1 mg), but this does not translate to a constant decane energy share. As it can be noted, the reactivity of the mixture decreases as the ammonia content increases, as evidenced by the increased ignition delay time and the larger combustion duration. Such result is expected, since the reactivity of the ammonia is very low. Indeed, adding ammonia to the syngas will lead to a decrease in the laminar flame speed thus explaining the longer combustion duration when ammonia is added. Moreover, ammonia has a very high auto-ignition temperature and is delaying the start of combustion. However, if considered as an impurity (i.e below 5%_{vol.} of the syngas composition), the presence of ammonia would not influence the resulting HRR and therefore the engine performances. The emissions of such blend remain yet to be characterized, since syngas can be defined as a low-NO_x fuel (as illustrated in Chapter 4), the addition of ammonia could strongly change that, due to the fuel-NO_x pathway arising from the burning of the NH_3 itself.

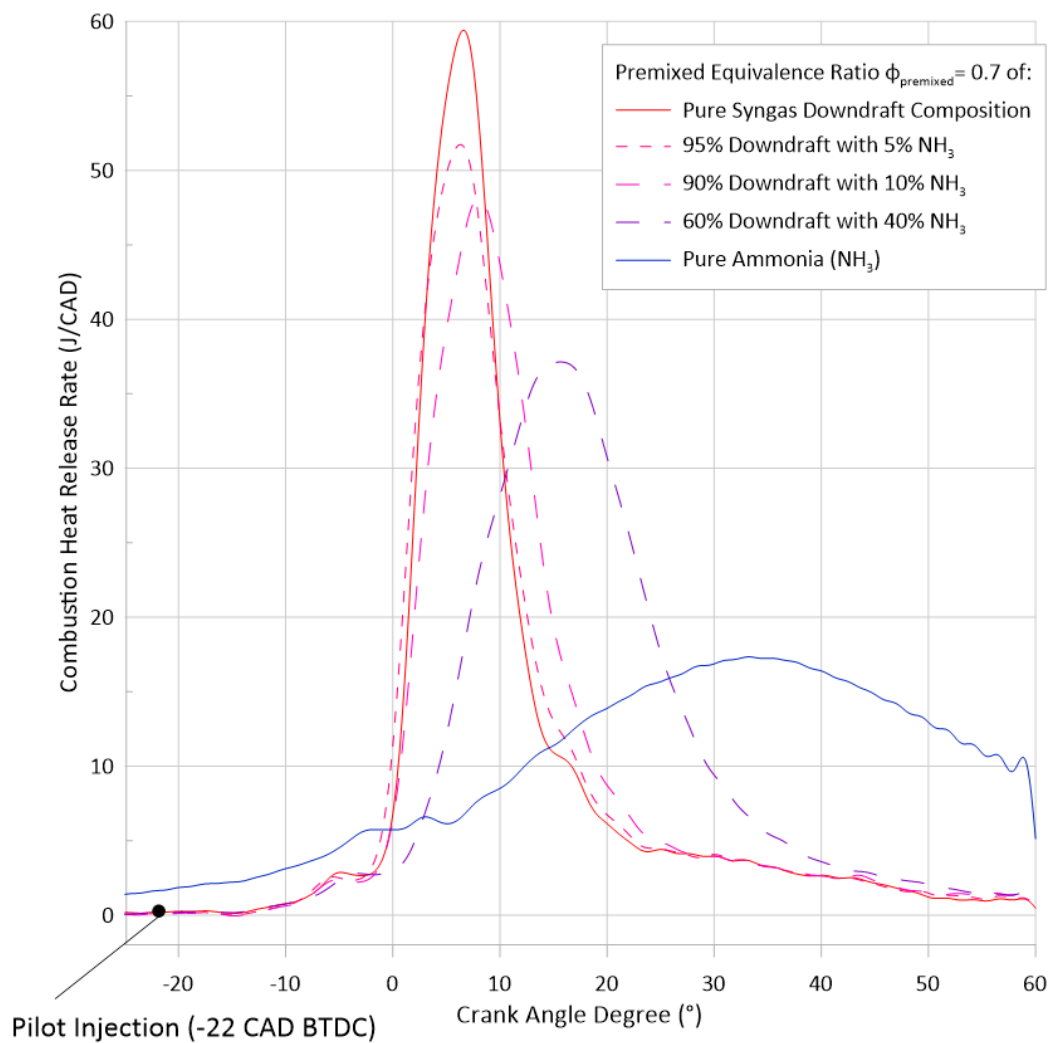


Figure 74: Example of Heat-Release Rate of Downdraft syngas as a function of ammonia shared quantity, ignition by decane pilot injection.

Bibliography

- [1] U. Azimov, E. Tomita, N. Kawahara, Y. Harada, Effect of syngas composition on combustion and exhaust emission characteristics in a pilot-ignited dual-fuel engine operated in PREMIER combustion mode, *Int. J. Hydrogen Energy* 36 (2011) 11985–11996. <https://doi.org/10.1016/j.ijhydene.2011.04.192>.
- [2] M. Mohon Roy, E. Tomita, N. Kawahara, Y. Harada, A. Sakane, Performance and emission comparison of a supercharged dual-fuel engine fueled by producer gases with varying hydrogen content, *Int. J. Hydrogen Energy* 34 (2009) 7811–7822. <https://doi.org/10.1016/j.ijhydene.2009.07.056>.
- [3] M. Sharma, R. Kaushal, Performance and exhaust emission analysis of a variable compression ratio (VCR) dual fuel CI engine fuelled with producer gas generated from pistachio shells, *Fuel* 283 (2021) 118924. <https://doi.org/10.1016/j.fuel.2020.118924>.
- [4] S. Shashikantha, P.P. Parikh, Spark Ignition Producer Gas Engine and Dedicated Compressed Natural Gas Engine - Technology Development and Experimental Performance Optimisation, in: *SAE Tech. Pap.*, 1999. <https://doi.org/10.4271/1999-01-3515>.
- [5] E. Monteiro, M. Bellenoue, J. Sotton, N.A. Moreira, S. Malheiro, Laminar burning velocities and Markstein numbers of syngas-air mixtures, *Fuel* 89 (2010) 1985–1991. <https://doi.org/10.1016/j.fuel.2009.11.008>.
- [6] E. Monteiro, A. Rouboa, Measurements of the laminar burning velocities for typical syngas-air mixtures at elevated pressures, *J. Energy Resour. Technol. Trans. ASME* 133 (2011) 1–7. <https://doi.org/10.1115/1.4004607>.
- [7] G.P. Oliveira, M.E. Sbampato, C.A. Martins, L.R. Santos, L.G. Barreta, R.F. Boschi Gonçalves, Experimental laminar burning velocity of syngas from fixed-bed downdraft biomass gasifiers, *Renew. Energy* 153 (2020) 1251–1260. <https://doi.org/10.1016/j.renene.2020.02.083>.
- [8] Kroch E, Ammonia as a fuel for motorbuses, *J. Inst. Pet.* (1945) 213–223.
- [9] IEA, Net Zero by 2050 A Roadmap for the global energy sector, (2021) 222.
- [10] Global Warming of 1.5 °C, (n.d.). <https://www.ipcc.ch/sr15/> (accessed October 25, 2023).
- [11] J. Guo, D. Kubli, P. Saner, The economics of climate change: no action not an option, *Swiss Re Inst.* (2021) 34.
- [12] European Commission, official website, (n.d.). https://commission.europa.eu/index_en (accessed May 18, 2023).
- [13] 2020 climate & energy package, (n.d.). https://climate.ec.europa.eu/eu-action/climate-strategies-targets/2020-climate-energy-package_en (accessed May 17, 2023).
- [14] J. Huang, B. Mendoza, J.S. Daniel, C.J. Nielsen, L. Rotstayn, O. Wild, Anthropogenic and natural radiative forcing, *Clim. Chang. 2013 Phys. Sci. Basis Work. Gr. I Contrib. to Fifth Assess. Rep. Intergov. Panel Clim. Chang.* 9781107057 (2013) 659–740. <https://doi.org/10.1017/CBO9781107415324.018>.
- [15] Global warming contributions by gas and source, World, 1950 to 2021, (n.d.). <https://ourworldindata.org/grapher/global-warming-by-gas-and-source?time=1950..latest> (accessed October 25, 2023).

- [16] M.W. Jones, G.P. Peters, T. Gasser, R.M. Andrew, C. Schwingshackl, J. Gütschow, R.A. Houghton, P. Friedlingstein, J. Pongratz, C. Le Quéré, National contributions to climate change due to historical emissions of carbon dioxide, methane, and nitrous oxide since 1850, *Sci. Data* 10 (2023). <https://doi.org/10.1038/S41597-023-02041-1>.
- [17] Eurostat, Shedding light on energy in the EU | 2022 Interactive Edition, 2022. <https://doi.org/10.2785/640865>.
- [18] V. Smil, *Energy Transitions: Global and National Perspectives (Expanded and updated edition)*, 2017.
- [19] L.R. Lynd, OVERVIEW AND EVALUATION OF FUEL ETHANOL FROM CELLULOSIC BIOMASS: Technology, Economics, the Environment, and Policy, *Ann. N.Y. Acad. Sci.* 21 (2003) 403–465. <https://doi.org/10.1146/ANNUREV.ENERGY.21.1.403>.
- [20] L.G. Schumacher, J. Van Gerpen, B. Adams, Biodiesel Fuels, in: *Encycl. Energy*, Elsevier, 2004: pp. 151–162. <https://doi.org/10.1016/B0-12-176480-X/00519-2>.
- [21] S. Achinas, V. Achinas, G.J.W. Euverink, A Technological Overview of Biogas Production from Biowaste, *Engineering* 3 (2017) 299–307. <https://doi.org/10.1016/J.ENG.2017.03.002>.
- [22] J.J. Bolívar Caballero, I.N. Zaini, W. Yang, Reforming processes for syngas production: A mini-review on the current status, challenges, and prospects for biomass conversion to fuels, *Appl. Energy Combust. Sci.* 10 (2022) 100064. <https://doi.org/10.1016/j.jaecs.2022.100064>.
- [23] A. Anand, A.K. Sakhiya, I. Aier, U. Kakati, V. Kumar, P. Kaushal, Assessment of electricity generation potential from biochar in Northern India, *Energy Clim. Chang.* 3 (2022) 100068. <https://doi.org/10.1016/J.EGYCC.2021.100068>.
- [24] INTERNATIONAL ENERGY AGENCY, *World Energy Outlook 2023*, 2023.
- [25] C. Ogg, *Environmental challenges associated with corn ethanol production*, 2008.
- [26] J.G. Speight, *The Biofuels Handbook*, The Royal Society of Chemistry, 2012. <https://doi.org/10.1002/anie.201108812>.
- [27] D. Schweitzer, A. Gredinger, M. Schmid, G. Waizmann, M. Beirrow, R. Spörl, G. Scheffknecht, Steam gasification of wood pellets, sewage sludge and manure: Gasification performance and concentration of impurities, *Biomass and Bioenergy* 111 (2018) 308–319. <https://doi.org/10.1016/j.biombioe.2017.02.002>.
- [28] A. Paykani, H. Chehrmonavari, A. Tsolakis, T. Alger, W.F. Northrop, R.D. Reitz, Synthesis gas as a fuel for internal combustion engines in transportation, *Prog. Energy Combust. Sci.* 90 (2022) 100995. <https://doi.org/10.1016/j.pecs.2022.100995>.
- [29] J. Hrbek, Status report on thermal biomass gasification in countries participating in IEA Bioenergy Task 33, (2016) 163.
- [30] Q. Zhou, C.S. Cheung, C.W. Leung, X. Li, Z. Huang, Effects of diluents on laminar burning characteristics of bio-syngas at elevated pressure, *Fuel* 248 (2019) 8–15. <https://doi.org/10.1016/j.fuel.2019.03.062>.
- [31] Y. Qian, S. Sun, D. Ju, X. Shan, X. Lu, Review of the state-of-the-art of biogas combustion mechanisms and applications in internal combustion engines, *Renew. Sustain. Energy Rev.* 69 (2017) 50–58. <https://doi.org/10.1016/j.rser.2016.11.059>.
- [32] L. Pizzuti, C.A. Martins, P.T. Lacava, Laminar burning velocity and flammability limits in biogas: A literature review, *Renew. Sustain. Energy Rev.* 62 (2016) 856–865. <https://doi.org/10.1016/j.rser.2016.05.011>.

- [33] A. Mertins, T. Wawer, How to use biogas?: A systematic review of biogas utilization pathways and business models, *Bioresour. Bioprocess.* 9 (2022). <https://doi.org/10.1186/s40643-022-00545-z>.
- [34] A.S. AlRamadan, S.M. Sarathy, J. Badra, Unraveling the octane response of gasoline/ethanol blends: Paving the way to formulating gasoline surrogates, *Fuel* 299 (2021) 120882. <https://doi.org/10.1016/j.fuel.2021.120882>.
- [35] X. Zhen, Y. Wang, An overview of methanol as an internal combustion engine fuel, *Renew. Sustain. Energy Rev.* 52 (2015) 477–493. <https://doi.org/10.1016/j.rser.2015.07.083>.
- [36] C. Sayin, M. Ilhan, M. Canakci, M. Gumus, Effect of injection timing on the exhaust emissions of a diesel engine using diesel–methanol blends, *Renew. Energy* 34 (2009) 1261–1269. <https://doi.org/10.1016/J.RENENE.2008.10.010>.
- [37] C.A. Sharp, S.A. Howell, J. Jobe, The Effect of Biodiesel Fuels on Transient Emissions from Modern Diesel Engines, Part I Regulated Emissions and Performance, *SAE Tech. Pap.* (2000). <https://doi.org/10.4271/2000-01-1967>.
- [38] F.Y. Hagos, A.R.A. Aziz, S.A. Sulaiman, Trends of syngas as a fuel in internal combustion engines, *Adv. Mech. Eng.* 2014 (2014). <https://doi.org/10.1155/2014/401587>.
- [39] M. Fiore, V. Magi, A. Viggiano, Internal combustion engines powered by syngas: A review, *Appl. Energy* 276 (2020) 115415. <https://doi.org/10.1016/j.apenergy.2020.115415>.
- [40] W.P. Chan, S.A.M.B. Yusoff, A. Veksha, A. Giannis, T.T. Lim, G. Lisak, Analytical assessment of tar generated during gasification of municipal solid waste: Distribution of GC–MS detectable tar compounds, undetectable tar residues and inorganic impurities, *Fuel* 268 (2020) 117348. <https://doi.org/10.1016/J.FUEL.2020.117348>.
- [41] P. Brequigny, E. Pacaud, C. Mounaim-Rousselle, Performances of a producer gas from sewage sludge gasification enriched with ammonia in a spark-ignition engine, *Biomass and Bioenergy* 171 (2023) 106731. <https://doi.org/10.1016/j.biombioe.2023.106731>.
- [42] L.J. Shadle, D.A. Berry, M. Syamlal, Coal Conversion Processes, Gasification, *Kirk-Othmer Encycl. Chem. Technol.* (2002). <https://doi.org/10.1002/0471238961.0701190913010801.A01.PUB2>.
- [43] T. Lieuwen, V. Yang, R. Yetter, eds., *Synthesis Gas Combustion*, CRC Press, 2009. <https://doi.org/10.1201/9781420085358>.
- [44] Gasification Plant Databases | netl.doe.gov, (n.d.). <https://www.netl.doe.gov/research/coal/energy-systems/gasification/gasification-plant-databases> (accessed May 27, 2023).
- [45] 2030 climate & energy framework, (n.d.). https://climate.ec.europa.eu/eu-action/climate-strategies-targets/2030-climate-energy-framework_en (accessed May 17, 2023).
- [46] B. Jenkins M., L. Bexter L., T. Miles R. Jr., T. Miles R., B.M. Jenkins, L.L. Baxter, T.R. Miles, T.R. Miles, Combustion Properties of Biomass, *Fuel Process. Technol.* 54 (1998) 17–46. [https://doi.org/10.1016/S0378-3820\(97\)00059-3](https://doi.org/10.1016/S0378-3820(97)00059-3).
- [47] World Power consumption | Electricity consumption | Enerdata, (n.d.). <https://yearbook.enerdata.net/electricity/electricity-domestic-consumption-data.html> (accessed May 28, 2023).
- [48] Understanding Global Warming Potentials | US EPA, (n.d.). <https://www.epa.gov/ghgemissions/understanding-global-warming-potentials> (accessed May 31, 2023).
- [49] J.G. Speight, *Gasification of Unconventional Feedstocks*, 2014.

0-14152-9.

- [50] R. Thomson, P. Kwong, E. Ahmad, K.D.P. Nigam, Clean syngas from small commercial biomass gasifiers; a review of gasifier development, recent advances and performance evaluation, *Int. J. Hydrogen Energy* 45 (2020) 21087–21111. <https://doi.org/10.1016/j.ijhydene.2020.05.160>.
- [51] P. Basu, *Biomass Gasification, Pyrolysis and Torrefaction: Practical Design and Theory*, 2013. <https://doi.org/10.1016/C2011-0-07564-6>.
- [52] U. Arena, Process and technological aspects of municipal solid waste gasification. A review, *Waste Manag.* 32 (2012) 625–639. <https://doi.org/10.1016/J.WASMAN.2011.09.025>.
- [53] A.G. Capodaglio, S. Bolognesi, Ecofuel feedstocks and their prospects, in: *Adv. Eco-Fuels a Sustain. Environ.*, Elsevier Ltd., 2018: pp. 15–51. <https://doi.org/10.1016/B978-0-08-102728-8.00002-4>.
- [54] C.S. Psomopoulos, A. Bourka, N.J. Themelis, Waste-to-energy: A review of the status and benefits in USA, *Waste Manag.* 29 (2009) 1718–1724. <https://doi.org/10.1016/J.WASMAN.2008.11.020>.
- [55] U. Arena, F. Di Gregorio, C. Amorese, M.L. Mastellone, A techno-economic comparison of fluidized bed gasification of two mixed plastic wastes, *Waste Manag.* 31 (2011) 1494–1504. <https://doi.org/10.1016/j.wasman.2011.02.004>.
- [56] S.G. Rao, *Experiments and Modelling Studies of Producer Gas based Spark-Ignited Reciprocating Engines*, 2003.
- [57] P.J. Woolcock, R.C. Brown, A review of cleaning technologies for biomass-derived syngas, *Biomass and Bioenergy* 52 (2013) 54–84. <https://doi.org/10.1016/j.biombioe.2013.02.036>.
- [58] A. V. Bridgwater, The technical and economic feasibility of biomass gasification for power generation, *Fuel* 74 (1995) 631–653. [https://doi.org/10.1016/0016-2361\(95\)00001-L](https://doi.org/10.1016/0016-2361(95)00001-L).
- [59] V. Belgiorno, G. De Feo, C. Della Rocca, R.M.A. Napoli, Energy from gasification of solid wastes, *Waste Manag.* 23 (2003) 1–15. [https://doi.org/10.1016/S0956-053X\(02\)00149-6](https://doi.org/10.1016/S0956-053X(02)00149-6).
- [60] J. Oakey, *Fuel Flexible Energy Generation*, Elsevier, 2016. <https://doi.org/10.1016/C2014-0-01769-8>.
- [61] V.S. Sikarwar, M. Zhao, P.S. Fennell, N. Shah, E.J. Anthony, Progress in biofuel production from gasification, *Prog. Energy Combust. Sci.* 61 (2017) 189–248. <https://doi.org/10.1016/j.pecs.2017.04.001>.
- [62] W. Marine Power, *Wärtsilä 31DF Product Guide*, (2022).
- [63] N. Bouvet, C. Chauveau, I. Gökalp, F. Halter, Experimental studies of the fundamental flame speeds of syngas (H₂/CO)/air mixtures, *Proc. Combust. Inst.* 33 (2011) 913–920. <https://doi.org/10.1016/j.proci.2010.05.088>.
- [64] J. Brandin, M. Tunér, I. Odenbrand, V. Lund, *Swedish Energy Agency Report Small Scale Gasification : Gas Engine CHP for Biofuels*, 2011.
- [65] *The Role of Low-Carbon Fuels in the Clean Energy Transitions of the Power Sector*, OECD, 2021. <https://doi.org/10.1787/a92fe011-en>.
- [66] N. Mahinpey, A. Farooqui, A. Abdalla, K. Asghari, Power generation from syngas, in: *Adv. Synth. Gas Methods, Technol. Appl.*, Elsevier, 2023: pp. 289–319. <https://doi.org/10.1016/B978-0-323-91878-7.00001-0>.
- [67] J. Ganjikunta, Design Considerations for Syngas Turbine Power Plants, *ASME 2015 Gas Turbine India Conf. GTINDIA 2015* (2016). <https://doi.org/10.1115/GTINDIA2015-1261>.

- [68] M. Fatiguso, A.R. Valenti, S. Ravelli, Comparative energy performance analysis of micro gas turbine and internal combustion engine in a cogeneration plant based on biomass gasification, *J. Clean. Prod.* (2023) 139782. <https://doi.org/10.1016/J.JCLEPRO.2023.139782>.
- [69] J. Ahrenfeldt, T.P. Thomsen, U. Henriksen, L.R. Clausen, Biomass gasification cogeneration - A review of state of the art technology and near future perspectives, *Appl. Therm. Eng.* 50 (2013) 1407–1417. <https://doi.org/10.1016/j.applthermaleng.2011.12.040>.
- [70] Interactive map: Share of District Heating and Cooling across Europe - Wedistrict, (n.d.). <https://www.wedistrict.eu/interactive-map-share-of-district-heating-and-cooling-across-europe/> (accessed October 7, 2023).
- [71] S. Bhaduri, F. Contino, H. Jeanmart, E. Breuer, The effects of biomass syngas composition, moisture, tar loading and operating conditions on the combustion of a tar-tolerant HCCI (Homogeneous Charge Compression Ignition) engine, *Energy* 87 (2015) 289–302. <https://doi.org/10.1016/j.energy.2015.04.076>.
- [72] S. Bhaduri, B. Berger, M. Pochet, H. Jeanmart, F. Contino, HCCI engine operated with unscrubbed biomass syngas, *Fuel Process. Technol.* 157 (2017). <https://doi.org/10.1016/j.fuproc.2016.10.011>.
- [73] F.Y. Hagos, A.R.A. Aziz, S.A. Sulaiman, Methane enrichment of syngas (H₂/CO) in a spark-ignition directinjection engine: Combustion, performance and emissions comparison with syngas and Compressed Natural Gas, *Energy* 90 (2015) 2006–2015. <https://doi.org/10.1016/j.energy.2015.07.031>.
- [74] G. Sridhar, R. Babu, Facts about Producer Gas Engine, in: *Paths to Sustain. Energy*, 2010. <https://doi.org/10.5772/13030>.
- [75] G. Sridhar, S. Dasappa, H. V. Sridhar, P.J. Paul, N.K.S. Rajan, Gaseous emissions using producer gas as fuel in reciprocating engines, *SAE Tech. Pap.* (2005). <https://doi.org/10.4271/2005-01-1732>.
- [76] Z. Ahmad, O. Kaario, C. Qiang, M. Larmi, Effect of pilot fuel properties on lean dual-fuel combustion and emission characteristics in a heavy-duty engine, *Appl. Energy* 282 (2021) 116134. <https://doi.org/10.1016/j.apenergy.2020.116134>.
- [77] A.M.L.M. Wagemakers, C.A.J. Leermakers, Review on the effects of dual-fuel operation, using diesel and gaseous fuels, on emissions and performance, *SAE Tech. Pap.* (2012). <https://doi.org/10.4271/2012-01-0869>.
- [78] Q. Peng, T. Rockstroh, M. Pamminer, C. Hall, Model predictive control of mixing controlled compression ignition operation for low reactivity fuels, *Control Eng. Pract.* 139 (2023) 105631. <https://doi.org/10.1016/j.conengprac.2023.105631>.
- [79] P. Singh, R. Kumar, S. Sharma, S. Kumar, Effect of Engine Parameters on the Performance of Dual-Fuel CI Engines with Producer Gas - A Review, *Energy and Fuels* 35 (2021) 16377–16402. <https://doi.org/10.1021/acs.energyfuels.1c02279>.
- [80] L. Wei, P. Geng, A review on natural gas/diesel dual fuel combustion, emissions and performance, *Fuel Process. Technol.* 142 (2016) 264–278. <https://doi.org/10.1016/j.fuproc.2015.09.018>.
- [81] Use of hydrogen in dual-fuel diesel engines, *Prog. Energy Combust. Sci.* 98 (2023) 101100. <https://doi.org/10.1016/J.PECS.2023.101100>.
- [82] M.R. Saxena, R.K. Maurya, P. Mishra, Assessment of performance, combustion and emissions characteristics of methanol-diesel dual-fuel compression ignition engine: A review, *J. Traffic Transp. Eng. (English Ed.)* 8 (2021) 638–680. <https://doi.org/10.1016/J.JTTE.2021.02.003>.

- [83] E. Nadimi, G. Przybyła, M.T. Lewandowski, W. Adamczyk, Effects of ammonia on combustion, emissions, and performance of the ammonia/diesel dual-fuel compression ignition engine, *J. Energy Inst.* 107 (2023). <https://doi.org/10.1016/j.joei.2022.101158>.
- [84] Q. Cheng, O. Kaario, Z. Ahmad, V. Vuorinen, M. Larmi, Effect of pilot fuel properties on engine performance and combustion stability in a tri-fuel engine powered by premixed methane-hydrogen and diesel pilot, *Int. J. Hydrogen Energy* 46 (2021) 37469–37486. <https://doi.org/10.1016/j.ijhydene.2021.09.053>.
- [85] E. Tomita, N. Fukatani, T. Komoda, N. Kawahara, K. Maruyama, Combustion in a supercharged biomass gas engine with micro-pilot ignition - effects of injection pressure and amount of diesel fuel, *J. KONES* 14 (2007) 513–520.
- [86] U. Azimov, E. Tomita, N. Kawahar, Combustion and Exhaust Emission Characteristics of Diesel Micro-Pilot Ignited Dual-Fuel Engine, in: *Diesel Engine - Combust. Emiss. Cond. Monit., InTech*, 2013: pp. 275–281. <https://doi.org/10.5772/54613>.
- [87] M.M. Roy, E. Tomita, N. Kawahara, Y. Harada, A. Sakane, Effect of fuel injection parameters on engine performance and emissions of a supercharged producer gas-diesel dual fuel engine, *SAE Tech. Pap.* 4970 (2009). <https://doi.org/10.4271/2009-01-1848>.
- [88] H. Park, E. Shim, J. Lee, S. Oh, C. Kim, Y. Lee, K. Kang, Comparative evaluation of conventional dual fuel, early pilot, and reactivity-controlled compression ignition modes in a natural gas-diesel dual-fuel engine, *Energy* 268 (2023) 126769. <https://doi.org/10.1016/j.energy.2023.126769>.
- [89] N. Balakrishnan, K. Mayilsamy, Effect of compression ratio on compression ignition engine performance with biodiesel and producer gas in mixed fuel mode, *J. Renew. Sustain. Energy* 6 (2014) 1–14. <https://doi.org/10.1063/1.4868026>.
- [90] A.P. Carlucci, A. Ficarella, D. Laforgia, L. Strafella, Improvement of dual-fuel biodiesel-producer gas engine performance acting on biodiesel injection parameters and strategy, *Fuel* 209 (2017) 754–768. <https://doi.org/10.1016/j.fuel.2017.07.100>.
- [91] C.A. Rinaldini, G. Allesina, S. Pedrazzi, E. Mattarelli, T. Savioli, N. Morselli, M. Puglia, P. Tartarini, Experimental investigation on a Common Rail Diesel engine partially fuelled by syngas, *Energy Convers. Manag.* 138 (2017) 526–537. <https://doi.org/10.1016/j.enconman.2017.02.034>.
- [92] H. Guo, W.S. Neill, B. Liko, The combustion and emissions performance of a syngas-diesel dual fuel compression ignition engine, *ASME 2016 Intern. Combust. Engine Fall Tech. Conf. ICEF 2016* (2016). <https://doi.org/10.1115/ICEF20169367>.
- [93] A.P. Carlucci, A. Ficarella, D. Laforgia, Potentialities of a Common Rail Injection System for the Control of Dual Fuel Biodiesel-Producer Gas Combustion and Emissions, *J. Energy Eng.* 140 (2014) 1–8. [https://doi.org/10.1061/\(asce\)ey.1943-7897.0000150](https://doi.org/10.1061/(asce)ey.1943-7897.0000150).
- [94] C.K. Law, *Combustion Physics*, 2006.
- [95] Y.B. Zeldovich, 16. Theory of Combustion and Detonation of Gases, in: *Sel. Work. Yakov Borisovich Zeldovich*, Vol. I, Princeton University Press, 1992: pp. 162–232. <https://doi.org/10.1515/9781400862979.162>.
- [96] C. Lhuillier, *Experimental and numerical investigation for the use of ammonia in Spark- Ignition engines*, 2020.
- [97] W.F. A., A review of some theoretical considerations of turbulent flame structure, *AGARD Conf. Proceeding*, 1975 (1975).
- [98] C.K. Wu, C.K. Law, On the determination of laminar flame speeds from stretched flames, *Symp. Combust.* 20 (1985) 1941–1949. [https://doi.org/10.1016/S0082-0784\(85\)80693-7](https://doi.org/10.1016/S0082-0784(85)80693-7).

- [99] P. Clavin, Dynamic behavior of premixed flame fronts in laminar and turbulent flows, *Prog. Energy Combust. Sci.* 11 (1985) 1–59. [https://doi.org/10.1016/0360-1285\(85\)90012-7](https://doi.org/10.1016/0360-1285(85)90012-7).
- [100] G.H. Markstein, ed., *Nonsteady Flame Propagation*, 1964.
- [101] A.P. Kelley, C.K. Law, Nonlinear effects in the extraction of laminar flame speeds from expanding spherical flames, *Combust. Flame* 156 (2009) 1844–1851. <https://doi.org/10.1016/j.combustflame.2009.04.004>.
- [102] V. Pessina, A. D’Adamo, C. Iacovano, S. Fontanesi, S. Martinez, P. Lacava, Numerical Simulation of Syngas Blends Combustion in a Research Single-Cylinder Engine, *SAE Tech. Pap.* 2019 (2019) 1–14. <https://doi.org/10.4271/2019-24-0094>.Abstract.
- [103] P. Brequigny, F. Halter, C. Mounaïm-Rousselle, T. Dubois, Fuel performances in Spark-Ignition (SI) engines: Impact of flame stretch, *Combust. Flame* 166 (2016) 98–112. <https://doi.org/10.1016/j.combustflame.2016.01.005>.
- [104] P. Brequigny, Fuel influence on combustion in Spark-Ignition Engine Flame Stretch Impact, UNIVERSITÉ D’ORLÉANS, 2014.
- [105] P.G. Aleiferis, J. Serras-Pereira, D. Richardson, Characterisation of flame development with ethanol, butanol, iso-octane, gasoline and methane in a direct-injection spark-ignition engine, *Fuel* 109 (2013) 256–278. <https://doi.org/10.1016/j.fuel.2012.12.088>.
- [106] C. Lhuillier, P. Brequigny, N. Lamoureux, F. Contino, C. Mounaïm-Rousselle, Experimental investigation on laminar burning velocities of ammonia/hydrogen/air mixtures at elevated temperatures, *Fuel* 263 (2020) 116653. <https://doi.org/10.1016/j.fuel.2019.116653>.
- [107] B. Galmiche, F. Halter, F. Foucher, Effects of high pressure, high temperature and dilution on laminar burning velocities and Markstein lengths of iso-octane/air mixtures, *Combust. Flame* 159 (2012) 3286–3299. <https://doi.org/10.1016/j.combustflame.2012.06.008>.
- [108] C. Endouard, F. Halter, C. Chauveau, F. Foucher, Effects of CO₂, H₂O, and Exhaust Gas Recirculation Dilution on Laminar Burning Velocities and Markstein Lengths of Iso-Octane/Air Mixtures, *Combust. Sci. Technol.* 188 (2016) 516–528. <https://doi.org/10.1080/00102202.2016.1138792>.
- [109] M. Di Lorenzo, P. Brequigny, F. Foucher, C. Mounaïm-Rousselle, Validation of TRF-E as gasoline surrogate through an experimental laminar burning speed investigation, *Fuel* 253 (2019) 1578–1588. <https://doi.org/10.1016/j.fuel.2019.05.081>.
- [110] F. Halter, T. Tahtouh, C. Mounaïm-Rousselle, Nonlinear effects of stretch on the flame front propagation, *Combust. Flame* 157 (2010) 1825–1832. <https://doi.org/10.1016/j.combustflame.2010.05.013>.
- [111] X. Gong, J. Huo, Z. Ren, C.K. Law, Extrapolation and DNS-mapping in determining laminar flame speeds of syngas/air mixtures, *Combust. Flame* 200 (2019) 365–373. <https://doi.org/10.1016/j.combustflame.2018.11.033>.
- [112] W. Han, P. Dai, X. Gou, Z. Chen, A review of laminar flame speeds of hydrogen and syngas measured from propagating spherical flames, *Appl. Energy Combust. Sci.* 1–4 (2020) 100008. <https://doi.org/10.1016/j.jaecs.2020.100008>.
- [113] M.P. Burke, Z. Chen, Y. Ju, F.L. Dryer, Effect of cylindrical confinement on the determination of laminar flame speeds using outwardly propagating flames, *Combust. Flame* 156 (2009) 771–779. <https://doi.org/10.1016/j.combustflame.2009.01.013>.
- [114] R.J. Moffat, Describing the uncertainties in experimental results, *Exp. Therm. Fluid Sci.* 1 (1988) 3–17. [https://doi.org/10.1016/0894-1777\(88\)90043-X](https://doi.org/10.1016/0894-1777(88)90043-X).

- [115] P. Brequigny, H. Uesaka, Z. Sliti, D. Segawa, F. Foucher, G. Dayma, Uncertainty in measuring laminar burning velocity from expanding methane-air flames at low pressures, in: 11th Mediterr. Combust. Symp., 2019: pp. 16–20.
- [116] Z. Chen, Effects of radiation on large-scale spherical flame propagation, *Combust. Flame* 183 (2017) 66–74. <https://doi.org/10.1016/j.combustflame.2017.04.031>.
- [117] J.C. Prince, C. Treviño, F.A. Williams, A reduced reaction mechanism for the combustion of n-butane, *Combust. Flame* 175 (2017) 27–33. <https://doi.org/10.1016/j.combustflame.2016.06.033>.
- [118] G. Bagheri, E. Ranzi, M. Pelucchi, A. Parente, A. Frassoldati, T. Faravelli, Comprehensive kinetic study of combustion technologies for low environmental impact: MILD and OXY-fuel combustion of methane, *Combust. Flame* 212 (2020) 142–155. <https://doi.org/10.1016/j.combustflame.2019.10.014>.
- [119] S. Ren, S.L. Kokjohn, Z. Wang, H. Liu, B. Wang, J. Wang, A multi-component wide distillation fuel (covering gasoline, jet fuel and diesel fuel) mechanism for combustion and PAH prediction, *Fuel* 208 (2017) 447–468. <https://doi.org/10.1016/j.fuel.2017.07.009>.
- [120] C.W. Zhou, Y. Li, U. Burke, C. Banyon, K.P. Somers, S. Ding, S. Khan, J.W. Hargis, T. Sikes, O. Mathieu, E.L. Petersen, M. AlAbbad, A. Farooq, Y. Pan, Y. Zhang, Z. Huang, J. Lopez, Z. Loparo, S.S. Vasu, H.J. Curran, An experimental and chemical kinetic modeling study of 1,3-butadiene combustion: Ignition delay time and laminar flame speed measurements, *Combust. Flame* 197 (2018) 423–438. <https://doi.org/10.1016/j.combustflame.2018.08.006>.
- [121] A. Kéromnès, W.K. Metcalfe, K.A. Heufer, N. Donohoe, A.K. Das, C.J. Sung, J. Herzler, C. Naumann, P. Griebel, O. Mathieu, M.C. Krejci, E.L. Petersen, W.J. Pitz, H.J. Curran, An experimental and detailed chemical kinetic modeling study of hydrogen and syngas mixture oxidation at elevated pressures, *Combust. Flame* 160 (2013) 995–1011. <https://doi.org/10.1016/j.combustflame.2013.01.001>.
- [122] L. Kawka, G. Juhász, M. Papp, T. Nagy, I.G. Zsély, T. Turányi, Comparison of detailed reaction mechanisms for homogeneous ammonia combustion, *Zeitschrift Für Phys. Chemie* 234 (2020) 1329–1357. <https://doi.org/10.1515/zpch-2020-1649>.
- [123] H. Yu, W. Han, J. Santner, X. Gou, C.H. Sohn, Y. Ju, Z. Chen, Radiation-induced uncertainty in laminar flame speed measured from propagating spherical flames, *Combust. Flame* 161 (2014) 2815–2824. <https://doi.org/10.1016/j.combustflame.2014.05.012>.
- [124] S. Wang, Z. Wang, X. Han, C. Chen, Y. He, Y. Zhu, K. Cen, Experimental and numerical study of the effect of elevated pressure on laminar burning velocity of lean H₂/CO/O₂/diluent flames, *Fuel* 273 (2020) 117753. <https://doi.org/10.1016/j.fuel.2020.117753>.
- [125] C. Prathap, A. Ray, M.R. Ravi, Investigation of nitrogen dilution effects on the laminar burning velocity and flame stability of syngas fuel at atmospheric condition, *Combust. Flame* 155 (2008) 145–160. <https://doi.org/10.1016/j.combustflame.2008.04.005>.
- [126] R. Shang, Y. Zhang, M. Zhu, Z. Zhang, D. Zhang, G. Li, Laminar flame speed of CO₂ and N₂ diluted H₂/CO/air flames, *Int. J. Hydrogen Energy* 41 (2016) 15056–15067. <https://doi.org/10.1016/j.ijhydene.2016.05.064>.
- [127] Y. Xie, X. Wang, H. Bi, Y. Yuan, J. Wang, Z. Huang, B. Lei, A comprehensive review on laminar spherically premixed flame propagation of syngas, *Fuel Process. Technol.* 181 (2018) 97–114. <https://doi.org/10.1016/j.fuproc.2018.09.016>.
- [128] D. Lapalme, F. Halter, C. Mounaïm-Rousselle, P. Seers, Characterization of thermodiffusive and hydrodynamic mechanisms on the cellular instability of syngas fuel blended with CH₄ or CO₂, *Combust. Flame* 193 (2018) 481–490. <https://doi.org/10.1016/j.combustflame.2018.03.028>.

- [129] Y. Xie, Q. Li, A review on mixing laws of laminar flame speed and their applications on H₂/CH₄/CO/air mixtures, *Int. J. Hydrogen Energy* 45 (2020) 20482–20490. <https://doi.org/10.1016/j.ijhydene.2019.10.136>.
- [130] H.J. Burbano, J. Pareja, A.A. Amell, Laminar burning velocities and flame stability analysis of H₂/CO/air mixtures with dilution of N₂ and CO₂, *Int. J. Hydrogen Energy* 36 (2011) 3232–3242. <https://doi.org/10.1016/j.ijhydene.2010.11.089>.
- [131] M. Metghalchi, J.C. Keck, Burning velocities of mixtures of air with methanol, isooctane, and indolene at high pressure and temperature, *Combust. Flame* 48 (1982) 191–210. [https://doi.org/10.1016/0010-2180\(82\)90127-4](https://doi.org/10.1016/0010-2180(82)90127-4).
- [132] S. Hu, J. Gao, C. Gong, Y. Zhou, X.S. Bai, Z.S. Li, M. Alden, Assessment of uncertainties of laminar flame speed of premixed flames as determined using a Bunsen burner at varying pressures, *Appl. Energy* 227 (2018) 149–158. <https://doi.org/10.1016/j.apenergy.2017.09.083>.
- [133] S. Zitouni, P. Brequigny, C. Mounaïm-Rousselle, Influence of hydrogen and methane addition in laminar ammonia premixed flame on burning velocity, Lewis number and Markstein length, *Combust. Flame* 253 (2023). <https://doi.org/10.1016/j.combustflame.2023.112786>.
- [134] F. Wu, W. Liang, Z. Chen, Y. Ju, C.K. Law, Uncertainty in stretch extrapolation of laminar flame speed from expanding spherical flames, *Proc. Combust. Inst.* 35 (2015) 663–670. <https://doi.org/10.1016/j.proci.2014.05.065>.
- [135] W.K. Metcalfe, S.M. Burke, S.S. Ahmed, H.J. Curran, A hierarchical and comparative kinetic modeling study of C1 - C2 hydrocarbon and oxygenated fuels, *Int. J. Chem. Kinet.* 45 (2013) 638–675. <https://doi.org/10.1002/kin.20802>.
- [136] W. Anggono, A. Hayakawa, E.C. Okafor, G.J. Gotama, S. Wongso, Laminar Burning Velocity and Markstein Length of CH₄/CO₂/Air Premixed Flames at Various Equivalence Ratios and CO₂ Concentrations Under Elevated Pressure, *Combust. Sci. Technol.* 00 (2020) 1–20. <https://doi.org/10.1080/00102202.2020.1737032>.
- [137] Z. Chen, On the extraction of laminar flame speed and Markstein length from outwardly propagating spherical flames, *Combust. Flame* 158 (2011) 291–300. <https://doi.org/10.1016/j.combustflame.2010.09.001>.
- [138] P. Brequigny, A. Soulé, C. Mounaïm-Rousselle, G. Dayma, F. Halter, Experimental and Numerical Study of the Laminar Burning Velocity of Biogas–Ammonia–Air Premixed Flames, *Energies* 17 (2024) 319. <https://doi.org/10.3390/en17020319>.
- [139] J.D. Munzar, B. Akih-Kumgeh, B.M. Denman, A. Zia, J.M. Bergthorson, An experimental and reduced modeling study of the laminar flame speed of jet fuel surrogate components, *Fuel* 113 (2013) 586–597. <https://doi.org/10.1016/j.fuel.2013.05.105>.
- [140] C. Ji, E. Dames, Y.L. Wang, H. Wang, F.N. Egolfopoulos, Propagation and extinction of premixed C₅-C₁₂ n-alkane flames, *Combust. Flame* 157 (2010) 277–287. <https://doi.org/10.1016/j.combustflame.2009.06.011>.
- [141] R.G. Papagiannakis, S.R. Krishnan, D.C. Rakopoulos, K.K. Srinivasan, C.D. Rakopoulos, A combined experimental and theoretical study of diesel fuel injection timing and gaseous fuel/diesel mass ratio effects on the performance and emissions of natural gas-diesel HDDI engine operating at various loads, *Fuel* 202 (2017) 675–687. <https://doi.org/10.1016/J.FUEL.2017.05.012>.
- [142] A. Srna, B. von Rotz, K. Herrmann, K. Boulouchos, G. Bruneaux, Experimental investigation of pilot-fuel combustion in dual-fuel engines, Part 1: Thermodynamic analysis of combustion phenomena, *Fuel* (2019) 115642. <https://doi.org/10.1016/J.FUEL.2019.115642>.

- [143] A. Srna, B. von Rotz, M. Bolla, Y.M. Wright, K. Herrmann, K. Boulouchos, G. Bruneaux, Experimental investigation of pilot-fuel combustion in dual-fuel engines, Part 2: Understanding the underlying mechanisms by means of optical diagnostics, *Fuel* 255 (2019). <https://doi.org/10.1016/j.fuel.2019.115766>.
- [144] A. Srna, M. Bolla, Y.M. Wright, K. Herrmann, R. Bombach, S.S. Pandurangi, K. Boulouchos, G. Bruneaux, Effect of methane on pilot-fuel auto-ignition in dual-fuel engines, *Proc. Combust. Inst.* 37 (2019) 4741–4749. <https://doi.org/10.1016/j.proci.2018.06.177>.
- [145] N. Stylianidis, U. Azimov, A. Maheri, E. Tomita, N. Kawahara, Chemical kinetics and CFD analysis of supercharged micro-pilot ignited dual-fuel engine combustion of syngas, *Fuel* 203 (2017) 591–606. <https://doi.org/https://doi.org/10.1016/j.fuel.2017.04.125>.
- [146] Z. Xu, M. Jia, Y. Li, Y. Chang, G. Xu, L. Xu, X. Lu, Computational optimization of fuel supply, syngas composition, and intake conditions for a syngas/diesel RCCI engine, *Fuel* 234 (2018) 120–134. <https://doi.org/10.1016/j.fuel.2018.07.003>.
- [147] M. Costa, M. La Villetta, N. Massarotti, D. Piazzullo, V. Rocco, Numerical analysis of a compression ignition engine powered in the dual-fuel mode with syngas and biodiesel, *Energy* 137 (2017) 969–979. <https://doi.org/10.1016/J.ENERGY.2017.02.160>.
- [148] G. Woschni, A universally applicable equation for the instantaneous heat transfer coefficient in the internal combustion engine, *SAE Tech. Pap.* (1967). <https://doi.org/10.4271/670931>.
- [149] A.E. Dhole, R.B. Yarasu, D.B. Lata, Effect of hydrogen and producer gas as secondary fuels on combustion parameters of a dual fuel diesel engine, *Appl. Therm. Eng.* 108 (2016). <https://doi.org/10.1016/j.applthermaleng.2016.07.157>.
- [150] E.G. Giakoumis, D.C. Rakopoulos, C.D. Rakopoulos, Combustion noise radiation during dynamic diesel engine operation including effects of various biofuel blends: A review, *Renew. Sustain. Energy Rev.* 54 (2016) 1099–1113. <https://doi.org/10.1016/J.RSER.2015.10.129>.
- [151] N. Kousheshi, M. Yari, A. Paykani, A.S. Mehr, G.F. de la Fuente, Effect of syngas composition on the combustion and emissions characteristics of a syngas/diesel RCCI engine, *Energies* 13 (2020). <https://doi.org/10.3390/en13010212>.
- [152] L. Xiang, H. Chu, F. Ren, M. Gu, Numerical analysis of the effect of CO₂ on combustion characteristics of laminar premixed methane/air flames, *J. Energy Inst.* 92 (2019) 1487–1501. <https://doi.org/10.1016/j.joei.2018.06.018>.
- [153] F. Halter, F. Foucher, L. Landry, C. Mounaim-Rousselle, Effect of dilution by nitrogen and/or carbon dioxide on methane and iso-octane air flames, *Combust. Sci. Technol.* 181 (2009) 813–827. <https://doi.org/10.1080/00102200902864662>.
- [154] C. Lhuillier, P. Brequigny, F. Contino, C. Mounaim-Rousselle, Experimental study on ammonia/hydrogen/air combustion in spark ignition engine conditions, *Fuel* 269 (2020) 117448. <https://doi.org/10.1016/j.fuel.2020.117448>.
- [155] D.C. Rakopoulos, C.D. Rakopoulos, E.G. Giakoumis, R.G. Papagiannakis, Evaluating Oxygenated Fuel's Influence on Combustion and Emissions in Diesel Engines Using a Two-Zone Combustion Model, *J. Energy Eng.* 144 (2018) 04018046. [https://doi.org/10.1061/\(ASCE\)EY.1943-7897.0000556](https://doi.org/10.1061/(ASCE)EY.1943-7897.0000556).
- [156] A. Srna, Experimental Characterization of Pilot-Fuel Ignition, Combustion, and Soot Formation in Dual-Fuel Combustion Systems, 2018. <https://doi.org/10.3929/ETHZ-B-000309334>.
- [157] H. Zhao, N. Ladommatos, Optical diagnostics for soot and temperature measurement in diesel engines, *Prog. Energy Combust. Sci.* 24 (1998) 221–255. [https://doi.org/10.1016/S0360-1285\(97\)00033-6](https://doi.org/10.1016/S0360-1285(97)00033-6).

- [158] A.G. Gaydon, *The Spectroscopy of Flames*, Springer Netherlands, Dordrecht, 1974. <https://doi.org/10.1007/978-94-009-5720-6>.
- [159] E. Mancaruso, M. Todino, B.M. Vaglieco, Study on dual fuel combustion in an optical research engine by infrared diagnostics varying methane quantity and engine speed, *Appl. Therm. Eng.* 178 (2020) 115623. <https://doi.org/10.1016/j.applthermaleng.2020.115623>.
- [160] R. Augusta, D.E. Foster, J.B. Ghandhi, J. Eng, P.M. Najt, Chemiluminescence measurements of homogeneous charge compression ignition (HCCI) combustion, *SAE Tech. Pap.* 2006 (2006). <https://doi.org/10.4271/2006-01-1520>.
- [161] A. Srna, G. Bruneaux, B. von Rotz, R. Bombach, K. Herrmann, K. Boulouchos, Optical Investigation of Sooting Propensity of n-Dodecane Pilot/Lean-Premixed Methane Dual-Fuel Combustion in a Rapid Compression-Expansion Machine, *SAE Int. J. Engines* 11 (2018) 1049–1068. <https://doi.org/10.4271/2018-01-0258>.
- [162] H.W. Huang, Y. Zhang, Syngas combustion radiation profiling through spectrometry and DFCD processing techniques, *Int. J. Hydrogen Energy* 37 (2012) 5257–5267. <https://doi.org/10.1016/j.ijhydene.2011.12.048>.
- [163] R.N. Dahms, G.A. Paczko, S.A. Skeen, L.M. Pickett, Understanding the ignition mechanism of high-pressure spray flames, *Proc. Combust. Inst.* 36 (2017) 2615–2623. <https://doi.org/10.1016/j.proci.2016.08.023>.
- [164] Z. Ahmad, J. Aryal, O. Ranta, O. Kaario, V. Vuorinen, M. Larmi, An Optical Characterization of Dual-Fuel Combustion in a Heavy-Duty Diesel Engine, *SAE Tech. Pap.* 2018-April (2018) 1–10. <https://doi.org/10.4271/2018-01-0252>.
- [165] C.J. Ulishney, C.E. Dumitrescu, Optical investigation of methane, ethane, or propane and diesel at low load RCCI conditions, (2023). <https://doi.org/10.1016/j.fuel.2023.129472>.
- [166] S. Wüthrich, P. Cartier, P. Süess, B. Schneider, P. Obrecht, K. Herrmann, Optical investigation and thermodynamic analysis of premixed ammonia dual-fuel combustion initiated by dodecane pilot fuel, *Fuel Commun.* 12 (2022) 100074. <https://doi.org/10.1016/j.jfueco.2022.100074>.
- [167] W. Sun, W. Zeng, L. Guo, H. Zhang, Y. Yan, S. Lin, G. Zhu, M. Jiang, C. Yu, F. Wu, An optical study of the combustion and flame development of ammonia-diesel dual-fuel engine based on flame chemiluminescence, *Fuel* 349 (2023) 128507. <https://doi.org/10.1016/j.fuel.2023.128507>.
- [168] F. Solferini de Carvalho, A. Peñaranda Mendoza, L. Ribeiro dos Santos, C. Henrique Rufino, E. Malheiro de Oliveira, M. Ferreira Silva, E. Blanco Machin, D. Travieso Pedroso, P. Teixeira Lacava, Experimental study of the methane and producer gas blends in an optical spark ignition engine: Combustion characteristics, thermodynamics and emissions, *Int. J. Engine Res.* 24 (2023) 2708–2726. <https://doi.org/10.1177/14680874221131117>.
- [169] F. Solferini de Carvalho, C.H. Rufino, E. Malheiro de Oliveira, A.P. Mendoza, L. Ribeiro dos Santos, E.B. Machin, D.T. Pedroso, P.T. Lacava, Experimental investigation of hydrogen-producer gas mixtures in an optically accessible SI engine, *Int. J. Hydrogen Energy* 58 (2024) 500–513. <https://doi.org/10.1016/j.ijhydene.2024.01.165>.
- [170] T. Shudo, Y. Nakajima, K. Tsuga, Combustion characteristics of H₂-CO-CO₂ mixture in an IC engine, *SAE Tech. Pap.* 2001 (2001). <https://doi.org/10.4271/2001-01-0252>.
- [171] T. Shudo, T. Nagano, M. Robavashi, Combustion characteristics of waste-pyrolysis gases in an internal combustion engine, *Int. J. Automot. Technol.* 4 (2003) 1–8.
- [172] S.D. Martinez-Boggio, S.S. Merola, P. Teixeira Lacava, A. Irimescu, P.L. Curto-Risso, Effect of Fuel and Air Dilution on Syngas Combustion in an Optical SI Engine, *Energies* 2019, Vol. 12, Page 1566 12 (2019) 1566. <https://doi.org/10.3390/EN12081566>.

- [173] A. Srna, R. Bombach, K. Herrmann, G. Bruneaux, Characterization of the spectral signature of dual-fuel combustion luminosity: implications for evaluation of natural luminosity imaging, *Appl. Phys. B Lasers Opt.* 125 (2019) 1–16. <https://doi.org/10.1007/s00340-019-7222-z>.
- [174] Q. Cheng, Z. Ahmad, O. Kaario, M. Larmi, Simultaneous Visualization of Natural Luminosity and Chemiluminescence of Dual Fuel Combustion in an Optically Accessible Engine, in: *SAE Tech. Pap.*, 2020. <https://doi.org/10.4271/2020-01-0309>.
- [175] X. Yu, K. Zha, X. Luo, D. Taraza, M. Jansons, Simulation and experimental measurement of CO₂^{*}, OH^{*} and CH₂O^{*} chemiluminescence from an optical diesel engine fueled with n-heptane, *SAE Tech. Pap.* 6 (2013). <https://doi.org/10.4271/2013-24-0010>.
- [176] J.M. Desantes, J.M. García-Oliver, W. Vera-Tudela, D. López-Pintor, B. Schneider, K. Boulouchos, Study of ignition delay time and generalization of auto-ignition for PRFs in a RCEM by means of natural chemiluminescence, *Energy Convers. Manag.* 111 (2016) 217–228. <https://doi.org/10.1016/J.ENCONMAN.2015.12.052>.
- [177] S. Schlatter, B. Schneider, Y.M. Wright, K. Boulouchos, N-heptane micro pilot assisted methane combustion in a Rapid Compression Expansion Machine, *Fuel* 179 (2016) 339–352. <https://doi.org/10.1016/j.fuel.2016.03.006>.
- [178] R. Rajasegar, A. Srna, T. Lee, Impact of Hydrogen on the Ignition and Combustion Behavior Diesel Sprays in a Dual Fuel, Diesel-Piloted, Premixed Hydrogen Engine, in: *SAE Int. J. Adv. Curr. Pract. Mobil.*, SAE International, 2023: pp. 1762–1776. <https://doi.org/10.4271/2023-24-0061>.
- [179] K. Kumar, G. Mittal, C.-J. Sung, Autoignition of n-decane under elevated pressure and low-to-intermediate temperature conditions, *Combust. Flame* 156 (2009) 1278–1288. <https://doi.org/10.1016/j.combustflame.2009.01.009>.
- [180] R. Rajasegar, A. Srna, T. Lee, Impact of Hydrogen on the Ignition and Combustion Behavior Diesel Sprays in a Dual Fuel, Diesel-Piloted, Premixed Hydrogen Engine, *SAE Tech. Pap. Ser. 1* (2023). <https://doi.org/10.4271/2023-24-0061>.
- [181] S. Gersen, H. Darneveil, H. Levinsky, The effects of CO addition on the autoignition of H₂, CH₄ and CH₄/H₂ fuels at high pressure in an RCM, *Combust. Flame* 159 (2012) 3472–3475. <https://doi.org/10.1016/j.combustflame.2012.06.021>.
- [182] G. Mittal, C.J. Sung, R.A. Yetter, Autoignition of H₂/CO at elevated pressures in a rapid compression machine, *Int. J. Chem. Kinet.* 38 (2006) 516–529. <https://doi.org/10.1002/KIN.20180>.
- [183] G. Mittal, C.J. Sung, M. Fairweather, A.S. Tomlin, J.F. Griffiths, K.J. Hughes, Significance of the HO₂ + CO reaction during the combustion of CO + H₂ mixtures at high pressures, *Proc. Combust. Inst.* 31 (2007) 419–427. <https://doi.org/10.1016/J.PROCI.2006.07.068>.
- [184] L.D. Thi, Y. Zhang, Z. Huang, Shock tube study on ignition delay of multi-component syngas mixtures – Effect of equivalence ratio, *Int. J. Hydrogen Energy* 39 (2014) 6034–6043. <https://doi.org/10.1016/J.IJHYDENE.2014.01.170>.
- [185] O. Mathieu, M.M. Kopp, E.L. Petersen, Shock-tube study of the ignition of multi-component syngas mixtures with and without ammonia impurities, *Proc. Combust. Inst.* 34 (2013) 3211–3218. <https://doi.org/10.1016/J.PROCI.2012.05.008>.
- [186] ArenaRed | CPBC / RCCI, (n.d.). <https://www.arenared.nl/cpbc+~+rcci> (accessed November 11, 2023).

Ricardo RABELLO DE CASTRO

Effet de la composition du gaz synthétique, 'Syngas', sur la combustion des moteurs bi-carburants

Résumé :

Le gaz de synthèse, également appelé 'syngas', est considéré comme un carburant alternatif prometteur pour lutter à la fois contre le réchauffement climatique et la gestion des déchets, deux défis majeurs de la société moderne. La composition chimique du gaz de synthèse dépend fortement des caractéristiques de la matière première et du processus utilisé pour sa production, et son efficacité en tant que carburant dans les moteurs à combustion. L'objectif principal de cette étude est de déterminer comment optimiser un moteur à combustion interne bicarburant (ICE) syngas/diesel pour différentes compositions de gaz de synthèse, ratios de substitution diesel et ratios d'équivalence gaz/air. Nous commençons par donner un aperçu des moyens de sa production et des compositions du gaz de synthèse pour sélectionner trois mélanges représentatifs de ses éléments de base. Ensuite, nous examinons les études sur le syngas/diesel (ou autre carburant à haute réactivité) pour déterminer comment chaque paramètre affecte les performances et les émissions du moteur. Dans le chapitre suivant, nous déterminons deux propriétés de combustion, à savoir les vitesses de flamme laminaire et les longueurs de Markstein, pour plusieurs conditions pertinentes pour le moteur et pour les trois compositions. Ensuite, nous poursuivons les expériences menées dans un moteur entièrement métallique (non translucide) pour mesurer les performances du moteur et les émissions d'échappement. Dans cette expérience, nous explorons comment le rapport énergétique syngas-diesel, le rapport d'équivalence gaz de synthèse/air prémélangé et les effets de la composition du gaz de synthèse produisent différents résultats de performance et émissions d'échappement. Enfin, nous effectuons des expériences dans un moteur optique Dual-Fuel pour déterminer le comportement des flammes et des radicaux, par analyse des images de combustion du moteur.

Mots clés : syngas, biocarburants, moteurs bi-carburant

Effect of the fuel composition of syngas on the combustion process in Dual-Fuel engine

Summary :

Synthesis Gas, also known as Syngas, is deemed as a promising alternative fuel to tackle both global warming and waste management - two major challenges for modern society. The chemical composition of syngas, however, is highly dependent on the characteristics of the feedstock and the process used in its production; and so is its efficiency as a fuel in combustion engines. The main goal of this study is to determine how to optimize a syngas/diesel Dual-Fuel Internal Combustion Engine (ICE) for different syngas compositions, diesel substitution ratios and syngas/air equivalence ratios. We start providing an overview of syngas production and compositions to select three representative mixtures of its basic elements. Afterwards, we review Dual-Fuel syngas/diesel (or a high-reactivity fuel) studies to determine how each parameter affects the engine performance and emissions. In the following chapter, we determine two combustion properties, namely, the laminar flame speeds and the Markstein lengths, for several engine-relevant conditions for the three compositions. Then, we proceed conducting experiments in a full-metal (non-translucid) engine to measure engine performance and exhaust emissions. In that experiment we explore how the syngas-diesel energy ratio, the premixed Syngas/air equivalence ratio and the Syngas composition effects, produce different performance results and exhaust emissions. Finally, we perform experiments in an optical Dual-Fuel engine to determine flame and radicals' behaviors, followed by an analysis of engine combustion images.

Keywords : syngas, biofuel, dual-fuel engine



Université d'Orléans –
Laboratoire PRISME
8 rue Léonard de Vinci
45 072 ORLÉANS Cedex 2
FRANCE

